

## Miniaturized Near-Earth Asteroid Fly-by Missions Navigation and AOCS Design

Casini, S.

**DOI**

[10.4233/uuid:537031a6-bb85-4e62-8a6a-f3380db04d8f](https://doi.org/10.4233/uuid:537031a6-bb85-4e62-8a6a-f3380db04d8f)

**Publication date**

2024

**Document Version**

Final published version

**Citation (APA)**

Casini, S. (2024). *Miniaturized Near-Earth Asteroid Fly-by Missions: Navigation and AOCS Design*. [Dissertation (TU Delft), Delft University of Technology]. <https://doi.org/10.4233/uuid:537031a6-bb85-4e62-8a6a-f3380db04d8f>

**Important note**

To cite this publication, please use the final published version (if applicable).  
Please check the document version above.

**Copyright**

Other than for strictly personal use, it is not permitted to download, forward or distribute the text or part of it, without the consent of the author(s) and/or copyright holder(s), unless the work is under an open content license such as Creative Commons.

**Takedown policy**

Please contact us and provide details if you believe this document breaches copyrights.  
We will remove access to the work immediately and investigate your claim.

# **MINIATURIZED NEAR-EARTH ASTEROID FLY-BY MISSIONS**

NAVIGATION AND AOCS DESIGN



# **MINIATURIZED NEAR-EARTH ASTEROID FLY-BY MISSIONS**

NAVIGATION AND AOCS DESIGN

## **Proefschrift**

ter verkrijging van de graad van doctor  
aan de Technische Universiteit Delft,  
op gezag van de Rector Magnificus prof. dr. ir. T.H.J.J. van de Hagen,  
voorzitter van het College voor Promoties,  
in het openbaar te verdedigen op donderdag 11 juli 2024 om 10:00 uur

door

**Stefano CASINI**

Master of Science in Space and Astronautical Engineering,  
Sapienza University of Rome, Rome, Italië,  
geboren te Rome, Italië.

Dit proefschrift is goedgekeurd door de

promotor: prof. dr. ir. P.N.A.M. Visser

copromotor: dr. A. Cervone

Samenstelling promotiecommissie:

Rector Magnificus,  
Prof. dr. ir. P.N.A.M. Visser,  
Dr. A. Cervone,

voorzitter  
Technische Universiteit Delft, promotor  
Technische Universiteit Delft, copromotor

*Onafhankelijke leden:*

Prof. dr. G.C.H.E. de Croon,  
Prof. dr. ir. A.J. van der Veen  
Dr. A. Menicucci  
Prof. dr. A. Golkar  
Prof. dr. M. Vasile  
Dr. S. Spretta

Technische Universiteit Delft  
Technische Universiteit Delft  
Technische Universiteit Delft  
Technische Universität München, Duitsland  
University of Strathclyde, Schotland  
Technische Universiteit Delft, reservelid



*Keywords:* Autonomous Navigation, Deep-Space CubeSat, AOCS, Attitude Determination

*Printed by:* IPSKAMP printing

*Front & Back:* The cover art symbolizes the passion for space exploration, which I still look at with a child's eyes. The idea is inspired by Banksy's Girl with Balloon, and it has been designed by Matteo Casini.

Copyright © 2024 by S. Casini

ISBN 000-00-0000-000-0

An electronic version of this dissertation is available at  
<http://repository.tudelft.nl/>.

Every unasked question has a definite 'no' as an answer.



# CONTENTS

<b>Summary</b>	<b>xi</b>
<b>Samenvatting</b>	<b>xiii</b>
<b>List of Abbreviations</b>	<b>xvii</b>
<b>List of Figures</b>	<b>xix</b>
<b>List of Tables</b>	<b>xxv</b>
<b>1 Introduction</b>	<b>1</b>
1.1 Deep-Space exploration history . . . . .	2
1.2 Miniaturized spacecraft: CubeSat . . . . .	4
1.2.1 Deep-space CubeSat trends . . . . .	5
1.3 Autonomous Navigation . . . . .	8
1.3.1 Optical Navigation . . . . .	9
1.3.2 X-Ray Pulsar Navigation . . . . .	9
1.3.3 Radiometric navigation . . . . .	10
1.3.4 Applicability to deep-space mission phases . . . . .	10
1.3.5 Navigation Requirements . . . . .	11
1.4 Research Questions . . . . .	12
1.4.1 RQ1 . . . . .	12
1.4.2 RQ2 . . . . .	13
1.4.3 RQ3 . . . . .	13
1.4.4 RQ4 . . . . .	13
1.5 Dissertation outline . . . . .	14
<b>2 Mission and Platform Design</b>	<b>15</b>
2.1 Mission Type Description . . . . .	16
2.2 Subsystems Analysis . . . . .	17
2.2.1 Payload . . . . .	17
2.2.2 Propulsion . . . . .	20
2.2.3 ADCS . . . . .	25
2.2.4 Communication . . . . .	28
2.2.5 On-Board data handling . . . . .	31
2.2.6 Power . . . . .	32
2.3 3U Platform . . . . .	35
2.4 Conclusions . . . . .	39



<b>3</b>	<b>AOCS Design for Miniaturized Asteroid Fly-By Missions</b>	<b>41</b>
3.1	Introduction . . . . .	42
3.2	Propulsion systems . . . . .	43
3.2.1	Chemical Propulsion analysis . . . . .	43
3.2.2	Electric Propulsion Analysis . . . . .	44
3.3	ACS Design . . . . .	57
3.3.1	Thrusters Orientation . . . . .	58
3.3.2	Control algorithms . . . . .	63
3.3.3	De-tumbling . . . . .	66
3.3.4	Reaction wheels desaturation . . . . .	69
3.3.5	Optimal firing tracking . . . . .	71
3.3.6	Asteroid Fly-By . . . . .	72
3.4	Conclusions . . . . .	74
<b>4</b>	<b>Line-of-Sight Optical Navigation</b>	<b>77</b>
4.1	Introduction . . . . .	78
4.2	LoS Navigation . . . . .	78
4.3	Simulation Approach . . . . .	79
4.4	Navigation Filter . . . . .	81
4.5	Performance indicators . . . . .	84
4.6	Parameters under analysis . . . . .	84
4.7	Semi-analytical geometry analysis . . . . .	86
4.8	Sensitivity analysis . . . . .	88
4.8.1	Position and Velocity RMSE . . . . .	89
4.8.2	Convergence Time . . . . .	92
4.9	Navigation for NEA missions . . . . .	95
4.9.1	Navigation Figure of Merit . . . . .	95
4.9.2	NEAs ephemeris propagation . . . . .	95
4.9.3	FoM computation . . . . .	96
4.9.4	NEAs fly-by mission examples . . . . .	96
4.10	Conclusion . . . . .	103
<b>5</b>	<b>Design and Testing of Star-Tracker Algorithms for Line-of-Sight Navigation</b>	<b>107</b>
5.1	Introduction . . . . .	108
5.2	Space Image Simulator . . . . .	109
5.2.1	Star simulation . . . . .	109
5.2.2	Planet Simulation . . . . .	110
5.2.3	Hardware Selection . . . . .	112
5.3	Attitude Estimation Chain Design . . . . .	114
5.3.1	Centroiding algorithm selection . . . . .	115
5.3.2	Star Identification . . . . .	117
5.3.3	Wahba's problem solver . . . . .	120
5.4	Planet centroiding . . . . .	120
5.5	Complete testing . . . . .	123
5.5.1	Venus Observation . . . . .	124
5.5.2	Jupiter Observation . . . . .	126

5.6	Synthetic-images-in-the-loop Navigation Analysis . . . . .	129
5.6.1	AEKF . . . . .	129
5.6.2	Analysis . . . . .	131
5.7	Conclusions. . . . .	136
<b>6</b>	<b>Combined Line-of-Sight Radiometric Navigation for distributed deep-space systems</b>	<b>139</b>
6.1	Introduction . . . . .	140
6.2	Distributed Space Systems Architectures . . . . .	141
6.3	Combined LoS and Crosslink Radiometric Navigation . . . . .	141
6.3.1	Performance of the two spacecraft DSS architecture . . . . .	147
6.3.2	Performance of the three spacecraft DSS architecture . . . . .	149
6.3.3	Mission to NEA example . . . . .	150
6.4	Conclusions. . . . .	152
<b>7</b>	<b>Conclusion</b>	<b>155</b>
7.1	Summary . . . . .	156
7.2	Main Findings and Conclusions. . . . .	156
7.3	Key Innovations and Contributions of the dissertation . . . . .	159
7.4	Recommendations . . . . .	161
	<b>Bibliography</b>	<b>164</b>
	<b>Acknowledgements</b>	<b>173</b>
<b>A</b>	<b>Navigation Requirements</b>	<b>177</b>
A.1	Asteroid ephemeris uncertainties . . . . .	177
A.1.1	(433) Eros uncertainties propagation . . . . .	178
A.1.2	(2100) Ra-Shalom uncertainties propagation . . . . .	179
A.2	Detectable Magnitude . . . . .	180
A.3	$\Delta V$ Capabilities . . . . .	181
A.4	Requirements definition . . . . .	182
	<b>Curriculum Vitae</b>	<b>187</b>
	<b>List of Publications</b>	<b>189</b>



# SUMMARY

The exploration of deep-space targets, either other planets, moons, or asteroids, has been a leitmotiv for space technology advancement since the early days of space exploration. Nowadays, the interest in Near-Earth Asteroids (NEA) missions has seen a rise because of the multiple objectives, such as planetary protection, in-situ resource exploitation, and scientific research on the evolution of the Solar System. In this framework, the increasing attention towards these missions can be powered by exploiting some of the most recent trends in space technology: miniaturization and autonomy.

This dissertation aims to fill different gaps in the design of miniaturized Near-Earth Asteroid (NEA) missions, which are a hot topic for the next decades of deep-space exploration. In this context, the gaps are identified in:

- the exploitation of a 3U CubeSat platform for such missions;
- the application of autonomous navigation technique for the cruise phase.

The first half of this dissertation delves into addressing the first gap by meticulously examining generic NEA missions. Initially, the essential characteristics of these missions are delineated and generic requirements are formulated. A thorough analysis of each pertinent subsystem is undertaken, scrutinizing the available Commercial-off-the-Shelf (COTS) options in the market. The investigation aims to identify adaptable components while distinguishing those necessitating bespoke design. The analysis culminates with the presentation of critical parameters such as mass, volume, and power budgets, and with the preliminary design of a 3U CubeSat platform within 4 kg of mass.

Later, the initial system design is extended, with a specific emphasis on the Attitude and Orbit Control System (AOCS). Following the refinement of previously introduced budgets, the analysis shifts its focus to evaluating the viability of COTS propulsion systems for NEA missions. First, chemical propulsion options are evaluated by solving Lambert's problem for over 13000 NEA nodal passages, identifying a large number of feasible mission scenarios with the AerojetRocketdyne MPS-130. Then, electric propulsion options are evaluated for a smaller NEAs set, because of the largest computational load, showing that for closer NEAs, electric propulsion offers comparable performance, but further away from the Earth it does not allow to reach many targets. Afterwards, the exploration of solutions and algorithms for the attitude control systems becomes paramount, first developing an optimized placement and orientation strategy for Reaction Control Thrusters (RCTs), used for reaction wheels desaturation. Then the detumbling and wheel desaturation problems are solved by implementing a Linear Quadratic Regulator (LQR), and finally, the asteroid and firing direction tracking problems are solved by implementing a Lyapunov direct controller.

The latter portion of the dissertation addresses the second identified gap by exploring optical line-of-sight navigation as an autonomous technique for NEA missions, by investigating various facets of this technique. Initially, a higher-level perspective analysis is carried out, examining the impact of observation geometry, measurement error, and tracking frequency on the efficacy of optical line-of-sight navigation. It is shown how the simultaneous observation of two planets offers superior navigation performance when compared to the single planet observation, and that these performances further improve when the separation angle between the two planets gets closer to  $90^\circ$ . The application of these considerations to NEA missions is discussed, demonstrating how the technique aligns with the navigation requirements outlined in the introduction, as with measurement errors in the range 1-10 arcsecs, the positioning error can be kept below 1000 km.

Then, the focus is narrowed to image processing to extract the line-of-sight direction from star-tracker images. Beginning with the development of a synthetic image simulator for testing, the analysis progresses to designing and testing the attitude estimation chain. This includes centroiding, star identification, and solving Wahba's problem. The centroiding algorithm is based on a Gaussian least squares fitting method, the star identification problem is solved by implementing a three-stars pattern recognition method, and finally, the rotation matrix is found by using a Singular Value Decomposition (SVD) method. A specialized illumination compensation algorithm is introduced for planet centroiding, resulting in a measurement error below 1 arcsecond. Finally, testing with synthetic images of Venus and Jupiter is conducted, leading to the development of an Adaptive Extended Kalman Filter (AEKF), which is an extension of the canonic Extended Kalman Filter (EKF), that allows taking into account a measurement noise distribution significantly different from being Gaussian.

Finally, NEA missions are analyzed from a different perspective, investigating the application of distributed space systems. The study particularly concentrates on the fusion of optical line-of-sight navigation and crosslink radiometric navigation. The analysis encompasses four distinct network configurations, comprising two or three satellites each. The promising outcomes underscore the applicability of the combined navigation technique, showcasing performance comparable to baseline techniques.

The culmination of this research underscores the preliminary feasibility of utilizing a 3U platform for NEA missions. Additionally, the study significantly advances our understanding of autonomous line-of-sight optical navigation techniques in the context of deep-space cruising, paving the way for further developments in the field.

# SAMENVATTING

De verkenning van het universum, of het nu gaat om andere planeten, manen of asteroïden, is een leidmotief geweest voor de vooruitgang van ruimtetechnologie sinds de het begin van de ruimtevaart. Tegenwoordig is de belangstelling voor missies naar Near-Earth Asteroids (NEA, aardscheerders) toegenomen vanwege diverse doelstellingen, zoals planetaire bescherming, exploitatie van aanwezige grondstoffen en wetenschappelijk onderzoek naar de evolutie van het zonnestelsel. In dit kader kan de toenemende aandacht voor deze missies worden verklaard door belangrijke recente trends in ruimtetechnologie: miniaturisatie en autonomie. Dit proefschrift heeft als doel verschillende vragen in het ontwerp van geminiaturiseerde missies naar NEA's te beantwoorden, die belangrijk zijn voor het komende decennium van ruimteverkenning. Hiertoe zijn de volgende onderwerpen geïdentificeerd:

- de exploitatie van een 3U CubeSat-platform voor dergelijke missies;
- de toepassing van autonome navigatietechnieken voor de cruise fase.

Het eerste deel van dit proefschrift gaat diep in op het aanpakken van het eerste ontwerp door generieke NEA-missies nauwgezet te onderzoeken. Aanvankelijk worden de essentiële kenmerken van deze missies uiteengezet en worden generieke eisen geformuleerd. Een grondige analyse van elk relevant subsysteem wordt uitgevoerd, waarbij de beschikbare Commercial-off-the-Shelf (COTS) opties op de markt worden onderzocht. Het onderzoek heeft tot doel aanpasbare componenten te identificeren en tegelijkertijd die te onderscheiden die een op maat gemaakt ontwerp vereisen. De analyse wordt afgerond met de presentatie van kritieke parameters zoals massa-, volume- en vermogensbudgetten, en met het voorlopige ontwerp van een 3U CubeSat-platform met een massa van 4 kg. Later wordt het initiële systeemontwerp uitgebreid, met speciale nadruk op het Attitude and Orbit Control System (AOCS, standregel- en baancontrolesysteem). Na de verfijning van eerder geïntroduceerde budgetten verschuift de analyse de focus naar de haalbaarheid van Commercial-off-the-Shelf (COTS) voortstuwingssystemen voor NEA-missies. Eerst worden chemische voortstuwingsopties geëvalueerd door Lambert's probleem op te lossen voor meer dan 13000 NEA-knoopdoorgangen, waarbij een groot aantal haalbare missiescenario's wordt geïdentificeerd met de AerojetRocketdyne MPS-130. Vervolgens worden elektrische voortstuwingsopties geëvalueerd voor een kleinere set NEA's, vanwege de zeer grote rekenlast, waarbij wordt aangetoond dat voor dichterbij gelegen NEA's elektrische voortstuwing vergelijkbare prestaties biedt, maar verder van de aarde niet in staat is om veel doelen te bereiken. Daarna wordt het verkennen van oplossingen en algoritmes voor de standregel-systemen van cruciaal belang, waarbij eerst een geoptimaliseerde plaatsings- en oriëntatiestrategie wordt ontwikkeld voor Reaction Control Thrusters (RCT's), die worden gebruikt voor de desaturatie van reactiewielen. Vervolgens worden de detumbling- en desaturatieproblemen opgelost door een

Linear Quadratic Regulator (LQR) te implementeren, en ten slotte worden de problemen met het volgen van de asteroïde en voortstuwingsrichting opgelost door een Lyapunov-controller te implementeren. Het laatste deel van het proefschrift behandelt het tweede geïdentificeerde onderwerp door optische line-of-sight navigatie te verkennen als een autonome techniek voor NEA-missies, door verschillende aspecten van deze techniek te onderzoeken. In eerste instantie wordt een analyse op hoog niveau uitgevoerd, waarbij de impact van observatiegeometrie, meetfouten en volgfrequentie op de doeltreffendheid van optische line-of-sight navigatie wordt onderzocht. Er wordt aangetoond hoe de gelijktijdige observatie van twee planeten superieure navigatieprestaties biedt in vergelijking met de observatie van één planeet, en dat deze prestaties verder verbeteren wanneer de scheidingshoek tussen de twee planeten dichterbij  $90^\circ$  komt. De toepassing van deze overwegingen op NEA-missies wordt besproken, waarbij wordt aangetoond hoe de techniek in lijn is met de navigatievereisten zoals uiteengezet in de inleiding, aangezien bij meetfouten in het bereik van 1-10 boogseconden de positioneringsfout onder de 1000 km kan worden gehouden. Vervolgens wordt de focus verlegd naar beeldverwerking om de richting van de line-of-sight te extraheren uit beelden van de stersensor. Beginnend met de ontwikkeling van een synthetische beeldsimulator voor testdoeleinden, gaat de analyse verder met het ontwerpen en testen van de oriëntatie-schattingketen. Dit omvat het centreren, de steridentificatie en het oplossen van Wahba's probleem. Het algoritme voor het centreren van de planeet is gebaseerd op een methode voor de kleinste-kwadratenmethode. Het steridentificatieprobleem wordt opgelost door een methode voor patroonherkenning van drie sterren te implementeren, en ten slotte wordt de rotatiematrix gevonden met behulp van Singular Value Decomposition (SVD). Er wordt een gespecialiseerd algoritme voor belichtingscompensatie geïntroduceerd voor het centreren van de planeet, wat resulteert in een meetfout onder 1 boogseconde. Ten slotte wordt er getest met synthetische beelden van Venus en Jupiter, wat leidt tot de ontwikkeling van een Adaptive Extended Kalman Filter (AEKF), een uitbreiding van de canonieke Extended Kalman Filter (EKF), die het mogelijk maakt rekening te houden met een meetruisverdeling die aanzienlijk verschilt van de Gaussische verdeling. Tot slot worden NEA-missies vanuit een ander perspectief geanalyseerd door de toepassing van gedistribueerde ruimtesystemen te onderzoeken. De studie concentreert zich met name op de fusie van optische line-of-sight navigatie en crosslink radiometrische navigatie. De analyse omvat vier verschillende netwerkconfiguraties, bestaande uit elk twee of drie satellieten. De veelbelovende resultaten benadrukken de toepasbaarheid van de gecombineerde navigatietechniek, met prestaties vergelijkbaar met basistechnieken. De afronding van dit onderzoek benadrukt de voorlopige haalbaarheid van het gebruik van een 3U-platform voor NEA-missies. Bovendien bevordert de studie aanzienlijk ons begrip van autonome line-of-sight optische navigatietechnieken in het kader van missies in de verre ruimte, waarmee de weg wordt vrijgemaakt voor verdere ontwikkelingen op dit gebied.

# LIST OF ABBREVIATIONS

**ADCS** Attitude Determination and Control System.

**AEKF** Adaptive Extended Kalman Filter.

**AOCS** Attitude and Orbit Control System.

**BOL** Beginning-Of-Life.

**BW** BandWidth.

**CoG** Center-of-Gravity.

**COTS** Commercial-off-the-shelf.

**CoV** Calculus of Variances.

**DN** Digital Number.

**DOD** Depth-Of-Discharge.

**DSNU** Dark Signal Non Uniformity.

**DSS** Distributed Space Systems.

**EKF** Extended Kalman Filter.

**EPS** Electric Power System.

**FEED** Field Emission Electric Propulsion.

**FoM** Figure-of-Merit.

**FoV** Field-of-View.

**GNC** Guidance Navigation and Control.

**GSD** Ground Sampling Distance.

**IC** Illumination Compensation.

**IR** InfraRed.



- LoS** Line-of-Sight.
- LQR** Linear Quadratic Regulator.
- LSFM** Least Squares Fitting Method.
- MISO** Multiple-Input Single-Output.
- MLI** Multi Layer Insulation.
- MO** Mission Objective.
- MP** Mission Philosophy.
- MR** Mission Requirement.
- MRP** Modified Rodrigues Parameters.
- NEA** Near Earth Asteroid.
- NIR** Near InfraRed.
- NLP** Non Linear Programming.
- OBC** OnBoard Computer.
- OCP** Optimal Control Problem.
- PCB** Printed Circuit Board.
- PSO** Particle Swarm Optimizator.
- QE** Quantum Efficiency.
- RCT** Reaction Control Thruster.
- RMS** Root Mean Squares.
- RMSE** Root Mean Squares Error.
- ROI** Region-Of-Interest.
- RQ** Research Question.
- RW** Reaction Wheel.
- SEE** Single Event Effect.
- SIS** Space Image Simulator.
- SOI** Sphere-Of-Influence.

**SRP** Solar Radiation Pressure.

**SSGTO** Super Synchronous Geostationary Transfer Orbit.

**SVD** Singular Value Decomposition.

**TCM** Trajectory Correction Manoeuvre.

**TID** Total Ionizing Dose.

**ToF** Time-of-Flight.

**UHF** Ultra High Frequency.

**VIS** Visible range.

**WB** Wahba's Problem.



# LIST OF FIGURES

1.1	Comet 67P/Churyumov-Gerasimenko imaged by the Rosetta’s camera (courtesy of ESA). . . . .	3
1.2	Ryugu imaged by the Hayabusa 2’s camera (courtesy of JAXA). . . . .	4
1.3	CubeSats sizing visualization (courtesy of NASA). . . . .	5
1.4	CubeSat missions evolution through time (Burkhard and Weston, 2021). . . . .	6
1.5	CubeSat mission types evolution through time (Burkhard and Weston, 2021). . . . .	6
1.6	LICIACube’s camera image (already processed in RGB) showing Didymos-Dimorphos and the ejecta plume (LICIACube-Dimorphos distance = 105 km). Credit ASI/NASA. . . . .	8
2.1	Ground Sampling Distance (GSD) as a function of the fly-by altitude, for off-the-shelf visible cameras, together with mass and volume characteristics. . . . .	19
2.2	Required $\Delta V$ at the perigee to inject the spacecraft into an escape orbit with certain $V_\infty$ . . . . .	21
2.3	Required specific impulse and propellant mass to deliver 385 m/s to a certain mass satellite. . . . .	23
2.4	Available $\Delta V$ using the ECAPS thrusters. Casini et al., 2021 . . . . .	23
2.5	Satellite mass evolution for the trajectory towards NEA 65679, exploiting the shape-based approach, for different propulsion systems specific impulse. . . . .	25
2.6	Thrust profile for the trajectory towards NEA 65679, exploiting the shape-based approach. . . . .	26
2.7	Angular rate as a function of fly-by characteristics. . . . .	27
2.8	Available data rate as a function of the distance from the Earth for different configurations. . . . .	30
2.9	Solar panel deliverable power as a function of the mission scenarios. . . . .	34
2.10	Volume budgets for Delfi-n3Xt, INSPIRE, and the instantiated platform (from left to right). . . . .	37
3.1	2D View of the Satellite bus. In light blue (top) is the RCT, in red is the payload, in grey the OBDH, in orange is the battery system, in green is the ADCS, in yellow and light yellow, are respectively the X-Band antenna and the X-Band transmitter, and in light blue (bottom) is the propulsion system. . . . .	42
3.2	3D View of the satellite bus showing the size of the solar panels. . . . .	42
3.3	2D View of the satellite bus, highlighting in yellow the x-band patch antennas. . . . .	43
3.4	Relation between departure date, encounter relative velocity and FoM, that is later explored in Chapter 4. . . . .	44

3.5	Enpulsion IFN performance in terms of mass evolution through time for a release outside Earth's SOI for the three closest targets. . . . .	55
3.6	ThrustMe NPT performance in terms of mass evolution through time for a release outside Earth's SOI for the three closest targets. . . . .	55
3.7	AAST MPT performance in terms of mass evolution through time for a release outside Earth's SOI for the three closest targets. . . . .	56
3.8	Enpulsion IFN performance in terms of mass evolution through time for a release outside Earth's SOI for the four furthest targets. . . . .	56
3.9	ThrustMe NPT performance in terms of mass evolution through time for a release outside Earth's SOI for the four furthest targets. . . . .	57
3.10	AAST MPT performance in terms of mass evolution through time for a release outside Earth's SOI for the four furthest targets. . . . .	57
3.11	3D view of the placement and orientation of the four RCTs. . . . .	62
3.12	RWs speed for satellite detumbling for positive rotation about the three axes. . . . .	67
3.13	RWs speed for satellite detumbling for positive rotation about the three axes using both RWs and RCTs. . . . .	68
3.14	RCTs actuation for satellite de-tumbling for positive rotation about the three axes using both RWs and RCTs. . . . .	68
3.15	RWs speed during fast desaturation manoeuvres. . . . .	70
3.16	RCTs actuation during fast desaturation manoeuvres. . . . .	70
3.17	RWs speed during slow desaturation manoeuvres. . . . .	71
3.18	RCTs actuation during slow desaturation manoeuvres. . . . .	71
3.19	First 200 seconds RWs speed for Earth Escape. . . . .	72
3.20	RWs speed for one orbit of the Earth Escape scenario. . . . .	73
3.21	Reference and true RWs speed during the Earth Escape orientation tracking. . . . .	73
3.22	RWs speed during NEAs fly-by at 10 km/s relative speed and 1000 km altitude. . . . .	74
3.23	Caption . . . . .	74
3.24	RWs speed during NEAs fly-by at 10 km/s relative speed and 1000 km altitude. . . . .	75
3.25	RWs speed during NEAs fly-by at 30 km/s relative speed and 1000 km altitude. . . . .	75
4.1	Schematics of the navigation observation geometry. . . . .	78
4.2	Position RMSE computed over a time interval of half a year, as a function of the initial date of the considered half-year time interval. Each line correspond to a simulation of the Monte Carlo. The scenario is a single tracking planet (P3), with a de-phasing angle equal to $0^\circ$ . The observation error is 1 arcsec. Tracking frequency is 1 obs/day, and initial position and velocity errors are respectively $10^5$ km and 0.1 km/s. . . . .	85
4.3	Log10(J) as a function of the planet semi-major axis and the de-phasing angle for the single planet tracking scenario. . . . .	87
4.4	Log10( $\lambda_P$ ) as a function of the de-phasing angles of P1 and P2. . . . .	88
4.5	Log10( $\lambda_P$ ) as a function of the de-phasing angles of P2 and P3. . . . .	89
4.6	Log10( $\lambda_P$ ) as a function of the de-phasing angles of P3 and P4. . . . .	90

4.7	3D position steady state RMSE as a function of the LoS standard deviation. Angles in the legend refer to the de-phasing angle. . . . .	91
4.8	3D velocity steady state RMSE as a function of the LoS standard deviation. Angles in the legend refer to the de-phasing angle. . . . .	91
4.9	Position error comparison between P2-P3 case, with $\beta = 90^\circ$ , and the observation of the pair Mars-Venus in three time intervals. $\sigma_{los} = 1$ arcsec. . . . .	93
4.10	Distribution in time of the FoM through time. In green the pair Mercury-Venus, in red the pair Earth-Mars, in yellow the pair Mercury-Earth, in cyan the pair Venus-Earth, in blue the remaining pairs. . . . .	97
4.11	Spatial distribution of the best $\log_{10}(\text{FoM})$ . . . . .	97
4.12	Ballistic trajectory towards 2008 UA202. . . . .	99
4.13	Angular separation planet LoS and Sun direction in the simulation time-frame for the trajectory towards 2008 UA202. . . . .	100
4.14	3D position error evolution in the simulation time-frame for three tracking frequencies, and the separation angle evolution (trajectory towards 2008 UA202). . . . .	100
4.15	Ballistic trajectory towards 2006 RH120. . . . .	102
4.16	Angular separation planet LoS and Sun direction in the simulation time frame for the trajectory towards 2006 RH120. . . . .	102
4.17	3D position error evolution in the simulation time-frame for three tracking frequencies, and the separation angle evolution (trajectory towards 2006 RH120). . . . .	103
5.1	Planet's apparent diameter for an observer placed at 1 AU distance from the Sun. The angle between spacecraft and planet position vectors is defined Observer Phasing Angle. . . . .	111
5.2	Venus Apparent Magnitude as a function of Observer distance and $\alpha$ 5.2a. Jupiter Apparent Magnitude as a function of Observer distance and $\alpha$ 5.2b. . . . .	112
5.3	Venus' elevation angle as a function of time . . . . .	114
5.4	Cumulative Attitude Estimation error as a function of the number of stars and 3D unit vector error. . . . .	116
5.5	Number of stars in the camera's FoV as a function of the boresight azimuth angle, for different apparent visual magnitudes $V$ . . . . .	117
5.6	3D angular vector as a function of the 2D u-component error in pixels. . . . .	118
5.7	CoG centroiding error [pixel] as a function of star magnitude and PSF radius 5.7a. LSFM centroiding error [pixel] as a function of star magnitude and PSF radius 5.7b . . . . .	118
5.8	Stars triplet geometrical features. . . . .	119
5.9	Visualization of the illumination angle. . . . .	122
5.10	Venus centroiding correction, simulated results as points, analytical results as lines. Small distance (0.3457 AU) in blue, medium distance (0.8659 AU) in red, and large distance (1.386 AU) in yellow. . . . .	122

5.11 Venus centroiding error as a function of the center location for illumination phase angle $60^\circ$ (left). Venus centroiding error as a function of the center location for illumination phase angle $150^\circ$ (right). Small distance in the plots corresponds to 0.3457 AU, large distance to 1.386 AU. . . . .	123
5.12 Venus observation complete chain testing with SIS. . . . .	124
5.13 Attitude estimation standard deviation as a function of the observation time (Venus high noise case). . . . .	125
5.14 Venus centroiding error mean value (a) and error standard deviation (b) (Venus high noise case). . . . .	125
5.15 Venus Azimuth and Elevation error mean values (a) and standard deviation (b) (Venus high noise case). . . . .	126
5.16 Average number of identified stars as a function of the observation time for Venus observation test case. . . . .	127
5.17 Attitude estimation standard deviation as a function of the observation time (Venus low noise case). . . . .	127
5.18 Venus centroiding error standard deviation (low noise) (a). Azimuth and Elevation error standard deviation (b) (Venus low noise case). . . . .	128
5.19 Attitude estimation standard deviation as a function of the observation time (Jupiter high noise case). . . . .	128
5.20 Jupiter centroiding error mean value (a). Centroiding error standard deviation (b) (Jupiter high noise case). . . . .	129
5.21 Jupiter Azimuth and Elevation error mean values (a). Azimuth and Elevation error standard deviation (b) (Jupiter high noise case). . . . .	129
5.22 Attitude estimation standard deviation as a function of the observation time (Jupiter low noise case). . . . .	130
5.23 Jupiter centroiding error standard deviation (low noise) (a). Azimuth and Elevation error standard deviation (Jupiter low noise case). . . . .	130
5.24 Earth-Mars transfer visualization . . . . .	132
5.25 Azimuth (a) and Elevation (b) mean value behaviours for Earth-Mars transfer. . . . .	132
5.26 Azimuth (a) and Elevation (b) standard deviation behaviours for Earth-Mars transfer. . . . .	133
5.27 x component error for $R_k$ value of 1 arcsec (EKF). Blue lines are the estimation error for each simulation, while red line is the $3\sigma$ boundary. . . . .	133
5.28 x component error for $R_k$ value of 2 arcsec (EKF). Blue lines are the estimation error for each simulation, while red line is the $3\sigma$ boundary. . . . .	134
5.29 x component error for $R_k$ initial value of 1 arcsec, and $\alpha = 0.7$ (AEKF). Blue lines are the estimation error for each simulation, while red lines are the $3\sigma$ boundaries. . . . .	134
5.30 3D position error as a function of the simulation epoch for different AEKF's memory factors and initial $R_k$ entries. . . . .	135
5.31 3D position error as a function of the simulation epoch for different AEKF's memory factors and initial $R_k$ entries. . . . .	136

6.1	Architecture A with two satellites, each of them equipped with a camera (a). Architecture B with two satellites, one equipped with two cameras and one without (b). The double side arrows represent the range information.	142
6.2	Architecture C with three satellites, two of them equipped with one camera each, and one of them without (a). Architecture D with three satellites, one of them equipped with two cameras, and the other two without (b). The double side arrows represent the range information. . . . .	142
6.3	Expected Inter-satellite range measurement error as a function of the inter-satellite data-rate. . . . .	147
6.4	Percentage change in 3D position estimation error between combined navigation architecture A and optical navigation with only one planet. In (a) the one planet is the second, while in (b) is the first. . . . .	149
6.5	Percentage change in 3D position estimation error between combined navigation architecture B and optical navigation with only one planet. In (a) the one planet is the second, while in (b) is the first. . . . .	149
6.6	Percentage change in 3D position estimation error between combined navigation and optical navigation with only two planets. Architecture A in (a), architecture B in (b) . . . . .	150
6.7	Percentage change in 3D position estimation error between combined navigation and optical navigation with only two planets. Architecture C in (a), architecture C with additional range in (b) . . . . .	151
6.8	Range profile in (a). 3-components position estimation for the single satellite equipped with two cameras, observing Mars and Venus (b). . . . .	151
6.9	3D Position estimation error for spacecraft 1 (a) and spacecraft 2 (b). In blue baseline solution, in red architecture A, in yellow architecture B. . . .	152
6.10	3D Velocity estimation error for spacecraft 1 (a) and spacecraft 2 (b). In blue baseline solution, in red architecture A, in yellow architecture B. . . .	153
A.1	Initial positions uncertainty ellipsoid for (433) Eros. . . . .	179
A.2	Final positions uncertainty ellipsoid for (433) Eros. . . . .	179
A.3	Initial positions uncertainty ellipsoid for (2100) Ra-Shalom. . . . .	180
A.4	Final positions uncertainty ellipsoid for (2100) Ra-Shalom. . . . .	180
A.5	Eros apparent magnitude at orbit's perihelion. . . . .	181
A.6	Eros apparent magnitude at orbit's aphelion. . . . .	181
A.7	(433) Eros visibility in terms of days before fly-by . . . . .	182
A.8	Allowable displacement for $\Delta V = 5/\text{ms}$ as a function of the thrust direction and the time interval between fly-by and manoeuvre dates. . . . .	183
A.9	Allowable displacement for $\Delta V = 10/\text{ms}$ as a function of the thrust direction and the time interval between fly-by and manoeuvre dates. . . . .	183
A.10	(433) Eros correction capabilities 8 days before fly-by . . . . .	184





# LIST OF TABLES

1.1	Navigation Techniques Comparison. . . . .	11
2.1	Mission Requirements definition. . . . .	16
2.2	Description of the mission phases. . . . .	17
2.3	COTS Cameras characteristics. . . . .	18
2.4	NEAs target retrieved from the JPL Small Body Database. . . . .	21
2.5	COTS Chemical Micro Propulsion Systems characteristics. . . . .	22
2.6	Results low thrust preliminary analysis. . . . .	26
2.7	COTS Electric Micro Propulsion Systems characteristics. . . . .	26
2.8	Integrated ADCS characteristics. . . . .	30
2.9	X-Band Transmitter characteristics. . . . .	30
2.10	X-Band Antenna characteristics. . . . .	30
2.11	COTS OBDH characteristics. . . . .	31
2.12	Power budgets of mission phases, based on components datasheets. . . . .	32
2.13	EPS characteristics. . . . .	35
2.14	Full platform Volume and Mass budget. . . . .	36
3.1	Main characteristics of the three electric micro-propulsion systems considered in the analysis. * The Dry Mass value for the ThrustMe NPT30-I2-1U is not available in the datasheet, so it has been approximated based on the other available parameters. . . . .	45
3.2	List and characteristics of seven NEAs analyzed in this study. . . . .	53
3.3	Earth escape trajectory results for the three electric propulsion systems. . . . .	54
3.4	COTS RCTs main characteristics. . . . .	58
3.5	Resulting design parameters for the four RCTs. . . . .	62
3.6	Required propellant mass for each axis de-tumbling. . . . .	69
3.7	Required propellant fast for RWs desaturation. . . . .	69
3.8	Required propellant mass for slow RWs desaturation. . . . .	72
4.1	Position mean and standard deviation RMSE [km] per scenario (two planets observation). The reported angle is the separation angle $\beta$ . The first listed planet for each scenario has a null de-phasing angle with the spacecraft, while the second planet's de-phasing angle is computed according to Equations 4.1-4.3. . . . .	92
4.2	Velocity mean and standard deviation RMSE [m/s] per scenario (two planets observation). The reported angle is the separation angle $\beta$ . The first listed planet for each scenario has a null de-phasing angle with the spacecraft, while the second planet's de-phasing angle is computed according to Equations 4.1-4.3. . . . .	92

4.3	Convergence time [days] per scenario (one planet observation) as a function of the measurement error. In the scenario column, the de-phasing angle is reported. . . . .	93
4.4	Convergence time [days] per scenario (two planets observation) as a function of the measurement error. The reported angle is the separation angle $\beta$ . The first listed planet for each scenario has a null de-phasing angle with the spacecraft, while the second planet's de-phasing angle is computed according to Equations 4.1-4.3. . . . .	94
4.5	Convergence time [days] per scenario (one planet observation) as a function of the tracking frequency. In the scenario column, the de-phasing angle is reported. . . . .	94
4.6	Convergence time [days] per scenario (two planets observation) as a function of the tracking frequency. The reported angle is the separation angle $\beta$ . The first listed planet for each scenario has a null de-phasing angle with the spacecraft, while the second planet's de-phasing angle is computed according to Equations 4.1-4.3. . . . .	95
5.1	TELEDYNE EV76C660 main characteristics . . . . .	113
5.2	MVL16MR characteristics . . . . .	114
5.3	Heliocentric orbit initial state. . . . .	135
6.1	Crosslink characteristics . . . . .	147
A.1	(433) Eros initial conditions and uncertainties . . . . .	178
A.2	(2100) Ra-Shalom initial conditions and uncertainties . . . . .	179

# 1

## INTRODUCTION

*I know that I know nothing*

Socrates

*This chapter is aimed at introducing the framework and the motivations behind the PhD research. First, some history of deep-space missions is presented. Later the focus is shifted to presenting the characteristics of CubeSats, with a focus on their current deep-space applicability. Then, concepts about autonomous navigation are highlighted. These sections aim both at introducing the reader to the background and at motivating the research line, which is defined by conceiving four Research Questions. Finally, the dissertation outline is presented.*

## 1.1. DEEP-SPACE EXPLORATION HISTORY

The exploration of deep space has been a captivating endeavour that has pushed the boundaries of human knowledge and technology for decades. From the early days of stargazing to the sophisticated space missions of the present era, humanity's quest to unravel the mysteries of the universe has been marked by relentless curiosity, groundbreaking discoveries, and remarkable technological advancements. Deep-space exploration encompasses the study and exploration of the celestial bodies of our Solar System. Over the last 50 years, space exploration missions have dramatically expanded our understanding of our Solar System.

The history of deep-space exploration has its roots in the tense Cold War framework, when the rivalry between USA and the Soviet Union led to an unimaginably fast technological advancement.

Nowadays the definition of deep-space missions is debated, as the International Telecommunication Union claims that the minimum distance is 0.01 AU (Publications, 2017), while the NASA deep-space network has been designed for distances above 16000 km (Renzetti, 1975). In this dissertation, due to the similarities with asteroid missions, also lunar missions are included in the classification.

The first human-made objects that have ever reached another body of the Solar System were the Soviet Luna 2 and Luna 3 in 1959 (Slyuta, 2021). The former was the first object impacting the lunar surface, while the latter transmitted images of the far side of the Moon for the first time.

Despite being preceded by Soviet missions, NASA's effort to reach the Moon in the sixties, with the program Apollo, led to the first manned mission on a Solar System body which was not the Earth (Jerde, 2021).

The interest towards our moon did not end with the Apollo program. Still, it continued for decades with unmanned missions, ranging from NASA Lunar Reconnaissance Orbiter (Vondrak et al., 2010), launched in 2009, and aimed to spot possible landing sites for future missions, to the currently ongoing Chinese Chang'e Missions, which include landers and rovers on the lunar surface to explore even further the satellite's characteristics (Pei et al., 2015).

NASA's Viking I and II missions in 1976 were the first Martian lander missions (Soffen, 1976), even though the first attempt for a Mars probe is dated 1960 with the unsuccessful of the former Soviet Union missions. The first successful fly-by of the red planet is dated 1965, with the NASA Mariner 4 (Leighton et al., 1965). The interest in Mars has been well preserved through the years, and only in the last 20 years, multiple missions from different space agencies have (or have tried) to reach the red planet. Particularly interesting are the NASA Mars Reconnaissance Orbiter (Graf et al., 2005), the ESA Mars Express (Pätzold et al., 2016), and the unsuccessful Exomars Schiaparelli (Vago et al., 2015). The list is not limited to satellites, but it includes also rovers, such as NASA Sojourner (Wilcox and Nguyen, 1998), NASA Spirit and Opportunity (Squyres, 2005), NASA Curiosity (Bennett et al., 2023), and NASA Perseverance (Farley et al., 2020) with its autonomous helicopter Ingenuity (Balaram et al., 2021).

Mariner 2 in 1962 was the first successful Venus fly-by mission (Sonett, 1963), followed by a set of numerous other missions also from the former Soviet Union and ESA. Particularly noteworthy were the gravity-assist fly-by passages for three iconic missions:

Galileo (Johnson et al., 1991), Cassini (Burton et al., 2001), and MESSENGER (McNutt Jr et al., 2008).

Galileo was a NASA mission of late 1989 aimed to explore Jupiter (Oneil and Mitchell, 1983), Cassini had a very successful mission towards Saturn in 1997 (Henry, 2002), and MESSENGER in 2004 had a successful mission towards Mercury (Solomon et al., 2007).

In 1977 the two famous NASA Voyager I and II missions were launched to reach the outer Solar System making a grand tour of the outer planets, and that still amazes us today (Kohlhase and Penzo, 1977).

In recent years, also thanks to technological advancements, the interest has grown towards small bodies (e.g. asteroids), with some innovative missions. NASA's Near Earth Asteroid Rendezvous (NEAR) Shoemaker spacecraft became the first to land on an asteroid, Eros, providing detailed data about its surface composition (Prockter et al., 2002). The European Space Agency's Rosetta spacecraft studied Comet 67P/Churyumov-Gerasimenko (Figure 1.1), deploying a lander called Philae, which made the first landing on a comet (Glassmeier et al., 2007). Japan's Hayabusa missions have explored asteroids Itokawa and Ryugu (Figure 1.2), successfully collecting samples and returning them to Earth for analysis (Watanabe et al., 2017; Yoshikawa et al., 2015). NASA OSIRIS-REx mission in 2016 explored the asteroid Bennu, and a capsule containing a fragment of the asteroid re-entered Earth on 24th September 2023 (Beshore et al., 2015). The latest asteroid mission was the NASA DART in 2023, which successfully impacted the asteroid Didymos, and served as a test of asteroid's trajectory change for planetary protection purposes (Cheng et al., 2023).

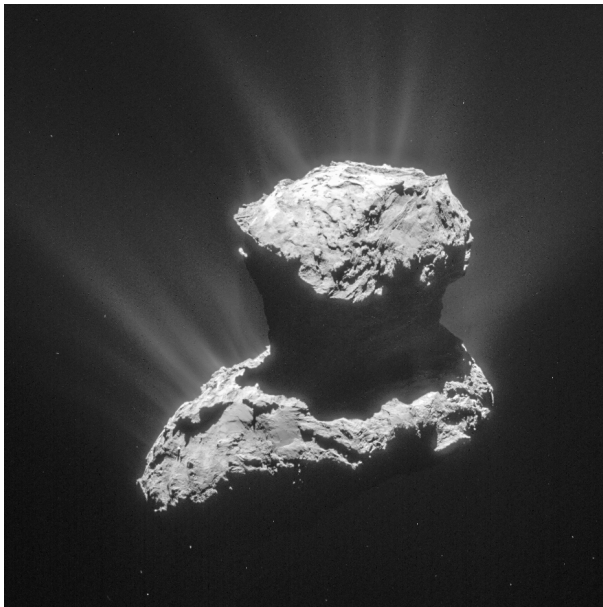


Figure 1.1: Comet 67P/Churyumov-Gerasimenko imaged by the Rosetta's camera (courtesy of ESA).

The list of deep-space missions is not limited to the ones presented before. Despite



Figure 1.2: Ryugu imaged by the Hayabusa 2's camera (courtesy of JAXA).

being large, it is not comparable to the large number of asteroids (and in particular NEAs) that may be explored in the near future. However, large spacecraft platforms that have characterized the first 60 years of deep-space exploration are not fully compatible with a large exploration of NEAs, due to the cost associated with the mission development and operations, but also because of the long preparation time. This 'problem' can be overcome, by exploiting the new trends of recent years that are broadening the access to space. This is the case of CubeSat, which represents a new trend in space exploration that is gaining more interest and applicability.

## 1.2. MINIATURIZED SPACECRAFT: CUBESAT

A CubeSat is a type of miniaturized satellite initially used for scientific research, technology demonstration, and educational purposes. Recently, operational CubeSats have also been employed for Earth Observation, gaining consent also in the private sector. The term "CubeSat" refers to a standardized design specification based on cubic units. These satellites are built in multiples of 10x10x10 centimeter cubic units, known as "1U". CubeSats can be composed of multiple units, such as 2U, 3U, 6U, 12U, or even more, depending on the specific mission requirements. Figure 1.3 shows the standard sizes of CubeSats (Cappelletti and Robson, 2021).

The CubeSat concept originated in the late 1990s at Stanford University in collaboration with California Polytechnic State University (Cal Poly). Professors Bob Twiggs of Stanford and Jordi Puig-Suari of Cal Poly, along with their students, developed the CubeSat standard to provide students with practical experience in designing, building,

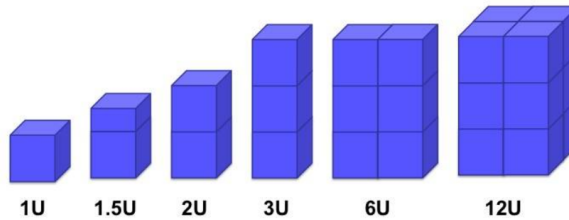


Figure 1.3: CubeSats sizing visualization (courtesy of NASA).

testing, and operating satellites (Puig-Suari et al., 2001).

The first CubeSat, named "CUBESAT 1U," was launched on June 30, 1999, aboard a Russian Start-1 rocket. This launch marked the beginning of the CubeSat era, demonstrating the feasibility of small, low-cost satellites for space research. The success of this mission paved the way for the development of more sophisticated CubeSat missions by universities, research institutions, and even commercial entities.

Over the years, the CubeSat standard has evolved, allowing for more complex and capable missions. Today, CubeSats continue to be a popular choice for educational institutions and small companies to conduct space experiments, gather scientific data, demonstrate new technologies in the space environment, and offer a range of services.

CubeSats are characterized by a high degree of standardization and adhere to a standard form factor, allowing for easy integration into launch vehicles. This standardization simplifies the design, manufacturing, and testing processes. (CalPoly, 2022)

Through the years, the amount of private companies producing COTS components for CubeSats has increased notably, and as of today, for each essential subsystem, there are multiple options offered worldwide.

Furthermore, due to their small size and standardized design, CubeSats often "piggyback" on larger satellite launches. They are placed into orbit as secondary payloads, reducing the cost of access to space.

Figures 1.4 and 1.5 show respectively the evolution through time of the CubeSats mission and size, and the purposes of such missions (Burkhard and Weston, 2021). After 2017-2018 the statistics show a peak and then a decrease in CubeSat missions because around those years there have been multiple Earth constellation missions and technology demonstration missions, while in more recent years the focus has been on operational satellites. Furthermore, after 2016 an increase of 6U CubeSats mission can be noticed, showing the interest in this format for its capabilities.

### 1.2.1. DEEP-SPACE CUBESAT TRENDS

In very recent years, also thanks to the effort of the private sector on advancing CubeSat technologies, the usage of these miniaturized satellites has also been expanded to deep-space applications.

The first mission showing CubeSat capabilities in scenarios far away from the Earth is Marco-A and -B, dated 2018, a pair of twin 6U CubeSats developed by JPL, built to



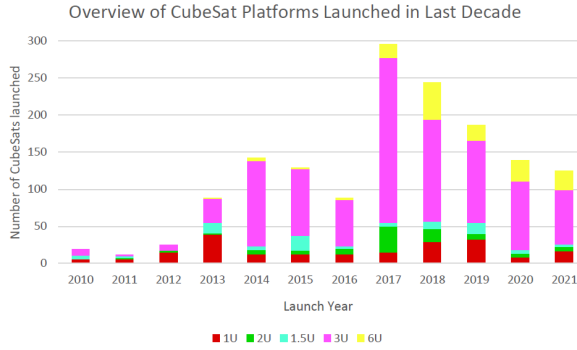


Figure 1.4: CubeSat missions evolution through time (Burkhard and Weston, 2021).

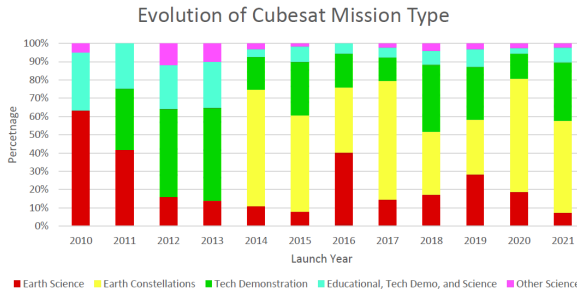


Figure 1.5: CubeSat mission types evolution through time (Burkhard and Weston, 2021).

accompany the InSight lander. This mission not only showed the functioning of such small satellites in harsh environments but also demonstrated how their capabilities can bring new functionalities to the mission and help the main system accomplish tasks. This was the case of Marco CubeSats, which served as a relay system for communication with the lander InSight during the descending phase (Klesh et al., 2018).

After this first demonstration in deep-space, the interest in CubeSats for such applications has seen a rise, and their applicability to a various number of scenarios has been proposed.

NASA has also been working through recent years on the INSPIRE CubeSat, a 3U architecture aimed to test the completely autonomous capabilities of a CubeSat in a deep-space scenario, following an Earth escape trajectory (Klesh et al., 2013).

CubeSats have been used for several lunar applications. This is the case of JPL Lunar Flashlight, a 6U CubeSat aimed to characterize water ice deposits on the lunar surface (Cohen et al., 2020), CAPSTONE, a 12 U CubeSat aimed to test the orbital stability for the Lunar Gateway (Cheetham et al., 2022), and the set of 10 CubeSats flying on Artemis 1:

- ArgoMoon, a 6U CubeSat with a hybrid propulsion system, monopropellant and cold gas thrusters, to provide attitude control (orientation) and orbital manoeuvring (Pirrotta et al., 2021);

- NEAScout, a 6U CubeSat equipped with solar sailing to reach a Near-Earth Asteroid, which unfortunately never established contact with the ground station (McNutt et al., 2014);
- Biosentinel, a 6U CubeSat aimed to characterize the impact of deep space radiation on DNA repair over a long time beyond low Earth orbit (Ricco et al., 2020);
- LunIR, a 6U CubeSat aimed to collect lunar surface spectroscopy and thermography (Freeman, 2022);
- Lunar ICECUBE, a 6U CubeSat aimed to prospect, locate, and estimate the amount and composition of water ice deposits on the Moon, which as of February 2023 did not communicate with ground (Malphrus et al., 2019);
- CubeSat for Solar Particles, a 6U platform aimed to orbit the Sun to study the dynamic particles and magnetic fields, but lost contact 57 minutes after deployment (Desai et al., 2019);
- Lunar Polar Hydrogen Mapper, a 6U CubeSat aimed to investigate the possible presence of water-ice on the Moon (Hardgrove et al., 2020);
- EQUULEUS, a 6U CubeSat aimed to measure the distribution of plasma that surrounds the Earth (plasmasphere) to help scientists understand the radiation environment in that region (Funase et al., 2020);
- OMOTENASHI, a 6U lunar lander that lost contact with the ground before initiating the descending phase (Hashimoto et al., 2019);
- Team Miles, a 6U cubeSat aimed to test the applicability of plasma thrusters in deep-space scenario, but contact was never established.\*

Moreover, several other missions are currently in development, such as LUMIO, a 12 U CubeSat aimed to characterize the meteorites' impact on the far side of the Moon (Speretta et al., 2019).

The Artemis-1 mission showed that interest was indeed not only for the Moon but also for other deep-space targets such as NEAs. This is testified by LICIACube, a 6U CubeSat that flew with the DART mission to the asteroid Didymos, and which again, similarly to Marco-A and -B, shows the complementarity of CubeSats missions to a larger platform, as it delivered a set of 600 images of the impact with the asteroids (Dotto et al., 2021). One of the images can be seen in Figure 1.6.

The continuation of the DART mission will be ESA Hera, which will characterize the post-impact scenario, and it will be accompanied by two 6U CubeSats namely Milani and Juventas, that will help the characterization and test the capabilities in such environments (Ferrari et al., 2021; Goldberg et al., 2019).

Another interesting CubeSat mission is the ESA M-ARGO, currently in early development, aimed to explore targets with less than 100 m of diameter to provide new insights into these unexplored objects, with a focus on the exploitability of in-situ resources.

\* <https://www.nasa.gov/centers-and-facilities/marshall/cube-quest-challenge-spotlight-team-miles/>

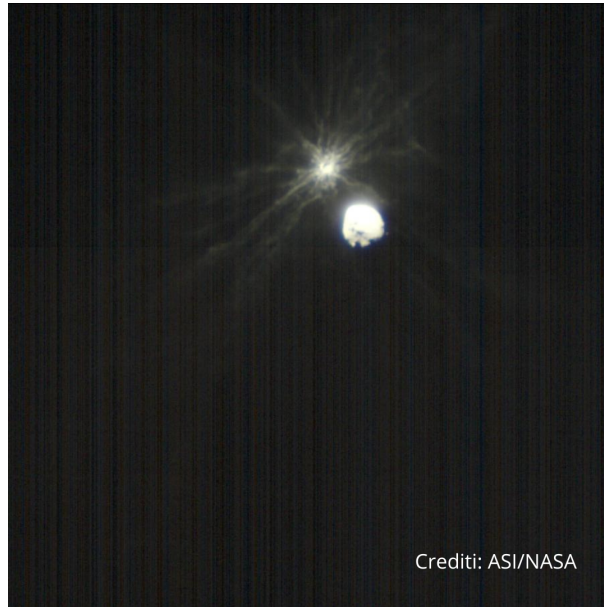


Figure 1.6: LICIACube's camera image (already processed in RGB) showing Didymos-Dimorphos and the ejecta plume (LICIACube-Dimorphos distance = 105 km). Credit ASI/NASA.

Moreover, it will try to demonstrate the fully autonomous capabilities in terms of an electric micro-propulsion system for Earth Escape and cruising towards a NEA, and it will carry onboard an optical navigation test payload (Franzese et al., 2021).

### 1.3. AUTONOMOUS NAVIGATION

One of the fundamentals to broaden the opportunities for deep-space CubeSats is the exploitation of autonomous navigation techniques. This comes from the necessity of reducing the ground segment operation cost, but also, as will be shown later, limiting the required onboard hardware demands to exploit lighter platforms.

The required navigation technique depends on the mission scenario. Three macro-categories can be highlighted:

- Optical navigation
- X-ray pulsar navigation
- Radiometric navigation

The three macro-categories have a clear point in common: they are based on collecting and processing the required measurements onboard, without the intervention of the ground segment. This is already a huge step, as for JPL Marco-A and -B, deep-space navigation was based on the usage of the X-Band Iris Transponder, whose presence onboard was influencing quite notably the mass, volume, and power budgets, in addition to the required ground segment operations (Klesh et al., 2018).

### 1.3.1. OPTICAL NAVIGATION

Optical navigation encompasses a range of methods used to determine spacecraft states, relative positions, and velocities in relation to a target body. This involves employing onboard optical sensors to estimate Line-of-Sight (LoS) to beacons or known locations on a surface. These sensors, with specific characteristics governing resolutions and sensitivities, compute a body's position in the camera reference frame and derive the target's location in space from its position in images. These methods are categorized based on the apparent size of the target body in the observed image, leading to divisions like unresolved and resolved center finding, limb-based, and surface landmark-based navigation (Andreis et al., 2021).

The primary advantage of optical navigation lies in its applicability across various mission phases, including cruise, fly-by, rendezvous, orbiting, and landing. Digital pictures serve as the data for vision-based navigation, but they contain noise sources like shot noise and read noise. Several deep space missions, including Deep Space 1, STARDUST, Deep Impact, and EPOXI, have utilized optical navigation methods such as JPL's Autonomous Optical System AutoNAV (Bhaskaran, 2012; Team et al., 2000). Furthermore, for the Deep Space 1 mission, the position error was lower than 150 km, and the velocity error was below 0.2 m/s during the cruise.

Optical navigation methods include Star-based and Celestial Navigation, which employ inertial pointing and bearing observations respectively. Relative Navigation generates bearing and/or position estimates for observed objects. Lastly, Terrain Relative Navigation combines onboard optical data with a landing area map to avoid landing hazards (Andreis et al., 2021).

Several deep-space small satellite missions have planned to use optical methods. For example, the BIRDY-T mission's In-Flight Orbit Determination system combines optical measurements, asynchronous triangulation, and a Kalman filter to determine its trajectory towards Mars (Hestroffer et al., 2018). The LUMIO mission utilizes the Moon's full disk size in images to estimate the spacecraft's position and velocity in a halo orbit at Earth–Moon L2. The Cislunar Explorers mission estimates positions in cislunar space by studying the sizes and locations of Earth, Moon, and Sun relative to each other (Franzese et al., 2018). The M-ARGO mission incorporates miniaturized onboard optical sensors to provide line-of-sight measurements, offering navigation accuracy on the order of kilometers for positions and meters per second for velocity components under good observation conditions (Franzese et al., 2021).

In summary, optical navigation offers significant advantages, providing moderate to high-accuracy navigation solutions compatible with all stages of a mission.

### 1.3.2. X-RAY PULSAR NAVIGATION

X-ray pulsar navigation utilizes periodic X-ray signals emitted by pulsars to estimate spacecraft states, determining the time and direction of pulse arrival through a single instrument. Stable neutron stars rotating nearly 1000 times per second offer a solution for autonomous navigation. The pulse time-of-arrival data is compared with an ephemeris database, enabling the determination or updating of spacecraft attitude, position, and velocity. This method provides the significant advantage of stabilizing onboard clocks via periodic pulse arrivals and is applicable not only in Earth's vicinity but also in deep

space. The Station Explorer for X-ray Timing and Navigation Technology (SEXTANT) mission demonstrated the achievability of a 10 km RSS position error for the International Space Station using this technique (Getchius et al., 2019; Sheikh et al., 2006).

Pulsar navigation methods for spacecraft positioning resemble optical celestial navigation. For instance, the Pulsar elevation method uses elevation angles and apparent body diameter to determine distance, enabling position determination with multiple X-ray sources. Another approach, limb occultation, utilizes the time a pulsar spends behind a planetary body to determine the body's chord length when its dimensions and source position are known. However, timing measurements from X-ray pulsars involve various error sources, including Poisson fluctuations and pulse frequency knowledge uncertainties (Hanson, 1996).

The CubeX mission aims to demonstrate this concept using two X-ray instruments onboard a CubeSat, employing X-ray millisecond pulsars in Lunar orbit. Unlike radio frequencies emitted by pulsars, which range from a few to several GHz, detecting X-ray signals necessitates large antennas, making it unfeasible for small satellites (Romaine et al., 2018).

In summary, pulsar navigation offers superior accuracy compared to optical navigation, achieving less than 0.1 km position accuracy at 1 AU with precise timing and pulsar position information. An important advantage lies in stabilizing onboard clocks using periodic pulsar signals. However, challenges include sensor size and required integration time, limiting operations in certain mission phases, such as close proximity (Sheikh et al., 2006).

### 1.3.3. RADIOMETRIC NAVIGATION

Radiometric observables between satellites, such as range and range-rate, offer a relative navigation solution for distributed satellite systems comprising multiple spacecraft. This approach proves especially valuable for small satellites, particularly those deployed from another spacecraft (mothercraft). In deep space small satellite missions, where power constraints limit onboard communication and data transmission capabilities, a one-hop link configuration is employed to transmit scientific data to the ground. Existing inter-satellite communication links can also serve navigation purposes (Hill and Born, 2007).

Achieving autonomous navigation without relying on ground-based observations requires observing the size, shape, and orientation of the spacecraft's orbit through radiometric measurements between satellites. For this purpose, one of the satellites must follow a unique trajectory, establishing itself as an absolute reference for the observability of the system (Turan et al., 2022a, 2023).

### 1.3.4. APPLICABILITY TO DEEP-SPACE MISSION PHASES

From what has been highlighted in the literature, autonomous navigation techniques can be employed in two different scenarios:

- Operation about the target body, which includes orbiting the body, fly-by, and orbiting Lagrangian points in the proximity of the body;
- Deep-Space Cruising, the heliocentric transfer from the Earth towards the target

body.

In the first case, a single spacecraft can take advantage of optical navigation, by exploiting centroiding or deep-learning-based techniques to estimate its state with respect to the observed body or eventually using terrain-based methods. All of them are included in optical navigation strategies. Otherwise, the use of a LIDAR can be helpful to estimate the state. In the case of multiple spacecraft, the use of crosslink radiometric navigation appears to be a viable solution to estimate with great accuracy the position and velocity. Optical navigation about the Moon, Mars, NEAs, or other celestial bodies has been widely investigated (Turan et al., 2022b).

In the second case, the LoS navigation technique appears to be the most viable because it would not need further onboard instrumentation, as star-trackers can be exploited, differently from X-ray pulsar-based navigation which would require additional hardware, despite the non-readiness of the technology. Crosslink radiometric navigation would not be an option as deep-space travelling spacecraft have very similar dynamics, and this similarity would not allow us to estimate the position and velocity of the satellites. A quick comparison between the three main techniques is presented in Table 1.1.

Technique	Hardware	Applicability	Accuracy
Optical Line-of-Sight	COTS Star trackers or Camera with custom algorithms	Cruise	$10^2 - 10^4$ km
X-Ray Pulsar	Custom detector with scalability problems	Cruise	up to 0.1 km
Radiometric	Crosslink communication systems with multiple satellites	Close-Proximity	$10^{-2} - 10^{-1}$ km

Table 1.1: Navigation Techniques Comparison.

For these reasons, it is interesting to investigate and further prove the applicability of autonomous LoS navigation in deep-space cruising scenarios. Together with it, it is interesting to exploit a combination with crosslink radiometric navigation in case of multiple satellites travelling in deep-space.

### 1.3.5. NAVIGATION REQUIREMENTS

In order to prove the applicability of LoS navigation to NEA missions, it is necessary to define the estimation error requirements, which qualify whether the technique can be implemented effectively. Each mission has custom requirements based on its characteristics, however, following the approach reported in Appendix A, it is possible to define a procedure that can be employed for each specific case, and that allows to define some general requirements, that are followed in the remaining of the dissertation. This approach involves calculating the propagated position errors of the target NEA, exploring the allowable trajectory correction capabilities of the propulsion system, and computing the visibility window of the target based on its magnitude characteristics. With this approach, it is possible to define the required position and velocity errors at the end of the

cruise, when the relative navigation with respect to the target is initialized. Following the calculations reported in Appendix A, for this dissertation, it is assumed a position error around  $3\sigma = 1000\text{km}$ , and a velocity error around  $3\sigma = 1e^{-4}\text{km/s}$ .

## 1.4. RESEARCH QUESTIONS

As it appears from the literature survey, the use of CubeSat for Earth application is well consolidated, while their use in deep-space is still under evaluation and study. In this framework, the application of CubeSat has been limited to 6U platforms in deep-space scenarios, and none of them employed a fully autonomous operations (including navigation) strategy.

The reduction of the size to 3U platforms is seen as a viable option, as the cost reduction associated with the mission would lower, increasing the number of interesting NEA targets that can be explored, allowing a wide set of new mission concepts involving distributed space systems, and reaching more prospective customers. The 3U form factor is an optimal compromise between lowering the cost and allocating onboard all the necessary systems to produce a valuable scientific return.

Especially if the goal is to further reduce the size of these satellites, going to a 3U platform, the exploitation of a fully autonomous strategy is deemed necessary. Furthermore, to reduce the size of the satellites, a stiff paradigm shift is required, where the most common redundancy approach is substituted by a multi-use approach, where the same onboard hardware can be exploited for multiple tasks. This is indeed the case for star-trackers, that are already onboard for attitude estimation.

For the above-mentioned reasons, the research carried out in this PhD is aimed **to assess the applicability of 3U autonomous CubeSats in deep-space scenarios, in particular for NEAs flyby, focusing on navigation and AOCS capabilities.**

The research is aimed to answer four formulated Research Questions (RQs).

### 1.4.1. RQ1

The first research question is focused on the systems engineering of a 3U CubeSat platform to enable NEAs flyby, and it is formulated as follows:

**RQ1: What are the advantages and limitations of designing a 3U CubeSat platform for NEAs fly-by missions?**

This research question can be subdivided into sub-research questions as follows:

- **RQ1.1:** which subsystems can be based on COTS components, and which ones require custom design?
- **RQ1.2:** is it possible to define a standard platform, whose design is valid for a large number of NEA targets without significant modification?
- **RQ1.3:** what scientific output can be achieved with such a platform, also in comparison with larger platforms?

### 1.4.2. RQ2

The second research question focuses on autonomous line-of-sight navigation on a high level, and can be formulated as follows:

**RQ2: To what extent LoS navigation can be exploited by deep-space CubeSats during a cruise towards a NEA?**

This research question can be again divided into subquestions:

- **RQ2.1:** what geometrical characteristics influence the accuracy of LoS navigation?
- **RQ2.2:** what measurement accuracy is needed to meet the mission requirements?
- **RQ2.3:** in what mission scenarios the exploitation of LoS navigation provides better performance?
- **RQ2.4:** what are the performances of combining LoS navigation with other navigation techniques to further improve the applicability?

### 1.4.3. RQ3

The third research question focuses on the star-trackers characteristics and algorithms for navigation, and it is formulated as:

**RQ3: What complete algorithm chain guarantees the extraction of accurate measurements for the navigation filter?**

Which is then divided into subquestions:

- **RQ3.1:** how do the hardware characteristics influence the accuracy?
- **RQ3.2:** what scenario characteristics influence the accuracy?
- **RQ3.3:** what is an optimal attitude estimation chain and what accuracy can be reached?
- **RQ3.4:** what centroiding algorithm, including illumination compensation, can be exploited?
- **RQ3.5:** how can synthetic images be simulated for algorithm testing?
- **RQ3.6:** how does the navigation algorithm need to be adapted to account for measurement characteristics?

### 1.4.4. RQ4

The last research question focuses on the AOCS for such missions, as it is formulated as:

**RQ4: What AOCS design guarantees the accomplishment of all the tasks for NEAs missions?**

which again can be divided into subquestions as:



- **RQ4.1:** what propulsion system can be employed to achieve the mission objectives?
- **RQ4.2:** how do propulsion capabilities for 3U CubeSat allow for Earth Escape?
- **RQ4.3** what hardware is required for the attitude control system?
- **RQ4.4** what is an efficient way to de-saturate reaction wheels in deep-space missions?

## 1.5. DISSERTATION OUTLINE

The dissertation is organized in such a way as to answer the formulated RQs.

Chapter 2 is aimed at answering RQ1. First, characteristics and requirements for NEA flyby missions are derived, followed by an analysis of the applicability of COTS components for each relevant subsystem.

Chapter 3 is aimed to answer RQ4. The focus is shifted on evaluating and characterizing the AOCs systems for such missions, focusing on the propulsion system in the first half, and on the sizing of the attitude control system in the second.

Chapter 4 is aimed at answering RQ2. The characteristics of LoS navigation systems, with a particular focus on the geometry condition and on the parameters' influence, are investigated, and some testing is performed for NEA scenarios.

Chapter 5 is aimed to answer RQ3. The core of the chapter is the simulation of synthetic images, and the development of algorithms to extract measurements from star tracker images.

Chapter 6 is part of a side project and aims to answer RQ2.5. The core is the development of a combined navigation technique LoS and crosslink radiometric for distributed deep-space systems.

The conclusion chapter highlights the main findings of the PhD research and addresses all the RQs.

# 2

## MISSION AND PLATFORM DESIGN

*As flames consumed the woodland's grace,  
Fleeing creatures raced at a frantic pace.  
A lion's roar pierced the smoky haze,  
A little bird held water, its hope ablaze.  
"You cannot douse the fire's furious might,  
Your stature feeble, lacking in might!"  
Yet, undeterred, the bird fixed its gaze,  
Revealing truth in its unwavering phrase:  
"Though small I be, aware of my plight,  
I offer aid, a flicker in the night."*

Ancient African Fabula poeticized by ChatGPT

*This chapter aims to explore the feasibility of employing a 3U CubeSat platform for NEAs fly-by. First, the mission characteristics are highlighted, drafting requirements that drive the design. Then, the relevant subsystems are analyzed, starting from the payload and propulsion system, going through Attitude Determination and Control System (ADCS), communication system, On-Board Data Handling (OBDH), and power system. The applicability of COTS components is analyzed for each subsystem. Finally, the mass and volume budgets are presented, showing the possibility of keeping the mass and volume respectively below 4 kg and 3U. The preliminary design highlighted in this chapter is later refined in Chapter 3, where the focus is shifted to a more in-depth design of the AOCS.*

## 2.1. MISSION TYPE DESCRIPTION

Numerous mission ideas have been suggested for studying NEAs and other small celestial bodies. These proposals usually involve a mothership that carries multiple CubeSats onboard, as seen in Michel et al., 2022, or independent missions, such as those described in R. Walker et al., 2017 and McNutt et al., 2014. The missions can either involve rendezvous or fly-by of the targets. Rendezvous missions permit more extensive exploration, but require a significantly greater  $\Delta V$ , making it difficult to design small, low-cost CubeSats. Fly-by missions have a much shorter scientific phase, but a much smaller  $\Delta V$  and simpler communication subsystem design.

This chapter presents a mission concept characterized by a NEA fly-by achieved after an Earth's escape, consistent with current space exploration trends. A single fly-by approach has been chosen instead of multiple ones, sometimes referred to as 'NEAs tour,' due to the complexity of the latter. Furthermore, the mission concept aims to employing a completely autonomous and COTS 3U CubeSat configuration to reduce launch mass and volume, as well as cost. The mission concept can be characterized by a Mission Objective (MO) and a Mission Philosophy (MP):

- MO: improve target Near Earth Asteroid dataset in terms of dimension, shape, rotational parameters, composition and ephemerides.
- MP: maximize the scientific return with limited cost, by COTS components, autonomous operations and Guidance, Navigation, and Control (GNC), commercial launcher, small size, and standard platform.

MO and MP translate in Mission Requirements (MR), summarized in Table 2.1.

Acronym	Mission Requirement
MR1	Total mass shall be below 4 kg
MR2	Total volume shall fit 3U
MR3	The spacecraft shall exploit a fully-autonomous navigation strategy
MR4	Mission duration shall not exceed 650 days
MR5	The platform shall exploit COTS components for all subsystems

Table 2.1: Mission Requirements definition.

Table 2.2 outlines the different phases of the proposed mission scenario. Initially, the CubeSat is deployed in an injection orbit around the Earth and undergoes a detumbling process. Subsequently, the propulsion system is engaged to launch the CubeSat on an Earth's escape trajectory, followed by the interplanetary cruise phase, and culminating in the close encounter phase (determined by the navigation switch from absolute to relative). After the scientific phase, the gathered data is transmitted to the ground segment, and finally, the spacecraft is placed in its final disposal trajectory. The length of each phase varies depending on the NEA target selected, and Table 2.2 presents the anticipated duration of each phase.

To achieve the injection orbit, a Super Synchronous Geostationary Transfer Orbit (SSGTO) has been chosen due to its high energy and commercial availability, which can

Phase	Acronym	Duration
Injection and Detumbling	ID	~ 1 day
Earth's Escape	EE	~ 3–10 days
Deep-Space Cruise	DSC	~ 100–900 days
Close Encounter	CE	~ 1–14 days
Scientific Acquisition	SA	~ 1–2 days
Data Transmission	DT	~ 2–3 days
Final Disposal	FD	~ 5–6 days

Table 2.2: Description of the mission phases.

further reduce expenses. The SSGTO has apogee and perigee altitudes of 295 km and 90,000 km, respectively.

## 2.2. SUBSYSTEMS ANALYSIS

According to reference Bouwmeester et al., 2017, a satellite's physical architecture serves as the foundation upon which all its functions and performance are based. It encompasses the satellite's breakdown into physical subsystems and components, their location, and their structural and electrical interfaces. Most CubeSat architectures utilize a modular stack of printed circuit boards (PCBs), with each subsystem represented by one (or more) PCBs. In addition to the conventional approach, innovative architectural concepts have been proposed over the years, including cellular, panel, plug-and-play, and lean electrical interfaces.

The following sections aim to define all the relevant subsystems, presenting the available COTS options and assessing their suitability and performance for the mission concept. The payload and scientific output are analyzed first. Then, each subsystem that constitutes the spacecraft bus is evaluated individually, with the propulsion system being one of the key driving subsystems due to its large mass and volume. The analysis presented here for the propulsion system serves as a preliminary assessment and design of the platform, and it is later refined in Chapter 3.

### 2.2.1. PAYLOAD

The exploration of NEAs is connected to three main objectives: scientific research on the evolution of the solar system, planetary protection, and the exploitation of in-situ resources. These objectives are related to the lack of accurate information about asteroids that can only be acquired through in-situ observation. A low-cost CubeSat can be used for NEA exploration to expand the available data set. A visible camera can be used to determine the shape, size, and rotation of the asteroid, while an IR spectrometer can be used to analyze its composition. Determining mass and density is more challenging but can be achieved through the Yarkovsky effect (Chesley et al., 2014) or by using a pair of CubeSats to measure their relative distance before, during, and after encountering the asteroid (L. Walker et al., 2021). Magnetic field residuals can also be measured using off-the-shelf magnetometers. A visible camera and IR spectrometer are the minimum set of required payloads for such missions, but COTS payloads for space missions are limited,

Camera	Mass [g]	Size [mm]	PP [W]	Res. [MP]	FoV [°]
Hyperion IM200 <sup>2</sup>	59	29 x 29 x 70.7	1000	4	20 x 20
CS Micro Camera System <sup>3</sup>	50	45 x 25 x 45	240	0.3	44 x 34
XCAM C3D <sup>4</sup>	85	95 x 91 x 27	845	1.3	38 x 31
SCS Space Gecko Imager <sup>5</sup>	390	56 x 97 x 96	2700	N/A	N/A
HyperScout Cosine <sup>6</sup>	1200	100 x 100 x 100	N/A	4	25 x 12
SS HyperScape100 <sup>7</sup>	1200	98 x 98 x 176	6000	4	2.22
SS MultiScape100 <sup>7</sup>	1200	98 x 98 x 176	6000	4	2.22
SS TrtiScape100 <sup>7</sup>	1100	98 x 98 x 176	6000	12	2.22

Table 2.3: COTS Cameras characteristics.

especially designed for Earth observation.

The scientific payload is typically the subsystem that is most tailored for a space mission, as it heavily relies on the mission's objectives. Currently, there are only a few COTS payloads available on the market, particularly for Earth observation. Additionally, the 3U configuration limits the types of instruments that can be used. While there is only one off-the-shelf option for an IR spectrometer, the Thoth Technology Argus 2000<sup>1</sup>, a wider range of visible cameras are available, whose characteristics are reported in Table 2.3, although only a handful are small enough to be included in a 3U CubeSat, as demonstrated in later sections.

The Ground Sampling Distance (GSD) is also a crucial parameter, as it measures the distance between two adjacent pixels in an image and determines the accuracy with which an asteroid's shape can be described. The optimal GSD value is difficult to determine due to the various sizes, shapes, and fly-by altitudes of the targets, but a maximum value of 50 m/pixel at 300 km altitude is feasible, as it would allow for at least 6x6 pixels to describe a 300 m diameter NEA, which is the minimum requirement for scientific output and relative navigation. However, a lower GSD would result in improved scientific output and navigation accuracy. Determining the minimum number of pixels needed to describe an asteroid would require further research and would depend on factors such as image extraction techniques and hardware constraints.

The GSD at a specific altitude can be obtained from the product datasheet provided by the manufacturers. In cases where this information is not available, it is still feasible to estimate the GSD at a given altitude by utilizing the fundamental characteristics of the camera:

$$GSD = \frac{hS_w}{f i m_w}, \quad (2.1)$$

<sup>1</sup> <http://thothx.com/home>,

<sup>2</sup> <https://www.aac-clyde.space/what-we-do/space-products-components/payloads/im200>,

<sup>3</sup> <https://crystalspace.eu/wp-content/uploads/2015/12/Camera-summary.pdf>,

<sup>4</sup> <https://www.xcam.co.uk/c3d-cubesat-camera>,

<sup>5</sup> [https://www.cubesatshop.com/wp-content/uploads/2016/11/SCS-Space-Gecko-Brochure\\_2016-11-14.pdf](https://www.cubesatshop.com/wp-content/uploads/2016/11/SCS-Space-Gecko-Brochure_2016-11-14.pdf),

<sup>6</sup> <https://www.cosine.nl/business-units/hyperscout/>,

<sup>7</sup> <https://simera-sense.com/>

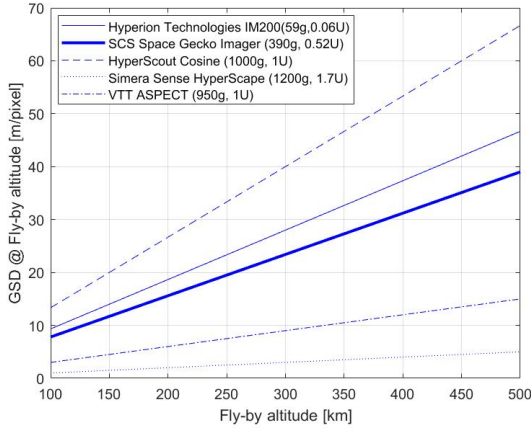


Figure 2.1: Ground Sampling Distance (GSD) as a function of the fly-by altitude, for off-the-shelf visible cameras, together with mass and volume characteristics.

Equation 2.1 uses the altitude ( $h$ ), sensor width ( $S_w$ ), image size in pixels ( $im_w$ ), and focal length ( $f$ ) to calculate the GSD. Figure 2 illustrates the GSD variation as a function of the fly-by altitude for the most promising COTS cameras and ASPECT (R. Walker et al., 2017), a Multi-spectral imager from VTT Technical Research Centre of Finland. While ASPECT is not a COTS instrument, its small size (1U), weight (950 g), and power consumption (7 W) make it a practical alternative to the COTS camera and spectrometer, particularly for larger applications. ASPECT is equipped with three acquisition channels (VIS, NearIR (IR), and ShortWave IR).

The comparison does not include other off-the-shelf components such as the Crystal Space Micro Camera System and XCAM C3D, which are compact but do not provide sufficient GSD for a significant scientific return. The AAC Hyperion IM200 is the most promising solution in terms of mass and volume and can also be used as a navigation camera. For larger CubeSats, the SCS Space Gecko Imager is an excellent alternative in terms of accuracy, and the Simera Sense HyperScape100 and MultiScape100 provide high resolution and the ability to perform VIS and NIR measurements with the same instrument. However, the AAC Hyperion IM200 is the best fit for this platform due to its low mass and volume. The only currently available off-the-shelf IR spectrometer is the Argus 2000, which is smaller than ASPECT's range and has a narrow FoV, but its mass and volume make it suitable for this application. These preliminary considerations provide insight into the typical and minimum payload required for a low-resources spacecraft exploring NEAs. However, a custom payload may still be necessary to achieve the desired scientific return, as the hardware design is strongly linked to the techniques used to extract data, such as determining the target's shape, rotational parameter, or composition. Therefore, the budget section includes configurations with and without payload to characterize the allowable mass and volume for a custom payload.

### 2.2.2. PROPULSION

The choice of the propulsion system is critical, as it defines the range of applications for the platform. In the following subsections, a preliminary analysis is presented for both chemical and electric propulsion options. They are needed at this point for the preliminary design of the platform, but the analysis will go more in-depth in Chapter 3.

#### CHEMICAL MICRO-PROPULSION

The NASA-JPL Small Body Database Browser (NASA JPL, 2023) was used to preliminarily calculate the necessary escape velocity  $V_\infty$  from Earth's Sphere-Of-Influence (SOI) for the spacecraft to be injected into an interplanetary transfer toward the desired NEA. The Mission Design Tool allows the user to input the name or code of a specific asteroid to receive information about the mission to the target, including required escape velocity, ToF, and departure date. Mission characteristics are calculated by solving Lambert's problem, which finds a trajectory giving two points in space and time Izzo, 2014. Table 2.4 presents a preliminary list of possible targets with their corresponding departure dates, ToF, and required escape velocity, which represent the minimum  $\Delta V$  solution. This list has been used here to derive preliminary conclusions about the propulsion system, but a larger list (based on navigation considerations) will be employed in later sections for more detailed analysis. Using the patched conics approach and recalling the SSGTO injection orbit, an estimated  $\Delta V$  can be calculated to deliver to the spacecraft at perigee to inject it on an escape hyperbola:

$$\Delta V = \sqrt{V_\infty^2 + \frac{2\mu}{r_{SSGTOp}}} - V_{SSGTOp} \quad (2.2)$$

where  $V_\infty$  is the hyperbolic excess velocity,  $\mu$  is the Earth gravitational parameter, and  $r_{SSGTOp}$  and  $V_{SSGTOp}$  are the radius and velocity at the perigee of the SSGTO. Figure 2.2 illustrates the relationship between the escape velocity  $V_\infty$  and the perigee  $\Delta V$ , as determined by Equation 2.2. The plot shows that a  $\Delta V$  budget of 385 m/s will ensure a hyperbolic excess velocity greater than 0.6 km/s, which is the highest escape velocity presented in Table 2.4. Consequently, 385 m/s can be assumed as the general  $\Delta V$  requirement for the escape trajectory and Trajectory Correction Manoeuvres (TCM(s)), whose allocated budget is in the range of 5-10 m/s as shown in the navigation requirements definition. Wheels de-saturation is addressed in Chapter 3. Further analysis can be performed to determine the optimal escape strategy, which may involve fractional apogee-raising manoeuvres due to the micro-propulsion system's limited burn time.

After establishing the general  $\Delta V$  requirement, an evaluation of the micro-propulsion system can be conducted. Solid propellant thrusters are not viable due to their limited ability to perform multiple burns, while cold gas micro propulsion systems have a low specific impulse. Liquid mono- and bi-propellant micro-propulsion systems are the optimal choice to inject the CubeSat on a transfer trajectory towards a NEA. Single thrusters and complete integrated micro-propulsion systems are both available on the market, with the former providing a more customized propellant mass, and the latter an off-the-shelf, ready-to-use system. Figure 2.3 illustrates the relationship between required specific impulse and propellant mass to deliver 385 m/s to a CubeSat, with varying Beginning-Of-Life (BOL) mass, and displays the micro-propulsion systems and their

Target	Departure Date	ToF [days]	$v_{\infty}$ [km/s]	Diameter [m]
99942 Apophis	06/08/2028	230	0.1	320
4660 Nereus	18/05/2028	100	0.2	330
35107	14/01/2025	205	0.2	929
161989 Cacus	17/12/2039	635	0.2	635
153201	03/04/2029	815	0.3	510
66391 Moshup	01/02/2036	115	0.3	1317
13651	03/04/2029	815	0.4	562
7482	08/04/2031	640	0.4	1052
4034 Vishnu	27/04/2033	510	0.4	420
142464	20/08/2034	625	0.5	886
138127	24/05/2027	260	0.5	754
65679	17/11/2036	615	0.5	918
1943 Anteros	20/12/2025	165	0.5	2300
2102 Tantalus	27/04/2034	635	0.5	1650
3200 Phaethon	04/03/2028	985	0.6	300
11500 Tomaiyowit	12/04/2035	235	0.6	738

Table 2.4: NEAs target retrieved from the JPL Small Body Database.

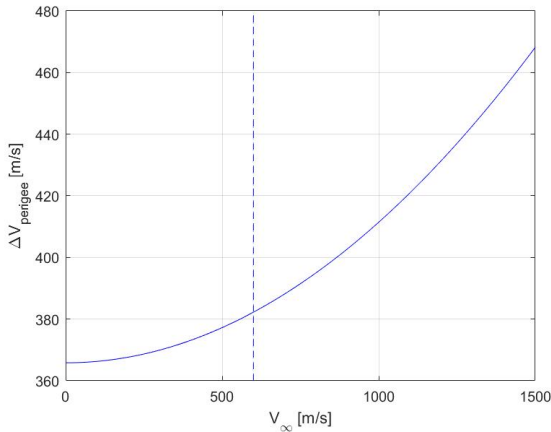


Figure 2.2: Required  $\Delta V$  at the perigee to inject the spacecraft into an escape orbit with certain  $V_{\infty}$ .



Product	Max T[mN]	Isp [s]	Dry-Wet mass [kg]	Volume
AR MPS-130	1250	206-235	1.06, 1.66/ 1.36, 2.76	1U/2U
AR MPS-120	1250	206-217	1.06, 1.48/1.36, 2.38	1U/2U
Vacco Green MiPS	400	190	3.0, 5.01	3U
Vacco Argomoon h-MiPS	100+ 4x25	190	1.43, 2.06	1.3U
NA EPSS C1	1000 (BOL)	213	1,1.2	1.3U
TU Hydros-C	1200	310	1.87,2.61	2.5U
Hyperion PM200	500	285	1.1, 1.41	1U
Hyperion PM400	1000	285	1.4, 2.025	2U

Table 2.5: COTS Chemical Micro Propulsion Systems characteristics.

characteristics, available in Table 2.5. The comparison is made among the VACCO MiPS<sup>8</sup>, VACCO ArgoMoon MiPS<sup>8</sup>, Aerojet Rocketdyne MPS-130<sup>9</sup>, Aerojet Rocketdyne MPS-120<sup>9</sup>, Busek BGT-X5<sup>10</sup>, NanoAvionics EPSS C1<sup>11</sup>, AAC Hyperion PM200 and PM400<sup>12</sup>, and Tethers Unlimited HYDROS-C<sup>13</sup>.

A semi-COTS option is represented by the ECAPS HPGP thrusters<sup>14</sup>, whose performances are shown in Figure 2.4, taking into account the different thruster masses. Both plots are obtained from the rocket equation. The issue related to using these thrusters is that the complete propulsion system, including the tank and feeding system, shall be custom designed. From the evaluation chart, the most promising solution is the Aerojet Rocketdyne MPS-130 1U, a mono-propellant micro propulsion system that can provide 385 m/s of  $\Delta V$  to a 3.9 kg CubeSat. Although the ECAPS HPGP 0.1 N thruster can offer a higher  $\Delta V$  or the same  $\Delta V$  to a heavier CubeSat, it would require additional design of the rest of the propulsion system (tank, feeding systems, etc.), making the platform non-off-the-shelf. Some options, such as EPSS C1, already incorporate the ECAPS HPGP thrusters.

The selection of the Aerojet Rocketdyne MPS-130 defines then the mass and volume requirements for the platform and the other subsystems, which need to fit the remaining 2U. Moreover, as this engine can deliver the required  $\Delta V$  to a CubeSat of a maximum of 3.9 kg, and it is characterized by a BOL mass of 1.7 kg, the remaining components of the platform should not exceed 2.2 kg of mass. This, again, shows that mass and volume for each component are driving parameters for the selection.

### ELECTRIC MICRO-PROPULSION

The assessment of electric micro-propulsion systems involves designing and optimizing low-thrust trajectories, which is a challenging task. The JPL Small-Body Database Browser Mission Design Tool provides some reference values for low-thrust trajectories towards specific asteroids. In recent years, trajectory optimization for fly-bys of NEAs has

<sup>8</sup> <https://www.cubesat-propulsion.com/>,

<sup>9</sup> <https://www.rocket.com>.

<sup>10</sup> <https://www.busek.com/bgtx5>,

<sup>11</sup> <https://nanoavionics.com/cubesat-components/cubesat-propulsion-system-eps/>,

<sup>12</sup> <https://www.aac-clyde.space/what-we-do/space-products-components/pm200>,

<sup>13</sup> <https://www.tethers.com/wp-content/uploads/2021/01/HYDROS-C-1.pdf>,

<sup>14</sup> <https://www.ecaps.space/products-overview-ecaps.php>

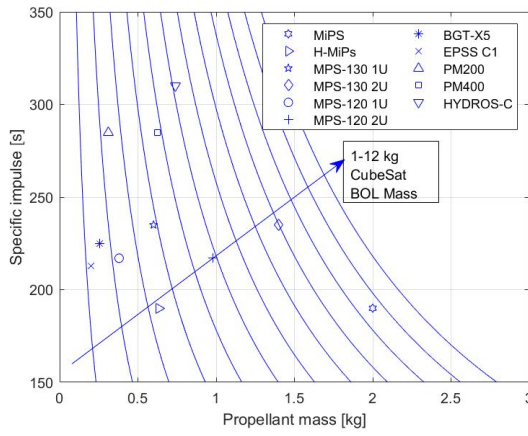


Figure 2.3: Required specific impulse and propellant mass to deliver 385 m/s to a certain mass satellite.

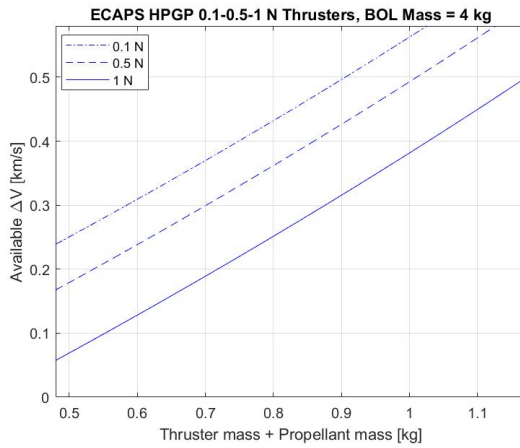


Figure 2.4: Available  $\Delta V$  using the ECAPS thrusters. Casini et al., 2021

been explored extensively, demonstrating the feasibility of such missions. Some studies have considered solar electric propulsion systems and electrospray thrusters, which have shown small  $\Delta V$  requirements for many NEAs, making them viable alternatives to rendezvous missions (Greco et al., 2018; Machuca et al., 2020).

However, using the rocket equation to compute the required propellant mass for electric thrusters is not possible, as it is based on a constant ejection velocity assumption, whereas low-thrust trajectories are based on variable thrust. Therefore, previous studies cannot be used for the preliminary evaluation of COTS electric micro-propulsion systems for asteroid fly-bys. A shape-based low-thrust trajectory design approach (Novak and Vasile, 2011) can be used to estimate the required propellant mass without going through a complete optimization, which is later explored in Chapter 3.

The spherical coordinates shaping trajectory design approach can generate an initial guess solution for the trajectory by imposing the shape and constraining the initial and final conditions. It is suitable for rendezvous low-thrust trajectory design, where the final condition matches the velocity and position of the target asteroid. However, it overestimates the required propellant mass for fly-by trajectory design, which is generally less expensive than rendezvous missions.

To overcome this limitation, some constraints can be imposed on the encounter with the asteroid, such as setting it at one of the two nodes (descending or ascending) of the asteroid orbit and using a 'fictitious' orbit with zero inclination to avoid expensive change-of-plane manoeuvres. Then, a grid search can be performed on three varying parameters: ToF final velocity, and node passage, to optimize the approach further.

Firstly, the minimum  $\Delta V$  is determined, and using the control acceleration profile, the mass and thrust profiles can be calculated as functions of the specific impulse and BOL mass of 4 kg. This is achieved by applying a set of equations, namely the 2nd Newton law and mass flow rate equation. However, it should be noted that the search grid's results are not necessarily optimal and can be improved by expanding the final velocity range and varying the in-plane angle. Nevertheless, at this stage, the estimated propellant mass provides a rough requirement that can be increased with a design margin. The evaluation process is carried out for all 16 NEAs in Table 2.4, and Table 2.6 presents the results for the ten NEAs with reasonable propellant mass for a 4 kg CubeSat. The other six NEAs require a propellant mass greater than 2.5 kg, and they have been excluded from the table. The maximum required propellant mass for the ten NEAs is 1.1 kg (for the lowest Isp of 2000 s), with thrust levels within 1.1 mN (excluding 4034 Vishnu). Finally, the extended results for one of the NEAs, 65679, are shown in Figures 2.5 and 2.6.

Available electric propulsion options characteristics are reported in Table 2.7. If electric propulsion systems with a specific impulse below 2000 s are used, the propellant mass required for the mission will be significantly impacted, making it less feasible. Hence, Sitael HT-100<sup>15</sup>, Mars Space LTD PPTCUP<sup>16</sup>, and Busek BHT-200<sup>17</sup> cannot be used for this mission. Instead, higher specific impulse options such as Busek BIT-3 ion thruster<sup>18</sup>, Mars Space LTD mini RF ion engine<sup>19</sup>, Empulsion IFM Micro 100<sup>20</sup> and Nano Thrusters<sup>21</sup> are considered. However, BIT-3 and IFM Micro 100 are too large for a 3U CubeSat and require at least 1.8U and 2.2U respectively, leaving insufficient space for other subsystems. Mars Space LTD mini RF ion engine, on the other hand, requires the additional design of the rest of the micro propulsion system and a large volume, making

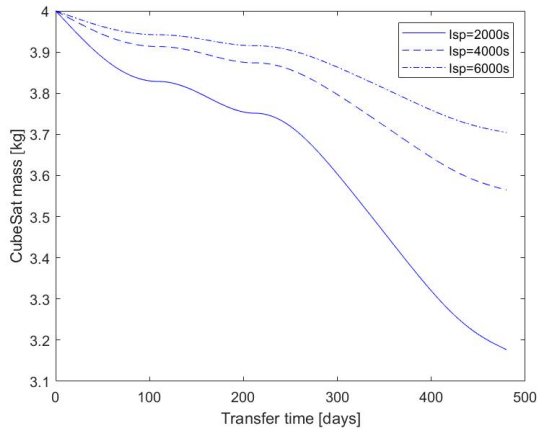


Figure 2.5: Satellite mass evolution for the trajectory towards NEA 65679, exploiting the shape-based approach, for different propulsion systems specific impulse.

it unsuitable. Although Enpulsion IFM Nano thruster occupies a small volume of around 0.8U, its maximum thrust level of 0.35 mN is insufficient for the analyzed NEAs. This preliminary analysis suggests that chemical propulsion for this application offers better performance. Additionally, high-thrust chemical propulsion systems are preferred over low-thrust electric propulsion systems as they allow impulsive manoeuvres, which are necessary given the short visibility times of the asteroids. For example, delivering 10 m/s to the satellite using the Aerojet Rocketdyne MPS-130 requires approximately 500 s, while for electric propulsion systems, the firing time can take several hours.

### 2.2.3. ADCS

The ADCS is a collection of various sensors (e.g., Sun sensors, star trackers, hall-sensors, etc.) used to determine the state of the spacecraft and actuators (e.g., reaction wheels, thrusters) used to control its orientation. There are many companies that offer integrated ADCS solutions, which include all necessary sensors and actuators along with processors that can perform most of the computations required for controlling the satellite. Therefore, these integrated solutions are the primary focus for ADCS selection. When selecting the ADCS for the mission discussed in this paper, pointing accuracy is the main parameter that influences the decision. The required pointing accuracy is primarily influenced by three factors: the FoV of the payload, the directional accuracy required for thrusting manoeuvres, and the maximum amount of pointing losses allowed for downlinking data. This means that the actual requirement for the pointing accu-

<sup>15</sup> <https://www.sitael.com/space/advanced-propulsion/electric-propulsion/hall-effect-thrusters/>,

<sup>16</sup> <https://mars-space.co.uk/gridded-ion-engine>,

<sup>17</sup> [http://busek.com/index\\_htm\\_files/70000700A%0BHT-200.pdf](http://busek.com/index_htm_files/70000700A%0BHT-200.pdf),

<sup>18</sup> [http://busek.com/index\\_htm\\_files/70010819E.pdf](http://busek.com/index_htm_files/70010819E.pdf),

<sup>19</sup> <https://mars-space.co.uk/gridded-ion-engine>,

<sup>20</sup> <https://www.enpulsion.com/order-old/ifm-micro-thruster/>,

<sup>21</sup> <https://www.enpulsion.com/order-old/ifm-nano-thruster/>

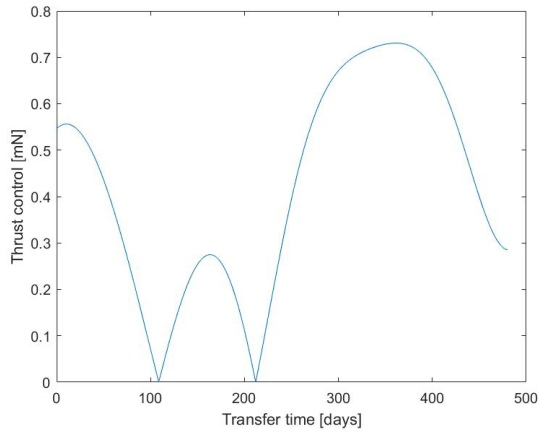


Figure 2.6: Thrust profile for the trajectory towards NEA 65679, exploiting the shape-based approach.

Target	Mp [g], Isp = 2000 s	Mp [g], Isp = 6000 s	ToF [days]	Max T [mN]
99942 Apophis	650	210	560	0.62
4660 Nereus	780	210	510	0.98
161989 Cacus	1100	400	590	1.10
13651	900	270	590	0.70
6482	900	310	590	1.05
4034 Vishnu	1400	450	530	1.60
65679	830	300	490	0.72
1943 Anteros	520	190	490	0.52
2102 Tantalus	850	300	480	1.00
11500 Tomaiyowit	1100	400	580	1.05

Table 2.6: Results low thrust preliminary analysis.

Product	Max T[mN]	Isp [s]	Dry-Wet mass [kg]	Volume
Mars Space LTD PPTCUP	0.09	640	N/A, 0.35	< 0.5 U
Busek BHT-200	13	1390	1.1, N/A	N/A
Busek BIT-3	1.1	2150	1.4, N/A	~ 1.8
Mars Space LTD mini RF	0.85	2500	0.3, N/A	< 0.6 U
ENPULSION Micro 100	1.35	1500-6000	2.6,3.9	1 U
ENPULSION Nano	0.35	2000-6000	0.68,0.9	0.8U

Table 2.7: COTS Electric Micro Propulsion Systems characteristics.

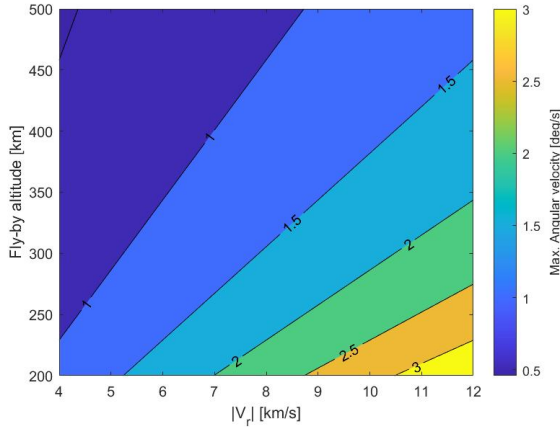


Figure 2.7: Angular rate as a function of fly-by characteristics.

racy will depend on the specific mission scenario, so in this analysis the aim is to have the lower pointing error possible meeting the mass and volume requirements. Although factors like jitter and agility are also essential for the performance of the payload and communication subsystem, they are not readily available in most cases.

During an asteroid fly-by, the ADCS must be able to dynamically track the target throughout all phases of the close approach, considering the relative angular velocity and the payload FoV. The ADCS's maximum slew rate should be greater than the maximum relative angular velocity. This assessment depends on the relative velocity and the altitude at the close encounter. Approximating the fly-by passage with the velocity perpendicular to the distance vector to the asteroid, it is possible to calculate the relative angular velocity during fly-by. Relative angular velocity is reported as a function of the fly-by relative velocity and fly-by altitude in Figure 2.7, which shows that the required slew rate is below  $1.5^\circ/s$  for altitudes above 450 km, even for high relative velocities (12 km/s). As the fly-by altitude decreases, the required slew-rate increases. Based on the available ADCS slew rate and relative velocity, the fly-by altitude of the target can be adjusted. Having sufficient momentum storage in the reaction wheel or a sufficient amount of propellant in the case of reaction thrusters is crucial for the performance of the actuators. Additionally, a solution for de-saturating the wheels is necessary. While magnetorquers are typically used for this purpose in LEO satellites, they are not viable in environments with negligible magnetic fields. Reaction thrusters are used in deep-space applications to provide a counter torque during momentum dumping. For CubeSats, there are only a few off-the-shelf options for reaction thrusters, including the Aurora Resistojet Module<sup>22</sup>, VACCO MiPS cold gas propulsion system<sup>23</sup>, and GomSpace NanoProp CGP3<sup>24</sup>. These options can effectively de-saturate reaction wheels, but additional subsystems designed exclusively for de-saturation can pose challenges in terms of CubeSat mass, and it is explored in Chapter 3. If possible, relying on the main engine for de-saturation would be ideal Pizzetti et al., 2023.

Multiple companies offer integrated ADCS solutions, whose characteristics are re-

ported in Table 2.8.

The Blue Canyon Technologies XACT-15<sup>25</sup> would be the best option for a standard CubeSat ADCS subsystem due to its fine declared pointing accuracy and flight heritage, but its large mass and volume make it unsuitable for this mission. AAC Hyperion iADCS-200<sup>26</sup> is a more compact solution, while CubeSpace 3-axis ADCS<sup>27</sup>, KU Leuven ADCS<sup>28</sup>, and Adcole Maryland Aerospace MAI-500<sup>29</sup> are heavier solutions. NanoAvionics 4RW0<sup>30</sup> is an excellent control system for deep-space applications, but its large mass, volume, and peak power consumption make it difficult to integrate into the compact platform presented here. Integrated off-the-shelf ADCS solutions typically use reaction wheels for attitude control rather than reaction thrusters, offering an advantage over an assembly of attitude sensors, actuators, and processors. Star trackers and Sun sensors are required for attitude determination and navigation purposes, and all the integrated options presented have space for allocation of multiple Sun sensors and a star tracker.

This section considers the trade-off between mass, volume, and pointing accuracy when evaluating the integrated ADCS options. The declared pointing accuracy for all options, except for the XACT-15, falls within the required range of 0.1-0.2 degrees ( $3\sigma$ ), with the XACT-15 offering the finest pointing accuracy. As all options meet the required pointing accuracy for the payload, mass and volume become important factors in selecting the best option. The AAC Hyperion iADCS200 is chosen as the best solution for this application due to its lower mass and volume, even though its declared pointing accuracy is less than 1 degree. Additionally, it provides a slew rate larger than 1.5 degrees per second, which is sufficient for keeping the target in the field of view at various fly-by altitudes and relative velocities, as shown in Figure 2.7. While the XACT-15's finer pointing accuracy would be beneficial for navigation purposes, careful analysis should be performed to evaluate the trade-off between its advantages and the increase in allowable volume and mass for the payload. It may be considered to replace the iADCS200 with XACT-15 if deemed necessary.

The preliminary analysis presented in this section is further refined in Chapter 3, where the hardware characteristics are combined with control algorithms to define the applicability.

#### 2.2.4. COMMUNICATION

This section focuses on X-Band communication systems for deep-space communications, as there are limited options available for Ka-Band. However, advancements in laser communication technologies may also be used in the future. The downlink is the main focus of communication analysis due to the previously mentioned autonomous

<sup>22</sup> [https://aurorapt.fi/2020site/wp-content/uploads/2020/08/AURORA\\_ARM\\_V3.pdf](https://aurorapt.fi/2020site/wp-content/uploads/2020/08/AURORA_ARM_V3.pdf),

<sup>23</sup> [https://www.vacco.com/images/uploads/pdfs/MIPS\\_standard\\_0714.pdf](https://www.vacco.com/images/uploads/pdfs/MIPS_standard_0714.pdf),

<sup>24</sup> <https://gomspace.com/shop/subsystems/attitude-orbit-control-systems/nanoprop-3u-propulsion.aspx>,

<sup>25</sup> [https://storage.googleapis.com/blue-canyon-tech-news/1/2020/06/BCT\\_DataSheet\\_Components\\_ACS\\_06\\_2020.pdf](https://storage.googleapis.com/blue-canyon-tech-news/1/2020/06/BCT_DataSheet_Components_ACS_06_2020.pdf),

<sup>26</sup> <https://hyperiontechnologies.nl/products/iadcs200/f>,

<sup>27</sup> <https://www.cubespace.co.za/products/gen-1/integrated-adcs/cubeadcs/>,

<sup>28</sup> [https://www.cubesatshop.com/wp-content/uploads/2018/10/KULADCS-Datasheet\\_v2.pdf](https://www.cubesatshop.com/wp-content/uploads/2018/10/KULADCS-Datasheet_v2.pdf),

<sup>29</sup> <https://www.satcatalog.com/datasheet/Adcole%20Maryland%20Aerospace%20-%20MAI-500.pdf>,

<sup>30</sup> <https://nanoavionics.com/cubesat-components/cubesat-reaction-wheels-control-system-satbus-4rw/>

navigation strategy. Syrlinks<sup>31</sup> offers various X-Band transmitters and antennas for CubeSat, such as EWC27, N-XONOS, SPAN-X-T2, and SPAN-X-T3, but their datasheets are not accessible. Meanwhile, Endurosat<sup>32</sup> and AAC Clyde Space<sup>33</sup> offer both X-Band transmitters and antennas with evaluated performances. COTS X-band transmitters list includes Endurosat X-band transmitter, AAC Clyde Space Pulsar-Data, Tethers Unlimited SWIFT-XTX<sup>34</sup>, Glavkosmos X-band transmitter<sup>35</sup>, InnoFlight SCR-106<sup>36</sup>, Sputnix X-band transmitter<sup>37</sup>, and Space-SI X-band transmitter<sup>38</sup>. Their characteristics are reported in Tables 2.9 and 2.10.

Observing the transmitters' data, it is interesting to explore the feasibility of the Endurosat and AAC Clyde Space components, as they offer 2 W of transmitting power, with a low mass and lower power consumption than the InnoFlight and Glavkosmos options.

The data rate in the telecommunication link budget is dependent on several factors, which can be rearranged using the classical link budget equation (Wertz et al., 2011):

$$R = 10^{\frac{1}{10}(P_t + L_{tr} + G_{ant} + L_p + L_{path} + L_{at} + G_r + DTP - SN - E_b/N_0 + LM + L_r)}, \quad (2.3)$$

In the evaluation of a deep-space scenario, various factors are taken into account, including  $P_t$  for transmitting power,  $L_{tr}$  for transmit loss,  $G_{ant}$  for antenna gain,  $L_p$  for pointing loss,  $L_{path}$  for space loss,  $L_{at}$  for atmospheric loss,  $G_r$  for receiver antenna gain, DTP for data to total power, SN for system noise, LM for link margin, and  $L_r$  for receiver loss. According to Wertz et al., 2011, the assumptions made for this evaluation are: required  $E_b/N_0$  is assumed to be 1dB, required link margin is 3 dB, the atmospheric loss is -0.3 dB, transmit loss is -2 dB, receiver loss is -1 dB, and DTP is -0.6 dB. Based on Equation (2.3), Figure 2.8 shows the maximum data rate for off-the-shelf antennas as a function of the distance from Earth. The ground antenna used for this evaluation is a Deep-Space Network (DSN) 34-m diameter antenna, with a receiving gain of 68.2 dBic, and a system noise density of -183.6 dBm/Hz. The actual time to downlink the dataset depends on factors such as ground station availability and the size of the dataset, which will require further investigation. The Earth-target distance will need to be considered to determine the appropriate dataset size and communication time relation. Additionally, the cost associated with the communication ground station will need to be evaluated, and less expensive ground antenna options will need to be considered.

Considering the allowed data rate, mass, volume, and power consumption, AAC Clyde Space Pulsar-Data is identified as the best option for this mission. Endurosat 4 × 4 patch antenna was identified as the most performant X-band antenna due to its higher gain (16 dBi), as it offers a higher data rate, while its mass (52 g) is only slightly larger than the other two best options (Endurosat 2 × 2 patch antenna with 23 g and AAC ClydeSpace with 29 g).

MarCO CubeSat carried onboard a deployable reflectarray. It has been not included in the analysis due to its large mass of 1 kg, which does not meet the strict requirements of the mission, despite its small storage volume (~ 0.1U) and high gain (~ 29dBi). However, it could be a valuable solution for larger CubeSat platforms (Klesh et al., 2018).

<sup>31</sup> <https://www.syrlinks.com/en/produits/all/space/nano-satellite>,

<sup>32</sup> <https://www.endurosat.com/products/?v=796834e7a283#cubesat-communication-modules>,

<sup>33</sup> <https://www.aac-clyde.space/satellite-bits/communications>

<sup>34</sup> <https://www.tethers.com/wp-content/uploads/2020/07/SWIFT-XTX.pdf>,



Product	Point. Err. [deg]	Volume [mm]	Mass [kg]	Power [W]
Hyperion iADCS200	« 1	95 x 90 x 32	0.43	1.4
Blue Canyon XACT-15	0.003	100 x 100 x 50	0.885	N/A
KU Leuven ADCS	0.11	100 x 100 x 50	0.715	1.4
CubeSpace ADCS	0.2	90 x 96 x 52	0.328	0.57
Adcole Maryland MAI-500	0.008-0.1	100 x 100 x 62.3	1.049	1.82

Table 2.8: Integrated ADCS characteristics.

Product	$P_t$ [W]	Vol. [mm]	Mass [kg]	$P_{consumption}$ [W]
Endurosat	2	90 x 95.9 x 23.6	0.27	27
AAC Pulsar-Data	2	96 x 90 x 11.7	0.13	<15
Tethers Unl. SWIFT-XTX	1.7	86 x 86 x 50	<0.5	24-42
Glavkosmos	2.5	87 x 93 x 28	0.38	16
InnoFlight SCR-106	2.5	82 x 82 x 25	0.25	30
Sputnix	1	89 x 93 x 27	0.19	15
Space-SI	1-2	N/A	0.5	10

Table 2.9: X-Band Transmitter characteristics.

Product	Gain [dBi]	Vol. [mm]	Mass [g]
Endurosat X-Band Patch Antenna	6	24 x 24 x 6.39	2.2
Endurosat 2x2 X-Band Patch Antenna	12	60 x 60 x 7.28	23.15
Endurosat 4x4 X-Band Patch Antenna	16	82.6 x 98 x 7.23	52.85
AAC Pulsar-XANT	7.75	36 x 36 x 4.7	<10
AAC Pulsar-XANT Plus	11.5	58 x 58 x 4.7	<29

Table 2.10: X-Band Antenna characteristics.

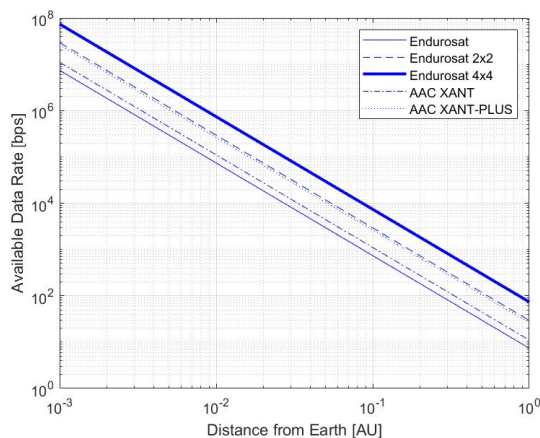


Figure 2.8: Available data rate as a function of the distance from the Earth for different configurations.

### 2.2.5. ON-BOARD DATA HANDLING

The On-Board Computer (OBC) of a satellite can have various functions depending on the satellite's configuration. In the mission described in this chapter, separate processors located in other subsystems handle functions such as attitude determination and control, and initial payload image processing. Therefore, the primary functions of the central OBC are assumed to be housekeeping, data processing and storage, autonomous operations, and communication.

Several factors determine whether a particular OBC is compatible with a mission. While factors such as the available peripherals and types of storage can be significant, this chapter focuses on power consumption, volume, mass, clock frequency, and memory storage for the trade-off analysis. Power, mass, and volume are critical due to the 3U design constraint. The clock frequency of the processor affects the number of computations that can be performed per second, along with other factors such as word size, which determine the OBC's potential functions. The mission requires high computational requirements for autonomy, navigation, and data processing. In addition to the clock frequency, data storage capacity is also crucial to increase the mission's scientific output. Table 2.11 presents the characteristics of the most promising COTS OBCs available.

Product	CF [Mhz]	Vol. [U]	Mass [g]	PC [mW]	MS [Gb]
Endurosat OBC <sup>39</sup>	216	0.23	58	340	0.256
AAC KRYTEN-M3 <sup>40</sup>	50	0.23	61.9	400	0.008
AAC S. OBC LEON3FT <sup>41</sup>	50	0.17	130	1300	2
AAC S. TCM LEON3FT <sup>42</sup>	50	0.17	134	1300	32
InnoFlight CFC-300 <sup>43</sup>	767	0.14	120	1000	16–384
AAC Hyperion CP400.85 <sup>44</sup>	500	0.01	7	550	7.5–64
GomSpace NanoMind A3200 <sup>45</sup>	64	0.02	24	170	0.160
SatRevolution Advanced OBC <sup>46</sup>	216	0.08	52	1000	0.008
ISIS iOBC <sup>47</sup>	400	0.12	100	400	4–32

Table 2.11: COTS OBDH characteristics.

<sup>35</sup> <https://www.trade.glavkosmos.com/catalog/spacecraft/telecommand-and-telemetry-system/receivers-transmitters/X-band-transmitter-for-Cubesat/>,

<sup>36</sup> <https://www.innoflight.com/product-overview/scr/scr-106/>,

<sup>37</sup> <https://sputnix.ru/tpl/docs/SPUTNIX%20-%20Cubesat%20-%20X-band%20transmitter%20-%20Datasheet.pdf>,

<sup>38</sup> <http://www.space.si/wp-content/uploads/2014/01/X-band-Transmitter-Flyer.pdf>

<sup>39</sup> <https://www.endurosat.com/products/?v=796834e7a283#cubesat-obc>,

<sup>40</sup> [https://www.aac-clyde.space/assets/000/000/102/KRYTEN\\_M3\\_original.pdf?1565617110](https://www.aac-clyde.space/assets/000/000/102/KRYTEN_M3_original.pdf?1565617110),

<sup>41</sup> [https://www.aac-clyde.space/assets/000/000/181/AAC\\_DataSheet\\_Sirius\\_OBC\\_-\\_updated\\_tables\\_original.pdf?1601990253](https://www.aac-clyde.space/assets/000/000/181/AAC_DataSheet_Sirius_OBC_-_updated_tables_original.pdf?1601990253),

<sup>42</sup> [https://www.aac-clyde.space/assets/000/000/182/AAC\\_DataSheet\\_Sirius\\_TCM\\_original.pdf?1601990743](https://www.aac-clyde.space/assets/000/000/182/AAC_DataSheet_Sirius_TCM_original.pdf?1601990743),

<sup>43</sup> <https://satsearch.co/products/innoflight-compact-flight-computer-cfc-300>,

<sup>44</sup> <https://hyperiontechnologies.nl/products/cp400-85-processing-platform/>,

<sup>45</sup> <https://gomspace.com/shop/subsystems/command-and-data-handling/nanomind-a3200.aspx>,

<sup>46</sup> <https://satrevolution.com/products/rec/>,

<sup>47</sup> <https://www.isispace.nl/product/on-board-computer/>

The Endurosat OBC, AAC Clyde Space KRYTEN-M3, AAC Hyperion CP400.85, GomSpace NanoMind A3200, and the ISIS iOBC have the advantage of low power usage over other options. Furthermore, when data storage capabilities and high clock frequencies are taken into consideration, the CP400.85 and ISIS iOBC are the most promising options. The required memory for the OBC to store data can be defined by the AAC Hyperion IM200 and Thoth Argus 2000 instruments used in the payload section. The data can be downlinked during or after the scientific phase, but on-board storage seems more promising for a low resource CubeSat. The on-board memory will be used to store VIS images from IM200, IR data from Argus 2000, and navigation data from the autonomous GNC system. The CP400.85 offers up to 48 minutes of scientific phase with its 64 GB optional memory, making it the best option for this application, particularly due to its compact volume, low mass, and large memory storage. However, the NEA target characteristics will influence the data acquisition strategy to ensure a complete scientific phase.

### 2.2.6. POWER

Table 2.12 presents the power requirements for each phase of the mission, which can be analyzed by examining the power consumption of all active subsystems. Nominal and peak power consumption data for most products can be found in their respective datasheets. Nominal refers to the average power consumption during normal operating conditions or stand-by, while Peak refers to the power input required during specific duties. During the phases involving the propulsion system, particularly the Earth escape phase, high power consumption is required. To limit power consumption during TCM manoeuvres, which will be faster, power consumption must be restricted during manoeuvre planning (apogee raising). For instance, 39 W of power is required for the propulsion system to be activated. Therefore, assuming an average power consumption for other subsystems during thrusting manoeuvres, the solar panels need to generate approximately 40 W of power at 1 AU. The ADCS subsystem requires power in all phases of the mission as it is responsible for pointing thrusters, cameras, sensors, and antennas. In the first two phases, the power demand for navigation can be computed using the GNSS receiver datasheet. However, in the other phases, it becomes more complex because it involves either star tracker and Sun sensors, or the payload camera.

Phase	Subsystems	Nominal [W]	Peak [W]
ID	ADCS, Navigation	1.6	4.6
EE	ADCS, Navigation, Propulsion, OBDH	2.1	44
DSC	ADCS, Navigation	1.4	4.5
CE	ADCS, Navigation, Propulsion, OBDH	2.7	45
SA	ADCS, Navigation, Payload, OBDH	4.6	8.5
DT	ADCS, Navigation, Communication, OBDH	17	23
FD	ADCS, Navigation, Propulsion	2.7	45

Table 2.12: Power budgets of mission phases, based on components datasheets.

Solar panels are the primary source of power for CubeSats, and there are several companies, such as AzurSpace, Emcore Corporation, Spectrolab, and Solaero Technologies, that produce solar cells which are assembled to form solar panels. The solar cells typi-

cally have an efficiency of around 0.3. For 3U CubeSats, there are various options available, from fixed panels to different configurations of deployable arrays. Deployable solar panels are necessary for deep-space missions, as seen on MaRCO (Klesh and Baker, 2019), Juventas (Goldberg et al., 2019), NEAScout (McNutt et al., 2014), and INSPIRE (Klesh et al., 2013).

Endurosat produces a 1-fixed, 1-deployable solar panel configuration for a 3U CubeSat<sup>48</sup>, each containing up to 7 Triple Junction Solar Cells InGaP/GaAs/Ge. However, the total mass of a single panel, which is below 300 g, does not fit with this application. ISIS offers a similar configuration made of GaAs solar cells<sup>49</sup>, with each 3U panel weighing around 150 g and delivering 6.9 W of power. NanoAvionics produces deployable solar panels configuration capable of generating 36.95 mW/cm<sup>2</sup> of power in LEO<sup>50</sup>.

GomSpace offers a different type of deployable configuration, characterized by double deployable solar arrays (135° version)<sup>51</sup>. The configuration has a total of 2 fixed panels and 4 deployable ones, with a total of 36 GaInP/GaAs/Ge solar cells, 30.18 cm<sup>2</sup> effective area each, generating up to 1.15 W per cell in LEO. DHV configuration is characterized by 42 triple junction GaAs solar cells giving around 29.6 W at 1AU for a total mass of 410 g<sup>52</sup>. However, the limitations of this configuration are the limited power generation of the fixed solar cells and the limited orientability of the panels.

MMA Design LLC overcomes these problems by offering totally deployable solar panels<sup>53</sup>. They have four slightly different HaWK configurations (17A-42, 17AB36, 17AS42, 17AS56) ranging from 42 to 56 solar cells, and from 36 to 56 W of power generation in LEO. HaWK 17AB36 configuration was installed on MarCO, and its orientability makes it a valid candidate for many other deep-space applications. Other deployable configurations have been designed by GomSpace for Juventas and M-Argo. The MMA Design HaWK 17AS42 configuration is selected for this application, using Spectrolab XTJ Prime solar cells, which are characterized by 0.307 efficiency.

The incoming power can be calculated as (Dida, 2019):

$$P_{in} = \eta A_{sa} \Phi L_d \cos(\theta), \quad (2.4)$$

The efficiency ( $\eta$ ), solar array area ( $A_{sa}$ ), solar flux ( $\phi$ ) at a certain distance from the Sun, inherent degradation factor ( $L_d = 0.9$ ), and incidence angle ( $\theta$ ) are related to each other. Figure 2.9 displays the available onboard power for a 42 Spectrolab XTJ Prime solar cell solar array (like HaWK 17AS42) at various incidence angles as a function of the distance from the Sun, expressed in AU. The maximum distance to the Sun in the graph corresponds to the maximum aphelion of the target asteroids.

The graph displays that the solar panels can provide over 10 W to the CubeSat for operation phase even in the farthest scenario and at an incidence angle of up to 60 degrees. Meanwhile, at around 1 AU and for low incidence angles, they can supply approximately 40 W to the CubeSat. These solar panels experience an efficiency reduction of 0.94 after ten years in LEO, but this effect is expected to be less severe due to the mission's

<sup>48</sup> <https://www.endurosat.com/products/?v=796834e7a283#cubesat-solar-panels>,

<sup>49</sup> <https://www.isispace.nl/product/solar-panels-complete-set/>,

<sup>50</sup> <https://nanoavionics.com/cubesat-components/cubesat-gaas-solar-panel/>,

<sup>51</sup> <https://gomspace.com/shop/subsystems/power/nanopower-dsp.aspx>,

<sup>52</sup> <https://dhvtechnology.com/>,

<sup>53</sup> <https://mmadesignllc.com/specs-table/>

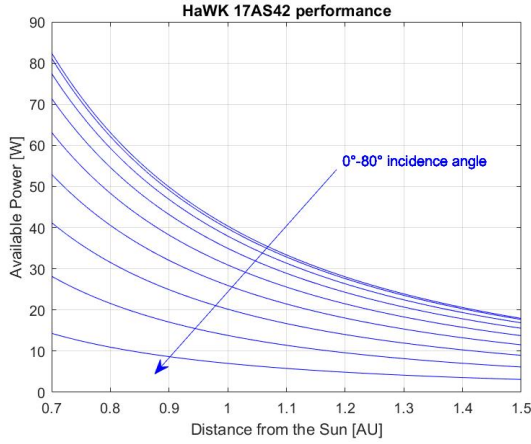


Figure 2.9: Solar panel deliverable power as a function of the mission scenarios.

shorter duration. Furthermore, during the final phases, the distance from the Sun will be heavily dependent on the target. If the distance is less than 1 AU, the larger solar flux should counterbalance the efficiency reduction. However, for greater distances, it may be necessary to use the secondary power system during peak power demand, or include additional solar cells in the system.

The market provides a broad selection of integrated battery and Electric Power System (EPS) options for use as the secondary power system. To determine the battery system requirement, a sample maximum power load of 20 W is taken from the average power consumption data of other subsystems, as few eclipses are expected during the mission lifetime, and a relatively low number of duty cycles (charge and discharge) are anticipated. This implies that a high depth-of-discharge (DOD), which is the percentage of the battery discharged, can be used, as a higher DOD lowers the number of required duty cycles for the battery. A DOD of 0.6 and a battery efficiency of 0.9101 are used as representative values, and the required battery capacity can be calculated as:

$$C = \frac{PT}{\eta DOD}, \quad (2.5)$$

The necessary capacity can be calculated using  $P$ ,  $T$ , and  $\eta$ , and comes out to be 18.51 Wh. Once the capacity is determined, the trade-off process focuses mainly on two factors: mass and volume. Several off-the-shelf components were considered, including the Endurosat EPS I Plus<sup>54</sup>, GomSpace P31u, GomSpace P31u with 4 batteries<sup>55</sup>, ISIS iEPS-A, ISIS iEPS-B, and ISIS iEPS-C<sup>56</sup>, whose characteristics are reported in Table 2.13.

Among these, the GomSpace P31u and ISIS iEPS-A were found to be the most suitable solutions for the application. While the GomSpace P31u has a slightly higher mass (200 g vs. 184 g) and lower battery capacity (19.5 Wh vs. 22.5 Wh), its lower volume ( $\sim 0.2U$  vs.  $\sim 0.23U$ ) makes it a more attractive option for this compact application. Therefore, for this project, the GomSpace P31u was selected, keeping in mind that the ISIS iEPS-A

Product	Mass [g]	Vol. [mm]	Capacity [Wh]	$P_{consumption}$ [mW]
Endurosat EPS I Plus	292	90.2 x 95.9 x 30	20.4	75
GomSpace P31u (+ BP4)	200 (+ 258)	89.3 x 92.9 x 25.6 (+94 x 84 x 23)	19.5 (38.5)	160 (160)
ISIS iEPS-A	184	96 x 92 x 26	22.5	N/A
ISIS iEPS-B	310	96 x 92 x 32	45	N/A
ISIS iEPS-C	360	96 x 92 x 36	45	N/A

Table 2.13: EPS characteristics.

is also a viable alternative.

### 2.3. 3U PLATFORM

Two reference 3U CubeSat platforms are introduced for comparison with the proposed platform: Delfi-n3xt (Bouwmeester et al., 2017) and INSPIRE (Klesh et al., 2013).

Delfi-n3Xt is a 3U CubeSat, launched on 21 November 2013. Its goals were pre-qualification of  $T^3\mu PS$  micropropulsion system, pre-qualification of multifunctional particle spectrometer, scientific radiation experiment of Si solar cells, qualification of a high efficiency modular communication platform, and proof-of-concept for a radiation risk-free implementation of commercial solid-state data storage devices. The original launch configuration was characterized by a modular subsystem approach and it includes ADCS, propulsion system, OBC, communication (primary and secondary radio transceiver, deployable antenna board, S-band radio interface board, and S-band radio transmitter), and power EPS, batteries, and batteries management). This configuration leaves 90 mm x 90 mm x 27 mm volume for the payload. To increase the available volume for the payload, two variant configurations were proposed. The lean configuration variant was based on removing all redundant systems, S-band transceiver dedicated board, and the secondary transceiver. Moreover, the spacing between the systems was removed using the stackable CS14 connector, which allows also OBC and EPS board height reduction. This configuration leaves a larger volume for the payload, with a stack height of 165 mm). A further improvement in payload available volume was given by the advanced configuration, whose integrated core units combines EPS control and distribution, the OBC, and the ADCS microcontroller. The payload available volume stack height was then increased up to 260 mm. The launch configuration of Delfi-n3Xt is taken as a reference for LEO CubeSats, for the comparison with the newly proposed platform (Bouwmeester et al., 2017).

Another interesting 3U platform is the one exploited by NASA/JPL INSPIRE project (Klesh et al., 2013), which is currently under development. The project is characterized by two identical CubeSats aimed to demonstrate nanosatellite capabilities in deep-space, especially in terms of communication, navigation, functionality, and payload-hosting technologies. The platform is also based on a modular subsystems approach,

<sup>54</sup> <https://www.endurosat.com/products/?v=796834e7a283#cubesat-power-modules>,

<sup>55</sup> <https://gomspace.com/UserFiles/Subsystems/datasheet/gs-ds-nanopower-p31u-27.pdf>,

<sup>56</sup> <https://www.isispace.nl/product/ieps-electrical-power-system/>

including ADCS (cold-gas thrusters and star tracker), power (EPS and batteries), communication (Iris X-band transponder for ground, Ultra High Frequency (UHF) radio and deployable antennas for crosslink capability between spacecraft), and command and data handling (which integrates also the UHF radio).

The main differences between the two platforms are related to their objectives. The first clear difference concerns the communication subsystem (S-band for Delfi-n3Xt, X-band and UHF for INSPIRE). Then, the ADCS, which is based on reaction wheels, Sun sensors and magnetometers for the former, while is based on a star tracker and cold-gas propulsion system for the latter. Moreover, both platforms exploit deployable solar panels, but with different deployment mechanisms. Delfi-n3Xt solar panel arrays consist in four 1U × 3U solar arrays, deployable across the short side. INSPIRE solar panel arrays are based on a 1-fixed 1-deployable (across the long side).

Based on the concepts and systems highlighted in the previous sections, an instantiated 3U platform is designed. Table 2.14 reports the list of the components, with mass and volume budgets. To fit the 3U volume, a modular subsystems approach has been exploited, and, as the volume budget sketch in Figure 2.10 shows, limiting the space between the components is necessary (in an approach similar to the lean and advanced Delfi-n3Xt platforms). A classical approach, placing the propulsion system and the payload at the extremities, has been exploited. However, the actual location of the subsystems will depend especially on the attitude control strategy in the various phases.

Component	Subsystem	Mass [g]	Volume [U]
Endurosat 3U Structure	-	285	3
Aerojet Rocketdyne MPS-130 1U	Propulsion	1700	1
GomSpace P31u	Power	200	~0.18
MMA Design HaWK 17AS42	Power	~ 300	3 (2D) x 2
AAC Hyperion iADCS200	ADCS	400	0.3
AAC Hyperion SS200 (x6)	ADCS	18	~0.007
AAC Clyde Space Pulsar Data	Communication	130	~0.1
Endurosat 4x4 Patch antenna	Communication	53	~0.07
AAC Hyperion CP400.85	OBDH	7	0.01
AAC Hyperion GNSS200	Navigation	3	~0.001
Total	-	3076	<2
+5% on each component dry mass	-	3220	"
+10% on total dry mass	-	3483	"
AAC Hyperion IM200	Payload	59	0.063
Thoth Technologies Argus 2000	Payload	300	~0.3
Total	-	3435	<3
+5% on each component dry mass	-	3598	"
+10% on total dry mass	-	3897	"

Table 2.14: Full platform Volume and Mass budget. .

The table reports the configuration with and without payload, in order to make clear the available mass and volume available for a custom payload. Clearly, for volume budget, only the components placed inside the structure have been considered; solar panels

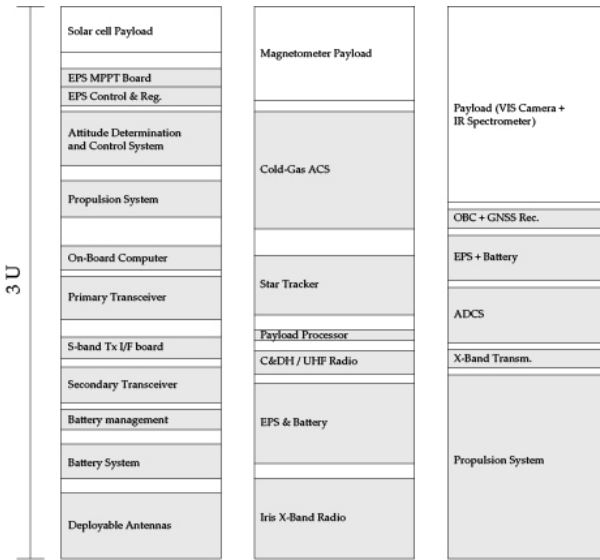


Figure 2.10: Volume budgets for Delfi-n3Xt, INSPIRE, and the instantiated platform (from left to right).

are folded respectively on two  $1U \times 3U$  external faces.

Recalling Figure 2.3, the propulsion system is able to deliver 385 m/s to a CubeSat with approximately 3900 kg BOL mass, it is clear that the mass budget is more critical than the volume one. From the first section of Table 15, it can be seen that less than 400 g and around 1U are available for the payload. The proposed payload (second section of the table) is within 1U and 400 g. Moreover, no information is available for the solar panels' deployment mechanism, which would add mass to the spacecraft. However, since a 5% margin on each component dry mass, and a 10% margin on the total dry mass, have been included, the additional mass is not seen as a problem. This margin is enough to include all the possible mass increases of the configuration if off-the-shelf components are used. In order to limit the mass budget criticality, three solutions may be considered:

- Consider a custom payload (as it has been suggested in the Payload section);
- Remove magnetorquers from the ADCS to lower the mass;
- Allow a smaller  $\Delta V$  (360–370 m/s).

Option 1 ensures a more customized scientific phase, but the mass constraint (below 400 g) increases the complexity of the design. Option 2 appears, as of today, as the best solution since magnetorquers can be used only in the early stages of the mission and especially for de-spinning purposes, which can eventually rely on reaction wheels. Option 3 is not recommended since it would lead to a reduction of the number of reachable targets.

Recalling the 3U CubeSat platforms described before and reported in Figure 2.10, the differences are evident. First, a large portion (1U) of the bus is occupied by the propel-



sion system, which for this platform plays the fundamental role of controlling the CubeSat's trajectory. Then, the propulsive manoeuvres require larger power demand, which converts into the need for larger deployable and orientable solar panels. Additionally, the use of integrated off-the-shelf systems allows to have dedicated processor units for many components. Moreover, one of the main differences relates to the use of the same component/subsystem to accomplish more than one function. It is the case of the star tracker, which should be used both for attitude determination and navigation in the second phase, the propulsion system, which besides the main function of orbit control, needs to ensure also reaction wheels de-saturation, or the payload camera, which should be used also as NAVcam for the third navigation phase. The differences between these physical platforms are then strongly related to the actual mission constraints and required functionalities.

Thermal subsystem design has not been included, as it depends on a detailed mission description which is required for future stages. The market offers a wide range of both passive and active solutions for CubeSat thermal control. Multi-Layers Insulation (MLI) has been widely used for space applications and many companies offer solutions: Sheldahl, Dunmore, Aerospace, Fabrication and Materials, MLI Concepts inc.. In particular, the Dunmore Aerospace Satkit including standard STARcrest materials, is optimized for small satellites and CubeSats, and it represents an excellent solution for deep-space CubeSats. Deployable radiators are currently produced by Thermal Management Technologies, and Kaneka Corporation together with JAXA proposed another excellent solution. Coatings (paint and tape) are offered by a wide range of companies: AZ Technology, MAP, Astral Technology Unlimited, Inc., Lord Techmark, Inc., Sheldahl, Akzo Nobel Aerospace Coatings. Sierra Lobo has developed a Sun shield, applicable to a 3U CubeSat (CryoCube), interesting in case of cryogenic experiments, but not needed in this application. A large number of flexible thermal straps, to allow passive thermal transfer to heat sink, in various materials: copper or aluminium by Thermal Management Technologies, K-Technology by Thermacore, Graphite Fiber by Technology Applications Inc.. Heat pipes for small satellites are offered by Advanced Cooling Technologies, Orbital ATK and Thermocoax. Concerning active thermal control, electric heaters are offered by Minco Products Inc. and All Flex Flexible Circuits LLC, while mini cryocoolers by Ricor-USA Inc., Create, Sunpower Inc, Northrop Grumman, and Lockheed Martin (NASA, 2022). For this platform, a passive control strategy can be adopted, as all the components work in wide temperature ranges (at least  $-20^{\circ}$ ,  $40^{\circ}$ ).

Concerning radiation, it may affect the CubeSat operations in two ways: Total Ionizing Dose (TID) and Single Event Effects (SEE). Many companies in the component datasheets claim their radiation tolerance. However few datasheets present information on the TID, so it is difficult to compare the performances among them. The few data available show a minimum TID tolerance of around 10 krad, with a peak up to 70 krad. Van Allen belt and solar particle flux may affect strongly the TID. For LISA pathfinder, a 100 krad TID has been computed around Sun-Earth Lagrangian points, while for a 3U CubeSat fly-bying an asteroid from the same point for 150 days, it has been computed a 10–20 krad TID with 0.5–1 mm thickness of aluminium shielding (Machuca et al., 2020). A proper radiation protection scheme needs to be designed for each application.

## 2.4. CONCLUSIONS

A review and applicability assessment of CubeSat technologies has been performed for the design of a 3U CubeSat aimed to perform a NEA fly-by and provide added scientific information on the object. Despite the many challenges related to the large constraints of the mission (mass, volume, power,  $\Delta V$  budgets), the feasibility of a 3U platform has been demonstrated, meeting all the MRs. The platform is composed of all the necessary components to make the CubeSat fully autonomous, during all the operational phases. As it has been highlighted, the main challenges are related to the navigation and AOCS subsystems, because to ensure fully autonomous platform, the uncertainties (especially related to asteroids ephemeris) need to be properly compensated by the coupling between navigation strategy/techniques and hardware support (star tracker performances and micro-propulsion system propellant budget for TCMs). The wheel de-saturation problem can be addressed with the main propulsion engine in the case of either orientable nozzles or multiple thrusters (as in the case of MPS-130), as it has been assumed in the ADCS section. Off-the-shelf electric propulsion systems appear at this stage less performant than their chemical counterpart, however, thanks to more detailed trajectory optimization approaches, their performances may be comparable, and the set of reachable targets may be extended. However, using electric micro-propulsion systems introduces two large challenges for a small satellite: the increased power demand and the increased mission time. Communication based on an X-band transmitter and antenna ensures an acceptable transmittable dataset, is also compliant with the short duration of the scientific phase. Clearly, if different scenarios will be considered, such as rendezvous with an extended scientific phase, the communication subsystem may become one of the driving components of the design, to allow the downlink of a larger dataset. The highlighted challenges in navigation are investigated in the next Chapters 4, 5, and 6, while an extensive analysis of the AOCS design is presented in Chapter 3.



# 3

## AOCS DESIGN FOR MINIATURIZED ASTEROID FLY-BY MISSIONS

*Ground control to Major Tom  
Commencing countdown, engines on  
Check ignition, and may God's love be with you.*

David Bowie - Space Oddity

*This chapter focuses on the AOCS analysis for deep-space CubeSat missions with a particular focus on NEA fly-by scenarios. First, the propulsion system is evaluated, analyzing the required propellant high-thrust  $\Delta V$  to reach NEAs. Then the attention is shifted to the electric propulsion options, and the examples of 7 NEAs are analyzed. After this, the Attitude Control System is investigated, exploring the reaction wheels' de-saturation in deep-space, together with optimal reaction thrusters placement and orientation for that. Then, with the defined hardware, other tasks are studied, namely initial de-tumbling, and reference frame tracking scenarios (e.g. keeping the asteroid in the FoV during fly-by, and thrusting in the correct directions). The results show that the current COTS options offer sufficient performance, and the majority of the tasks are feasible.*

---

The algorithms exploited in this chapter were developed by Steven Verwer in the framework of its MSc thesis that I co-supervised.

### 3.1. INTRODUCTION

This chapter is devoted to the analysis of the AOCS for a 3U CubeSat mission aimed to fly by a NEA. The first half of the chapter is dedicated to the analysis of the micro-propulsion system, which has been investigated only briefly in Chapter 2. The second half of the chapter is devoted to the sizing and performance analysis of the Attitude Control System (ACS), where different attitude control tasks are investigated in terms of hardware, control algorithms, and performance. Before diving into the specific analysis for AOCS, the 3U CubeSat architecture that has been defined earlier in Chapter 2 shall be refined in order to obtain those characteristics that will be the boundary conditions for the analysis.

Figures 3.1, 3.2, and 3.3 show a 3D multiple view of the satellite model, which is an improved version of the architecture proposed in Chapter 2. While ADCS, OBC, X-Band transmitter and antennas, battery system, and solar panels remain the same, there is an additional Reaction Control Thrusters (RCT) system, whose sizing is based on the GomSpace NanoPropC3GT (350 g and 0.5 U), and the camera used as the payload is the one of NEAScout for simplicity (390 g and 63 mm x 63 mm x 71 mm), as in the previous chapter it has been highlighted the possibility of a custom payload (McNutt et al., 2014). The two additional components are allocated in the volume that was highlighted for Payload in Chapter 2. Furthermore, by analyzing the CubeSat with a 3D model, it is possible to fit all the required subsystems in the 3 U volume. This leads to an architecture mass of 2.14 kg excluding the propulsion system. For this analysis, margins are excluded for simplicity.

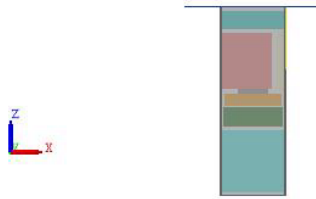


Figure 3.1: 2D View of the Satellite bus. In light blue (top) is the RCT, in red is the payload, in grey the OBDH, in orange is the battery system, in green is the ADCS, in yellow and light yellow, are respectively the X-Band antenna and the X-Band transmitter, and in light blue (bottom) is the propulsion system.

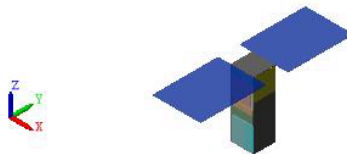


Figure 3.2: 3D View of the satellite bus showing the size of the solar panels.

To compute the inertia matrix necessary for the attitude control analysis, the considered micro propulsion system is the Aerojet Rocketdyne MPS-130 (as highlighted in



Figure 3.3: 2D View of the satellite bus, highlighting in yellow the x-band patch antennas.

previous sections), leading to the following inertia matrix:

$$J_s = \begin{bmatrix} 0.05290 & 0.00000 & -0.00048 \\ 0.00000 & 0.04020 & 0.00000 \\ -0.00048 & 0.00000 & 0.02141 \end{bmatrix} [kg \cdot m^2] \quad (3.1)$$

Finally, the calculated center of mass is the following:

$$\vec{R}_{CoM} = [0.00140528 \quad 0.00000000 \quad -0.01161993] [m] \quad (3.2)$$

## 3.2. PROPULSION SYSTEMS

This section is devoted to investigating the use of a micro-propulsion system on the 3U CubeSat architecture. In Chapter 2, a preliminary analysis of a limited number of NEA targets showed the better applicability of chemical thrusters over electric ones. So this section aims to expand the set of analyses presented previously, especially for electric propulsion. First, the list of NEAs targets based on navigation considerations (later presented in Chapter 4) is explored, solving the Lambert Problem, for chemical propulsion options. Later, the focus is shifted to a detailed analysis of the low-thrust options. First, the COTS propulsion systems options are presented, then the general framework where the analysis is performed is presented, and finally, the results are shown and analyzed.

### 3.2.1. CHEMICAL PROPULSION ANALYSIS

In Chapter 2, the Aerojet Rocketdyne MPS-130 has been demonstrated to be the best option for a 3U CubeSat, as it is capable of delivering approximately 370 m/s of  $\Delta V$  to a 3.8 kg satellite. In this section, the Lambert problem is solved for each NEA's nodal passages listed in Chapter 4.

The NEA nodal passages are chosen as encounter points, and the Lambert problem is solved for a range of ToF values from 50 to 500 days, using the Earth's state as the initial condition. The solution with the lowest  $\Delta V$  is identified and saved, which corresponds to the required impulse at the exit of the Earth's SOI to achieve the desired transfer trajectory. The relative fly-by velocity at the encounter can also be computed and analyzed. The plot shows also the corresponding FoM of each nodal passage, despite the focus of this analysis on the  $\Delta V$ . Recalling Figure 2.2, by delivering all  $\Delta V$  at the perigee of the SSGTO, it is possible to reach Earth escape velocity up to approximately 600 m/s, and as can be noticed in the plot, there is a large number of NEA that can be reached with this propulsive effort.

It can be concluded that, as highlighted in Chapter 2, the chemical propulsion MPS-130 is a valid option for a 3U CubeSat aimed to fly-by NEAs.

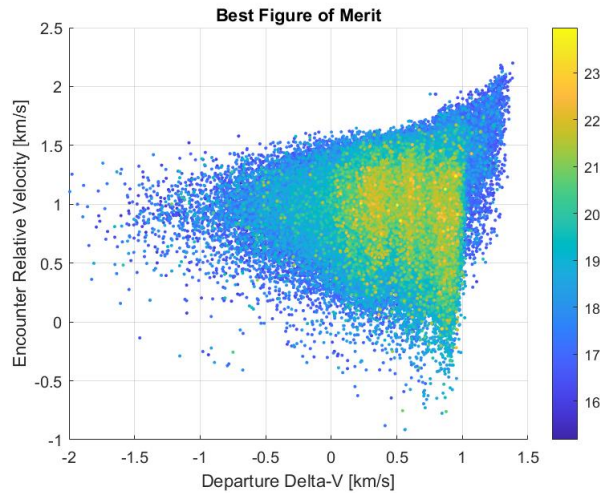


Figure 3.4: Relation between departure date, encounter relative velocity and FoM, that is later explored in Chapter 4.

### 3.2.2. ELECTRIC PROPULSION ANALYSIS

In Chapter 2, the preliminary analysis does not focus on the electric propulsion system design, as its complexity requires deeper evaluations. Instead, it offers a preliminary evaluation that serves as a foundation for the platform design. As attention transitions to a more comprehensive analysis of the AOCS in this section, a more intricate examination of electric propulsion options becomes imperative.

The following subsections are meant to present the COTS options for low-thrust, define the mathematical framework of the analysis, and show results.

#### ELECTRIC MICRO-PROPULSION OPTIONS

As of today, the electric micro-propulsion options that fit the 3U CubeSat architecture depicted in the previous chapter are three. The volume is not the only driving parameters, but it is used here as a filter to select the systems that are compared later in the Chapter. Enpulsion offers a FEEP (Field Emission Electric Propulsion) system<sup>1</sup>, that has a heritage of 28 systems currently in orbit. ThrustMe offers the NPT30-I2-1U<sup>2</sup>, which is a gridded ion thruster fueled with iodine, that can be stored solid on board and simplify notably the operations associated with the integration. AASC offers the MPT<sup>3</sup>, with 4 PUCK, which is again an ion thruster with solid propellant.

<sup>1</sup> <https://www.enpulsion.com/wp-content/uploads/ENP2018-001.G-ENPULSION-NANO-Product-Overview.pdf>,

<sup>2</sup> [https://www.thrustme.fr/base/stock/ProductBannerFiles/2\\_thrustme-npt30-i2.pdf](https://www.thrustme.fr/base/stock/ProductBannerFiles/2_thrustme-npt30-i2.pdf),

<sup>3</sup> <https://www.aasc.space/tech-specs>

In Table 3.1, the main characteristics of the three propulsion systems are reported for a first high-level comparison.

System	Enpulsion IFN Nano	ThrustMe NPT30-I2-1U	AASC MPT
Thrust	0.05-0.4 mN	0.3 - 1.1 mN	0.001-1.6 mN
$I_{sp}$	2000-6000 s	up to 2400 s	up to 1773 s
Wet Mass	1300 g	1200 g	1100 g
Dry Mass	1080 g	900 g*	740 g
Volume	1 U	1 U	0.67 U
Max Power	10-45 W	43-81 W	1-133 W

Table 3.1: Main characteristics of the three electric micro-propulsion systems considered in the analysis. \* The Dry Mass value for the ThrustMe NPT30-I2-1U is not available in the datasheet, so it has been approximated based on the other available parameters.

### APPROACH FOR THE EARTH ESCAPE TRAJECTORY GENERATION

The first leg of the trajectory generation is the escape from the Earth's attraction. As explained in the previous section, this would allow to have a standalone nanosatellite mission, which would broaden the possibilities. However, this may be a very challenging and demanding task to be accomplished by a nanosatellite. A good compromise for the launch would be to get injected in a SSGTO, which is a high-energy transfer orbit, but still commercial, so piggy-share would still reduce the cost.

For a chemical propulsion system, if almost instant burn can be assumed, firing can be split into several perigee passages in order to maximize the efficiency of the manoeuvre. For a low-thrust electric system, instant burn is not applicable anymore.

A convenient framework to study the Earth escape is to express the state of the spacecraft in spherical coordinates, relative to a non-rotating geocentric reference frame, whose x-axis is aligned with the direction of Aries, the z-axis with the North pole, and letting the XY plane to be aligned with the ecliptic plane. Then the state of the spacecraft can be expressed as:

$$\vec{X} = [r, \phi, \dot{r}, \dot{\phi}, m]^T \quad (3.3)$$

where  $r$  is the radius,  $\phi$  is the angle, and  $m$  is the mass. The spacecraft dynamics can be characterized by the following time-derivative equations:

$$\ddot{r} = a_r + r\dot{\phi}^2 \quad (3.4)$$

$$\ddot{\phi} = \frac{a_\phi}{r} - \frac{2\dot{r}\dot{\phi}}{r} \quad (3.5)$$

$$\dot{m} = -u \frac{T_{max}}{I_{sp} g_0} \quad (3.6)$$

where  $a_r$  and  $a_\phi$  are the acceleration acting on the spacecraft. The term  $\dot{m}$  is the temporal variation of the satellite's mass, and it has not to be confused with the mass flow rate of the propulsion system. The acceleration term is a combination of the acting forces on



the spacecraft, which in this study are limited to the main attraction from the Earth, the  $J_2$  term, the drag braking, and clearly the thrust from the propulsion system:

$$a_r = -\frac{\mu}{r^2} - 2\frac{\mu}{r}J_2\left(\frac{R}{r}\right)^2 - C_D\frac{1}{2}\rho\frac{A}{m}\dot{r}\|\dot{r}\| + u\frac{T_{max}}{m}\cos(\alpha) \quad (3.7)$$

$$a_\phi = -C_D\frac{1}{2}\rho\frac{A}{m}r\dot{\phi}\|\dot{\phi}\| + u\frac{T_{max}}{rm}\sin(\alpha) \quad (3.8)$$

where  $T_{max}$  is the maximum Thrust,  $u$  is the thrust actuation percentage,  $\alpha$  is the optimal thrusting direction,  $C_D$  is the drag coefficient,  $\rho$  is the air density,  $A$  is the effective satellite surface.

Regarding the trajectory generation, optimizing the transfer leg would ensure a fuel-consumption reduction, but with a very large escaping time. For this reason, it has been chosen to employ a so-called heuristic law, which assumes a constant max thrusting in the velocity direction of the satellite, as it increases the orbital energy, independently of the shape of the orbit (Morante et al., 2021). This can be easily derived from the definition of the specific orbital energy:

$$\epsilon = \frac{1}{2}\vec{v}\vec{v} - \frac{\mu}{\|\vec{r}\|} \quad (3.9)$$

that can be derived in:

$$\dot{\epsilon} = \vec{v}\dot{\vec{v}} - \frac{\mu\vec{r}\dot{\vec{r}}}{\|\vec{r}\|^3} \quad (3.10)$$

which shows that maximum energy change is when the velocity is maximized with an acceleration direction in the same direction.

So, the optimal firing direction can be assumed:

$$\vec{u}^* = \frac{\vec{v}}{\|\vec{v}\|} \quad (3.11)$$

which leads to the optimal thrusting law:

$$a^* = a\tan 2(r\dot{\phi}, \dot{r}), \quad \text{with } u^* = 1 \quad (3.12)$$

#### APPROACH FOR THE INTERPLANETARY CRUISE TRAJECTORY GENERATION

Optimizing a low-thrust trajectory for deep-space missions is a common topic in the space sector, and it is usually referred to as the Optimal Control Problem (OCP), whose solution can be obtained by a multitude of methods (Morante et al., 2021). The general approach includes the minimization of a certain performance index, which is often related either to fuel consumption or ToF and can be expressed mathematically as:

$$\min(J) = \Phi(\vec{X}, t)|_{t=t_f} + \int_{t_0}^{t_f} L(\vec{X}, \vec{u}(t), t)dt \quad (3.13)$$

where the control vector  $\vec{u}$  has to belong to the control space at each time instant, and where the state vector  $\vec{X}$  is subjected to certain dynamics, then can be expressed as:

$$\dot{\vec{X}} = f(\vec{X}, \vec{u}, t) \quad (3.14)$$

The term  $\Phi$  is referred to the terminal cost function and it quantifies whether the final optimized state matches with the imposed final constraint, while  $L$  is the so-called path cost function, which quantifies the 'effort' in reaching the desired final state. Going more in-depth, when the terminal cost function is null, it is referred to as the Bolza problem, while when the path cost function is null, the problem is named Mayer (Chai et al., 2019).

In the case of low-thrust trajectory optimization for a satellite the state and state dynamics can be expressed respectively as:

$$\dot{\vec{X}} = [\vec{r}(t), \vec{v}(t), m(t)]^T \quad (3.15)$$

$$\dot{\vec{X}} = \begin{bmatrix} \frac{T_{max}(t)\vec{u}(t)}{m(t)} + \sum_{i=1}^n \frac{\mu_i(\vec{r}(t) - \vec{r}_i(t))}{\|\vec{r}(t) - \vec{r}_i(t)\|^3} + \vec{a}_p(t) \\ \vec{v}(t) \\ -\frac{T_{max}\|\vec{u}(t)\|}{I_{sp}(t)g_0} \end{bmatrix} \quad (3.16)$$

subjected to the constraint that the control state needs to belong to the 3D control state space and with its norm within 0 and 1, for each time in the domain.

Once the mathematical problem has been defined, the solution can be obtained with different methods, which are usually divided into three macro categories: indirect and direct methods (both of them numerical), or analytical (Chai et al., 2019).

**Indirect approaches** are based on describing the control input as a function of the state together with a set of other parameters in order to ensure optimality in the time interval. Examples of indirect methods are the Calculus of Variation (CoV) and the Lyapunov control parametrization. These are characterized by solving the OCP without minimizing directly  $J$ . There is a large number of methods to solve the problem, but the most common is the single-shooting. **Direct approaches** involve the reformulation of the OCP into a nonlinear programming problem (NLP) aiming to optimize directly  $J$ . This is done by expressing the control input as a sum of known functions, as Fourier series. This is followed by integration over the time interval with the  $J$  calculations, and the  $J$  is optimized by changing weighting parameters. Also, direct approaches can be solved with single-shooting, or eventually multiple-shooting methods. On the other hand, **analytic approaches** usually require large assumptions for solving the problem, which end up in the worst results. Eventually, these methods are useful for preliminary analysis, or eventually to generate first guesses for numerical methods (Chai et al., 2019).

In this analysis, we decided to implement indirect approaches because the final goal is the comparison among propulsion systems because they ensure finding solutions which are global optimum, while direct methods, despite they may converge to a better solution, do not ensure that global optimum unless additional parameters are added to the calculations, which of course complicate it. Moreover, for direct methods,  $J$  would include a non-zero value for the final mass, unless propellant mass is as well a design parameter.

The problem is subsequently subject to parameterization, including Blended Control, Calculus of Variations, and Lyapunov Control (Chai et al., 2019). Following parameterization selection, the problem transforms into a numerical optimization challenge, addressed using one of several methods: single-shooting, multiple-shooting, collocation, gradient-based, or differential inclusion. As highlighted in the introductory section

of this chapter, the design space associated with low-thrust trajectory optimization is frequently characterized by strong non-linearity and non-convexity. These factors warrant careful consideration when selecting an appropriate numerical optimization technique. In general, optimization methods aim to minimize or maximize a function comprising one or more objectives. Within the realm of numerical optimization, two main method categories emerge, namely local optimization methods and global optimization methods. The key distinction lies in their objectives, where global optimization methods seek to identify a minimum across the entire design space, while local optimization methods target local minima based on an initial estimate. Local optimization methods rely on Hessian matrices, gradients, or function values to converge towards a minimum from an initial design point. In contrast, global optimization methods do not always follow a mathematical path toward a minimum but strive to reach proximity to the global minimum of an OCP. Global optimization methods can be further subdivided into deterministic methods that narrow the design space towards the global minimum, stochastic methods that handle objectives or constraints involving randomness, and heuristic methods that explore the design space using intelligent strategies such as evolutionary algorithms or swarm-based algorithms.

Research papers, exemplified by Jiang et al., 2012, underscore the effectiveness of a hybrid approach that combines both global optimization strategies and local optimization methods for addressing the low-thrust trajectory problem or achieving an acceptable solution. The paper employs an indirect optimization approach, which guarantees optimality when boundary equality constraints are met. Nevertheless, Jiang et al., 2012 construct an objective function for numerical optimization, defined as the Cartesian vector norm of equality constraints combined with the propellant used at the trajectory's end. This approach contradicts the mathematical definition of CoV-based indirect optimization, which asserts that the Bolza problem, aimed at minimizing the performance parameter  $J$ , transforms into a pure boundary value problem during indirect optimization. The validity of the hybrid approach proposed by Jiang et al., 2012 lies in its utilization of a global optimization method to obtain an initial estimate sufficiently close to the global minimum, followed by a local optimization method to converge to that minimum. Consequently, this approach has been adopted for the framework presented in this dissertation.

For the hybrid numerical optimization approach, the particle swarm optimization method has been chosen as the global optimization technique due to its effectiveness in generating a suitable initial estimate for the local optimization algorithm. Particle swarm optimization employs a population-based strategy to explore optimal solutions within an extensive search space, swiftly and efficiently identifying promising areas for the local optimization algorithm to initiate. As for the local optimization method, the Levenberg-Marquardt algorithm has been selected, given its well-established status and widespread use in efficiently converging to global minima. The combination of the particle swarm optimization method with the Levenberg-Marquardt algorithm enhances the overall efficiency and effectiveness of the optimization process, facilitating improved convergence.

In the CoV, the performance index is converted into a set of rules and costates describing the evolution of the control as a function of the initial condition. The state and

costates vectors are respectively expressed as:

$$\vec{\chi} = [\chi_1, \dots, \chi_n]^T \quad (3.17)$$

$$\vec{\Lambda} = [\lambda_{\chi_1}, \dots, \lambda_{\chi_n}]^T \quad (3.18)$$

so that the performance index can be expressed as:

$$J = \phi(\vec{\chi}, t = t_f) + \int_{t_0}^{t_f} L(\vec{\chi}, \vec{u}, t) + \vec{\Lambda}^T (f(\vec{\chi}, \vec{u}, t) - \dot{\vec{\chi}}) dt \quad (3.19)$$

Then the optimum is found by applying a certain  $\delta \vec{u}$  generating a certain  $\delta \vec{\chi}$  and  $\delta J$ . Then the minimum can be associated to those values of  $\vec{\Lambda}$  and  $\dot{\vec{\Lambda}}$  which produce  $\delta J = 0$ . The Hamiltonian is defined as:

$$H(\vec{\chi}, \vec{u}, t, \vec{\Lambda}) = L(\vec{\chi}, \vec{u}, t) + \vec{\Lambda}^T (f(\vec{\chi}, \vec{u}, t)) \quad (3.20)$$

while the solution for the optimal control can be found by solving:

$$\delta J = \left[ \left( \frac{\partial \phi}{\partial \vec{\chi}} - \vec{\Lambda}^T \right) \delta \vec{\chi} \right]_{t=t_f} + [\vec{\Lambda}^T \delta \vec{\chi}]_{t=t_0} + \int_{t_0}^{t_f} \left( \frac{\partial H}{\partial \vec{\chi}} + \vec{\Lambda}^T \right) \delta \vec{\chi} + \left( \frac{\partial H}{\partial \vec{u}} \delta \vec{u} \right) dt = 0 \quad (3.21)$$

which allows the definition of the boundary optimality conditions and the costate differential equation that again ensures optimality. It is worth noticing how in this numerical method, the cost function does not enter the iterations, and it is indirectly optimized.

In order to write the CoV problem for the low-thrust trajectory optimization, the approach suggested by Kluever, 1993 is followed, which solves at the same time fuel and energy design objectives, by introducing a perturbed performance index. Starting from the two performance indexes. respectively fuel and energy:

$$J_f = \frac{T_{max}}{I_{sp} g_0} \int_{t_0}^{t_f} \|\vec{u}\| dt \quad (3.22)$$

$$J_e = \frac{T_{max}}{I_{sp} g_0} \int_{t_0}^{t_f} \|\vec{u}\|^2 dt \quad (3.23)$$

the two can be mixed in:

$$J = \frac{T_{max}}{I_{sp} g_0} \int_{t_0}^{t_f} \|\vec{u}\| - \epsilon \|\vec{u}\| [1 - \|\vec{u}\|] dt \quad (3.24)$$

where  $\epsilon$  is the fuel-to-energy-optimality-ratio with  $0 < \epsilon < 1$ . However, this eventually can be expanded with a logarithmic penalty in order to force the magnitude of the control to be in the range 0-1 without producing discontinuities:

$$J = \frac{T_{max}}{I_{sp} g_0} \int_{t_0}^{t_f} \|\vec{u}\| - \epsilon [(-\|\vec{u}\|) \ln(\|\vec{u}\|) - (1 - \|\vec{u}\|) \ln(1 - \|\vec{u}\|)] dt \quad (3.25)$$

When it comes to applying this theory to the optimization of a low-thrust trajectory towards a NEA, the state dynamics can be initially simplified by assuming the only Sun gravitational attraction:

$$\dot{\vec{\chi}}(\vec{\chi}(t), \vec{u}(t), t) = \begin{bmatrix} \vec{v}(t) \\ \frac{\mu_{sun}(\vec{r}(t) - \vec{r}_{sun}(t))}{\|\vec{r}(t) - \vec{r}_{sun}(t)\|^3} + \frac{T_{max}}{m(t)} \vec{u}(t) \\ -\frac{T_{max}\|\vec{u}(t)\|}{I_{sp}g_0} \end{bmatrix} \quad (3.26)$$

By assuming this dynamics, the cost function and the Hamiltonian for the CoV method can be respectively expressed as:

$$J = \frac{T_{max}}{I_{sp}g_0} \int_{t_0}^{t_f} y(\vec{\chi}(t), \vec{u}(t), t) dt \quad (3.27)$$

$$H(\vec{\chi}(t), \vec{u}(t), \vec{\Lambda}(t), t) = \frac{T_{max}}{I_{sp}g_0} [y(\vec{\chi}, \vec{u}, t)] + \vec{\lambda}_r^T \vec{v} + \vec{\lambda}_v^T \left( \frac{T_{max}}{m} \vec{u} + \vec{a}_p \right) - \lambda_m \frac{T_{max}}{I_{sp}g_0} \|\vec{u}\| \quad (3.28)$$

In this case, the optimality condition can be expressed as:

$$H(\vec{\chi}^*, \vec{u}^*, \vec{\Lambda}^*, t) \leq H(\vec{\chi}^*, \vec{u}, \vec{\Lambda}^*, t) \quad (3.29)$$

which leads to the optimal control function:

$$\vec{u}^* = \underset{\vec{u}}{\operatorname{argmin}} \frac{T_{max}}{I_{sp}g_0} y(\vec{\chi}, \vec{u}, t) + \vec{\lambda}_v^T \frac{T_{max}}{m} \vec{u} - \lambda_m \frac{T_{max}}{I_{sp}g_0} \|\vec{u}\| \quad (3.30)$$

In order to calculate the  $\vec{u}$  vector, one of the three cost functions has to be chosen. As already remarked, the perturbed fuel index is convenient in this approach. By recalling the definition of the integral performance function (Eq. 3.24), the optimal control function becomes:

$$\begin{aligned} \vec{u}^* = \underset{\vec{u}}{\operatorname{argmin}} & \frac{T_{max}}{I_{sp}g_0} \|\vec{u}\| - \epsilon [(-\|\vec{u}\|) \ln(\|\vec{u}\|) - (1 - \|\vec{u}\|) \ln(1 - \|\vec{u}\|)] \\ & + \vec{\lambda}_v^T \frac{T_{max}}{m} \vec{u} - \lambda_m \frac{T_{max}}{I_{sp}g_0} \|\vec{u}\| \end{aligned} \quad (3.31)$$

By imposing the optimality condition:

$$\frac{\partial H}{\partial u} = 0 \quad (3.32)$$

it is possible to find the following relation:

$$\frac{T_{max}}{I_{sp}g_0} \frac{\vec{u}}{\|\vec{u}\|} \left[ 1 - \epsilon \ln \left( \frac{1 - \|\vec{u}\|}{\|\vec{u}\|} \right) - \lambda_m \frac{T_{max}}{I_{sp}g_0} \right] + \vec{\lambda}_v^T \frac{T_{max}}{m} = 0 \quad (3.33)$$

Then, recalling the optimal control direction equation:

$$\vec{u}^* = -\beta(t) \frac{\vec{\lambda}_v}{\|\vec{\lambda}_v\|} \quad (3.34)$$

it is possible to find the value of  $\beta$  by plugging Eq. 3.34 in Eq. 3.33:

$$\beta = \frac{1}{1 + e^{\frac{1-SF}{\epsilon}}} \quad (3.35)$$

where:

$$SF(\vec{\chi}, \vec{\Lambda}, t) = \|\vec{\lambda}_v\| \frac{I_{sp} g_0}{m} + \lambda_m \quad (3.36)$$

Then, the boundary conditions have to be defined, which needs to quantify how well the spacecraft reaches the target at a certain final time  $t_f$ . The ToF is variable in this case. Remembering the definition of the perturbed fuel-efficient performance index and adding the equality constraints:

$$J = \phi(\vec{\chi}_{t_f}, t_f) + \frac{T_{max}}{I_{sp} g_0} \int_{t_0}^{t_f} y(\vec{\chi}(t), \vec{u}(t), t) dt \quad (3.37)$$

remembering that  $y(\vec{\chi}(t), \vec{u}(t), t)$  is the perturbed fuel-efficient integral performance index, and  $\phi$  is the terminal function, which can be defined as:

$$\phi(\vec{\chi}_{t_f}, t_f) = \vec{r}(t_f) - r_{NEA}(t_f) = 0 \quad (3.38)$$

Then including the Lagrangian multipliers, and defining the Hamiltonian:

$$H(\vec{\chi}(t), \vec{\Lambda}(t), \vec{u}(t), t) = y(\vec{\chi}(t), \vec{u}(t), t) + \vec{\Lambda}^T(t) f(\vec{\chi}(t), \vec{u}(t), t) \quad (3.39)$$

$$J = \phi(\vec{\chi}_{t_f}, t_f) = \frac{T_{max}}{I_{sp} g_0} \int_{t_0}^{t_f} \left[ X(\vec{\chi}(t), \vec{\Lambda}(t), \vec{u}(t), t) - \dot{\vec{\Lambda}}^T \vec{\chi}(t) \right] dt \quad (3.40)$$

$$+ \vec{\Lambda}^T(t_0) \vec{\chi}(t_0) - \vec{\Lambda}^T(t_f) \vec{\chi}(t_f)$$

Then to maximize or minimize it, it has to be computed:

$$\delta J = \left[ \left( \frac{\partial \phi}{\partial \vec{\chi}} \right) \delta \vec{\chi} \right]_{t=t_f} + [\Lambda^T \delta \vec{\chi}]_{t=t_0} \frac{T_{max}}{I_{sp} g_0} \int_{t_0}^{t_f} \left[ \left( \frac{\partial H}{\partial \vec{\chi}} - \dot{\Lambda}^T(t) \right) \delta \vec{\chi} + \frac{\partial H}{\partial \vec{u}} \delta \vec{u} \right] dt = 0 \quad (3.41)$$

which implies that all terms must vanish at each time instant:

$$\dot{\Lambda} = - \frac{\partial H}{\partial \vec{\chi}} \quad (3.42)$$

$$\frac{\partial H}{\partial \vec{u}} = 0 \quad (3.43)$$

$$\Lambda_j(t_f) = free \quad if \quad \delta \chi_j = 0 \quad (3.44)$$

$$\frac{\partial \phi}{\partial \chi_j} \quad if \quad \delta \chi_j = 0 \quad (3.45)$$

and if  $\vec{\chi}(t_0)$  is known  $\Lambda(t_0)$  is free as well. The Lagrangian multipliers are the same size as the state vector, for simplicity, they are defined as:

$$\Lambda = \begin{bmatrix} \vec{\lambda}_r \\ \vec{\lambda}_v \\ \lambda_m \end{bmatrix} \quad (3.46)$$

Then the combination of cost function, Hamiltonian and spacecraft dynamics leads to the re-formulation of the Hamiltonian:

$$H(x, u, t, \Lambda) = \frac{T_{max}}{I_{sp}g_0} \tilde{u}(t) - \epsilon [(-\tilde{u}(t)) \ln(\tilde{u}(t)) - (1 - \tilde{u}(t)) \ln(1 - \tilde{u}(t))] + \Lambda^T \begin{bmatrix} \tilde{v}(t) \\ \frac{\mu_{sun}(\tilde{r}(t) - \tilde{r}_{sun}(t))}{\|\tilde{r}(t) - \tilde{r}_{sun}(t)\|^3} + \frac{T_{max}}{m(t)} \tilde{u}(t) \\ -\frac{T_{max}\|\tilde{u}(t)\|}{I_{sp}g_0} \end{bmatrix} \quad (3.47)$$

Optimal thrust magnitude and direction are found as a function of the state :

$$u^* = \beta = \frac{1}{1 + e^{\frac{1 - SF(\tilde{x}, \Lambda)}{\epsilon}}} \quad (3.48)$$

$$SF(\tilde{x}, \Lambda) = \|\tilde{\lambda}_v\| \frac{I_{sp}g_0}{m + \lambda_m} \quad (3.49)$$

$$\tilde{\alpha} = -\frac{\tilde{\lambda}_v}{\|\tilde{\lambda}_v\|} \quad (3.50)$$

Now, only the lagrangian derivatives are missing:

$$\dot{\tilde{\lambda}}_r = -\sum_{i=1}^n \left[ \frac{\mu_i \tilde{\lambda}_v}{\|\tilde{r} - \tilde{r}_i\|^3} - \frac{3\mu_i [\tilde{r} - \tilde{r}_i]^T \tilde{\lambda}_v}{\|\tilde{r} - \tilde{r}_i\|^5} (\tilde{r} - \tilde{r}_i) \right] \quad (3.51)$$

$$\dot{\tilde{\lambda}}_v = \tilde{\lambda}_r \quad (3.52)$$

$$\dot{\lambda}_m = -\|\tilde{\lambda}_v\| \frac{T_{max}}{m^2} u \quad (3.53)$$

which are subjected to the following boundary conditions:

$$\phi(\tilde{x}_{t_f}, t_f) = \tilde{r}(t_f) - \tilde{r}_{NEA}(t_f) = 0 \quad (3.54)$$

$$\tilde{\lambda}_r(t_f) = free \quad (3.55)$$

$$\tilde{\lambda}_v(t_f) = \frac{\partial \phi}{\partial \tilde{v}} \Big|_{t=t_f} = 0 \quad (3.56)$$

$$\lambda_m(t_f) = \frac{\partial \phi}{\partial m} \Big|_{t=t_f} = 0 \quad (3.57)$$

One intriguing aspect of the co-state equations, optimal thrust function, and boundary constraints lies in their scaling by one or more co-states. This signifies that the co-state derivatives, optimal thrust function, and boundary constraints are solely influenced by the ratios of the co-states, not their absolute values. This knowledge becomes valuable during the optimization of initial co-states, as it allows the confinement of the initial co-states within a unit hyper-sphere. This constraint significantly narrows down the design space for numerical optimization. Jiang et al., 2012 also observed this relationship in a rendezvous mission and applied this method of design space reduction in the context of designing a fuel-efficient low-thrust trajectory for a Mars rendezvous mission using a CoV-based approach.

### TEST CASES

The capabilities of electric propulsion systems will be evaluated through the model previously described, applied to the mission design for seven different NEA targets, employing the three electric micro-propulsion systems previously presented. The selection of the targets is from the list presented in Chapter 4, as a function of the navigation conditions. From this list, the first three targets of Table 3.2 are targets at about 1 AU from the Sun, while the remaining four targets have a distance between 0.5 to 0.7 AU, to cover different scenarios. These targets are different from the ones considered in the preliminary analysis in Chapter 2, as they are chosen for their relevance from the navigation observability perspective. The approach dates are particularly convenient under the navigation perspective ascending or descending nodal passages. It is important to note, that selecting nodal passages is already a pre-optimization, as expensive change-of-plane maneuvers are limited. Their characteristic at the approaching date is reported in Table 3.2.

Asteroid Code	X (km)	Y (km)	Z (km)	Encounter Date
2018CN2	102696965.57	-84426751.75	430659.00	07-08-2031
2017YL1	13443682.24	142864356.54	17323.43	14-12-2029
2013WY43	62889336.87	138968700.78	12716.04	25-11-2026
2020QN1	-35230206.1	108960648.74	-13641.66	04-01-2030
163693	22339498.14	-87769735.20	-298590.83	08-10-2032
2017WV13	-21509416.34	-76608898.69	163636.88	02-10-2032
2012BX34	46204832.00	-59012656.47	328202.71	02-08-2031

Table 3.2: List and characteristics of seven NEAs analyzed in this study.

As previously remarked, the CoV problem is solved first by finding a global solution using a particle swarm optimization method (namely in Matlab 'particleswarm'). The swarm size has been set to 14000, which corresponds to the number of parameters 7 times 2000, chosen because a lower swarm size can converge to sub-optimal minima (or even no solutions), while a larger size that would exceed the available RAM memory leading again to no solution.

Other important parameters are the inertia range of the particles, the social-adjustment weight, and the self-adjustment weight. The first balances exploration and exploitation in the optimization process by controlling the impact of the current velocity of a particle on its future velocity. The second and the third determine respectively the influence of a particle's global and personal best. The inertia range has been set within 0.4-0.9, while the other two weights have been set to 1.49, following the suggestions reported in Jiang et al., 2012.

Finally, the maximum stall iterations were chosen to be 20, while the total iterations were limited to 200. Furthermore, to reduce the computational load for each iteration, the integration tolerances have been set to  $10^{-3}$ , which means about  $5 \cdot 10^6$  km of error, which for a first guess is deemed to be sufficient. On the other hand, the local optimization is based on the Levenberg-Marquardt algorithm, using a forward finite difference scheme. The used Matlab function is 'fsolve'. This case is way more sensitive, and for this reason, the absolute tolerance was set to  $10^{-13}$ , leading to an error of 50 km. Thanks



to the built-in function in Matlab, it was possible to use the parallel computing option to reduce the simulation time.

#### ANALYSIS WITH EARTH ESCAPE TRAJECTORY

One of the challenges of having a standalone CubeSat aimed to reach an asteroid for science relates to the escape from the Earth attraction because it defines whether a commercial launch can be exploited to lower the cost, or if a piggy-back launch solution is deemed necessary to release the spacecraft already outside the Earth's SOI.

Similar to the chemical propulsion case explored in Chapter 2, the release condition is considered to be from a SSGTO transfer orbit, characterized by a perigee of 295 km and an apogee approximately of 90000 km. Starting the escape manoeuvre and ending it when the specific orbital energy is zero, meaning escape from the attraction, leads to the results presented in Table 3.3.

System	NPT	IFN	MPT
$m_p$ [g]	338 (300)	296 (220)	433 (360)
ToF [days]	83.7	260	53.2

Table 3.3: Earth escape trajectory results for the three electric propulsion systems.

The results presented in the table show that the required propellant mass to escape the Earth is larger than the available one in the COTS option for all three micropropulsion systems. It has to be remarked that this scenario, with continuous trusting along the velocity direction of the spacecraft, represents an optimal time-of-flight manoeuvre, but certainly does not minimize the required propellant mass. To minimize the propellant mass need, one may think of avoiding continuous firing. In this scenario, trusting arcs around the perigee can exploit optimal firing conditions to minimize the required propellant mass, sacrificing the escape time. However, as this is only the first leg of the transfer, and it has to be followed by the interplanetary leg, even a very improvement in the consumption perspective, would not allow improvement in the performance, as the ToF would significantly increase. For this reason, the interplanetary trajectory needs to be analyzed.

#### ANALYSIS WITHOUT EARTH ESCAPE TRAJECTORY

The previous section showed how the Earth escape may be challenging, so the case of having a satellite that already escaped the Earth is considered here. This case has not been considered for chemical propulsion systems, however it is part of the comparison, because it shows how chemical propulsion enables a CubeSat releases around the Earth, while electric allows it only if custom design is possible (larger  $m_p$  available).

The three closer targets reported in Table 3.2 are used. The initial condition is set coincident with the Earth's position and velocity at the specific departure date. Figures 3.5, 3.6, and 3.7 show the behaviour of the satellite mass as a function of the time epoch, respectively for IFN, NPT, and MPT, for the three closer targets (highlighted in the legend of the plots).

The results show that 8 out of 9 scenarios are feasible in terms of required propellant, remembering from Table 3.1 that the IFN has about 220 g, the NPT around 300 g, and the

MPT 360 g. The only scenario where the limit COTS propellant mass is exceeded is the NEA 2012BX34 when using the MPT, as it requires approximately 400 g. However, this value is just 40 g larger than the COTS availability, so an eventual larger custom tank may allow also the reachability of this target.

Furthermore, remembering the results of the Earth Escape, and highlighting that many of these closer targets scenarios require a small amount of propellant mass, such as for NEA 163693 using Enpulsion IFN, it is possible to assume that the combination of a propellant optimized escape trajectory and a slight customization of the propellant tank can lead to the use of electric propulsion system for a set of closer targets.

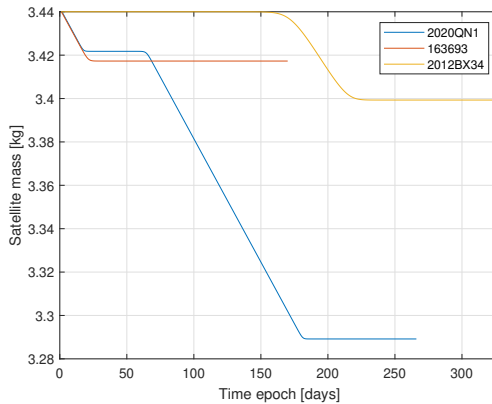


Figure 3.5: Enpulsion IFN performance in terms of mass evolution through time for a release outside Earth's SOI for the three closest targets.

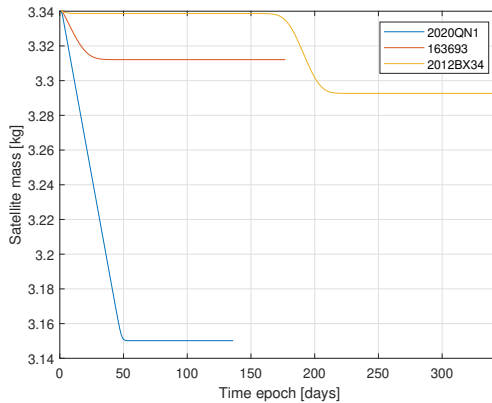


Figure 3.6: ThrustMe NPT performance in terms of mass evolution through time for a release outside Earth's SOI for the three closest targets.

The results for the remaining 'further' NEA targets are reported respectively in Fig-

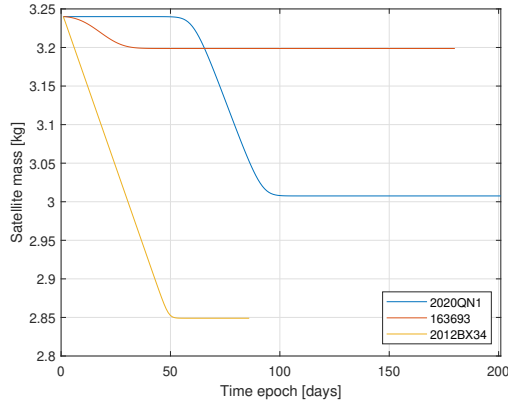


Figure 3.7: AAST MPT performance in terms of mass evolution through time for a release outside Earth's SOI for the three closest targets.

ures 3.8, 3.9, and 3.10. For all the twelve considered scenarios, the COTS propellant mass is not sufficient to travel to the asteroid. Eventually, it would be possible if extra propellant mass could be carried onboard, however, the further the targets are the less probable it is they will be reachable.

Comparing electric and chemical propulsion systems, it appears as of today that the latter provides better performance for this application. Electric propulsion systems do not allow Earth Escape, and even if the satellite is released outside Earth's SOI, only closer targets are reachable. On the other hand, the chemical propulsion section shows a large number of reachable targets. So, nowadays, chemical propulsion systems appear to be more performant than their electric counterpart.

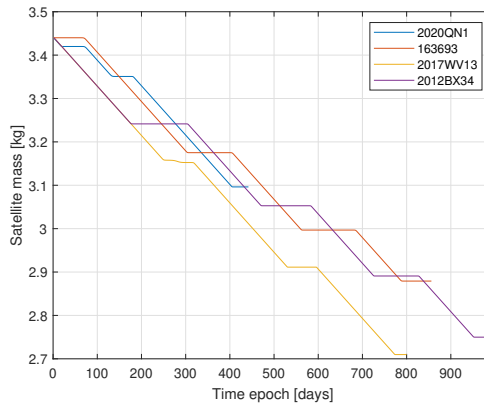


Figure 3.8: Empulsion IFN performance in terms of mass evolution through time for a release outside Earth's SOI for the four furthest targets.

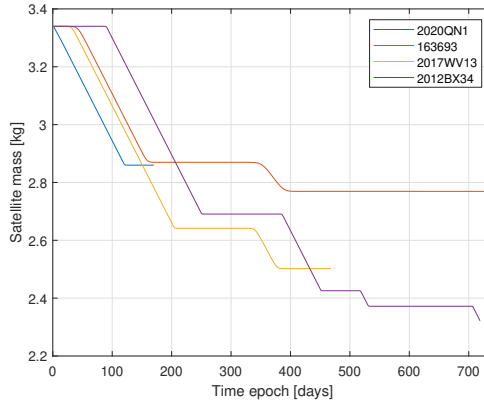


Figure 3.9: ThrustMe NPT performance in terms of mass evolution through time for a release outside Earth's SOI for the four furthest targets.

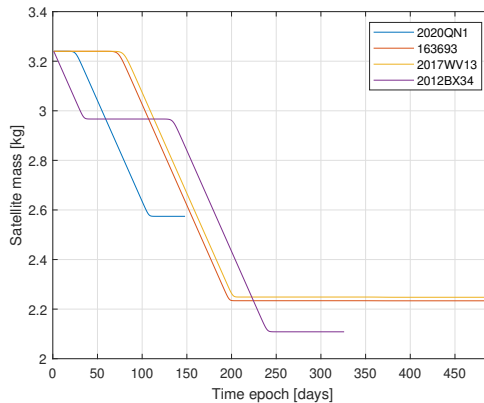


Figure 3.10: AAST MPT performance in terms of mass evolution through time for a release outside Earth's SOI for the four furthest targets.

### 3.3. ACS DESIGN

The control system of a CubeSat devoted to fly-by NEA has to be capable of accomplishing several tasks, and three of the most important are:

- Initial de-tumbling
- Tracking of the optimal firing direction
- Asteroid tracking during fly-by

In addition to these, other tasks can involve re-orientation for data transmission or solar panel exposure in the Sun's line-of-sight, together with a navigation observation strategy. However in this dissertation we have been focusing on these three as

re-orientation for data transmission is not extensively challenging, re-orientable solar panels are considered, and the dissertation core aims to have a passive LoS navigation strategy.

All tasks can be accomplished by the use of reaction wheels, considering that carrying onboard magnetorquers is not in line with deep-space scenarios, and even if they can be employed either for initial de-tumbling and/or Earth escape, their additional mass and volume would not be beneficial for the mission budgets.

Reaction wheels however encounter the classical problem of saturation, which means that they reach their limit rotational speed, and they cannot be used anymore to control the orientation of the spacecraft. In order to de-saturate the reaction wheels, a secondary attitude control system is required, which allows momentum dumping of the wheels. This is usually done with magnetorquers around the Earth, but in deep-space is clearly not an option. Using the main propulsion system would be possible either if multiple thrusters are available, or if the only thruster is throatable, but again this leads to a very large de-saturation time (Pizzetti et al., 2023). A more appropriate option involves the use of a separate cold gas system, which can also be used for de-tumbling or other eventual tasks. For a cold gas system is convenient to have multiple thrusters, and their optimal placement and orientation are analyzed in the next sections.

### 3.3.1. THRUSTERS ORIENTATION

Reaction thrusters are demanded onboard primarily for reaction wheels de-saturation, and secondly to perform de-tumbling if the reaction wheels do not have enough capabilities to do so.

Two possible options that can be considered are the Aurora Propulsion Technology ARM-A and the GomSpace NanoProp, whose characteristics are reported in Table 3.4:

RCT System	Aurora ARM-A	GomSpace NanoProp
Thrust level [mN]	0.6 - 4	1
$I_{sp}$ [s]	100	60-110
Wet Mass [kg]	0.35 - 0.5	0.35
Volume [U]	0.35 - 0.5	0.5
Number of thrusters	4	4
Power Consumption while Firing [W]	3 - 5 /mN	<2

Table 3.4: COTS RCTs main characteristics.

However, the thrusters' orientation is sufficiently standard and it is not optimized for the specific wheels de-saturation scenario. So, in this section, the goal is to start considering a similar system, in terms of mass, volume, and thrust level, and to analyse an optimized thruster orientation to maximize the angular acceleration (both positive and negative) around each rotational axis, and at the same time minimizing the acceleration around the other axes. In such a way, the required propellant for wheel desaturation is minimized.

## OPTIMIZATION APPROACH

Consequently, the optimization problem can be formulated as follows:

$$L_1 = \max\left(\frac{M_x}{I_{xx}}, 0\right), L_2 = \max\left(-\frac{M_x}{I_{xx}}, 0\right) \quad (3.58)$$

$$L_3 = \max\left(\frac{M_y}{I_{yy}}, 0\right), L_4 = \max\left(-\frac{M_y}{I_{yy}}, 0\right) \quad (3.59)$$

$$L_5 = \max\left(\frac{M_z}{I_{zz}}, 0\right), L_6 = \max\left(-\frac{M_z}{I_{zz}}, 0\right) \quad (3.60)$$

where  $M$  and  $I$  represent respectively the torque and inertia moment about a specific axis, and the objective for a given case  $i$  is denoted as  $L_i$ .

Accordingly, the penalties for each case, denoted as  $P_{i,k}$ , can be expressed as:

$$\begin{aligned} P_{1,1} = P_{2,1} &= \left| \frac{M_y}{Y_{yy}} \right|, P_{1,2} = P_{2,2} = \left| \frac{M_z}{Y_{zz}} \right| \\ P_{3,1} = P_{4,1} &= \left| \frac{M_x}{Y_{xx}} \right|, P_{3,2} = P_{4,2} = \left| \frac{M_z}{Y_{zz}} \right| \\ P_{5,1} = P_{6,1} &= \left| \frac{M_x}{Y_{xx}} \right|, P_{5,2} = P_{6,2} = \left| \frac{M_y}{Y_{yy}} \right| \end{aligned}$$

In order to combine these multiple objectives effectively, a logarithmic addition strategy is employed. This strategy ensures that each angular acceleration is maximized in both the positive and negative directions for each axis. The rationale behind using logarithmic addition is that solely maximizing a single or a subset of objectives would result in a poorer performance metric compared to an equal maximization of all objectives. This is similar to the concept of summing the roots of the objectives for values greater than one. The choice of logarithmic addition over summing the roots is preferable because the objectives may not necessarily fall within the range of one to infinity; they can also be below one. Therefore, by summing the logarithms of the objectives, a design can be obtained that optimizes all rotational axes instead of selectively optimizing certain axes. Optimizing a subset of axes would yield a lower performance index.

Thus, the penalties are incorporated in a similar manner, enabling the expression of the performance index to minimize as:

$$\min_{\vec{\xi}_{act}} J = \sum_{i=1}^6 \sum_{k=1}^2 \log_{10}(vP_{i,k}) - \sum_{i=1}^6 \log_{10}(L_i) \quad (3.61)$$

where  $\vec{\xi}_{act}$  represents the design parameters for the placement, orientation, and allocation of thrusters in the six angular acceleration cases. The penalty scaling factor  $v$  prioritizes the minimization of penalties over the maximization of torques.

To solve this minimization problem, a direct optimization method is required due to it being a multiple-input-single-output (MISO) problem without the need for integration actions. This implies that the problem can be tackled using a global optimization scheme, a gradient-based optimization scheme, or a hybrid optimization approach combining both global and gradient-based methods.

It is evident that the minimization problem contains  $\max()$  functions within  $L_i$ , which suggests that the performance index function may exhibit discontinuities in its design space. Consequently, gradient-based methods are unsuitable for these specific regions. Therefore, an initial global optimization approach is employed. The PSO method is chosen for global optimization as it can effectively handle the nonlinear and non-convex nature of the problem. The solution obtained from the PSO method serves as an initial guess for a subsequent gradient-based optimization method, which aims to locate a true local minimum. Depending on the initial guess, this local minimum could potentially be the global minimum, although confirmation would require an exhaustive grid search rather than relying solely on the PSO method.

### PARAMETRIZATION

In order to parameterize the positioning and orientation of the thrusters on the satellite's surface, it is assumed that the satellite can be characterized by a super-ellipsoid shape. The general inside-outside function of a super-ellipsoid is provided in Barr, 1981 as:

$$g(x, y, z) = \left( \left( \frac{x}{A} \right)^r + \left( \frac{y}{B} \right)^r \right)^{r/t} + \left( \frac{z}{C} \right)^t \quad (3.62)$$

The parameters  $r$  and  $z$  are used to determine the squareness of the super-ellipsoid in the  $xy$ -plane and  $z$ -direction, respectively. The scaling factors  $A$ ,  $B$ , and  $C$  are responsible for stretching the super-ellipsoid along the  $x$ ,  $y$ , and  $z$  axes. For instance, a 3U CubeSat with dimensions of  $0.1 \times 0.1 \times 0.3$  m can be described using the parameters  $A = 0.1^2$ ,  $B = 0.1^2$ ,  $C = 0.3^2$ , while the squareness is assumed to be  $r = t = 8$ . By setting  $g(x, y, z) = 1$ , the super-ellipsoid surface function is derived. In Barr, 1981, it is demonstrated that the super-ellipsoid can be represented using angular coordinates, which offer improved spatial resolution in regions with higher curvature.

The angular coordinates for the surface are defined within the ranges  $\pi/2 \leq v \leq \pi/2$  and  $\pi \leq w \leq \pi$ . By taking the partial derivatives of the surface equation  $g = 1$ , it is possible to obtain the vector normal to the surface. In Barr, 1981, the partial derivatives of  $g$  are expressed in terms of the angular surface parameters using the following expressions:

$$x = A \cdot \text{sgn}(\cos(v)) \cdot \|\cos(v)\|^{2/t} \cdot \text{sgn}(\cos(w)) \cdot \|\cos(w)\|^{2/r} \quad (3.63)$$

$$y = B \cdot \text{sgn}(\cos(v)) \cdot \|\cos(v)\|^{2/t} \cdot \text{sgn}(\sin(w)) \cdot \|\sin(w)\|^{2/r} \quad (3.64)$$

$$z = C \cdot \text{sgn}(\sin(v)) \cdot \|\sin(v)\|^{2/t} \quad (3.65)$$

Having established that the thruster's location can be defined using the angular coordinates  $v$  and  $w$ , and the normal vector to the satellite's surface is determined for any given location, the next step is to parameterize the direction of the thruster. One approach is to rewrite the normal vector as a unit direction vector and subsequently transform this vector into spherical coordinates. This transformation can be mathematically expressed as follows:

$$n_x = \frac{\partial g}{\partial x} = \frac{1}{A} \cos(v)^{2-2/t} \cos(w)^{2-2/r} \quad (3.66)$$

$$n_y = \frac{\partial g}{\partial y} = \frac{1}{B} \cos(v)^{2-2/t} \sin(w)^{2-2/r} \quad (3.67)$$

$$n_z = \frac{\partial g}{\partial z} = \frac{1}{C} \sin(v)^{2-2/t} \quad (3.68)$$

Since it is possible to express the thruster direction as a function of the normal unit vector, where the parameters solely modify the local direction relative to the surface normal of the satellite, the thruster direction in Cartesian coordinates can be formulated as follows:

$$x = \sin(\phi + \phi_d) \cos(\theta + \theta_d) \quad (3.69)$$

$$y = \sin(\phi + \phi_d) \sin(\theta + \theta_d) \quad (3.70)$$

$$z = \cos(\phi + \phi_d) \quad (3.71)$$

where the orientation of the thruster with respect to the local normal vector on the surface of the satellite can be described using the direction parameters  $\theta_d$  and  $\phi_d$ . These parameters determine the thruster's orientation.

The final set of parameters, denoted as  $u_n$ , is used to characterize a thruster. These parameters represent the percentages of thrust allocated for the six different angular accelerations across the various axes of rotation. For instance, in the case of four RCTs, if thrusters 2 and 3 are firing while thruster 1 is partially active, and thruster 4 is not providing any thrust, it results in a pure negative angular acceleration around the y-axis of the satellite.

To fully describe the configuration of four thrusters, a vector of 40 design parameters is utilized, including  $v_i, w_i, \theta_{d,i}, \phi_{d,i}, u_{i,k}$  where  $k = 1 : 6$ .

Once the parameters for the optimization problem have been determined, it is necessary to establish a mapping between the desired control torque and the corresponding thruster actuation. This mapping is achieved through an allocation matrix, which links the desired accelerations for each rotational axis in both positive and negative directions to unit thrust actions. The allocation matrix can be represented as:

$$A_u = \begin{bmatrix} u_{1,1} \dots u_{1,4} \\ \dots \dots \dots \\ u_{6,1} \dots u_{6,4} \end{bmatrix} \quad (3.72)$$

The desired control torque  $\vec{M}_{RCT}$  can be effectively translated to the estimated thrust actions using the following equation:

$$\begin{bmatrix} u_{RCT,1} \\ u_{RCT,2} \\ u_{RCT,3} \\ u_{RCT,4} \end{bmatrix} = A_u^T F_{RCT,max}^{-1} \begin{bmatrix} \max(J_s^{-1} \vec{M}_{RCT}, 0) \\ \max(-J_s^{-1} \vec{M}_{RCT}, 0) \end{bmatrix} \quad (3.73)$$

The actual torque generated by the combined Reaction Control Thrusters (RCTs) can be computed using the following formula:

$$M_{RCT,true} = \sum_{n=1}^4 u_{RCT,i} p_{RCT,i} \vec{x} \vec{F}_{RCT,i,max} \quad (3.74)$$



### OPTIMAL PLACEMENT AND ORIENTATION

The optimization process has yielded a solution that effectively maximizes angular accelerations in desired directions while minimizing unwanted accelerations in other directions.

The results indicate a strong correlation between the thrusters' orientations, positions, and thrust allocations with the generated angular acceleration around the intended axis of rotation, as well as the undesired acceleration in other rotational directions. To achieve pure angular accelerations along all axes of rotation, the thrusters need to be strategically oriented, allowing for a linear combination of their actions.

Based on the findings, it is evident that placing four thrusters at the top of the 3U CubeSat is a viable and feasible solution, without interference from the positioned solar panels. The solution to the optimization process is shown visually in Figure 3.11, while the resulting design parameters are reported in Table 3.5.

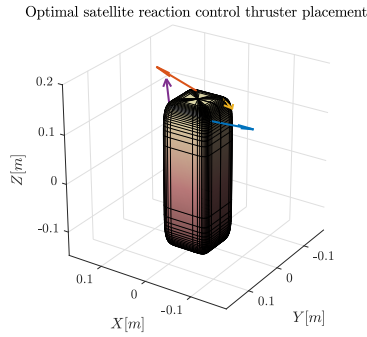


Figure 3.11: 3D view of the placement and orientation of the four RCTs.

Thruster	$v$ [rad]	$w$ [rad]	$\theta_d$ [rad]	$\phi_d$ [rad]
1	2.92181	0.60939	0.52444	0.99137
2	-1.26727	1.44218	-1.04703	-1.04365
3	-2.81819	1.28307	1.02817	-0.95590
4	0.25251	0.97006	0.49274	-1.00693

Table 3.5: Resulting design parameters for the four RCTs.

The results for the allocation matrix are presented in the following equation:

$$A_u = \begin{bmatrix} 0.89270 & 0.01089 & 0.01893 & 0.98118 \\ 0.11173 & 0.99960 & 0.00008 & 0.69814 \\ 0.97285 & 0.99488 & 0.00441 & 0.02443 \\ 0.14382 & 0.99701 & 0.80020 & 0.00241 \\ 0.97899 & 0.00107 & 0.98529 & 0.18989 \\ 0.00146 & 0.07522 & 0.97005 & 0.99874 \end{bmatrix} \quad (3.75)$$

A possible improvement of the results can be obtained by refining the formalization of

the multiple-objective optimization problem to include penalties for thrusting near sensors or through external solar panels. Additionally, exploring a Pareto front that encompasses multiple sets of solutions rather than a single solution would be a valuable avenue to pursue.

### 3.3.2. CONTROL ALGORITHMS

This section is intended to present the attitude dynamics description and the control algorithms to accomplish the required tasks. For the de-tumbling and reaction wheels desaturation, the selected control algorithm is a LQR. For tracking the optimal reference frame, either NEA fly-by or optimal firing thrust, the algorithm is a Lyapunov direct controller.

#### ATTITUDE REPRESENTATION

The best choice for the attitude description goes to the use of the modified Rodrigues parameters (MRP), whose definition as a function of the quaternions is:

$$\vec{\psi} = \frac{\vec{q}}{1 + q_4} \quad (3.76)$$

which implies that the transformation matrix from frame B to frame N can be expressed in MRPs as:

$$C_B^N = I_{3 \times 3} - 4 \frac{1 - \vec{\psi}^T \vec{\psi}}{(1 + \vec{\psi}^T \vec{\psi})^2} Q(\vec{\psi}) + 8 \frac{1}{(1 + \vec{\psi}^T \vec{\psi})^2} Q^2(\vec{\psi}) \quad (3.77)$$

where Q is the cross-multiplication matrix.

With some maths, the derivative of the MRP can be expressed as:

$$\dot{\vec{\psi}} = \frac{1}{2} [I_{3 \times 3} + Q(\vec{\psi}) + \vec{\psi} \vec{\psi}^T - \frac{1}{2} (1 + \vec{\psi}^T \vec{\psi}) I_{3 \times 3}] \vec{\omega} = G(\vec{\psi}) \vec{\omega} \quad (3.78)$$

When it comes to tracking a reference frame it is convenient to define the following quantity as it is the difference between the current and the target reference frame:

$$\delta \vec{\psi} = \frac{(1 - \|\vec{\psi}_r\|^2) \vec{\psi} + (1 - \|\vec{\psi}\|^2) - \vec{\psi}_r - 2 \vec{\psi} x(-\vec{\psi}_r)}{1 + \|\vec{\psi}\|^2 \|\vec{\psi}_r\|^2 - 2 \vec{\psi}(-\vec{\psi}_r)} \quad (3.79)$$

Then it is necessary to relate the angular rotation in the reference frame, to our current frame:

$$\delta \vec{\omega} = \vec{\omega} - [\vec{\omega}_r]_B = \vec{\omega} - C_R^B(\delta \vec{\psi}) \vec{\omega}_r \quad (3.80)$$

which then leads to the derivative term:

$$\delta \dot{\vec{\omega}} = \dot{\vec{\omega}} - C_R^B(\delta \vec{\psi}) [\dot{\vec{\omega}}]_R + \vec{\omega} x C_R^B(\delta \vec{\psi}) [\vec{\omega}_r]_R \quad (3.81)$$

#### LQR CONTROLLER

To derivation of a LQR starts by defining a linear time-invariant system as:

$$\dot{x} = Ax + Bu \quad (3.82)$$

which can be associated to a cost function:

$$J = \int_0^{\infty} [x^T Q x + u^T R u + x^T N u] dt \quad (3.83)$$

where both Q and R are positive semi-definite matrices. In order to find the optimality condition, the J index must be derived. Defining the controller as:

$$u = K x \quad (3.84)$$

where K is the gain matrix defined as:

$$K = -(B^T S B + R)^{-1} (B^T S A + N^T) \quad (3.85)$$

where the S matrix can be found by solving the Riccati equation:

$$A^T S A - S - (A^T S B + N)(B^T S B + R)^{-1} (B^T S A + N^T) + Q = 0 \quad (3.86)$$

#### REFERENCE FRAME TRACKING

Reference frame tracking is a macro-category which includes the tracking of the optimal firing direction and the fly-by of the asteroid. These cases, apparently different, are very similar from the dynamics perspective because the final goal of the controller is not to bring the state of the spacecraft to a certain value, but it is rather connected to point it dynamically in a certain direction. For this reason, the choice of the controller we made tends to privilege more the stability rather than the propellant performance. This leads to the definition of a Lyapunov direct controller, which is convenient from this perspective.

#### LYAPANUOV'S DIRECT CONTROLLER

The theory of Lyapunov stability (Schaub and Junkins, 2003) is the basis for this method. Starting from there, the definition of a Lyapunov function starts from the work of Tsiotras, 1995, which proposes to use a logarithmic term instead of the standard  $(1 + \delta\vec{\psi}^T \delta\vec{\psi})$ :

$$V(\delta\vec{\psi}, \delta\vec{\omega}) = \frac{1}{2} \delta\vec{\omega}^T K_1 \delta\vec{\omega} + 2K_3 \ln(1 + \delta\vec{\psi}^T \delta\vec{\psi}) \quad (3.87)$$

whose derivative is:

$$\dot{V}(\delta\vec{\psi}, \delta\vec{\omega}) = \delta\dot{\vec{\omega}}^T K_1 \delta\vec{\omega} + \frac{4K_3}{1 + \delta\vec{\psi}^T \delta\vec{\psi}} 1 + \delta\vec{\psi}^T G(\delta\vec{\psi}) \delta\vec{\omega} \quad (3.88)$$

which again translates into:

$$\dot{V}(\delta\vec{\psi}, \delta\vec{\omega}) = \delta\dot{\vec{\omega}}^T K_1 \delta\vec{\omega} + \delta\vec{\psi}^T K_3 \delta\vec{\omega} \quad (3.89)$$

The Lyapunov function is defined as stable if it is negative semidefinite, so it is smart to propose a control input that implies:

$$\dot{V}(\delta\vec{\psi}, \delta\vec{\omega}) = -\delta\vec{\omega}^T K_2 \delta\vec{\omega} \quad (3.90)$$

where  $K_2$  is a so-called positive definite angular velocity feedback gain matrix. The combination of the equations allows to drive the stability constraint:

$$-\delta\vec{\omega}^T K_2 \delta\vec{\omega} = \delta\dot{\vec{\omega}}^T K_1 \delta\vec{\omega} + \delta\vec{\psi}^T K_3 \delta\vec{\omega} \quad (3.91)$$

which can be rewritten as:

$$0 = \delta\vec{\omega}^T [K_1 \delta\dot{\vec{\omega}} + K_3 \delta\vec{\psi} + K_2 \delta\vec{\omega}] \quad (3.92)$$

which with some maths can be rewritten as a function of the required control vector:

$$\vec{u} = -\vec{\omega} x J_s \vec{\omega} - \vec{\omega} x \vec{h}_\omega - K_1 (C_R^{B_s} \vec{\omega}_r - \vec{\omega} x C_R^B \vec{\omega}_r) + K_2 \delta\vec{\omega} + K_3 \delta\vec{\psi} \quad (3.93)$$

where the gain matrices have been redefined for simplicity:

$$K_1 = J_s J_1^{-1} \quad (3.94)$$

$$K_2 = J_s J_1^{-1} K_2 \quad (3.95)$$

$$K_3 = J_s J_1^{-1} K_3 \quad (3.96)$$

In the specific case when respectively (for  $n=1:3$ ):

$$\dot{\omega}_{r,n} = 0 \quad (3.97)$$

$$\omega_{r,n} = 0 \quad (3.98)$$

$$\psi_{r,n} = 0 \quad (3.99)$$

the control vector can be expressed as:

$$\vec{u} = -\vec{\omega} x J_s \vec{\omega} - \vec{\omega} x \vec{h}_\omega + K_2 \delta\vec{\omega} + K_3 \delta\vec{\psi} \quad (3.100)$$

### NEA FLY-BY

This dissertation operates under the assumption that the anticipated relative fly-by velocity under the most unfavourable circumstances is 35 km/s, leading to a specific maximum angular acceleration requirement of around 0.01 mrad/s<sup>2</sup>. To monitor the asteroid's motion, the same transformations employed for tracking in the LVLH frame can be applied. The asteroid's orientation in MRP representation can be derived from its polar tracking orientation. This involves initially computing the quaternion representing the rotation from the inertia frame to the asteroid tracking frame:

$$q_w = \frac{1}{2} \sqrt{2 + 2(\hat{e}_x \dot{\hat{x}} + \hat{e}_y \dot{\hat{y}})} \quad (3.101)$$

$$q_x = \frac{(\hat{e}_y \hat{z} - \hat{e}_x) \hat{y}}{\sqrt{2 + 2(\hat{e}_x \dot{\hat{x}} + \hat{e}_y \dot{\hat{y}})}} \quad (3.102)$$

$$q_x = \frac{(\hat{e}_x \hat{z} - \hat{e}_y) \hat{x}}{\sqrt{2 + 2(\hat{e}_x \dot{\hat{x}} + \hat{e}_y \dot{\hat{y}})}} \quad (3.103)$$

$$q_w = \frac{1}{2} \sqrt{2 + 2(\hat{e}_x \dot{x} - \hat{e}_y \dot{y})} \quad (3.104)$$

where:

$$\hat{e}_x = [\cos\psi, \sin\psi, 0]^T \quad (3.105)$$

$$\hat{e}_y = [-\sin\psi, \cos\psi, 0]^T \quad (3.106)$$

$$\hat{e}_z = [0, 0, 1]^T \quad (3.107)$$

So the MRP for the asteroid tracking frame is expressed as:

$$\vec{\psi} = \frac{[q_x, q_y, q_z]^T}{1 + q_w} \quad (3.108)$$

while angular velocity and acceleration can be expressed respectively as:

$$\vec{\omega} = [0, 0, \dot{\psi}]^T \quad (3.109)$$

$$\dot{\vec{\omega}} = [0, 0, \ddot{\psi}]^T \quad (3.110)$$

Using the same approach for the tracking Earth reference frame, the reaction wheel torque can be expressed as:

$$\vec{T} = -W_{z,\omega}^{-1} \vec{\omega} x J_s \vec{\omega} - W_{z,\omega}^{-1} \vec{\omega} x \vec{h}_\omega - W_{z,\omega} K_1 (C_R^B \dot{\vec{\omega}}_r - \vec{\omega} x C_R^B \vec{\omega}_r) - W_{z,\omega}^{-1} K_2 \delta \vec{\omega} + W_{z,\omega}^{-1} K_\delta \vec{\psi} \quad (3.111)$$

### 3.3.3. DE-TUMBLING

De-tumbling the spacecraft means compensating for eventual undesired angular velocities of the spacecraft right after the release. It is important to reduce zero the tumbling velocity, so the spacecraft will be able to perform its tasks. It is difficult to define what initial angular condition the spacecraft will encounter in real life. For this reason, the same approach followed by LUMIO is chosen, since the deployment conditions are expected to be similar, and the initial tumbling of the satellite in all directions is set to 30 deg/s (Romero Calvo et al., 2019).

To accomplish the de-tumbling process, four methods are viable: employing only reaction wheels, using reaction wheels in conjunction with RTCs, combining reaction wheels with magnetorquers, or utilizing RTCs alone.

Usually de-tumbling around the Earth is accomplished by magnetorquers, which offer a very convenient option. However, to have a lighter architecture aimed to go to deep-space, the paradigm of reducing the onboard hardware leads to considering the use of RW or RCT, or a combination of those. The method that solely employs RTCs is not considered due to its close resemblance to the combination of reaction wheels and RTCs. The key distinction lies in its lower torque output for de-tumbling, leaving the reaction wheels with some residual spin. Consequently, this residual spin must be reduced after the de-tumbling manoeuvre. The benefits of using various de-tumbling methods are analyzed in the subsequent sections.

The de-tumbling control is actuated following a LQR strategy as highlighted before in this chapter. The LQR problem can be solved by exploiting the inbuilt functions in Matlab, however, the Q and R matrices have to be defined. An initial tuning led us to choose the following values:

$$Q = \text{diag} \left[ \left( \frac{1}{0.001} \right)^2, \left( \frac{1}{0.001} \right)^2, \left( \frac{1}{0.001} \right)^2, \left( \frac{1}{10} \right)^2, \left( \frac{1}{10} \right)^2, \left( \frac{1}{10} \right)^2, \left( \frac{1}{0.1} \right)^2, \left( \frac{1}{0.1} \right)^2, \left( \frac{1}{0.1} \right)^2 \right] \quad (3.112)$$

while the R matrix can be defined as a function of the characteristics of the satellite:

$$R = \text{diag} \left[ \left( \frac{1}{\tau_{RW}} \right)^2, \left( \frac{1}{\tau_{RW}} \right)^2, \left( \frac{1}{\tau_{RW}} \right)^2, \left( \frac{1}{\tau_{RCT}} \right)^2, \left( \frac{1}{\tau_{RCT}} \right)^2, \left( \frac{1}{\tau_{RCT}} \right)^2 \right] \quad (3.113)$$

### DETUMBLING USING REACTION WHEELS ONLY

The first option to de-tumble the satellite is to use only Reaction Wheels (RWs). This of course would be a very convenient scenario, as the employment of only one set of actuators would simplify notably the control. However, as can be noticed from Figure 3.12, the required angular speed of the reaction wheels reaches quickly saturation. This implies either to desaturate the wheels during the process or to lower the speed leading to higher detumbling times. Both cases are not ideal, especially the desaturation, because if RCT shall be used to desaturate the wheels, then it would be more convenient to use it directly to de-tumble the spacecraft.

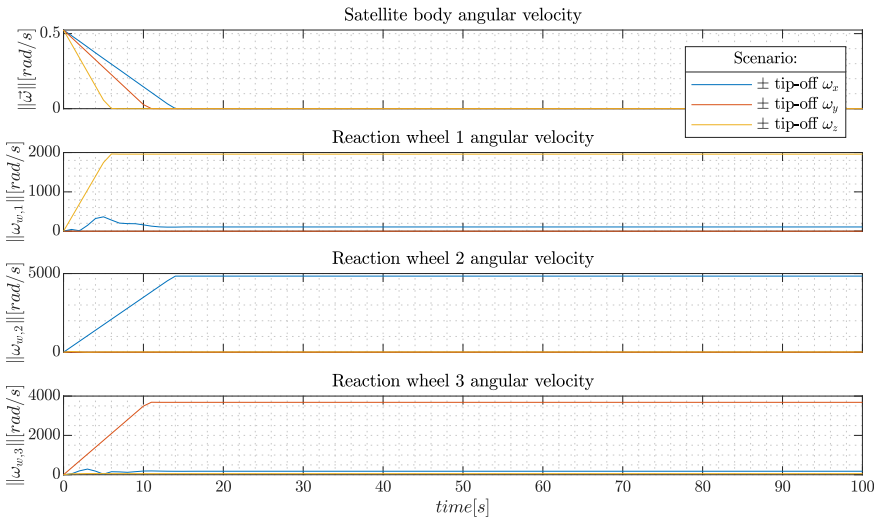


Figure 3.12: RWs speed for satellite detumbling for positive rotation about the three axes.

### DETUMBLING USING REACTION WHEELS AND RCT

By combining the actuation of the RCT and RW, detumble performance improves. As can be noticed from Figure 3.13, the RWs do not reach their saturation limit and the satellite detumbles from the large initial rotation within 5 minutes. Figure 3.14, presents the required thruster actuation to de-tumble the spacecraft.

Deeper analyses are required in order to assess whether these RW and RCT actuation profiles are in line with the actual hardware capabilities, however, interpolating results

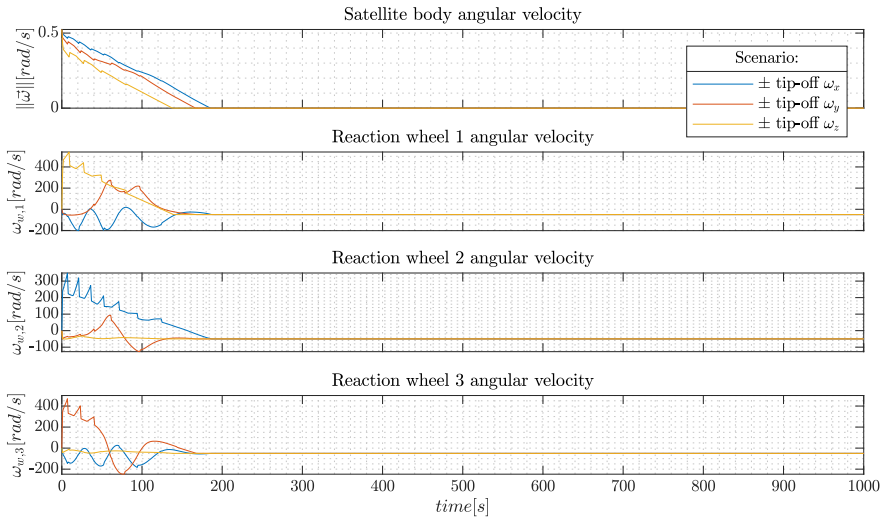


Figure 3.13: RWs speed for satellite detumbling for positive rotation about the three axes using both RWs and RCTs.

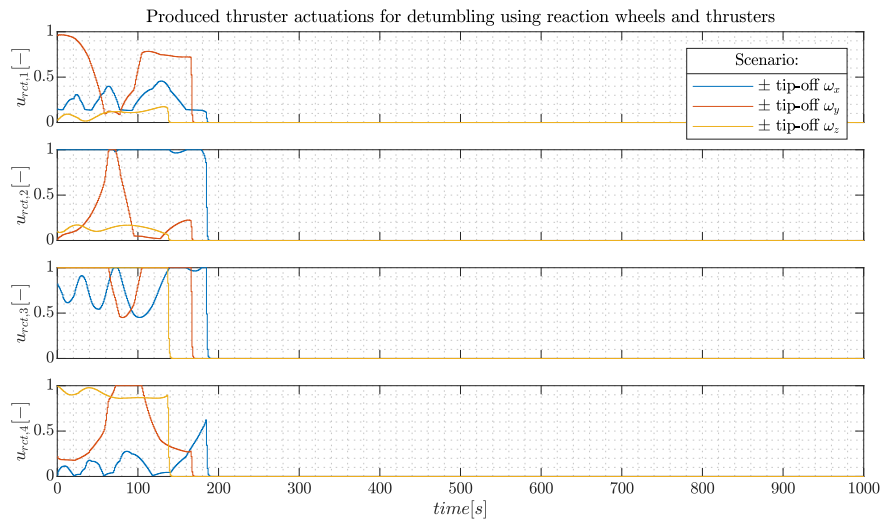


Figure 3.14: RCTs actuation for satellite de-tumbling for positive rotation about the three axes using both RWs and RCTs.

should be allowed to bring profiles that are both in line with the required de-tumbling and with hardware capabilities.

Assuming thrusters with characteristics similar to the Aurora ARM-A, the required propellant mass for the de-tumbling around the three directions negative and positive

are respectively reported in Table 3.6.

Detumbling axis	Required propellant
x+	0.374 g
x-	0.357 g
y+	0.273 g
y-	0.293 g
z+	0.399 g
z -	0.278 g

Table 3.6: Required propellant mass for each axis de-tumbling.

### 3.3.4. REACTION WHEELS DESATURATION

To desaturate the reaction wheels in situations where a properly defined and significant magnetic field is absent along the trajectory to the NEA, RCTs must be employed. The same control algorithms used for the de-tumbling case can be applied here.

The simulation is focused on de-saturating one reaction wheel at a time, considering an initial angular velocity of 1000 rad/s, corresponding to the saturation limit for Hyperion RWs. In each separate scenario, one RW is considered to have reached its saturation limit, while the other two have an initial null angular speed. Furthermore, the RW target angular velocity is not set as null, but to - 50 rad/s, as RW manufacturers usually suggest not to keep the reaction wheels at low or null angular velocity.

The initial analysis uses the following tuned matrix:

$$Q = \text{diag} \left[ \left( \frac{1}{0.001} \right)^2, \left( \frac{1}{0.001} \right)^2, \left( \frac{1}{0.001} \right)^2, \left( \frac{1}{100} \right)^2, \left( \frac{1}{100} \right)^2, \left( \frac{1}{100} \right)^2, \left( \frac{1}{0.1} \right)^2, \left( \frac{1}{0.1} \right)^2, \left( \frac{1}{0.1} \right)^2 \right] \quad (3.114)$$

The results are presented in Figures 3.15 and 3.16, while Table 3.7 shows the required propellant mass for each case.

RWs axis	Required propellant mass
x+	0.138 g
x-	0.074 g
y+	0.078 g
y-	0.136 g
z+	0.055 g
z -	0.076 g

Table 3.7: Required propellant fast for RWs desaturation.

As it can be noticed the reduction of the reaction wheel speed occurs very quickly, between 50 and 80 seconds. If the reaction wheels want to be desaturated at a lower rate to not stress the mechanical components, the following matrix can be adopted:

$$Q = \text{diag} \left[ \left( \frac{1}{0.001} \right)^2, \left( \frac{1}{0.001} \right)^2, \left( \frac{1}{0.001} \right)^2, \left( \frac{1}{1000} \right)^2, \left( \frac{1}{1000} \right)^2, \left( \frac{1}{1000} \right)^2, \left( \frac{1}{0.1} \right)^2, \left( \frac{1}{0.1} \right)^2, \left( \frac{1}{0.1} \right)^2 \right] \quad (3.115)$$



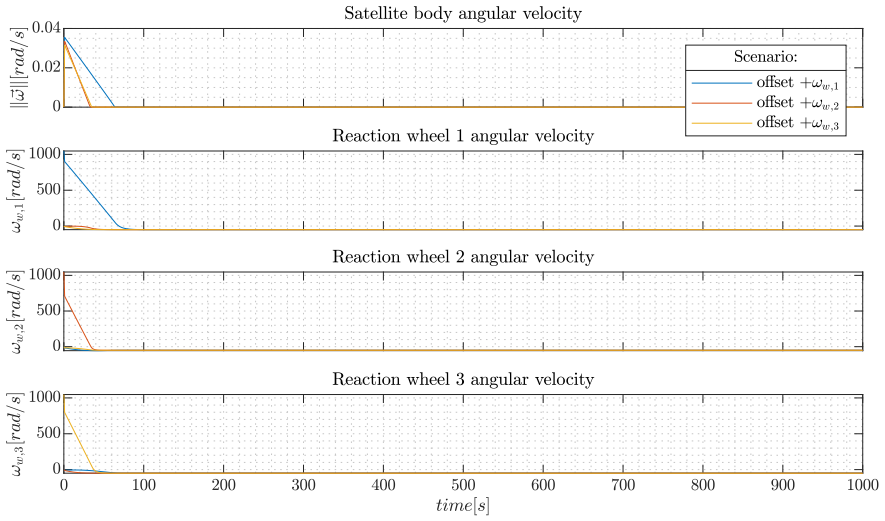


Figure 3.15: RWs speed during fast desaturation manoeuvres.

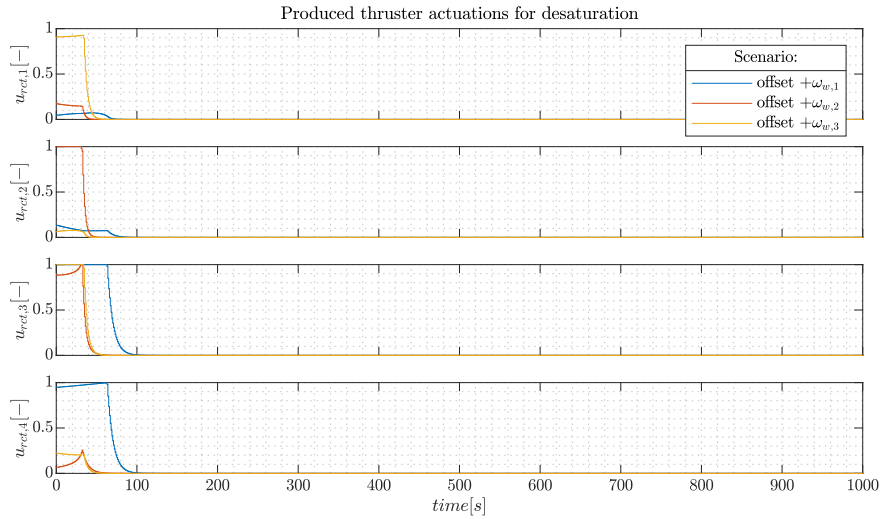


Figure 3.16: RCTs actuation during fast desaturation manoeuvres.

The results are reported in Figures 3.17 and 3.18, where the RWs speed reduction occurs at a noticeably lower rate than in the previous case. Table 3.8 shows the required propellant mass, which is quite similar to the previous case.

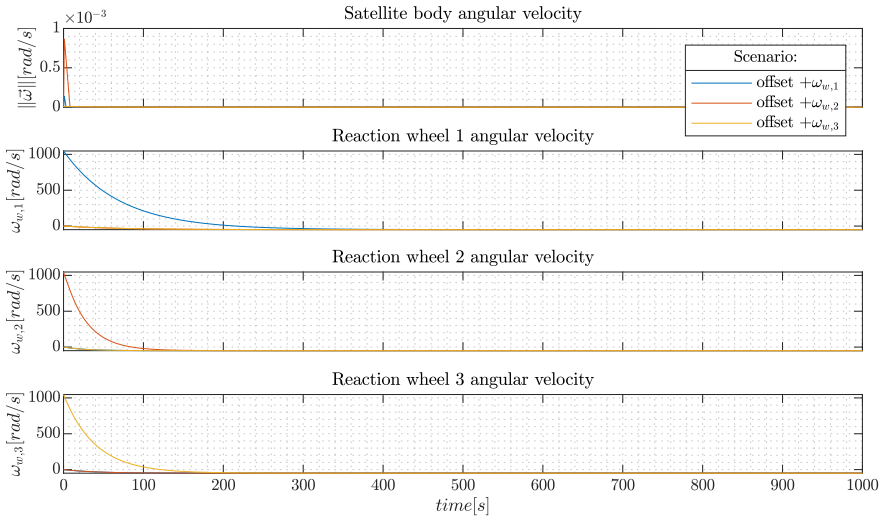


Figure 3.17: RWs speed during slow desaturation manoeuvres.

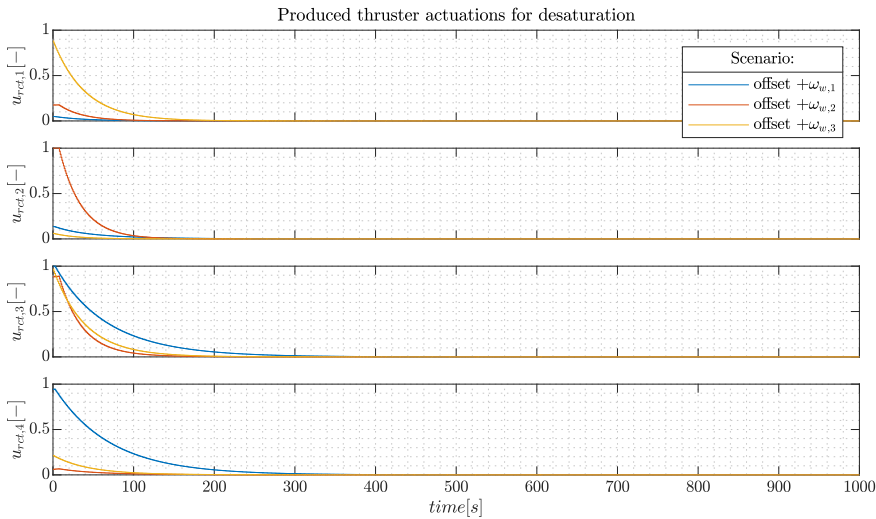


Figure 3.18: RCTs actuation during slow desaturation manoeuvres.

### 3.3.5. OPTIMAL FIRING TRACKING

For the optimal direction firing tracking only the reaction wheels are sufficient. The example is carried out in the Earth Escape for simplicity but can be easily applied to other mission scenarios. Figures 3.19 and 3.20 show respectively the first 200 seconds of reaction wheels actuation and the rest of one orbit revolution. The first plot shows basically what happens when in a completely different setting the spacecraft needs to start

RWs axis	Required propellant mass
x+	0.137 g
x-	0.073 g
y+	0.080 g
y-	0.135 g
z+	0.057 g
z-	0.075 g

Table 3.8: Required propellant mass for slow RWs desaturation.

3

re-orienting to initiate the escape phase. The second plot shows the behaviour of the reaction wheels to follow the optimal direction throughout the escape. Finally, Figure 3.21 shows how the resulting satellite orientation follows strictly the required reference orientation.

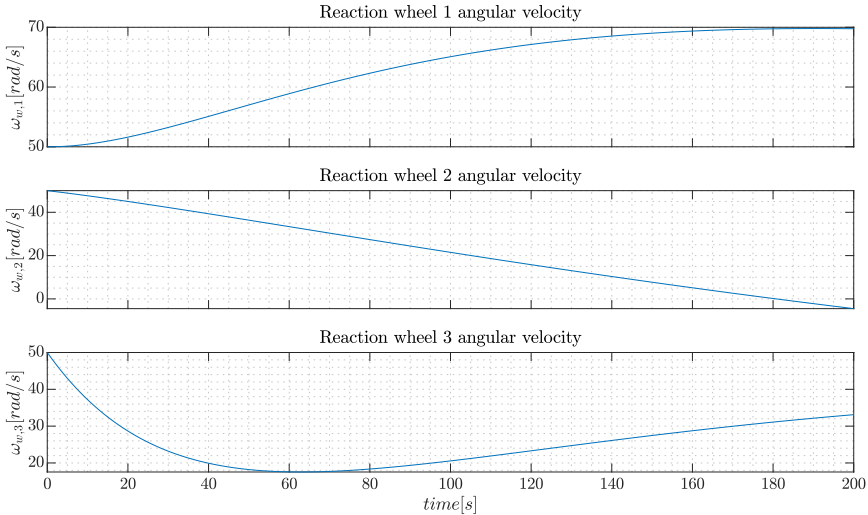


Figure 3.19: First 200 seconds RWs speed for Earth Escape.

### 3.3.6. ASTEROID FLY-BY

Similarly to the previous case, the objective of this analysis is to keep the asteroid in the payload FoV during the rapid fly-by. However, depending on the mission characteristics, many different characteristics can influence the required control input. So different test scenarios are evaluated. What is important, is to avoid de-saturation maneuver during the process, so it is better to keep the reaction wheels' speed within the limit. The first two plots (Figures 3.22 and 3.23) show the behaviour respectively for a relative fly-by velocity of 10 km/s and 30 km/s, at an altitude of 1000 km, with initial RW speeds of 0 deg/s.

Both cases do not require particularly challenging RW speed levels, however as it has

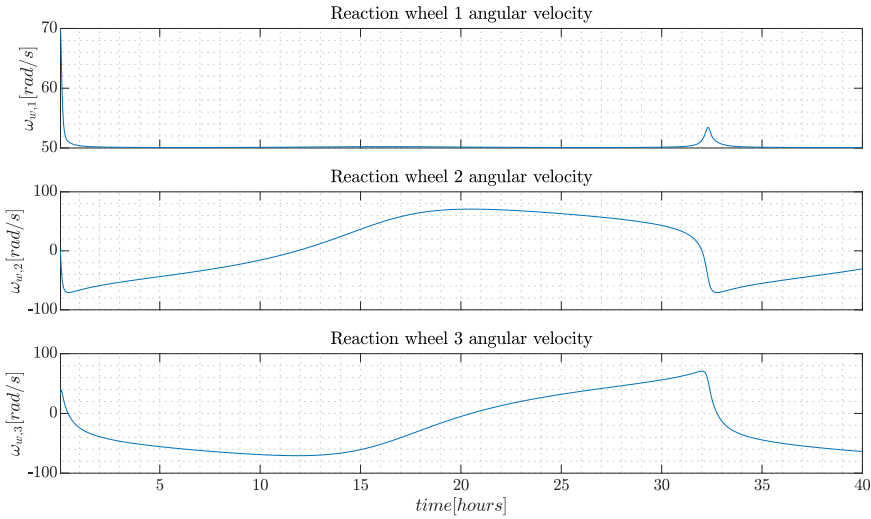


Figure 3.20: RWs speed for one orbit of the Earth Escape scenario.

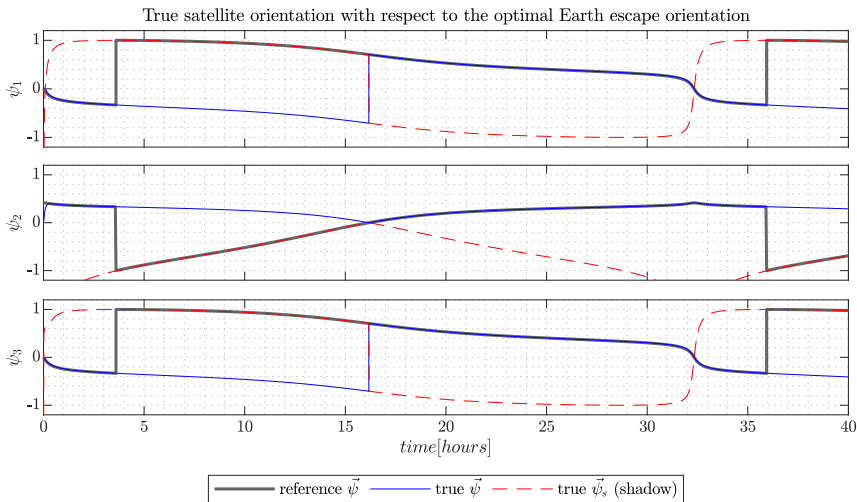


Figure 3.21: Reference and true RWs speed during the Earth Escape orientation tracking.

been already remarked, Reaction wheels better perform if they are kept at a low constant speed. For this reason, an additional case with reaction wheel initial speed around +/- 50 rad/s is considered and shown in Figures 3.24 and 3.25. Also in these cases, the Reaction Wheels present an acceptable level and seem to be performing well in the case.

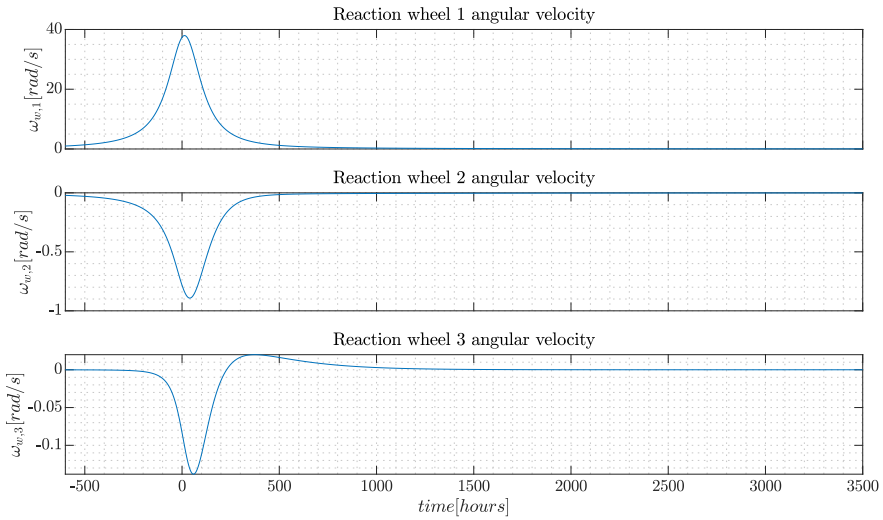


Figure 3.22: RWs speed during NEAs fly-by at 10 km/s relative speed and 1000 km altitude.

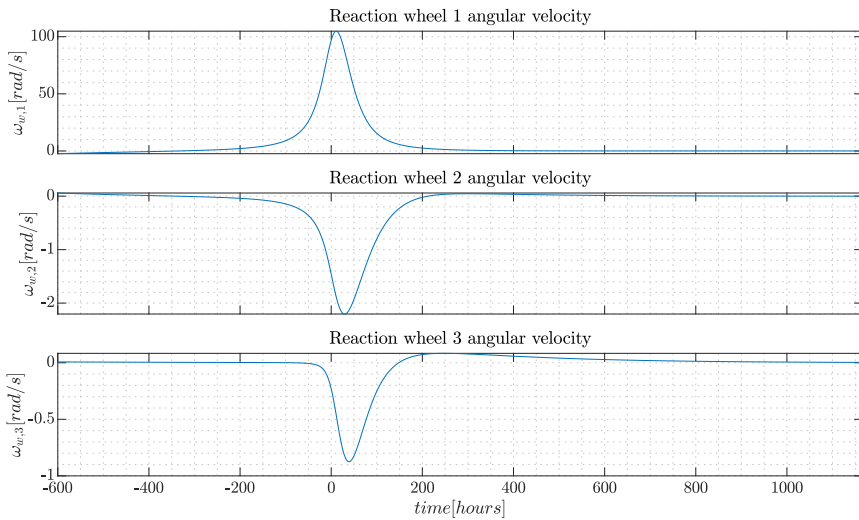


Figure 3.23: Caption

### 3.4. CONCLUSIONS

This chapter presented an analysis of both the propulsion system and attitude control system to close the loop initiated in Chapter 2. With a focus on the available COTS, and the design of basic algorithms, it has been preliminary shown that:

- The Earth escape is a very challenging procedure that is partially possible with high

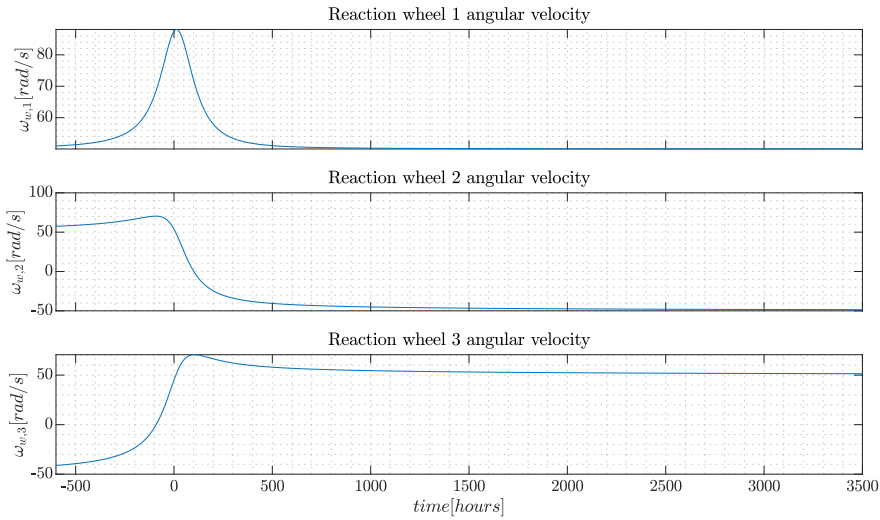


Figure 3.24: RWs speed during NEAs fly-by at 10 km/s relative speed and 1000 km altitude.

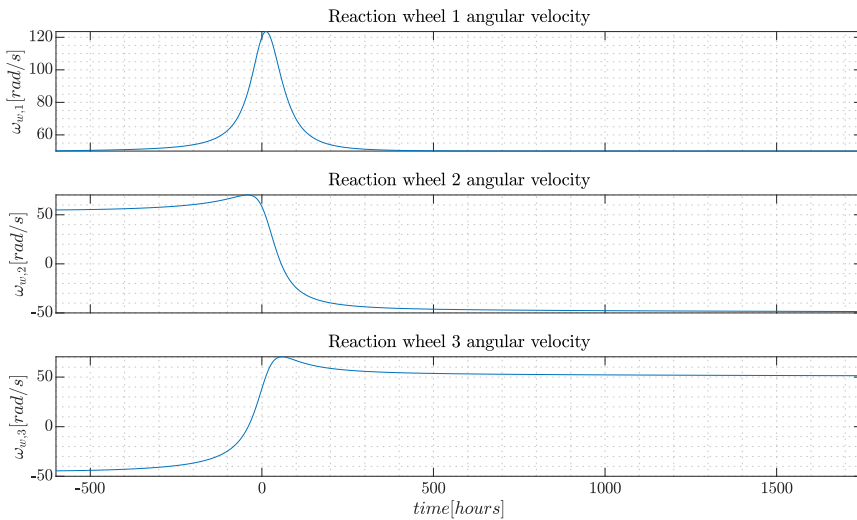


Figure 3.25: RWs speed during NEAs fly-by at 30 km/s relative speed and 1000 km altitude.

thrust, but very complicated with the available COTS electric propulsion options;

- electric propulsion system that fits a 3U CubeSat structure only allows close targets to be explored, while chemical propulsion systems open up different possibilities;
- Earth escape missions would be possible with electric propulsion for closer targets with slight customization of the propulsion system;

- RW similar to the Hyperion RW200 have sufficient capabilities to enable the majority of the tasks;
- Having a reaction thrust system with the characteristics of the AURORA ARM-A, with the optimized orientation found in the chapter, allows both to desaturate efficiently the reaction wheels and to detumble the spacecraft at large initial rates.

This chapter has investigated one of the two main challenges highlighted in Chapter 2, the one related to the finest design of attitude and orbit control system for a miniaturized deep-space mission. The other highlighted challenge, related to autonomous navigation, is investigated in the next chapters, however it is important to remark that, in the design of space missions, navigation and AOCS are always interconnected topics, as one's design influences the other's design and viceversa.

# 4

## LINE-OF-SIGHT OPTICAL NAVIGATION

*Seconda stella a destra, questo e' il cammino,  
e poi dritto fino al mattino.  
Poi la strada la trovi da te,  
porta all'isola che non c'e'.*

Edoardo Bennato - L'isola che non c'e'

*This chapter explores the application of Line-of-Sight Optical Navigation for deep-space missions. First, the information matrix is analyzed to show the influence of the geometry between the spacecraft and the observed planet(s). Then, a Monte Carlo approach is used to investigate the influence of measurement error (ranging from 0.1 to 100 arc-sec), and tracking frequency (ranging from four observations per day to one observation every two days). The simulation is based on a set of four planets, which do not follow the common heliocentric dynamics but rotate around the Sun with the same (distance-independent) angular velocity of the spacecraft. This approach allows the separation of scenario-dependent behaviours from navigation intrinsic properties, as the same relative geometry between observer and observed objects is maintained during the whole simulation. Considerations are then applied to Near-Earth Asteroid fly-by mission scenarios for the definition of the navigation strategy and hardware requirements. In addition, a Figure-of-Merit is used to rate NEA nodal passages as a function of their LoS observability. The results provide a useful guide for the next-generation autonomous navigation system, for both the definition of hardware requirements and the design of an appropriate navigation strategy, which is later explored in Chapters 5 and 6.*

---

Parts of this chapter have been published in Casini, Cervone, Monna, and Gill, [2022](#) and Casini, Monna, et al., [2022](#).



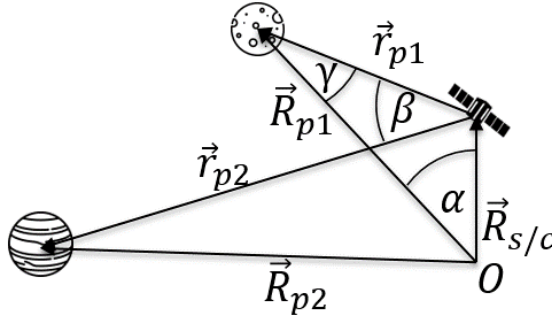


Figure 4.1: Schematics of the navigation observation geometry.

## 4.1. INTRODUCTION

Chapter 2 has highlighted the need to employ autonomous navigation techniques for miniaturized deep-space missions, in particular when the chosen platform is a 3U Cube-Sat, because it allows for reduced onboard need, and reduced ground segment demands. While navigation around a target object, being it a planet, moon, or asteroid, has been extensively investigated in the literature, less attention has been dedicated to navigation during the cruise phase. For this reason, as it has been depicted in the introduction chapter, the focus will be on optical line-of-sight navigation during the cruise. The upcoming sections will detail the different characteristics associated with the navigation analysis. Initially, LoS navigation will be discussed, followed by a description of the simulation method that emphasizes the dynamic features. Subsequently, the formulation of the EKF will be introduced, and then the performance indicators and the parameters under analysis will be defined.

## 4.2. LOS NAVIGATION

LoS navigation involves observing celestial bodies, such as planets, moons, or small bodies, to determine the spacecraft's state. This is achieved by using an onboard camera or star-tracker to obtain directions to these bodies, which are then processed in a navigation filter along with the ephemerides of the observed objects stored onboard. The filter incorporates spacecraft dynamics to estimate the spacecraft's state, such as its position and velocity in a heliocentric frame. Both observation and estimation phases can be performed autonomously onboard. The problem's geometry is illustrated in Figure 4.1, where the de-phasing angle  $\alpha$  is defined as the angular separation between the spacecraft's position vector and the position vector of the observed planet. The separation angle  $\beta$  is identified as the angular separation between the two LoS vectors  $\vec{r}_{p1}$  and  $\vec{r}_{p2}$  centred on the spacecraft position.

The separation angle  $\beta$  can be expressed as a function of the LoS vectors as:

$$\beta = \text{acos}\left(\frac{\vec{r}_{p1} \cdot \vec{r}_{p2}}{\|\vec{r}_{p1}\| \cdot \|\vec{r}_{p2}\|}\right) \quad (4.1)$$

Then, it is possible to express the separation angle as a function of the de-phasing angles by substituting the following formulation for the LoS vectors, obtained by exploiting the Carnot theorem:

$$\vec{r}_{p1} = \sqrt{(\vec{R}_{sc})^2 + (\vec{R}_{p1})^2 - 2\vec{R}_{sc}\vec{R}_{p1}\cos(\alpha_1)} \quad (4.2)$$

$$\vec{r}_{p2} = \sqrt{(\vec{R}_{sc})^2 + (\vec{R}_{p2})^2 - 2\vec{R}_{sc}\vec{R}_{p2}\cos(\alpha_2)} \quad (4.3)$$

The choice of exploring LoS navigation rather than other autonomous navigation techniques, such as pulsar-based or radiometric navigation, is reported in Chapter 1. Perhaps, cameras and/or star-trackers are supposed to be carried onboard in each deep-space miniaturized mission, and the possibility to exploit them also for navigation during cruise, rather than incorporating additional hardware, is definitely appealing. A standalone CubeSat holds the potential to determine its state solely by observing the direction of celestial bodies. This self-sufficiency eliminates the dependence on a ground station or other satellites, which would have been necessary for radiometric techniques. Despite potentially offering lower performance compared to Pulsar-based navigation, the higher readiness level of LoS navigation hardware renders it an optimal choice for deep-space missions, particularly NEA missions. In the context of NEA missions, as highlighted in the introduction chapter, it is crucial to maintain a position error below 1000 km. The subsequent subsections will delve into investigating the feasibility of meeting this requirement. Simultaneous observation of multiple bodies can be achieved with the availability of multiple imagers onboard or can be done asynchronously if only one camera is available or if slew manoeuvres are needed to centre the target in the FoV. However, for the subsequent analysis, the focus will be on simultaneous imaging.

### 4.3. SIMULATION APPROACH

The objective of this study is to offer new insights into the impact of specific parameters on LoS navigation performance. To achieve this goal, a new simulation approach is used to generate generalized conclusions. Since LoS navigation is heavily dependent on the problem's geometry, simulating realistic mission scenarios involving specific planets, times, and spacecraft orbits can be challenging and limit the scope of the conclusions. Furthermore, the constantly changing geometry would affect the results, and defining the steady-state behaviour of the estimation would be difficult. Therefore, a set of four planets has been simulated, which maintain the same angular separation with the spacecraft throughout the simulation by forcing their orbital speed to be equal to the spacecraft. The four planets are referred to as P1 (0.4 AU), P2 (0.8 AU), P3 (1.8 AU), and P4 (5.2 AU), and the spacecraft's orbit is assumed circular and heliocentric, with a radius of 1 AU, which is suitable for simulating a possible NEAs region mission. The circular orbit is chosen to have a symmetric simulation for the analysis, but it does not limit the applicability of the technique to only circular orbits. The relative inclination of the orbits is assumed to be small, as NEAs are usually encountered near their ascending or descending nodal passages to avoid expensive change-of-plane manoeuvres. Although the 3D problem becomes 2D with these orbits, it is still consistent with actual mission scenarios. This approach allows for a simplified definition of the information matrix,

and the analysis focuses on the actual parameters under scrutiny, with all other factors fixed.

In a later section, the selection of the angular separation between the simulated planets is justified after conducting a geometry analysis.

A simulation duration of 730 days has been chosen, which corresponds to two complete orbits of the spacecraft around the Sun. Additionally, many ballistic transfers to NEAs have a shorter ToF.

The implementation of a 2-body problem dynamics has been used for both the semi-analytical approach and the sensitivity analysis.

$$\vec{f} = -\mu_{Sun} \frac{\vec{r}}{r^3} \quad (4.4)$$

The solar gravitational parameter  $\mu_{Sun}$  is used in conjunction with the heliocentric position vector  $\vec{r}$  of the spacecraft for calculations. In the semi-analytical approach, the circularity of the orbits and 2-body problem dynamics lead to a simplified analytical formulation, as demonstrated. Additionally, in the sensitivity analysis, the simulation model allows for a focus on intrinsic characteristics.

Conversely, the propagation of trajectories in Section 4.9.3, where realistic mission scenarios are analyzed, relies on a higher-fidelity model. This model includes the 2-body problem with planetary gravitational disturbances (up to Saturn) and Solar Radiation Pressure (SRP). The SRP can be expressed as:

$$\vec{f} = -\mu_{Sun} \frac{\vec{r}}{r^3} + \sum_{k=1}^6 \mu_k \frac{\vec{r}_{pk}}{r_{pk}^3} - \sum_{k=1}^6 \mu_k \frac{\vec{r}_k}{r_k^3} + \vec{a}_{SRP} \quad (4.5)$$

The vectors  $\vec{r}_{pk}$  represent the spacecraft's position relative to the planets, while  $\vec{r}_k$  is the heliocentric position vector of the planets. The gravitational parameters of the planets are denoted by  $\mu_k$ . In the model, SRP is treated as a cannonball, as described in Jean et al., 2019:

$$\vec{a}_{SRP} = \frac{2P_{SRP}}{B} \vec{r} \quad (4.6)$$

The SRP acceleration that aligns with the spacecraft position vector is represented by  $\vec{a}_{SRP}$ , while  $P_{SRP}$  denotes the pressure exerted on the spacecraft by solar radiation. The mass-to-area ratio of the spacecraft is indicated by  $B$ . These values can be calculated as follows:

$$P_{SRP} = \frac{P_0}{c} \left( \frac{R_0}{r} \right)^2 \quad (4.7)$$

$$B = \frac{m}{A} \quad (4.8)$$

The expression for  $P_{SRP}$  is derived from the solar flux  $P_0$  at 1 AU ( $1367 \text{ W/m}^2$ ), the speed of light  $c$  ( $2.998 \cdot 10^8 \text{ m/s}$ ), the Sun-Earth mean distance  $R_0$ , spacecraft-Sun distance  $r$ , spacecraft mass  $m$ , and spacecraft surface area exposed to SRP  $A$ , assuming a unitary reflectivity coefficient.

For the simulation, a Monte Carlo approach has been employed. Each scenario is simulated 200 times, and the results are presented as the mean value of specific performance indicators, explained in the next subsections. Each Monte Carlo trial involves a different initial state guess and a distinct set of observations, both of which are generated by adding Gaussian noise (with a specific standard deviation) to the actual initial state and the simulated measurements.

#### 4.4. NAVIGATION FILTER

Instead of a batch approach, a sequential estimation technique has been selected for this analysis and application. Even though real-time operations are not required during the cruise, a batch approach could still be employed. However, since this analysis is intended for use with an autonomous deep-space CubeSat, a sequential algorithm is preferred. This is because a smaller amount of data needs to be stored onboard, and a constant update of the state estimation enables eventual manoeuvres and operations.

The problem is formulated using an Extended Kalman Filter, as described in Wertz et al., 2011. The state that requires estimation is the spacecraft's six-dimensional Cartesian state, expressed in a heliocentric frame.

$$\vec{X} = [x \quad y \quad z \quad v_x \quad v_y \quad v_z] \quad (4.9)$$

The Extended Kalman Filter is fed with measurements that indicate the directions to one or more planets. These measurements are expressed in terms of azimuth  $\theta$  and elevation  $\phi$ , with respect to the observer (e.g. the spacecraft).

$$\vec{Y} = \begin{bmatrix} \theta \\ \phi \end{bmatrix} \quad (4.10)$$

Directions to planets are expressed in the same heliocentric frame as:

$$\hat{r}_{pk} = \frac{\vec{r}_k - \vec{r}}{|\vec{r}_k - \vec{r}|} = \begin{bmatrix} x_{los,k} \\ y_{los,k} \\ z_{los,k} \end{bmatrix} \quad (4.11)$$

The heliocentric planet position vector is denoted by  $\vec{r}_k$ . The spacecraft attitude is assumed to be known, as it is considered in later sections to define the LoS measurement error range. The general equations for the state dynamics and observation in the Extended Kalman Filter can be expressed as follows:

$$\dot{\vec{X}} = f(\vec{X}(t), \vec{u}(t)) \quad (4.12)$$

$$\vec{Y} = h(\vec{X}(t), \vec{u}(t)) = \begin{bmatrix} \arctan\left(\frac{y_{los,k}}{x_{los,k}}\right) \\ \arcsin(z_{los,k}) \end{bmatrix} \quad (4.13)$$

The control vector is denoted by  $\vec{u}$ , but it is not implemented in this analysis since ballistic trajectories are being considered. The vector  $\dot{\vec{X}}$  contains the time-derivatives of the state vector, which is expressed as a function  $f$  of both the state and control vectors.

In the Monte Carlo analysis, it is based on Equation 4.4, while in the realistic mission scenario analysis, it is based on a reduced version of Equation 4.5. The computed measurements vector for each observed body is denoted by  $\vec{Y}$  and is expressed as a function  $h$  of both the state and control vectors.

In the following equations, bold characters indicate matrices. The state is propagated within the filter by solving the differential Equation 4.4, while the covariance matrix is propagated as:

$$\bar{\mathbf{P}}_{\mathbf{k}} = \Phi^T(t_k, t_{k-1}) \hat{\mathbf{P}}_{\mathbf{k}-1} \Phi(t_k, t_{k-1}) + \mathbf{Q} \quad (4.14)$$

where  $\Phi(t_k, t_{k-1})$  is the state transition matrix and  $\mathbf{Q}$  is the process noise matrix:

$$\mathbf{Q} = \begin{bmatrix} 10^{-12} & 0 & 0 & 0 & 0 & 0 \\ 0 & 10^{-12} & 0 & 0 & 0 & 0 \\ 0 & 0 & 10^{-12} & 0 & 0 & 0 \\ 0 & 0 & 0 & 10^{-10} & 0 & 0 \\ 0 & 0 & 0 & 0 & 10^{-10} & 0 \\ 0 & 0 & 0 & 0 & 0 & 10^{-10} \end{bmatrix} \quad (4.15)$$

The diagonal values of the matrix  $\mathbf{Q}$  have been adjusted based on a high-fidelity propagator for the trajectory and a 2-body problem propagator in the EKF. While keeping the position elements small does not significantly affect performance, the velocity entries require more attention. Analysis of various 1 AU orbits in different time epochs has suggested that a value between  $10^{-9}$  and  $10^{-10}$  can maintain the estimation error within the  $3\sigma$  boundaries. Therefore, for the following analyses, a value of  $10^{-10}$  has been used, assuming that the dynamics is perfectly modelled in the filter. Similarly, for the realistic mission scenarios presented in Section 5, small values are appropriate as the largest disturbances are modelled in the EKF propagator. The precise tuning of the matrix  $\mathbf{Q}$  depends on the time propagation interval. In this report, various tracking frequencies are analyzed, but  $\mathbf{Q}$  is kept constant as no formal tuning is performed, and further analysis is left for future work. Nevertheless, the results are not significantly affected. Additionally, following the approach reported in Carpenter and D'Souza, 2018, the elements of  $\mathbf{Q}$  relative to two tracking frequencies in this analysis would differ by less than an order of magnitude.

The state transition matrix is calculated at each time interval by integrating the following equation:

$$\dot{\Phi}(t) = \mathbf{F}\Phi(t) \quad (4.16)$$

where  $\mathbf{F}$  is the Jacobian of the state, and in the 2-body problem formulation can be expressed as:

$$\mathbf{F} = \begin{bmatrix} 0 & 0 & 0 & 1 & 0 & 0 \\ 0 & 0 & 0 & 0 & 1 & 0 \\ 0 & 0 & 0 & 0 & 0 & 1 \\ -\frac{\mu_s(1-3x^2)}{r^3} & 3\mu_s \frac{x}{r^5} & 3\mu_s \frac{xz}{r^5} & 0 & 0 & 0 \\ 3\mu_s \frac{xy}{r^5} & -\frac{\mu_s(1-3y^2)}{r^3} & 3\mu_s \frac{yz}{r^5} & 0 & 0 & 0 \\ 3\mu_s \frac{xz}{r^5} & 3\mu_s \frac{yz}{r^5} & -\frac{\mu_s(1-3z^2)}{r^3} & 0 & 0 & 0 \end{bmatrix} \quad (4.17)$$

The state vector and covariance matrix update can be then expressed as:

$$\vec{X}_k = \vec{X}_k + \mathbf{K}_k(\vec{Y}_k - \vec{Y}_k) \quad (4.18)$$

$$\hat{\mathbf{P}}_k = (\mathbf{I} - \mathbf{K}_k \mathbf{H}_k) \bar{\mathbf{P}}_k \quad (4.19)$$

The state vector after propagation is represented by  $\vec{X}_k$ , while the updated state vector is represented by  $\hat{X}_k$ . The measurements vector and the computed measurements vector are respectively denoted as  $\vec{Y}_k$  and  $\vec{Y}_k$ . The propagated covariance matrix is  $\bar{\mathbf{P}}_k$ , while the updated covariance matrix is  $\hat{\mathbf{P}}_k$ . The observation matrix and the Kalman gain matrix can be expressed as  $\mathbf{H}_k$  and  $\mathbf{K}_k$ , respectively.

$$\mathbf{H}_k = \begin{bmatrix} \frac{y_{los,1}}{r_{los,1}^2} & -\frac{x_{los,1}}{r_{los,1}^2} & 0 & 0 & 0 & 0 \\ \frac{x_{los,1}z_{los,1}}{r_{los,1}^3 \sqrt{1 - \frac{z_{los,1}^2}{r_{los,1}^2}}} & \frac{y_{los,1}z_{los,1}}{r_{los,1}^3 \sqrt{1 - \frac{z_{los,1}^2}{r_{los,1}^2}}} & \frac{z_{los,1}^2 - r_{los,1}^2}{r_{los,1}^3 \sqrt{1 - \frac{z_{los,1}^2}{r_{los,1}^2}}} & 0 & 0 & 0 \\ \frac{y_{los,2}}{r_{los,2}^2} & -\frac{x_{los,2}}{r_{los,2}^2} & 0 & 0 & 0 & 0 \\ \frac{x_{los,2}z_{los,2}}{r_{los,2}^3 \sqrt{1 - \frac{z_{los,2}^2}{r_{los,2}^2}}} & \frac{y_{los,2}z_{los,2}}{r_{los,2}^3 \sqrt{1 - \frac{z_{los,2}^2}{r_{los,2}^2}}} & \frac{z_{los,2}^2 - r_{los,2}^2}{r_{los,2}^3 \sqrt{1 - \frac{z_{los,2}^2}{r_{los,2}^2}}} & 0 & 0 & 0 \end{bmatrix} \quad (4.20)$$

$$\mathbf{K}_k = \bar{\mathbf{P}}_k \mathbf{H}_k^T (\mathbf{H}_k \bar{\mathbf{P}}_k \mathbf{H}_k^T + \mathbf{R}_k)^{-1} \quad (4.21)$$

where  $\mathbf{R}_k$  is the observation covariance matrix, assumed constant in this analysis:

$$\mathbf{R}_k = \begin{bmatrix} \sigma_{los1}^2 & 0 & 0 & 0 \\ 0 & \sigma_{los1}^2 & 0 & 0 \\ 0 & 0 & \sigma_{los2}^2 & 0 \\ 0 & 0 & 0 & \sigma_{los2}^2 \end{bmatrix} \quad (4.22)$$

In Equation 4.20, the observation matrix is tailored for the double-planets observation scenario. For the single-planet observation case, the matrix is reduced to the first two rows.

Realistic missions require accounting for light-time delay and velocity aberration corrections. Light-time delay refers to the time it takes for light to travel from the observed body to the spacecraft, which must be considered in order to access ephemerides at the appropriate time. The delay can also be affected by the onboard timing knowledge. Velocity aberration is a shift in the position of the observed object due to the relative tangential velocity between the observer (i.e., spacecraft) and the observed object (i.e., planet). These effects can be easily corrected using the EKF. Light-time delay can be corrected by iterating the ephemerides access time based on the computed distance between the observer and the body. Velocity aberration can be corrected by estimating the angular shift algebraically (Karimi and Mortari, 2015). First it is needed to define the relation by the true direction with the observed as:

$$r_{\hat{los}} = \frac{\hat{r}_{obs} \sin \theta_{true} - \hat{v} \sin \epsilon}{\sin \theta_{obs}} \quad (4.23)$$

where  $\theta_{obs}$  is the observed angle between the spacecraft velocity and the LoS direction, while  $\epsilon$  is the aberration angle, and  $\theta_{true}$  is the true angle between velocity and LoS vectors. They are related by:

$$\theta_{true} = \theta_{obs} + \epsilon \quad (4.24)$$

The aberration angle can be computed as:

$$\tan \epsilon = \frac{\frac{c}{v} \sqrt{1 - (\hat{r}_{obs}^T \hat{v})^2}}{1 - \frac{c}{v} (\hat{r}_{obs}^T \hat{v})} = \frac{\frac{v}{c} \sin \theta_{obs}}{1 - \frac{v}{c} \cos \theta_{obs}} \quad (4.25)$$

If also the relativistic correction described by the special relativity is included, the relation is:

$$\cos \theta_{obs} = \frac{\cos \theta_{true} + \frac{v}{c}}{1 + \frac{v}{c} \cos \theta_{true}} \quad (4.26)$$

These corrections are only applied in the realistic mission scenarios of the later section because, for the simulation benchmark of the first sections, they add complexity without providing valuable insights.

## 4.5. PERFORMANCE INDICATORS

Within this work, two performance indicators are used to evaluate the navigation technique. The first indicator is the 3D Root-Mean-Square-Error (3D-RMSE or simply RMSE) of both position and velocity over the last half year, when steady-state has been reached, as will be shown later. The second indicator is the convergence time, which quantifies the time needed to reach the steady-state behaviour of the filter. As there is no unique way to define convergence time, a custom criterion is defined in this work. The mean position 3D-RMSE is set as the threshold for each scenario and the average position error evolution is computed. When the error goes below the threshold, the solution is considered to be steady-state, and the convergence time is recorded. Figure 4.2 shows the behaviour of the position RMSE for a test case, where the RMSE position error computed over a time interval of half-year is shown as a function of the initial date of the time interval. After an initial large RMSE, the curves tend to flatten as steady-state approaches. This convergence time criterion is particularly suitable for this sensitivity analysis because a variable error in the measurements results in a variable steady-state RMSE. Therefore, defining a unique threshold to quantify whether the error has converged or not is reductive. With this approach, each test case has its relative threshold for defining steady-state achievement.

## 4.6. PARAMETERS UNDER ANALYSIS

The aim of this study is to investigate how two design parameters affect navigation performance. The first parameter is the LoS measurement error, which is the angular error of the measured direction to the observed body that is provided to the filter. This value depends on factors such as attitude determination performance (which is influenced by star tracker characteristics), image processing to compute the centre of the observed

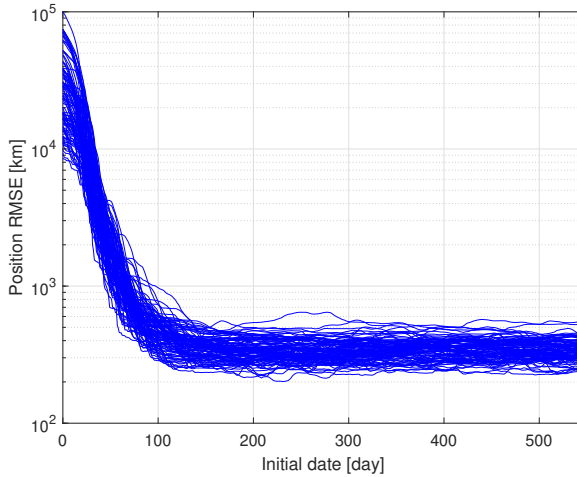


Figure 4.2: Position RMSE computed over a time interval of half a year, as a function of the initial date of the considered half-year time interval. Each line correspond to a simulation of the Monte Carlo. The scenario is a single tracking planet (P3), with a de-phasing angle equal to  $0^\circ$ . The observation error is 1 arcsec. Tracking frequency is 1 obs/day, and initial position and velocity errors are respectively  $10^5$  km and 0.1 km/s.

body and observation scenario, which is extensively explored in Chapter 5. Additionally, systematic errors such as mounting offset can also be considered. For the simulation, Gaussian noise is added to the computed azimuth and elevation, and the noise standard deviation  $\sigma_{los}$  varies from 0.1 arcsecs to 100 arcsecs, covering four orders of magnitude. Current small satellite star trackers typically offer attitude knowledge ranging from a few arcsecs to several tens of arcsec. However, these values are usually determined by onboard algorithms that need to balance estimation error and speed for real-time applications. For deep-space cruising applications, speed performance can be sacrificed to achieve lower estimation error, so a 0.1 arcsec error is also studied. This is done to understand what could be the navigation error impact of improving the current state-of-the-art technology performance, that is investigated later in Chapter 5.

The second parameter studied is the tracking frequency, which is the time interval between two subsequent observations provided to the filter. This parameter can be adjusted based on the navigation strategy, and operational and power requirements. The study aims to determine whether a higher frequency of observations improves the solution from a global and local perspective. Four tracking frequencies are selected: one observation every two days, one per day, two per day, and four per day. Higher tracking frequencies would be possible for onboard instrumentation, but in cruising scenarios are not required. Furthermore, in realistic scenarios, due to the slow dynamic of the heliocentric frame, two observations very close in time do not provide the filter significantly different information.



### 4.7. SEMI-ANALYTICAL GEOMETRY ANALYSIS

The performance of this technique heavily relies on the geometrical conditions, specifically the de-phasing and separation angles, as well as the distances between the objects. To evaluate the impact of these parameters on performance, the information matrix can be examined. The information matrix is defined as:

$$\Lambda = \sum_{k=1}^n \Phi^T(t_k, t_0) \mathbf{H}_k^T \mathbf{W} \mathbf{H}_k \Phi(t_k, t_0) \quad (4.27)$$

The previously defined observation matrix at time  $t_k$  is represented by  $\mathbf{H}_k$ , while  $\Phi(t_k, t_0)$  is the state-transition matrix, and  $\mathbf{W}$  is the weight matrix which is the inverse of  $\mathbf{R}$ . The covariance matrix  $\mathbf{P}$  is the inverse of  $\Lambda$  and its eigenvalue roots signify the axis of the error ellipsoid in its principal frame. This analysis compares the performance of different geometries based on these eigenvalues. As  $\mathbf{W}$  is a constant diagonal matrix with equal elements, it can be taken out of the sum, and the matrix computed and inverted for analysis is:

$$\tilde{\Lambda} = \sum_{k=1}^n \Phi^T(t_k, t_0) \mathbf{H}_k^T \mathbf{H}_k \Phi(t_k, t_0) \quad (4.28)$$

The matrix, which depends solely on the problem's geometry, can be evaluated for the entire simulation duration (assuming a tracking frequency of one observation per day). Subsequently, the eigenvalues of its inverse can be computed. It should be noted that the problem is nearly two-dimensional in a practical scenario, so in this analysis, it is assumed that the state vector consists of four components. For a 2D orbital problem with circular motion, the state transition matrix can be represented as:

$$\Phi(t_k, t_0) = \begin{bmatrix} \cos(n\Delta t) & 0 & \frac{\sin(n\Delta t)}{n} & 0 \\ 0 & \cos(n\Delta t) & 0 & \frac{\sin(n\Delta t)}{n} \\ -n \sin(n\Delta t) & 0 & \cos(n\Delta t) & 0 \\ 0 & -n \sin(n\Delta t) & 0 & \cos(n\Delta t) \end{bmatrix} \quad (4.29)$$

In this problem, the elevation angle is assumed to be zero, meaning that only the azimuth angle is observable. Moreover, the separation angle between the objects is kept constant throughout the simulation, which allows the observation matrix  $\mathbf{H}_k$  to be expressed as:

$$\mathbf{H}_k = \begin{bmatrix} \frac{r_1 \sin(\alpha_1 + n\Delta t) - r \sin(n\Delta t)}{r_{p1}^2} & -\frac{r_1 \cos(\alpha_1 + n\Delta t) - r \cos(n\Delta t)}{r_{p1}^2} & 0 & 0 \\ \frac{r_2 \sin(\alpha_2 + n\Delta t) - r \sin(n\Delta t)}{r_{p2}^2} & -\frac{r_2 \cos(\alpha_2 + n\Delta t) - r \cos(n\Delta t)}{r_{p2}^2} & 0 & 0 \end{bmatrix} \quad (4.30)$$

The matrix given above applies to the scenario where two bodies are observed and holds variables such as  $\alpha_1$  and  $\alpha_2$  (de-phasing angles with planets 1 and 2),  $r_1$  and  $r_2$  (planets heliocentric radii),  $r$  (spacecraft heliocentric radius), and  $r_{p1}$  and  $r_{p2}$  (spacecraft-planets distances). On the other hand, in the single-planet tracking scenario, this matrix reduces to the first row only. While the inversion of  $\tilde{\Lambda}$  is essential for this analysis, it has been demonstrated in Ma et al., 2016 that the single-planet tracking case is not entirely observable. This results in instability while inverting  $\tilde{\Lambda}$ , so a new definition is provided:

$$J = \frac{1}{\text{trace}(\tilde{\Lambda}_{\mathbf{UL}})} \quad (4.31)$$

The analysis focuses on quantifying the performance of different geometries by computing and inverting the  $\tilde{\Lambda}$  matrix. This matrix is based solely on the geometry of the problem and can be calculated for the entire simulation duration. The eigenvalues of its inverse provide information about the error ellipsoid's axis in its principal frame, which is used to compare the performance of different geometries. The analysis is performed on the upper-left 2x2 partition of  $\tilde{\Lambda}$ , denoted as  $\tilde{\Lambda}_{\mathbf{UL}}$ , to focus on the position estimation. The metric used to assess the performance of geometry is  $J$ , which is lower for more favourable geometries for line-of-sight navigation. The results in Figure 4.3 show that for a 1AU orbit, tracking planets with a lower semi-major axis leads to better estimates, despite the fixed relative geometry. However, this optimal observation scenario is difficult to achieve in real missions due to Sun illumination. In realistic scenarios where the geometry is not fixed, better estimates from the observation of inner planets are not only linked to a quicker measurement change but also to an intrinsic property of the technique.

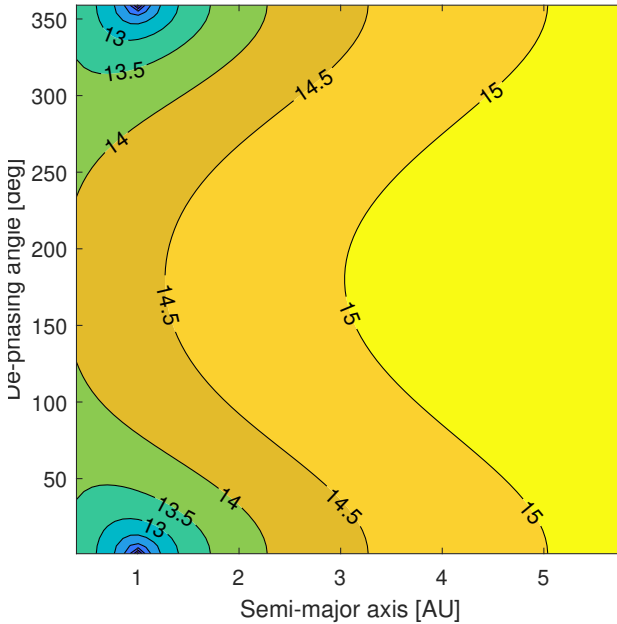


Figure 4.3:  $\text{Log}_{10}(J)$  as a function of the planet semi-major axis and the de-phasing angle for the single planet tracking scenario.

In contrast, in the case of double-planets tracking, the problem is fully observable, and the inverse of  $\tilde{\Lambda}$  can be computed easily. The sum of the eigenvalues of  $\mathbf{P}_{\mathbf{UL}}$ , denoted as  $\lambda_p$ , can be used to assess the impact of the geometry. Unlike the single-planet

tracking scenario, this case involves four varying parameters: the two semi-major axes and the two de-phasing angles. Therefore, to present the results, two parameters are fixed, while the influence of the other two is shown. Thus, three cases have been considered: observation of P1-P2, P2-P3, and P3-P4. The figures (4.4, 4.5, and 4.6) depict the results for these cases. The plots show that the larger error (represented by a high value in the plots) occurs when the separation angles are close to either  $0^\circ$  or  $180^\circ$  for all the scenarios. The separation angle cannot be observed directly from the plots, but it can be geometrically computed for the specific set of planets, given the two de-phasing angles. It can be observed that there are extensive regions with lower performance index  $\text{Log}_{10}(\lambda_p)$ , that are associated with more favourable observation conditions and a predicted lower estimation error. Contrarily, the plot regions associated with a larger performance index are smaller, highlighting that in the high majority of the scenarios, the observation conditions are favourable for LoS navigation.

4

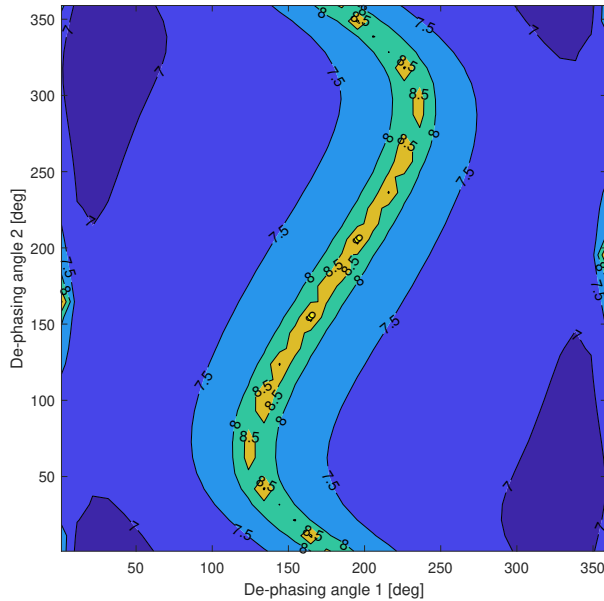


Figure 4.4:  $\text{Log}_{10}(\lambda_p)$  as a function of the de-phasing angles of P1 and P2.

#### 4.8. SENSITIVITY ANALYSIS

The upcoming subsections present the outcomes of the sensitivity analysis conducted on the LoS measurement error and tracking frequency. Initially, the focus is on the RMSE, followed by the analysis of convergence time.

The analysis of LoS measurement error demonstrates the influence of various noise levels in measurements. The tracking frequency is maintained at one observation per

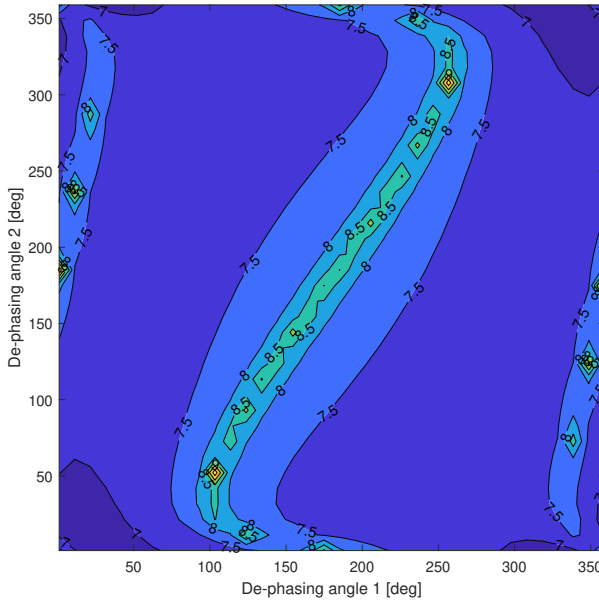


Figure 4.5:  $\text{Log}_{10}(\lambda_\rho)$  as a function of the de-phasing angles of P2 and P3.

hour, whereas the initial state error is sampled with a standard deviation of  $10^5$  km for position and 0.1 km/s for velocity. The initial position dispersion is chosen to be large due to two primary reasons. Firstly, it enables demonstrating the potential of LoS navigation to minimize the error even with poor initial conditions. Secondly, as demonstrated later in this chapter, only one test case has an RMSE larger than  $10^5$  km, thus enabling a fair comparison between the test cases. The initial velocity dispersion is selected to maintain the same ratio between the order of magnitude of position and velocity for a 1 AU orbit.

The analysis of tracking frequency aims to examine the impact of the number of observations in a given time interval. The LoS measurement error is maintained at 1 arcsec, while the initial position and velocity dispersion are again considered to be  $10^5$  km for position and 0.1 km/s for velocity, respectively.

#### 4.8.1. POSITION AND VELOCITY RMSE

To begin, the single-planet scenario is analyzed. Simulations are carried out for both  $\alpha = 0^\circ$  and  $\alpha = 90^\circ$  de-phasing angles. The choice has been made according to the results shown in Figure 4.3, because the former typically represents a scenario with lower RMSE, while the latter corresponds to a larger error scenario.

The outcomes are presented in figures 4.7 and 4.8. These plots illustrate how the steady-state RMSE for both position and velocity increases with the LoS measurement error. Specifically, for lower  $\sigma_{los}$  values, the position RMSE ranges from approximately

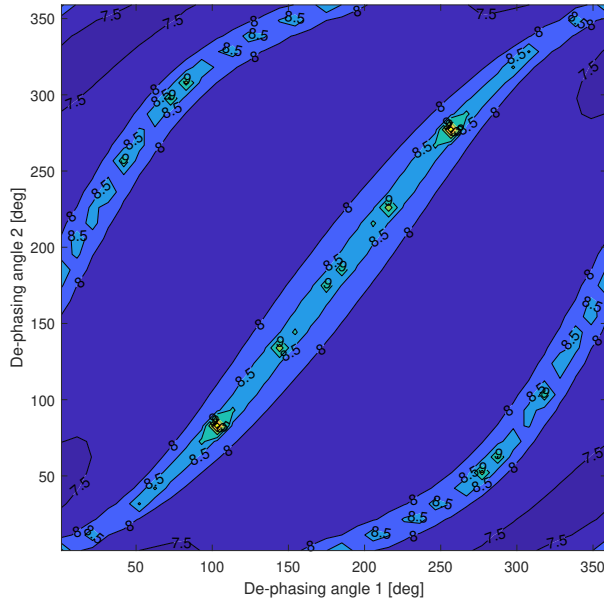


Figure 4.6:  $\text{Log}_{10}(\lambda_p)$  as a function of the de-phasing angles of P3 and P4.

70 km to 3199 km, while the velocity RMSE varies between 0.03 m/s and 0.62 m/s. Conversely, for larger  $\sigma_{los}$  values, the position RMSE ranges from approximately 2231 km to 246110 km, while the velocity RMSE spans from approximately 0.44 m/s to 47.9 m/s.

Eight combinations of planets, de-phasing angle, and separation angle are examined for the two-planet observation scenario. The optimal conditions are for a de-phasing angle near  $0^\circ$  and a separation angle near  $90^\circ$ , but for inner planets, it may not always be achievable. In each combination, the pair's inner planet is placed in an orbit with a de-phasing angle of  $0^\circ$ . Next, the P1-P2 pair is considered with a separation angle of  $50^\circ$ , which is nearly the maximum allowable by the geometry, which can be computed with Equations 4.1-4.3. For comparison, the other two pairs, P1-P3 and P1-P4, are considered with the same separation angle, while the remaining five combinations have a separation angle of  $90^\circ$ .

Like the single-planet tracking scenario, the impact of the observation error on the RMSE is presented in Tables 4.1 and 4.2, showing the mean RMSE of position and velocity, respectively, for each scenario, along with the standard deviation. Once again, there is a significant impact on the performance of the observation error, resulting in a position RMSE ranging from approximately 25-90 km in the lower error scenario and 2000-7000 km in the larger error scenario. For the velocity RMSE, the ranges are approximately 0.026-0.41 m/s and 0.4-1.3 m/s, respectively. Despite the apparent large difference between the position and velocity RMSE (which was also noted in the single-planet observation case), these results are consistent with the order of magnitude of the prob-

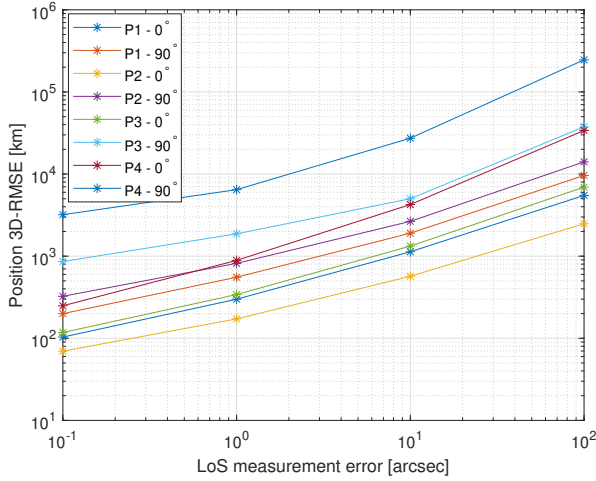


Figure 4.7: 3D position steady state RMSE as a function of the LoS standard deviation. Angles in the legend refer to the de-phasing angle.

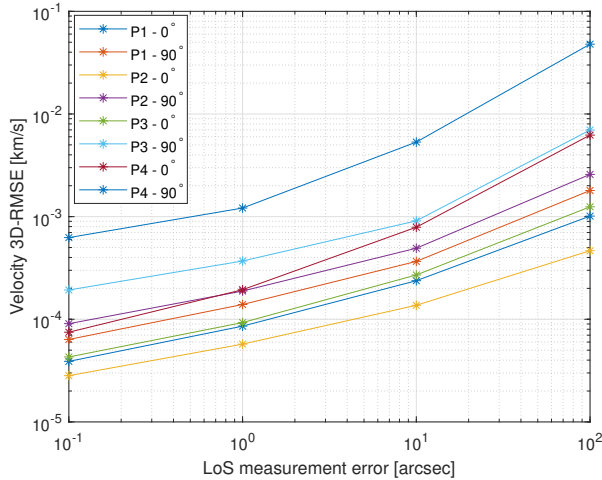


Figure 4.8: 3D velocity steady state RMSE as a function of the LoS standard deviation. Angles in the legend refer to the de-phasing angle.

lem since the position vector components are roughly in the order of  $10^8$  km, while the velocity ones are in the order of a few tens of km/s.

Furthermore, it is worth noting that tracking two planets instead of just one produces a systematic and significant improvement in performance. This can be seen especially by comparing the single-planet case of  $P4 - 90^\circ$  with the double-planet case of  $P2, P4 - 90^\circ$ , where the position RMSE of the former, with an observation error of 0.1

arcsec (approximately 3199 km), is greater than the position RMSE of the latter, with an observation error of 100 arcsec (approximately 2508 km).

Scenario	0.1 arcsec	1 arcsec	10 arcsec	100 arcsec
P1,P2 - 50°	25.87 (2.60)	142.26 (21.04)	664.45 (133.23)	3548.90 (1017.52)
P1,P3 - 50°	37.28 (4.18)	215.27 (40.57)	1020.27 (228.39)	4664.17 (1596.13)
P1,P4 - 50°	90.98 (19.28)	309.321 (45.09)	1078.14 (234.51)	5389.70 (1497.96)
P1,P3 - 90°	39.81 (5.56)	234.75 (42.47)	1068.23 (235.51)	5000.60(1593.57)
P1,P4 - 90°	84.95 (16.19)	311.44 (48.98)	1102.91 (232.68)	5420.52 (1515.73)
P2,P3 - 90°	33.99 (4.54)	180.00 (34.80)	555.01 (106.15)	2437.18 (599.17)
P2,P4 - 90°	78.53 (16.16)	191.83 (31.51)	574.71 (106.74)	2508.57 (709.41)
P3,P4 - 90°	89.40 (17.77)	362.67 (61.17)	1329.94 (311.21)	6931.25 (1923.71)

Table 4.1: Position mean and standard deviation RMSE [km] per scenario (two planets observation). The reported angle is the separation angle  $\beta$ . The first listed planet for each scenario has a null de-phasing angle with the spacecraft, while the second planet's de-phasing angle is computed according to Equations 4.1-4.3.

Scenario	0.1 arcsec	1 arcsec	10 arcsec	100 arcsec
P1,P2 - 50°	0.026 (0.002)	0.049 (0.006)	0.143(0.031)	0.659 (0.175)
P1,P3 - 50°	0.029 (0.002)	0.066 (0.014)	0.221 (0.050)	0.867(0.303)
P1,P4 - 50°	0.040 (0.005)	0.089 (0.013)	0.224 (0.049)	0.980 (0.277)
P1,P3 - 90°	0.030 (0.002)	0.071 (0.013)	0.232 (0.050)	0.914 (0.283)
P1,P4 - 90°	0.039 (0.005)	0.091 (0.015)	0.241 (0.054)	0.100 (0.317)
P2,P3 - 90°	0.026 (0.002)	0.062 (0.010)	0.147 (0.0266)	0.459(0.100)
P2,P4 - 90°	0.035 (0.005)	0.064 (0.010)	0.139 (0.027)	0.468(0.119)
P3,P4 - 90°	0.041 (0.005)	0.101 (0.019)	0.271 (0.062)	1.345 (0.368)

Table 4.2: Velocity mean and standard deviation RMSE [m/s] per scenario (two planets observation). The reported angle is the separation angle  $\beta$ . The first listed planet for each scenario has a null de-phasing angle with the spacecraft, while the second planet's de-phasing angle is computed according to Equations 4.1-4.3.

#### 4.8.2. CONVERGENCE TIME

The purpose of this subsection is to present the results regarding convergence time, specifically how fast the estimation error reduces. Nonetheless, before delving into the findings, some explanations are necessary. Although the notion of steady-state is clear-cut for the fixed-geometry scenario, and therefore the definition of convergence time is unambiguous, the same cannot be said for a practical setting. Figure 4.9 reports the comparison between the ideal P2-P3 case, with the observation of Mars-Venus in three different time intervals. As the plot shows, the fixed-geometry case result represents the asymptotic solution also in terms of convergence time. The best observation condition evolution (separation angle  $\beta = 90^\circ$ ) has a shorter convergence time compared to the other three position error evolutions, which present an oscillatory behaviour as the observation condition varies through time. The observation condition also influences the convergence time, as better measurements produce a quicker error decrease, as can be

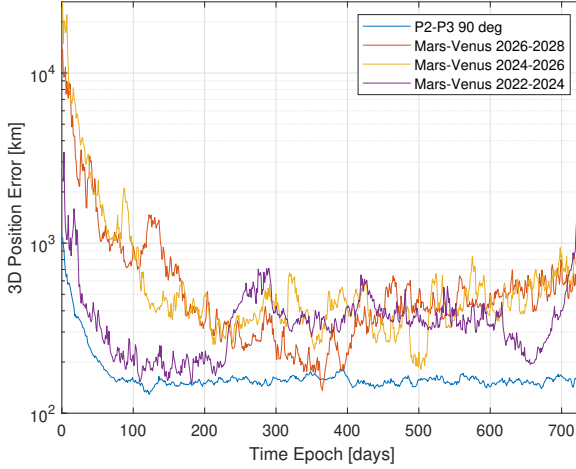


Figure 4.9: Position error comparison between P2-P3 case, with  $\beta = 90^\circ$ , and the observation of the pair Mars-Venus in three time intervals.  $\sigma_{los} = 1$  arcsec.

noticed by comparing purple lines with orange and yellow ones. The results presented in this subsection for the fixed-geometry simulation benchmark investigate these behaviours.

In the single-planet case, LoS measurement error significantly impacts the convergence time, as shown in Table 4.3. All scenarios exhibit a noticeable increase in convergence time as the observation error rises. When  $\sigma_{los} = 100$  arcsec, the 3D-RMSE for the  $P4 - 90^\circ$  scenario, as seen in Figure 4.7, is in the same order of magnitude as the initial guess error, making the calculation of convergence time inapplicable for this scenario.

Scenario	0.1 arcsec	1 arcsec	10 arcsec	100 arcsec
P1 - $0^\circ$	162	185	283	521
P1 - $90^\circ$	154	235	375	636
P2 - $0^\circ$	174	197	243	418
P2 - $90^\circ$	160	217	405	539
P3 - $0^\circ$	163	198	370	551
P3 - $90^\circ$	228	281	477	617
P4 - $0^\circ$	188	283	521	628
P4 - $90^\circ$	447	532	638	N/A

Table 4.3: Convergence time [days] per scenario (one planet observation) as a function of the measurement error. In the scenario column, the de-phasing angle is reported.

The results for convergence time in the double-planets scenario are presented in Table 4.4, and they demonstrate a similar trend as the single-planet tracking scenario. However, observing two planets results in faster convergence compared to the single-planet tracking case.



Scenario	0.1 arcsec	1 arcsec	10 arcsec	100 arcsec
P1,P2 - 50°	31	89	271	457
P1,P3 - 50°	50	121	314	491
P1,P4 - 50°	44	196	321	566
P1,P3 - 90°	39	102	300	604
P1,P4 - 90°	44	168	295	562
P2,P3 - 90°	44	104	213	434
P2,P4 - 90°	95	144	233	428
P3,P4 - 90°	69	191	343	553

Table 4.4: Convergence time [days] per scenario (two planets observation) as a function of the measurement error. The reported angle is the separation angle  $\beta$ . The first listed planet for each scenario has a null de-phasing angle with the spacecraft, while the second planet's de-phasing angle is computed according to Equations 4.1-4.3.

4

The results of the single-planet tracking scenario, presented in Table 4.5, demonstrate that the convergence time is impacted by the tracking frequency. The extent to which the convergence time drops with an increase in the tracking frequency varies across different cases. Nevertheless, it is apparent that the geometry of the problem plays a role in determining the convergence time, and generally, increasing the tracking frequency leads to faster convergence to the steady-state. Additionally, it is noteworthy that doubling the tracking frequency results in a reduction of the convergence time by several tens of days in many scenarios. This information is valuable for informing the navigation strategy based on mission requirements.

Scenario	0.5/day	1/day	2/day	4/day
P1 - 0°	202	185	175	141
P1 - 90°	244	235	170	167
P2 - 0°	198	197	176	133
P2 - 90°	276	217	186	175
P3 - 0°	230	198	167	142
P3 - 90°	346	281	245	216
P4 - 0°	376	283	221	191
P4 - 90°	588	532	478	444

Table 4.5: Convergence time [days] per scenario (one planet observation) as a function of the tracking frequency. In the scenario column, the de-phasing angle is reported.

The findings for the double-planets observation scenario are presented in Table 4.6. It can be observed that the steady-state is attained at a faster rate compared to the single-planet tracking scenario, even at lower tracking frequencies. For instance, in the double-planet scenario, the convergence time is below 230 days, whereas in the single-planet scenario, it is frequently longer. Increasing the tracking frequency by a factor of two results in a decrease in the convergence time by several tens of days, thereby resulting in a faster convergence in all test cases.

Scenario	0.5/day	1/day	2/day	4/day
P1,P2 - 50°	144	89	71	63
P1,P3 - 50°	168	121	75	59
P1,P4 - 50°	214	196	128	88
P1,P3 - 90°	188	102	91	61
P1,P4 - 90°	190	168	152	58
P2,P3 - 90°	132	104	57	50
P2,P4 - 90°	172	144	129	106
P3,P4 - 90°	226	191	147	96

Table 4.6: Convergence time [days] per scenario (two planets observation) as a function of the tracking frequency. The reported angle is the separation angle  $\beta$ . The first listed planet for each scenario has a null de-phasing angle with the spacecraft, while the second planet's de-phasing angle is computed according to Equations 4.1-4.3.

## 4.9. NAVIGATION FOR NEA MISSIONS

The results presented in the previous sections for the fixed-geometry simulation benchmark are useful to understand the intrinsic properties and characteristics of the navigation technique. In this section, the focus of the analysis is shifted towards more realistic mission scenarios, whose results are analyzed according to the results presented in previous sections. First, a Figure of Merit (FoM) available in the literature is used to confirm the geometry results already presented and to investigate the observation conditions for NEA missions. Later, two NEA mission scenarios are investigated, and their results are analyzed in accordance to the results of the fixed-geometry simulation.

### 4.9.1. NAVIGATION FIGURE OF MERIT

The geometry considerations for the case of observing two planets are combined into a FoM that measures the "quality" of an observation geometry (Franzese and Topputo, 2020). The FoM is mathematically defined as:

$$FoM = \frac{1 + \cos^2 \beta}{\sin^4 \beta} (\vec{R}_{p1} - \vec{R}_{p2})(L_2 + L_1)(\vec{R}_{p1} - \vec{R}_{p2}) \quad (4.32)$$

where:

$$L_k = I - \hat{r}_{pk}^T \hat{r}_{pk} \quad (4.33)$$

The FoM employed in this study to prioritize the NEAs' nodal passages during 2023-2033 decade for determining the most advantageous LoS navigation scenarios, comprises of a dyadic product of LoS vectors and a 3x3 identity matrix denoted as "I". It's important to note that the FoM alone does not establish a direct correlation with the projected navigation accuracy. Therefore, several test cases are evaluated to demonstrate the relationship between the FoM and the accuracy of navigation.

### 4.9.2. NEAS EPHEMERIS PROPAGATION

NEODyS-2<sup>1</sup> provided the ephemeris data for 26822 NEAs on 17-12-2020, which includes the orbital parameters for these objects. To simplify and expedite computation, a 2-body

problem dynamics is employed for propagating the ephemeris based on the Sun gravitational parameter, denoted as " $\mu_{sun}$ ", and the heliocentric spacecraft position, represented by " $r$ ". Although a high-fidelity dynamics model, accounting for gravitational disturbances of the planets and solar radiation pressure, can yield more precise results, the computation of FoM is not expected to vary significantly. Thus, for the preliminary analysis presented in this study, the 2-body problem approximation is deemed acceptable. The decade between 2023-2033 is of particular interest in this research for two reasons: firstly, it's focused on the near future to evaluate the technique's applicability for ongoing missions such as M-ARGO (Franzese et al., 2021). Secondly, larger propagation intervals tend to increase uncertainties in the propagated position due to simplified dynamics.

### 4.9.3. FOM COMPUTATION

After propagating the orbital parameters, the ascending and descending nodal passages are identified for each NEA, which are considered plausible encounter conditions for future missions as they lay on the Ecliptic and don't require costly change-of-plane manoeuvres. The FoM is then computed for each pair of visible planets at these nodal passages, based on a Sun exclusion angle that determines whether the planet is visible or not. The FoM is computed for a range of planets from Mercury to Saturn as these are more feasible to observe with CubeSat hardware. A total of 15 pairs of planets are possible, and the NEAs are ranked based on the minimum FoM at each passage among these pairs. The results are available on GitHub (<https://github.com/stphano/NEAs-ranking>).

The study analyzed a total of 265067 nodal passages, with the goal of identifying the lower FoM for each of them, and found that the best FoM per nodal passage ranges from  $10^{15}$  to  $10^{24}$ , with lower FoM corresponding to pairs of Mercury-Venus or Venus-Earth and higher FoM corresponding to scenarios where only Jupiter and Saturn are visible. Less than 1 percent of scenarios had no observable pairs, while almost 13 percent of cases had all planets visible, providing significant flexibility for mission planning. For 870 NEAs, the FoM was less than  $10^{16}$  at least once in the decade under analysis, and in these scenarios the lowest estimation error can be expected. The distribution of the minimum computed FoM for each nodal passage is shown in Figure 4.10, revealing that optimal observation scenarios repeat periodically through time, with the Mercury-Venus or Venus-Earth pair being the most favourable. Furthermore, in a ECLIPJ2000 reference frame, the distribution of the FoM is shown in a 2D space in Figure 4.11. It is apparent that there exists a specific ring where the observable geometry is not conducive to LoS navigation. Within this ring, there are still favourable geometries available, but increasing the distance from the ring enhances the FoM as the encounter points move closer to Jupiter.

### 4.9.4. NEAS FLY-BY MISSION EXAMPLES

The purpose of this section is to demonstrate the impact of a non-fixed geometry scenario, which was briefly discussed in the introduction of the previous section. The two NEAs fly-by missions selected for the test cases were designed using the JPL Small-Body Mission-Design Tool (NASA JPL, 2023), which provides access to a large dataset and al-

<sup>1</sup> <https://newton.spacedys.com/neodys/>

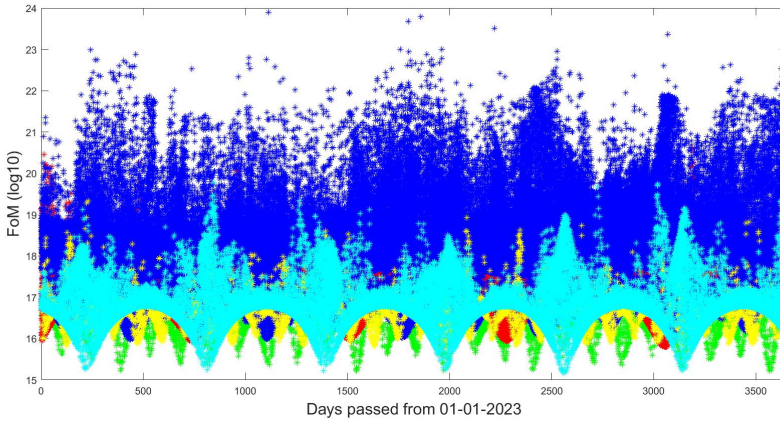


Figure 4.10: Distribution in time of the FoM through time. In green the pair Mercury-Venus, in red the pair Earth-Mars, in yellow the pair Mercury-Earth, in cyan the pair Venus-Earth, in blue the remaining pairs.

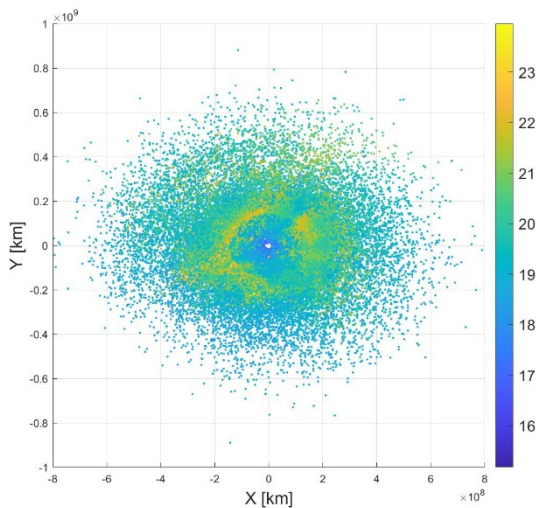


Figure 4.11: Spatial distribution of the best  $\log_{10}(\text{FoM})$ .

lows for the design of missions towards NEA targets. A high-thrust (ballistic) scenario was considered. Although the tool solved Lambert's problem and provided the departure and arrival dates for ballistic transfer from Earth to a certain NEA, it did not generate the trajectory, providing only the module of the excess velocity at departure, without directional information. Therefore, the trajectory was generated separately. The analysis was performed in an ECLIPJ2000 reference frame centred in the Sun. The heliocentric position of Earth was obtained from Spice Toolkit at the recommended departure date.

The position of the target NEA at the arrival date was obtained from the ephemerides generator of JPL Horizon (NASA JPL, 2023). Then, the ballistic trajectory was computed by separately solving Lambert's problem (Izzo, 2014). Once the departure velocity was computed, the initial condition of the spacecraft was assumed to be the same as Earth's position at the departure time and with the computed velocity from the solution to Lambert's problem. The two asteroids considered were 2008 UA202 and 2006 RH120, which had the lowest excess velocity and the lowest relative velocity at the encounter, respectively, computed by the JPL Small-Body Mission-Design Tool.

In the previous section, it is assumed that planets are visible throughout the simulation time frame, which is a strong assumption. While this assumption was made to investigate the intrinsic properties of the method, in realistic scenarios, the planet's visibility must be taken into account. The planet is generally not visible when the angle between the direction to it and the direction to the Sun, measured from the spacecraft, is smaller than the Sun exclusion angle. Each hardware, such as a camera or star-tracker, has its Sun exclusion angle, which depends on its characteristics, particularly the baffle. When the angle is lower, the instrument needs to be turned off because the sunlight can blind the sensor. For this analysis, a Sun exclusion angle of  $30^\circ$  has been chosen, based on star-tracker characteristics for CubeSat as highlighted in Chapter 2. This issue primarily concerns the observation of inner planets, which are also the best option for tracking to achieve lower error. Therefore, a smart tracking strategy involves observing inner bodies when possible and switching to outer bodies when the former are not visible. In the following test cases, this approach is used to define which planets to observe at each time epoch. The observation of the Earth is neglected in the next examples because the initial condition assumes that the spacecraft's position coincides with Earth's position, making the line-of-sight direction measured in the first portion of the simulation unrealistic. In a more detailed mission scenario, the initial condition should be coincident with the exit from Earth's sphere-of-influence. However, this is not the focus of this report. Additionally, the observability of the Earth in the first mission phases should be analyzed based on hardware characteristics, as the planet disk may not fit the camera field-of-view or may be too bright for the camera sensor, similar to the Sun. Additionally, as stated in previous section, the trajectory generation utilizes a more sophisticated model. Conversely, the filter's propagator utilizes a 2-body dynamics approach and accounts for planetary perturbations when their magnitude exceeds a specific threshold. This necessitates an expansion of the previously established  $\mathbf{F}$  matrix. To incorporate each planetary disturbance, the subsequent matrix must be appended to the lower-left  $3 \times 3$  section of  $\mathbf{F}$ :

$$\tilde{\mathbf{F}}_{\mathbf{k}} = \begin{bmatrix} -\mu_k \frac{(1-3\frac{x_{los,k}^2}{r_{los,k}^2})}{r_{los,k}^3} & 3\mu_k \frac{x_{los,k}y_{los,k}}{r_{los,k}^5} & 3\mu_k \frac{x_{los,k}z_{los,k}}{r_{los,k}^5} \\ 3\mu_k \frac{x_{los,k}y_{los,k}}{r_{los,k}^5} & -\mu_k \frac{(1-3\frac{y_{los,k}^2}{r_{los,k}^2})}{r_{los,k}^3} & 3\mu_k \frac{y_{los,k}z_{los,k}}{r_{los,k}^5} \\ 3\mu_k \frac{x_{los,k}z_{los,k}}{r_{los,k}^5} & 3\mu_k \frac{y_{los,k}z_{los,k}}{r_{los,k}^5} & -\mu_k \frac{(1-3\frac{z_{los,k}^2}{r_{los,k}^2})}{r_{los,k}^3} \end{bmatrix} \quad (4.34)$$

The higher fidelity model used for the trajectory generation assumes a cannonball SRP model, whose general parameters have been defined in previous section. For these test-cases, a 3U CubeSat is considered, with  $m = 4$  kg, and  $A = 0.03$  m<sup>2</sup> (assuming the large side of the CubeSat is completely facing the Sun).

Both light-time delay and velocity aberration are taken into account, following the procedure described in Karimi and Mortari, 2015.

Differently from the benchmark used in the previous section, the definition of steady-state behaviour is more complicated for a realistic mission scenario, as the changing geometry of the problem influences the behaviour of the estimation. In the next subsections, when the EKF provides low estimation error, it will be referred to as a 'pseudo' steady-state, meaning that the best estimation has been reached, but it is still subjected to small changes (in the order of few hundreds of km for  $\sigma_{LOS} = 1$  arcsec) due to variations of the geometry. Alternatively, this can be interpreted as reaching a local steady-state solution for the given instant geometry.

Results of the Monte Carlo simulation are presented as the evolution through time of the average position error, for a fixed LoS error ( $\sigma_{LOS} = 1$  arcsec), and initial position and velocity error sampled respectively within  $10^5$  km and 0.1 km/s.

#### TEST-CASE 1 - 2008 UA202

The trajectory generated by solving Lambert's problem is shown in Figure 4.12. The departure and arrival dates are respectively 22-07-2028 and 20-10-2029, so the ToF corresponds to 455 days. A full revolution around the Sun is needed to reach the target.

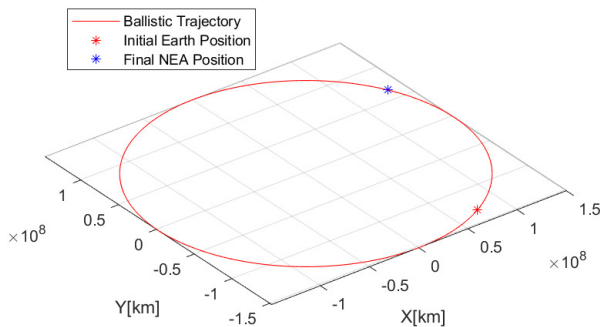


Figure 4.12: Ballistic trajectory towards 2008 UA202.

As already remarked, not all the planets are visible through the whole simulation time frame, because a certain Sun exclusion angle has to be guaranteed. Figure 4.13 shows that only Mars is constantly visible throughout the whole simulation, so following the inner planet tracking strategy, before simulation date 110 and after 360, the observed

pair is Venus-Mars, while in the middle is Mars-Jupiter.

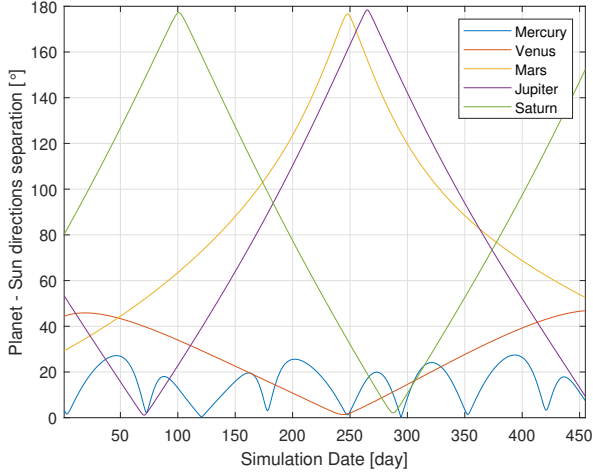


Figure 4.13: Angular separation planet LoS and Sun direction in the simulation timeframe for the trajectory towards 2008 UA202.

The results of the simulation are reported in Figure 4.14, where, for a fixed LoS error, the evolution of the position error is shown as a function of the simulation date for three tracking frequencies. On the other hand, the purple curve shows the evolution of the separation angle between the two observed planets. Discontinuities in the separation angle are due to changes in the observed pair of planets. The evolution of the position

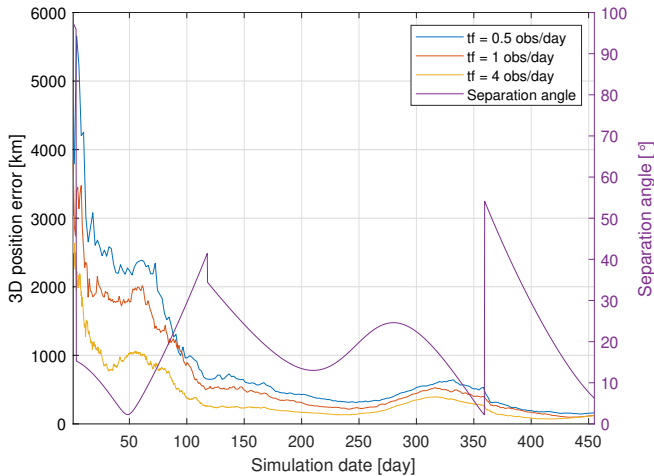


Figure 4.14: 3D position error evolution in the simulation time-frame for three tracking frequencies, and the separation angle evolution (trajectory towards 2008 UA202).

error can be described with the help of the results presented in previous sections. Concerning geometry, small separation angles produce larger errors. This can be noticed in the proximity of simulation date 50. In the simulation interval between dates 270 and 360, an error increase can again be noticed. However, the error peak is not reached at the minimum separation angle. This is because this simulation interval is also characterized by larger gravitational disturbances, that decrease around date 340. So the error around date 350 seems comparable to the error around date 300, despite a different separation angle. This test case is then useful also to highlight that the estimation error does not rely exclusively on the hardware characteristics, or observation strategy and geometry, but depends also on the actual dynamics and on the technique to account for gravitational disturbances in the navigation filter.

Moreover, it can be noticed that the observation of the pair Venus-Mars produces lower position error than the pair Mars-Jupiter, as predicted in previous sections, and as it is evident in the error decrease after the simulation date 360. As already mentioned, it is difficult to define the steady-state behaviour for a geometry-changing simulation, however, it is evident how a higher tracking frequency lets the position error decrease quicker (with a delay in the order of tens of days), however, when a pseudo-steady-state solution is reached, the tracking frequency does not impact significantly the error, as remarked before, and as it can be noticed at the end of the simulation. Finally, the position error at the end of the simulation (so at the NEA approach), is  $\sim 200$  km, as expected, where for the case P2-P3, with separation angle  $90^\circ$ , the RMSE was 180 km. Case P2-P3 is really similar to the observation Venus-Mars, and the larger error is due to a smaller separation angle. The error in the final phase of the simulation can be considered pseudo-steady-state, and this is because the medium-large ToF gives sufficient time to the EKF to produce an accurate estimation of the state.

#### TEST-CASE 2 - 2006 RH120

The trajectory to reach the NEA target is shown in Figure 4.15. The departure and arrival dates are respectively 26-05-2028 and 04-11-2028, with ToF = 162 days. This trajectory is shorter in time than the previous one, and a full revolution around the Sun is not achieved.

Figure 4.16 shows the angular separation of the planets, so following the same strategy, before simulation date 30 the observed pair is Jupiter-Saturn, after 30 and before 66 the observed pair is Mars-Jupiter, and then for the rest of the simulation, it is Venus-Mars. Similarly to the previous section, the results are presented in Figure 4.17, where the position error evolution for different tracking frequencies can be observed.

Analogous conclusions on the separation angle can be highlighted. However, differently from the previous case, the effect of a higher tracking frequency on the position error is in the order of some hundreds of km, because for this shorter ToF the EKF does not reach a pseudo-steady-state behaviour. This is also remarked by the error at the end of the simulation which oscillates between 500 and 1000 km (depending on the tracking frequency), which is larger than the error in the previous case, despite the same pair of planets being observed, even with a larger separation angle. This again shows how a higher tracking frequency is important to converge quickly to a better estimate, especially when the ToF is not sufficient to reach a pseudo-steady-state behaviour. So, depending on the mission positioning requirements, it may be necessary either to increase



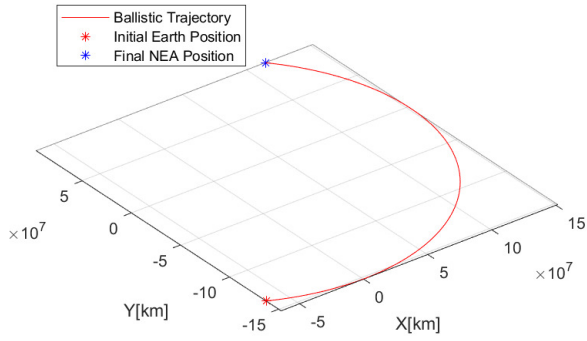


Figure 4.15: Ballistic trajectory towards 2006 RH120.

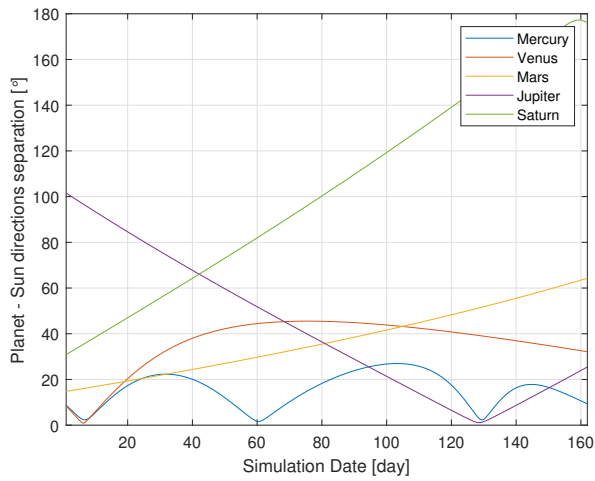


Figure 4.16: Angular separation planet LoS and Sun direction in the simulation time frame for the trajectory towards 2006 RH120.

the tracking frequency, or to improve the LoS measurement, either at the software or hardware level.

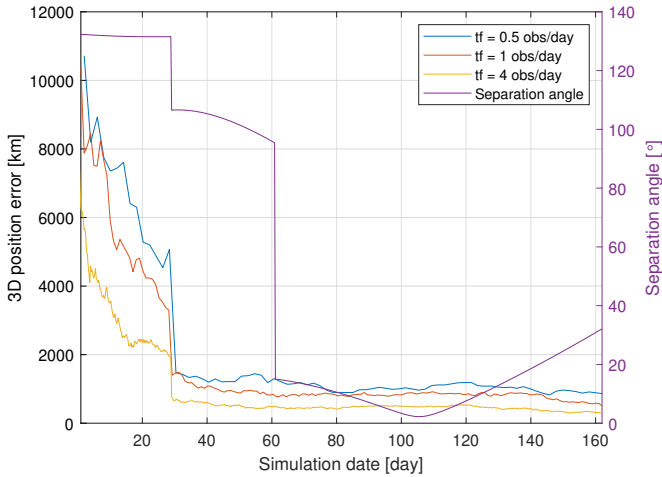


Figure 4.17: 3D position error evolution in the simulation time-frame for three tracking frequencies, and the separation angle evolution (trajectory towards 2006 RH120).

## 4.10. CONCLUSION

The chapter presented an analysis of the line-of-sight navigation technique for the state estimation of a deep-space spacecraft, with a particular emphasis on the impact of geometric and design parameters on performance. This work investigates the impact of both hardware-driven parameters (LoS measurement error), and navigation strategy parameters (tracking frequency) on two performance indicators, namely position/velocity RMSE and convergence time. At the same time, geometrical considerations are reported, showing the impact of the de-phasing angle, especially in the single tracking planet scenario, and of the separation angle, which is defined in the two tracking planets scenario. The analysis framework is based on a set of planets, which rotate around the Sun with the same orbital speed as the simulated spacecraft. With this approach, the intrinsic impact of the relative geometry can be highlighted, having a simulation which is not scenario dependent (specific spacecraft orbit, planets orbit, time-frame, etc.). The general results highlighted with this approach are then exploited in the description of two realistic NEA fly-by scenarios, showing how the considerations derived in a general framework are related to specific mission cases.

Concerning the geometry, the de-phasing angle analysis has shown a significant impact on the accuracy of the method. In general, it can be remarked that tracking a planet which lies on the same radial vector as the spacecraft is beneficial to the accuracy; this leaves room for further analysis on the use of fine or coarse Sun sensors, which appears to be of great interest, as their compact mass and volume can be easily integrated in CubeSat systems. For the two planets tracking case, also the separation angle plays an important role, as when it approaches  $90^\circ$ , the accuracy of the method increases.

Regarding the LoS measurement error, it largely influences both the performance of the method in terms of RMSE and convergence time. The RMSE does not scale down

with the same factor as the observation error (which scales with a factor of 10 in this analysis), but still exponentially. The convergence time decrease is evident with more accurate observations, as in almost all the considered scenarios, the convergence time (for a tracking frequency of 1 obs/day) is higher than 300 days for  $\sigma_{los} = 100$  arcsec, while it goes below 200 days for the majority of the scenarios with  $\sigma_{los} = 0.1$  arcsec. Moreover, comparing the results of the single planet and the two planets tracking, it is evident that both position and velocity RMSE, and convergence time improve significantly with the observation of two planets rather than one. So again, a LoS autonomous navigation system properly designed should always maximize the time during which two planets are observed.

On the other hand, the tracking frequency analysis shows a minor effect on the RMSE. While the convergence time is influenced by the tracking frequency, in fact increasing the tracking frequency from one observation every two days to four observations per day produces a decrease of the convergence time of at least 50 days in most scenarios, the position and velocity RMSE is not systematically affected. Convergence times in the order of hundreds of days suggest that to achieve a small estimation error at the end of the cruise, LoS navigation should be performed during a large portion of the transfer, eventually increasing the tracking frequency when the spacecraft is approaching the target.

As shown in the realistic mission scenarios, considering the accuracy at the end of the trajectory, larger ToF allows for relaxed requirements on LoS measurement error and tracking frequency, as the technique has 'sufficient time' to provide an accurate estimation, while for smaller ToF a higher tracking frequency or a lower LoS measurement error can be used to compensate the fact that the filter does not achieve the pseudo steady-state behaviour. The results shown for the NEA fly-by cases are analyzed and described by means of the general results obtained before.

These results demonstrate numerically that the current state-of-the-art CubeSat technology is sufficiently accurate to ensure the applicability of LoS navigation to deep-space cruising, as for  $\sigma_{los}$  in the range 10-100 arcsec, the 1000 km requirement position accuracy can be met, with an evident performance improvement in the two planets tracking case. These values are acceptable for many mission scenarios involving CubeSat cruising in deep-space, such as NEAs fly-by, as these position errors allow trajectory correction maneuvers achievable with micro-propulsion system technology (R. Walker et al., 2017). Moreover, achievable navigation accuracy is comparable to that of the CubeSat INSPIRE, whose estimated navigation accuracy is  $\sim 500$  km relatively close to the Earth, and  $\sim 1000 - 2000$  km further away, using the Iris X-band transponder inspire.

However, if the space application requires higher accuracy, achieving  $\sigma_{los} = 0.1$  arcsec would be particularly interesting in order to reduce drastically the RMSE, having an accurate autonomous navigation system in deep-space, but also to give more flexibility to the navigation strategy design, as it would allow quicker convergence to the steady-state. Still concerning the navigation strategy, increasing the tracking frequency would allow quicker convergence, but the price to pay in terms of operations and power requirements may not be always worth it, so trade-offs in each mission scenario are definitely suggested.

For these reasons, Chapter 5 is dedicated to investigating the algorithms and hard-

ware to retrieve measurements with a  $\sigma_{los}$  in the range 1-10 arcsec, in order to further analyze the applicability of the technique to real scenarios.



# 5

## DESIGN AND TESTING OF STAR-TRACKER ALGORITHMS FOR LINE-OF-SIGHT NAVIGATION

*E quindi uscimmo a riveder le stelle.*

Dante Alighieri - Inferno XXXIV, 139

*This chapter investigates the capabilities of exploiting optical line-of-sight navigation using star trackers, and it expands the analysis of Chapter 4 by going through the actual working principle of a star-tracker. First, a synthetic image simulator is developed to generate realistic images, which is later exploited to test the star-tracker's performance. Then, generic considerations regarding attitude estimation are drawn, highlighting how the camera's characteristics influence the accuracy of the estimation. The full attitude estimation chain is designed and analyzed in order to maximize the performance in a deep-space cruising scenario. After that, the focus is shifted to the planet-centroiding algorithm, with particular emphasis on the illumination compensation routine, which is shown to be fundamental to achieving the required navigation accuracy. The influence of the center of the planet within the singular pixel is investigated, showing how this uncontrollable parameter can lower performance. Finally, the complete algorithms chain is tested with the synthetic image simulator in a wide range of scenarios. The final promising results show that with the selected hardware, even in the higher noise condition, it is possible to achieve a direction's azimuth and elevation angles error in the order of 1-2 arcsec for Venus, and below 1 arcsec for Jupiter, for a spacecraft placed at 1 AU from the Sun. Finally, an integrated navigation simulation is derived, and the design of an AEKF is carried out to account for measurement behaviours, showing how the 1000 km position requirement can be met.*

---

Parts of this chapter have been published in Casini, Cervone, Monna, and Visser, [2023](#) and Casini, Monna, et al., [2023](#)

## 5.1. INTRODUCTION

Chapter 4 presented a high-level analysis of LoS navigation, where the navigation algorithm has been investigated imposing a certain Gaussian noise on the measurement. This approach is exploitable for preliminary analysis, but to go in-depth into the actual measurement behaviour, the functioning of the star-tracker, both at the hardware and algorithms levels, shall be investigated. This is the focus of Chapter 5.

The objective of this chapter is to review the current state-of-the-art star tracker algorithms for attitude determination and to design a complete estimation chain that maximizes performance in deep-space cruising scenarios. The chapter focuses on the performance of these algorithms in various deep-space missions. Together with attitude, the planet-centroiding algorithm is developed, paying particular attention to the Illumination Compensation (IC) algorithm. Attitude estimation and planet centroiding are intrinsically related in LoS optical navigation because measurements shall enter the navigation filter in the form of Azimuth and Elevation:

$$az = \operatorname{atan}\left(\frac{y_{los}}{x_{los}}\right) \quad (5.1)$$

$$el = \operatorname{asin}(z_{los}) \quad (5.2)$$

where  $x, y, z_{los}$  are the components of the unit vector pointing from the spacecraft to the observed object. This vector should be computed in a heliocentric frame because within the filter it is matched with the actual LoS, which can be easily computed in the same frame. So, planet centroiding computes the LoS vector in a camera frame, and this information shall be converted to a heliocentric frame to be used within the filter. This is done with the rotation matrix computed by solving the attitude estimation:

$$\vec{r}_{los}^h = R_b^h \cdot \vec{r}_{los}^b \quad (5.3)$$

where  $\vec{r}_{los}^h$  and  $\vec{r}_{los}^b$  are respectively the LoS vector in a heliocentric and body (or camera) frame, while  $R_b^h$  is the rotation matrix between them, obtained by solving the attitude estimation. Then, the algorithms are tested on a developed Space Image Simulator (SIS), implementing the characteristics of specific hardware, and the performance is highlighted.

This work is intended to fill the gap in the literature, as preliminary analysis has shown promising performance for the application of autonomous LoS navigation to real deep-space cruising mission scenarios. However, all of these studies considered out-of-the-loop the actual image processing and observation scenario, whose importance is shown in this chapter. In fact, these analyses assumed a constant standard deviation error on the measurement generation, based on star-tracker characteristics, which in reality is not the case. First, each planet has a different centroiding estimation error which is based on its observation characteristics. Secondly, even the same planet presents different estimation errors as a function of the actual observation scenario. So, this chapter is intended to pose the basis to perform image-in-the-loop navigation analysis, to further prove the feasibility of exploiting LoS navigation in real missions.

The chapter is organized as follows: first, the SIS is presented, focusing on the needed improvement for LoS navigation analysis. Also, the selected hardware (sensor and lens)

that is later used for performance analysis is presented. The decision to present these two pieces of work at the beginning of the manuscript is because they are exploited in the definition of appropriate algorithms, even before the complete testing. Later, the complete attitude estimation chain is evaluated and designed. Furthermore, the planet-centroiding algorithm, with IC, is developed. Finally, the SIS is used to generate a wide range of observation scenarios for Venus and Jupiter in order to test the full LoS extraction chain. The analysis has been limited to two representative planets allowing proper testing. To conclude the chapter, the image simulation and process to obtain measurements are coupled with navigation analysis, defining synthetic images-in-the-loop approach for testing, which led to the design of an AEKF as a navigation filter.

## 5.2. SPACE IMAGE SIMULATOR

The numerical results presented later in the text are obtained with the help of a space image simulator, that has been developed for this application. While the simulation of stars has been sufficiently consolidated, the simulation of planet images is not. This is especially the case when the planet disks are particularly small (e.g. the case of LoS optical navigation) and when blur is applied (e.g. the case of using star trackers).

### 5.2.1. STAR SIMULATION

The baseline to simulate stars in the FoV is inspired by Marin and Bang, 2020. The intensity of the stars (e.g. the number of readout electrons from the sensor) is calculated as a function of the sensor and lens system characteristics and of the visual magnitude of the star. The number of emitted photons is also a function of the given wavelength, and the conversion from photons to electrons is again a function of it since the Quantum Efficiency (QE) is wavelength-dependent. However, in this simulator, this is left out because the increased complexity would not add much to the analysis. The central V-band wavelength is selected ( $\lambda = 555.6$  nm). The number of photons (later converted to electrons) is calculated for a reference star ( $\alpha$ -Lyrae, with apparent magnitude 0.03 in the central V-band), and then each other star's photons number is computed by scaling as a function of the magnitude. Going briefly to it, starting with the Planck-Einstein equation, it is possible to express the number of electrons read by the sensor for  $\alpha$ -Lyrae as:

$$F_{e-} = 3.44 \cdot 10^{-8} \cdot QE \cdot \lambda \cdot T_{lens} \cdot \pi R_{lens}^2 \cdot \frac{BW}{c \cdot h} \cdot \tau \quad (5.4)$$

where the constant term is the emitting flux for the star at the chosen  $\lambda$ , QE defines the percentage of photons successfully converted into electrons,  $T_{lens}$  is the lens transmissivity which defines the percentage of photons passing through the lens,  $R_{lens}$  is the lens aperture radius, BW is the bandwidth,  $c$  is the speed of light,  $h$  the Planck's constant, and  $\tau$  is the exposure time.

In star trackers, lens defocusing is done on purpose in order to increase the accuracy of the star centroiding. As stars are at infinite distances, they can be considered point-source light emitters, which implies that their light may be focused on only one pixel. This of course limits the accuracy to the resolution of the pixel. It is common practice to blur the light information over several surrounding pixels, and with this approach, the



centroiding accuracy can reach a sub-pixel level. The simulator implements a Gaussian blurring function as:

$$I_{e-}(u) = \frac{1}{\sqrt{2\pi}\sigma_{PSF}} \cdot e^{-\frac{u-u_c}{2\sigma_{PSF}^2}} \quad (5.5)$$

where  $I_{e-}(u)$  is the distribution function of the electrons as a function of the  $u$ -component of the 2D sensor frame (same equation for the  $v$ -component),  $u_c$  is the  $u$ -component star center, and  $\sigma_{PSF}$  is the blurring radius. By integrating this function in both components for each pixel, it is possible to calculate the total fraction of the electrons hitting a particular pixel as a function of the actual center of the stars and the blurring radius. Once the number of electrons for each pixel has been calculated, the conversion to Digital Number DN can be approximated as:

$$DN = n_{e-|pixel} \cdot \frac{BitDepth}{Q_{sat}} \quad (5.6)$$

where  $n_{e-|pixel}$  is the number of electrons per pixel, while  $Q_{sat}$  is the pixel saturation capacity, which quantifies the maximum number of electrons that can be read out by the singular pixel. This conversion is based on the assumption that the maximum DN is associated with saturation. This is often not the case, as the maximum DN is usually associated with a slightly lower value. However to simplify the analysis, and as no CMOS datasheet reports this detail, it has been assumed like this.

The star 2D center location is another important parameter that needs to be computed. By assuming a Pinhole Camera model, the 3D unit vector can be converted into 2D sensor coordinates as:

$$u = \frac{u_{max}}{2} \cdot \frac{y}{x} \cdot \left(\tan \frac{a_h}{2}^{-1} + 1\right) \quad (5.7)$$

$$v = \frac{v_{max}}{2} \cdot \frac{z}{x} \cdot \left(\tan \frac{a_v}{2}^{-1} + 1\right) \quad (5.8)$$

where  $u_{max}$  and  $v_{max}$  are the horizontal and vertical pixel resolution,  $a_h$  and  $a_v$  are the horizontal and vertical FoV, and  $x, y, z$  are the three components of the star direction unit vector. The SIS may be further improved by including eventual distortions, however, for this analysis, a complete calibration has been considered, in order to focus on the important basic aspects.

### 5.2.2. PLANET SIMULATION

Once the star background has been simulated, attention can be devoted to representing accurately the planet. The approach presented in Christian, 2010 can be exploited and extended for this purpose. The method is a purely geometric approach which computes if a certain pixel is lighted by a certain surface point of the planet. This method works very accurately when the apparent angular size of the planet is sufficiently large that the pixel resolution can describe its shape. However, this approach does not provide directly a fraction of light per pixel, and for this reason, when the planet's apparent size is comparable to the size of the pixel, this method does not provide reliable information on how the light is spread over the pixels. For this reason, for the simulation, each pixel is divided

into a grid of subpixels. The number of subpixels can vary as a function of the apparent size of the planet. Figure 5.1 below shows the apparent size in arcsec of the planetary disks having an observer placed at a 1AU distance from the Sun. This distance has been chosen because this study is particularly interesting for NEAs exploration, which are defined as those asteroids whose perihelion is below 1.3 AU.

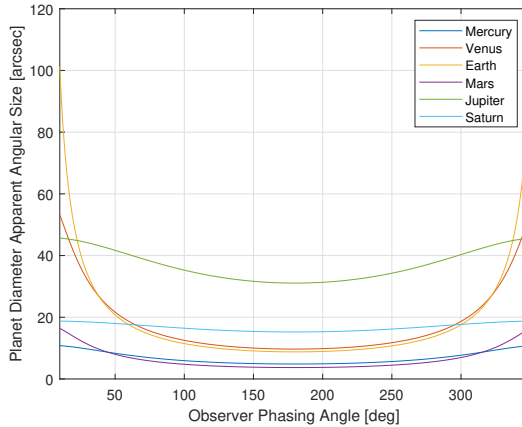


Figure 5.1: Planet's apparent diameter for an observer placed at 1 AU distance from the Sun. The angle between spacecraft and planet position vectors is defined Observer Phasing Angle.

The subpixel grid shall have a dimension which guarantees to represent the shape of the planet with sufficiently good accuracy. However, a large size of the grid impacts quite significantly the computational length. So, a compromise between the accuracy and computational load suggested choosing a grid of 200 x 200 for Venus. As it will be shown in the next subsection, the selected hardware has a pixel angular size of 67 arcsecs. Since 5.1 shows that the minimum observable radius for Venus is approximately 15 arcsecs, this selected grid allows to represent the shape of the planet with at least 45 subpixels, which is sufficient to describe the light distribution across different pixels. The apparent size of Jupiter is always above 30 arcseconds, meaning that a subgrid of 100 x 100 is sufficient to always describe the shape of the planet. With the subpixel grid, it is possible to simulate the illumination condition with sufficiently good accuracy and finally to blur the image. Once the image has been blurred, the subpixels are summed up in order to compute the percentage of total electrons that hits each pixel. This is still not sufficient to calculate the intensity of the pixel. To do so, it is possible to calculate the apparent visual magnitude of the planet following the approach reported in Mallama and Hilton, 2018, and then, similarly to the process used for stars, this value is converted first into the number of electrons, and finally to DN. The basic equation to approximate the apparent magnitude of a planet as a function of the illumination condition is:

$$V = 5 \log_{10}(rd) + V_1(0) + c_1 \alpha + c_2 \alpha^2 + \dots \quad (5.9)$$

where  $r$  is the planet's distance from the Sun,  $d$  is the observer distance, and  $\alpha$  is the illumination phase angle. Each planet is characterized by its own coefficients mostly

based on Earth on ground observation. Venus apparent magnitude can be computed as:

$$V = 5 \log_{10}(rd) - 4.384 - 1.044 \cdot 10^{-3} \alpha + 3.687 \cdot 10^{-4} \alpha^2 - 2.814 \cdot 10^{-6} \alpha^3 + 9.938 \cdot 10^{-9} \alpha^4 \quad (5.10)$$

$$V = 5 \log_{10}(rd) + 236.05828 - 2.8191 \alpha + 8.39034 \cdot 10^{-3} \alpha^2 \quad (5.11)$$

where the first equation refers to illumination phase angles below  $160^\circ$ , while the second for larger values.

Similarly, Jupiter's apparent magnitude can be approximated as:

$$V = 5 \log_{10}(rd) - 9.395 - 3.7 \cdot 10^{-4} \alpha + 6.16 \cdot 10^{-4} \alpha^2 \quad (5.12)$$

$V = 5 \log_{10}(rd) - 9.428 - 2.5 \log_{10}(1.0 - 1.507 \cdot \frac{\alpha}{180} - 0.363 \cdot (\frac{\alpha}{180})^2 - 0.062 \cdot (\frac{\alpha}{180})^3 + 2.809 \cdot (\frac{\alpha}{180})^4 - 1.876 \cdot (\frac{\alpha}{180})^5)$  where the first equation applies to the illumination phase angles below  $12^\circ$ . Figures 5.2a and 5.2b show the apparent magnitudes of Venus and Jupiter as a function of the illumination phase angle and of the distance planet-observer. The range of distances has been chosen for each of the two planets considering an observer placed at a distance of 1 AU from the Sun. It is important to remark that the star tracker is usually associated with a Sun-exclusion angle (as discussed in Chapter 4), so part of these phase angle-distance combinations is not actually observable. This depends especially on the characteristics of the hardware, and it usually applies on a larger scale to inner planets. The change of slope in the Venus plot is related to the transition between the Equations 5.10 and 5.11. This phenomenon is associated with forward scattering by liquid droplets in Venus' atmosphere Mallama and Hilton, 2018.

5

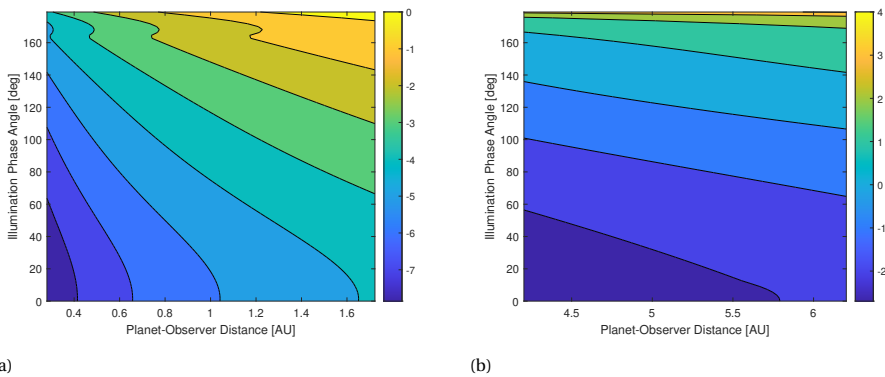


Figure 5.2: Venus Apparent Magnitude as a function of Observer distance and  $\alpha$  5.2a. Jupiter Apparent Magnitude as a function of Observer distance and  $\alpha$  5.2b.

### 5.2.3. HARDWARE SELECTION

The space image simulator needs as input the characteristics of the sensor and the lenses, which define the range of performance of the algorithms later described in the chapter. There is a wide range of CMOS sensors available on the market, however, not always the datasheet is complete enough for simulations following the approach described above,

especially because of the background noise description. Moreover, space applications require stricter requirements in terms of testing and validation, especially connected to radiation. For this reason, for this analysis and application, the attention has been focused on the TELEDYNE EV76C660<sup>1</sup>, as it is a CMOS sensor developed and tested for space applications. Moreover, its datasheet is particularly detailed and offers noise performance in two different scenarios, which allows seeing how the noise impacts the accuracy of the algorithm. The details of the sensor are reported in Table 5.1.

Resolution	1280 x 1024 [pixels]
Pixel Size	5.3 x 5.3 [ $\mu$ m]
Bit depth	10 [bits]
Qsat	8.4 [ke-]
Dark signal @25C	31 [LSB/s]
Dark signal @65C	600 [LSB/s]
QE @ 400-700 nm	0.6-0.8

Table 5.1: TELEDYNE EV76C660 main characteristics

Some remarks are necessary. Quantum Efficiency has been assumed constant to 0.8. The QE profile as a function of the wavelength is reported in the datasheet. For  $\lambda > 450$  nm, QE is above 70%, while for  $\lambda = 500$  nm, it is around 80%. Regarding noise, the dark signal is usually associated with a combination of factors, some of which can't be completely modelled. As the majority of dark current is dependent on the thermally induced electrons, this process can be associated with a Poisson distribution. Again, this is only an assumption and a full characterization of the sensor when it comes to real testing is required. Moreover, the datasheet reports also Dark Signal Non-Uniformity (DSNU), which characterizes a different response of every single pixel, related to various aspects such as manufacturing. For example, some rows or columns may be brighter than others. However, this is a complicated value to be translated in a simulation, as the mean value reported in a datasheet does not really offer information on how the non-uniformity is distributed across the sensor. For this reason, in this analysis, it is neglected, but if hardware-in-the-loop testing is possible, it will be important to characterize it.

The chosen lens is the MVL16M23<sup>2</sup>, as it is compatible with a sensor with form factor 1/1.8", and because it allows having a vertical FoV of approximately 20°, which is compliant with the application, as the final goal is to implement these algorithms for deep-space missions. Usually, these are associated with cruising in the same plane as the ecliptic. Implementing a passive navigation strategy is based on avoiding or limiting the re-orientation of the satellite to observe visible bodies. So, in order to maximize the observability time length, the camera's boresight direction should lay in the ecliptic plane. Then, a vertical FoV of at least 20° ensures that Venus' elevation is never outside the FoV. In fact, Venus' orbit presents an inclination of 3.39°. Figure 5.3 shows the evolution of Venus' elevation with respect to the ecliptic, considering an observer coincident with the Earth. Moreover, and this is clear, the larger the FoV, the larger the number of stars that can be detected, but this will be discussed in the next section.

<sup>1</sup> <https://imaging.teledyne-e2v.com/products/2d-cmos-image-sensors/ruby-1-3m-ev76c660-ev76c661/>,

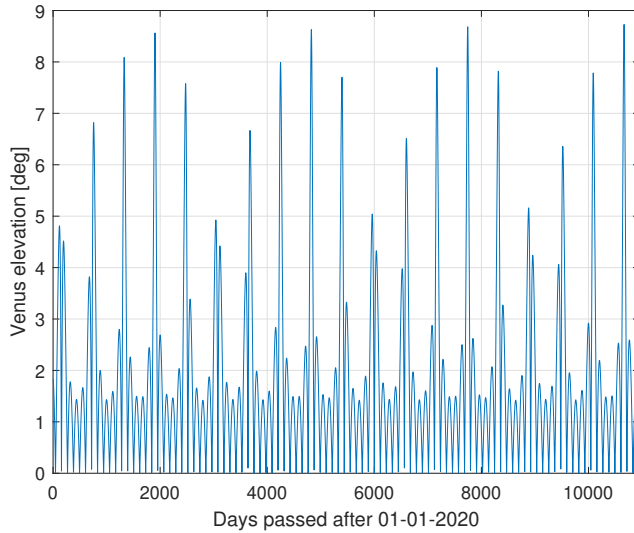


Figure 5.3: Venus' elevation angle as a function of time

The characteristics of the lens system are reported in Table 5.2. The transmissivity value is averaged in the considered bandwidth.

Focal length	16 [mm]
Aperture diameter	f/1.4 [mm]
Transmissivity @350-750 nm	0.8

Table 5.2: MVL16MR characteristics

### 5.3. ATTITUDE ESTIMATION CHAIN DESIGN

The design of star tracker algorithms for attitude estimation is a topic that has been widely investigated in recent years. The complete attitude estimation chain can be divided into fundamental intermediate steps: star detection, centroiding, star identification, and rotation matrix estimation. During the stars detection process, the 2D image is scanned, looking for bright pixels that can be associated with the presence of a star. It is common practice to associate with a pixel the presence of a star when its DN is larger than the mean DN of the dark background plus five times its standard deviation (Liebe, 2002). In addition, to reduce the number of operations, a pixel is saved as a candidate star if its DN is larger than its neighbouring pixels' DN. However, this is a limitation for those stars that can saturate more than one pixel, but they are so few that they can be treated separately. For all the candidate stars, the centroid needs to be computed. The

<sup>2</sup> <https://www.thorlabs.com/thorproduct.cfm?partnumber=MVL16M23>

centroiding is the process of analyzing the intensities of pixels belonging to a candidate star to define as accurately as possible the location of the center within the brightest pixel. Once a list of candidate stars' centers has been defined, 2D coordinates shall be associated with an ID of a star. This process is usually done by matching some angular characteristics of star patterns with a precomputed matching catalogue, stored onboard. Finally, the rotation matrix between the inertial and body reference frames can be computed, by solving the well-known Wahba's Problem (WP) (Wahba, 1965), which is meant to minimize the following index:

$$J(R) = \frac{1}{2} \sum_{k=1}^N \|w_k - Rv_k\|^2 \quad (5.13)$$

where  $N$  is the number of measurements,  $w_k$  are the inertial reference vectors,  $v_k$  are the measured directions in the body frame, and  $R$  is the rotation matrix from the body to the inertial frame, which characterizes the attitude of the spacecraft.

In the following subsections, each intermediate step is analyzed in order to define the most appropriate algorithm as a function of the mission scenario. In fact, the deep-space cruising navigation scenario does not require necessarily high-speed algorithms, which are on the other hand needed for attitude determination systems of satellites devoted to Earth observation or communication. So speed performance can be partially sacrificed if this implies higher attitude estimation performance which directly reflects in better navigation performance. As shown in Chapter 4, the LoS measurement error is the trigger parameter for navigation accuracy. For this reason, for the algorithms selection process, improved accuracy will be the final objective.

### 5.3.1. CENTROIDING ALGORITHM SELECTION

Before diving into the definition of the most appropriate algorithm for computing the center of a star, it is interesting to analyze how different parameters impact the accuracy of the attitude estimation. First, it is possible to relate two important parameters: the accuracy of the 3D unit vector of a star and the number of stars in the FoV. Figure 5.4 shows the behaviour of the cumulative attitude estimation error, defined as the sum of roll, pitch, and yaw angle errors, as a function of the number of stars in the FoV and the error on the 3D unit vector. It can be highlighted that to obtain a performant attitude estimation system (e.g. well below 50 arcsecs), the number of stars should be at least 15, and the angular error possibly below 5 arcsecs.

Concerning the number of stars in the FoV, this is highly dependent on both the actual FoV, and the limiting magnitude defined by the hardware characteristics. Figure 5.5 shows the number of stars in the FoV, for an observer placed on the Ecliptic with the camera's boresight in the same plane, as a function of the azimuth of the boresight direction, for the vertical FoV of the camera system considered in this dissertation. For example, with a limiting magnitude of 6, the minimum number of stars in the FoV is around 15, which is compliant with our previous requirement.

Finally, also the pixel size plays a role, as shown in Figure 5.6. Clearly, the lower the pixel size the lower the error in the 3D unit vector with the same 2D error in pixel units. As the plot shows, for a 5 micron pixel size, it would be optimal to have a centring error below 0.05 pixels. In this work, two centroiding algorithms are analyzed. The first is the

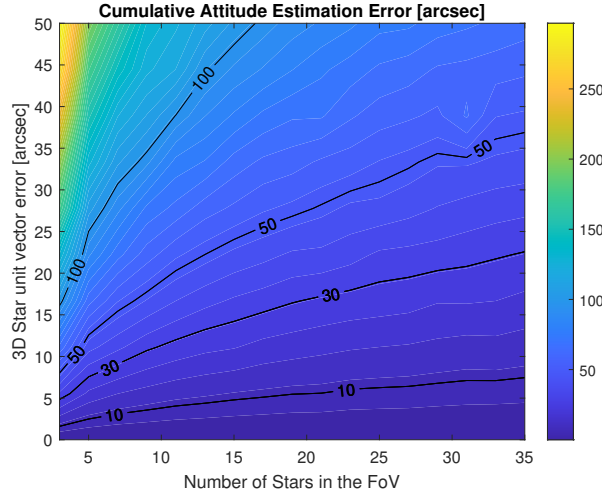


Figure 5.4: Cumulative Attitude Estimation error as a function of the number of stars and 3D unit vector error.

5

standard center-of-gravity (CoG) method. The center is defined as:

$$u_c = \frac{\sum_{k=1}^n \sum_{j=1}^n I(u_k, v_j) \cdot u_k}{\sum_{k=1}^n \sum_{j=1}^n I(u_k, v_j)} \quad (5.14)$$

where  $u_c$  is one of the 2D coordinates,  $I(u_k, v_j)$  is the DN of the pixel,  $u_k$  is one of the pixel coordinates, and  $n$  is the size of the Region-of-Interest (ROI). A specular equation can be derived for  $v_c$ . This is always the quickest method, however, it is usually associated with lower centroiding performance.

The second is a Least Squares Fitting Method (LSFM). For each component ( $u, v$ ), the process is the following. First for each row or column in the ROI, a marginal is defined as:

$$I_{m,u_i} = \sum_{j=-nb}^{nb} I(u_i, v_j) \quad (5.15)$$

where  $I(u_i, v_j)$  is again the intensity of a given pixel, while  $nb$  is the radius of the ROI, considering  $I(u_0, v_0)$  as the central pixel. Then, the Least Squares Problem is formulated as:

$$S(\beta) = \sum_{i=-nb}^{nb} (I_{m,u_i} - f(u_i, \beta))^2 \quad (5.16)$$

where  $\beta = (a, u_c, \sigma_u)$  is the vector containing the unknown parameter, including the center of the star. The function  $f$  corresponds to the Gaussian blurring, and can be written as:

$$f(u_i, \beta) = ae^{-\frac{(u_i - u_c)^2}{2\sigma_u^2}} \quad (5.17)$$

To solve for the center of the star ( $u_c, v_c$ ) the Levenberg-Marquardt algorithm can be used.

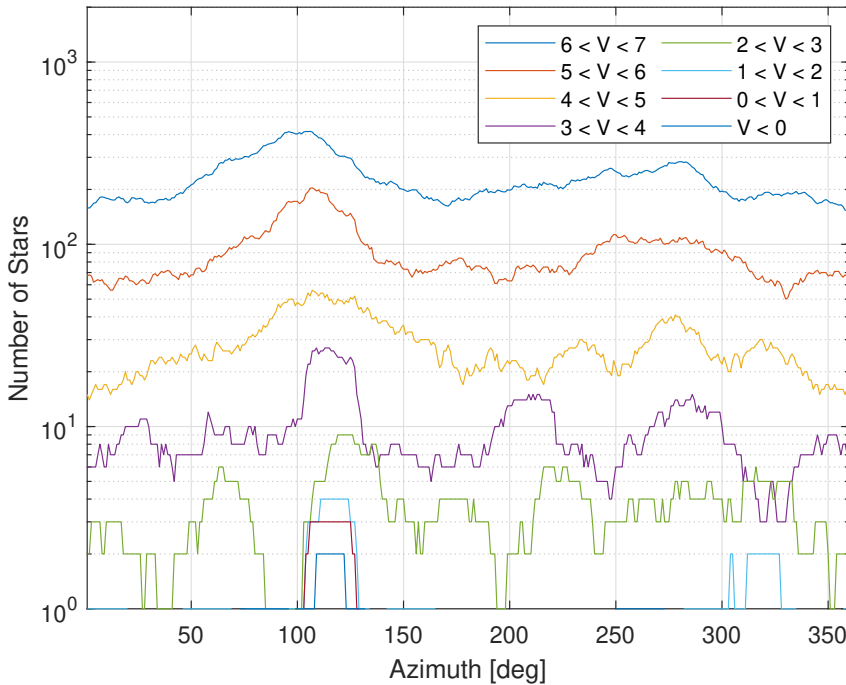


Figure 5.5: Number of stars in the camera's FoV as a function of the boresight azimuth angle, for different apparent visual magnitudes  $V$ .

For this analysis a  $3 \times 3$  ROI has been selected, as for many star magnitudes, the noise would be predominant in outer pixels, risking to lower the accuracy. However, larger ROI ( $5 \times 5$ ) in low noise conditions could be an option.

To compare the two centroiding algorithm, the intrinsic properties are explored by removing the background dark current noise and testing the algorithms on the actual number of electrons read by the detector (following the approach defined in section 2). In this way, also the quantization noise is removed from the analysis.

Figures 5.7a and 5.7b show the error as a function of the intensity of the star and the  $\sigma_{PSF}$  for the two methods. The CoG method has an optimal spreading radius around 0.5 pixel, while LSFM has a larger dependency on the magnitude. Comparing the two, it is clear that the LSFM offers better centroiding performance, for a wide range of radius, so it is the selected algorithm for the chain. Moreover, for the rest of the analysis the blurring radius is set to 1 pixel.

### 5.3.2. STAR IDENTIFICATION

Star Identification is the process of associating an ID to each spotted star in the image, so that later on the unit vector can be compared to their corresponding inertial ones to estimate the rotation matrix. Through the years, this has been sufficiently investi-



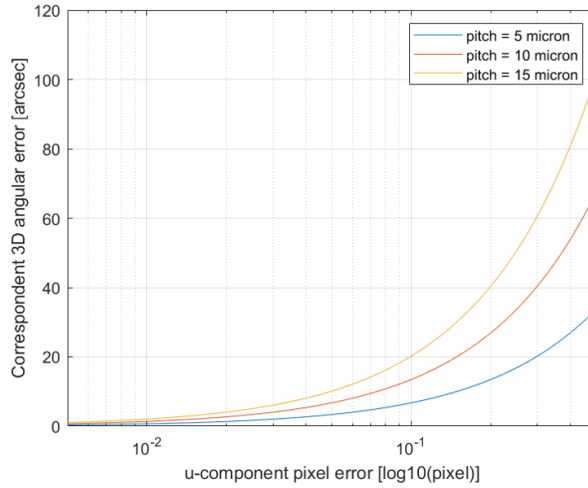


Figure 5.6: 3D angular vector as a function of the 2D u-component error in pixels.

5

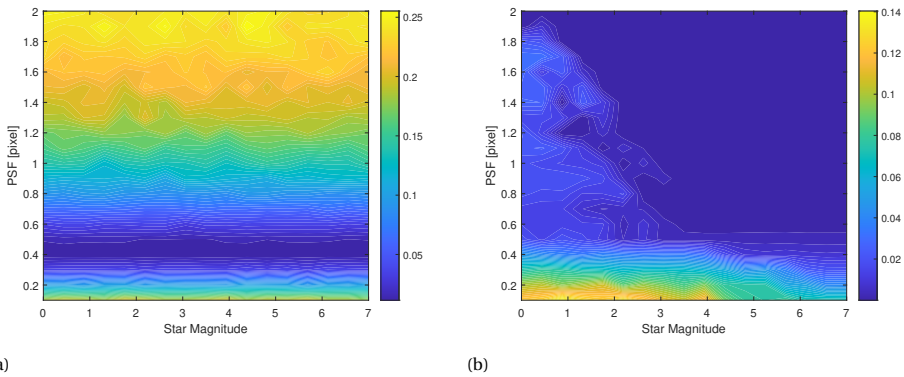


Figure 5.7: CoG centroiding error [pixel] as a function of star magnitude and PSF radius 5.7a. LSF centroiding error [pixel] as a function of star magnitude and PSF radius 5.7b

gated and consolidated. There is a wide range of identification algorithms, ranging from brightness based, to neural networks, up to the most common ones based on geometric features matching. Surveys of methods can be found in Spratling and Mortari, 2009 and Rijlaarsdam et al., 2020, comparing the advantages and disadvantages of various algorithms depending on the scenarios where the spacecraft is operating. An example is given by the algorithm proposed in Schiattarella et al., 2017, which is characterized by a large number of false stars, so robustness against falsely detected stars is needed. In general, together with robustness, speed and matching catalogue size are the parameters that shall be investigated to select the most appropriate algorithm. In this application, as remarked in previous sections, speed is not a priority for the cruising perse,

but catalogue size and robustness are. A triangle-based matching algorithm has been developed because of its robustness and limited catalogue size, which is fundamental in this application considering that planetary ephemerides shall be stored as well on-board. Another option would have been a Polestar algorithm (Silani and Lovera, 2006), or one of its derived methods, however, the increase in robustness is not worth a sufficiently larger catalogue (as both pattern and geometric characteristics catalogues shall be built). Moreover, even if speed is not the main trigger for the selection, the Polestar in the original paper has been proved to be six times slower than a triangle matching method based on the original Liebe's algorithm (Schwarz, 2015). The triangle matching method exploited in this work is an extension of the algorithm presented in Visser, 2017. The method is based on defining three geometrical quantities characterizing a triplet of stars, Figure 5.8. The central star defines an angle  $\gamma$  with its two neighbouring stars.

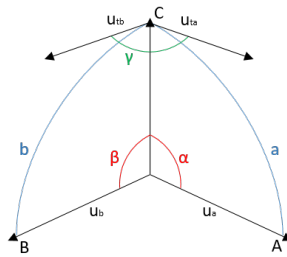


Figure 5.8: Stars triplet geometrical features.

Then the angular distances between the central star and the two neighbors can be used. However, despite in the original Liebe's method the 2D projections being used, in Visser, 2017 it has been found that defining 3D quantities can help the distribution of the catalogue to be uniform and being more precise. So Figure 5.8 shows the 3D formulation of the star triplets. First,  $\sin(\alpha)$  and  $\sin(\beta)$  can be defined as:

$$\sin(\alpha) = \|\vec{u}_a \times \vec{u}_c\| \quad (5.18)$$

$$\sin(\beta) = \|\vec{u}_b \times \vec{u}_c\| \quad (5.19)$$

Then, the definition of  $\gamma$  is slightly more challenging, and it starts by defining:

$$\vec{y}_{ta} = \vec{u}_a - \vec{u}_c(\vec{u}_a \cdot \vec{u}_c) \quad (5.20)$$

$$\vec{y}_{tb} = \vec{u}_b - \vec{u}_c(\vec{u}_b \cdot \vec{u}_c) \quad (5.21)$$

and finally:

$$\gamma = \text{atan2}(\|\vec{u}_{ta} \times \vec{u}_{tb}\|, \vec{u}_{ta} \cdot \vec{u}_{tb}) \quad (5.22)$$

To build the onboard catalogue, only stars with minimum brightness 6 have been considered. If magnitude 7 was considered as the limit, the catalogue would have been trice larger, however in the magnitude range 6-7 usually stars are not always recognizable with a larger noise. Moreover as shown in Figure 5.5 there are always at least 15 stars with a magnitude below 6 in the FoV. The other parameter to be set is the number of

neighbour stars with which a pattern is computed and recorded in the catalogue. Again a compromise for the length of the catalogue is to have 12 close stars, which leads to 66 triplets for each star, which leads to a catalogue length of 300894 patterns.

For identification, each triplet of stars can be arranged in six different combinations. All the combinations are compared to the catalogue, and for those, the ID of the stars composing the triplet that has the better match are recorded. To match a pattern  $\gamma$ ,  $\sin(\alpha)$ , and  $\sin(\beta)$  shall be within a threshold. Then, if multiple patterns are matched, the one with the lowest Root-Mean-Square (RMS) is recorded as a candidate. Finally, for each candidate star, the assigned ID is the one with more hits, if they are at least three.

### 5.3.3. WAHBA'S PROBLEM SOLVER

Once a sufficient amount of stars has been identified, the process of comparing the 3D unit vectors of those stars, with their heliocentric ones is used to find the rotation matrix, and therefore to estimate the attitude. To solve the WP, several algorithms have been presented: Davenport-Q, Quest, SVD, and many more (Spratling and Mortari, 2009). The SVD method is consolidated as it gives the best possible accuracy, together with numerous other advantages such as its stability and the possibility of providing the expected accuracy.

First, the matrix  $N$  is defined as:

$$N = BR^T = \sum_{k=1}^n v_k w_k^t \quad (5.23)$$

which can be decomposed with an SVD as:

$$N = U\Sigma V^T \quad (5.24)$$

and finally, the optimal rotation matrix can be found as:

$$R_{opt} = U[1, 0, 0; 0, 1, 0; 0, 0, \det(UV)]V^T \quad (5.25)$$

## 5.4. PLANET CENTROIDDING

Planet centroiding is the process of determining the center of the planet imaged on the sensor. As shown in the previous section, planets are significantly brighter than the average star, which means that with the same exposure time, the pixels can saturate more easily. So, counterintuitively, the blurring is helping also planets, despite their discrete apparent size, as the central pixels will be often saturated. For planet centroiding, again two macro-categories of algorithms are possible. A basic CoG algorithm is the easiest to be implemented, while a fitting method, similar to the one implemented for star centroiding, is slightly more difficult. This is because, for point-source light information, a simple relation can be established between the pixel intensity and the center. For a discrete element like a planet, this function is a combination of two functions: the shape function and the blurring function. To have an accurate solution, in the fitting process, the planet shall be discretized in a sufficient number of point-source emitters, which makes the algorithm computationally expensive. On the other hand, a CoG method, in combination with the blurring, offers sufficient performance when the full disk is visible, while the error deteriorates in harsh illumination conditions.

To solve this issue, two approaches are investigated: a 'brute force' and an analytical one. The brute force method is the least elegant, as it is based on associating to the observation of some correction tables, pre-computed based on hardware characteristics, that are entered with the illumination phase angle. This method has some limits, as the number of scenarios stored onboard is limited and it requires interpolating numbers. Of course, despite being the least elegant, it may be computationally cheaper, and if the hardware is properly characterized, it can provide very good accuracy. Figure 5.10 shows the correction table for Venus. An option can be to report the correction for three typical distances and then interpolate depending on the actual mission scenario.

On the other hand, it has been possible to derive an analytical formulation for the correction shift as a function of the illumination condition. Looking at a sphere in the 3D frame (Figure 5.9), it is possible to write the equation of the terminator line as a function of the illumination angle. This can be done by intersecting the equation of the sphere and the plane perpendicular to the illumination vector. If then this is projected in the observation plane, the equation of the terminator lines is:

$$f_s(x) = \sqrt{R^2 - x^2} \quad (5.26)$$

$$f_{is}(x) = \sqrt{R^2 - x^2(1 + \tan^2\theta)} \quad (5.27)$$

where  $R$  is the sphere radius and  $\theta$  is the illumination angle. With these equations, it is possible to calculate analytically the center of gravity of the planet as:

$$u_{pc} = \frac{\int u f_s \pm \int u f_{is}}{\int f_s \pm \int f_{is}} \quad (5.28)$$

By integrating this equation and simplifying we reach the formulation:

$$u_{shift} = \frac{+4}{-3} R \frac{\sqrt{c}}{\pi c} \frac{c-1}{\sqrt{c} \pm 1} \quad (5.29)$$

with:

$$c = (1 + \tan^2\theta) \quad (5.30)$$

which gives as output the shift that has to be applied to the computed center of gravity as a function of the apparent radius of the planet and the illumination phase angle. Figure 5.10 shows the computed shift for the observation of Venus. As can be seen, it matches the behaviour of the correction table.

However, before diving into the numerical results, it is important to highlight some aspects. Due to the pixel quantization and pixel saturation, the centroiding algorithm, and the illumination compensation algorithm, are not the only actors playing a role. With the same observation condition, the actual planet's center location within the single pixel influences the distribution of light among the pixels, which in combination with pixel quantization and saturation creates a variable behaviour of the centroiding error. As an example, Figures 5.11a and 5.11b show the behaviour of the centroiding error as a function of the pixel center in four observation conditions of Venus. The plots show how the shift in the center's u-component within pixel 640, which is central in the selected sensor, generates a variable centroiding error. Figure 5.11a shows this behaviour

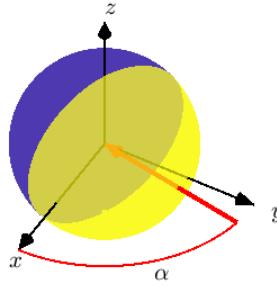


Figure 5.9: Visualization of the illumination angle.

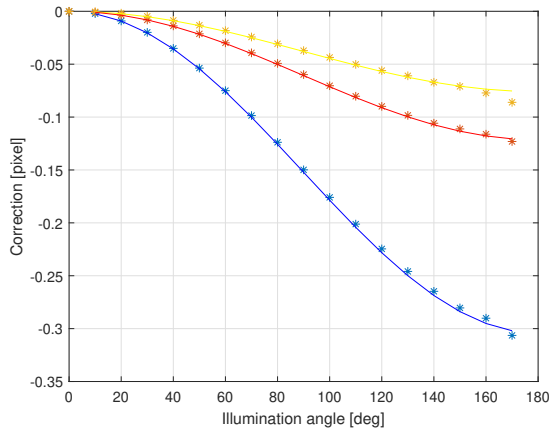


Figure 5.10: Venus centroiding correction, simulated results as points, analytical results as lines. Small distance (0.3457 AU) in blue, medium distance (0.8659 AU) in red, and large distance (1.386 AU) in yellow.

for small and large distances of the observer, for an illumination phase angle of  $60^\circ$ . The oscillation is in the order of 0.03 pixels, but it is important to notice that despite the oscillation, the IC algorithm keeps reducing the computation error. On the other hand Figure 5.11b shows the same for a poorer illumination condition with phase angle  $150^\circ$ . In this case the error is larger and is in the order of 0.08 pixels. In this case, the IC algorithm is only partially able to contain the error in some location, nevertheless the overall performance is still slightly improved.

These plots are not meant to fully characterize all the possible combinations of behaviour, but are meant to explain that the actual center of the planet within the pixel might play a role and influence the accuracy of the centroiding, as oscillations within 0.05 pixel might occur. This value may seem small, but actually it corresponds to few arcsecs, posing a limitation in cutting down below to 0.1 arcsec accuracy. This is however an 'uncontrollable' parameter with state-of-the-art technologies for CubeSats, as it would require an extremely high pointing accuracy.

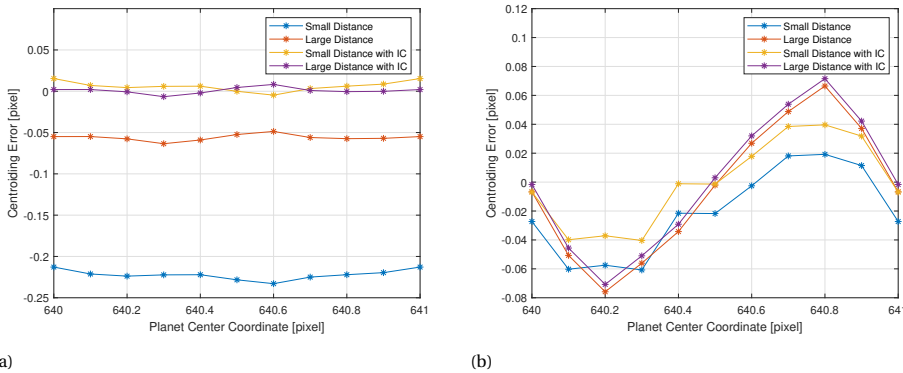


Figure 5.11: Venus centroiding error as a function of the center location for illumination phase angle  $60^\circ$  (left). Venus centroiding error as a function of the center location for illumination phase angle  $150^\circ$  (right). Small distance in the plots corresponds to 0.3457 AU, large distance to 1.386 AU.

## 5.5. COMPLETE TESTING

This section is intended to show the results of testing the full LoS extraction chain with the SIS. To do so, the observer has been considered coincident with Earth's position on the first day of each month between 2024-2028. As the center within the pixel has been explored in the previous section, the center of the planet has been considered perfectly aligned with the boresight direction of the sensor. The results are presented as either the mean value or standard deviation for a Monte Carlo simulation with 40 trials. First, the results of Venus observation are presented, and then Jupiter. In both cases, high noise and low noise scenarios have been considered (as reported in Table 5.1), giving priority to the low case. Figure 5.12 shows the results of a full chain testing for Venus observation.

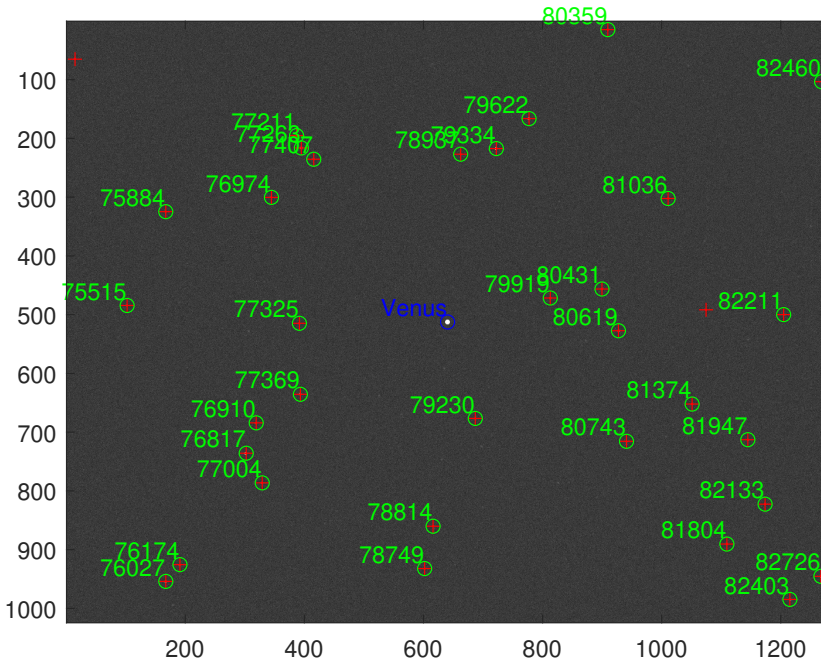


Figure 5.12: Venus observation complete chain testing with SIS.

### 5.5.1. VENUS OBSERVATION

For the larger noise case, the attitude estimation results are presented in Figure 5.13. As it was expected, the roll error is significantly larger than the pitch-yaw ones, which are very close to each other, with small variations depending on the specific stars distribution in the FoV. In general, the peaks of the roll error are associated with an average lower number of observed stars.

Regarding the planet centroiding, results are shown in Figures 5.14a and 5.14b. Figure 5.14a shows the mean centroiding error at each observation scenario. This shows how in a large majority of scenarios the IC algorithm works perfectly, while in extremely poor observation conditions, it induces a small bias in the centroiding. Figure 5.14b shows that despite the bias of the IC algorithm, most of the observation scenarios have a  $\sigma$  in the order of 0.002 pixels, while in a few cases, it is six times larger. These observation scenarios are however associated with an illumination phase angle very close to  $180^\circ$ , which in realistic mission scenarios will not be observed because the Sun exclusion angle cannot be guaranteed.

Remarking that the main goal of this algorithm is to provide the navigation filter with the direction of the object in a heliocentric frame, it is possible to compute the difference between the azimuth and elevation and the computed one. This is because the actual navigation algorithm runs optimally with the measurement fed as azimuth and

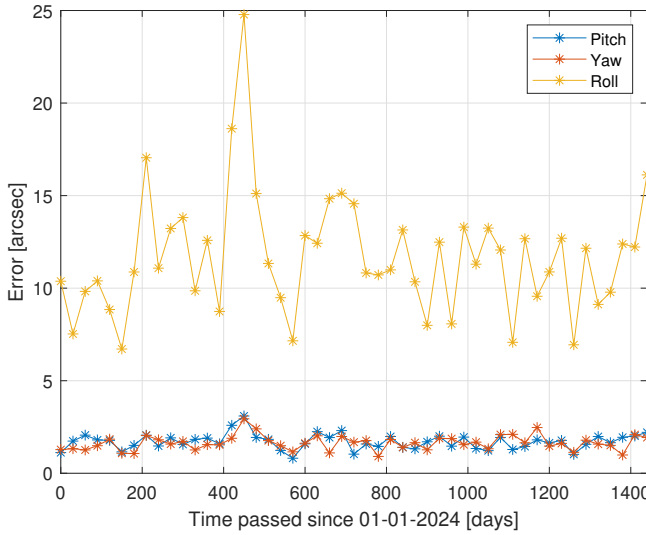


Figure 5.13: Attitude estimation standard deviation as a function of the observation time (Venus high noise case).

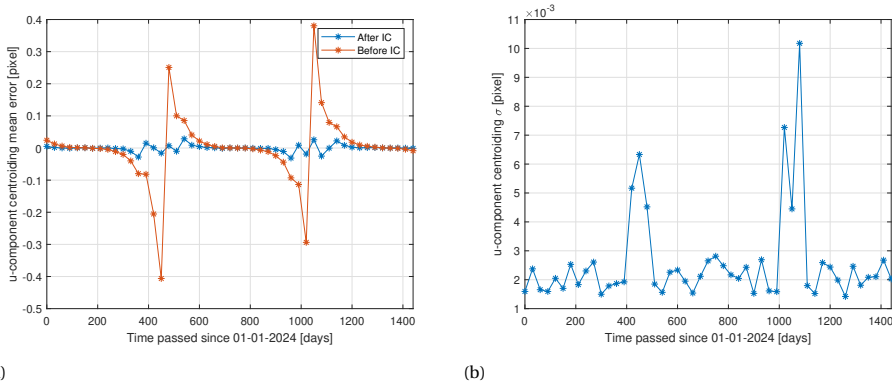


Figure 5.14: Venus centroiding error mean value (a) and error standard deviation (b) (Venus high noise case).

elevation computed in a heliocentric frame. This allows also to observe the actual link between attitude estimation and planet’s centroiding. So, Figures 5.15a and 5.15b show respectively the mean and standard deviation of both. As it can be noticed, the mean value has a bias in the proximity of poorly illuminated conditions, and the  $\sigma$  have peaks corresponding to the pick of the u-component error. The additional oscillations are then related to the combination of planet’s centroiding and attitude estimation. This again testifies that for a navigation analysis, the two can’t be completely separated, and assuming a constant  $\sigma$  for azimuth and elevation measurements is a limiting approach.



Moreover, it is important to remark how in the vast majority of the cases, both azimuth and elevation have a mean value error between  $-1$  and  $1$  arcsecs, while the standard deviation is between  $1$  and  $2$  arcsecs. This, according to the results presented in Chapter 4 shows that this method is appropriate to achieve position estimation error well below  $1000$  km.

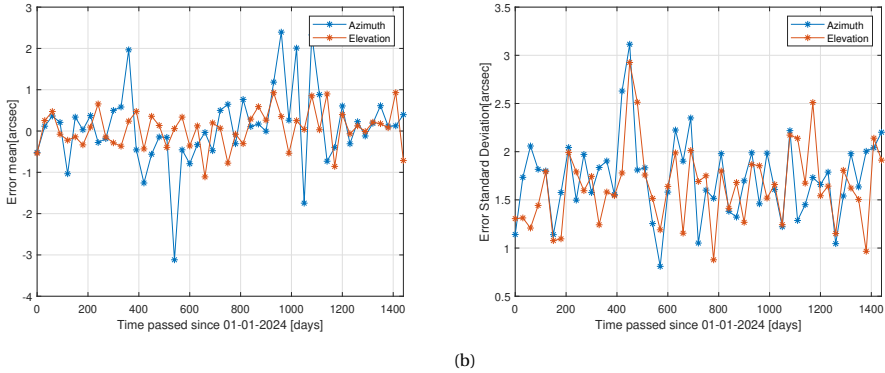


Figure 5.15: Venus Azimuth and Elevation error mean values (a) and standard deviation (b) (Venus high noise case).

For the low noise case, as could be expected, the attitude estimation is improved. This is linked both to a better centroiding performance and also to a slightly larger average number of identified stars, as shown in Figure 5.16.

These differences result in a lower roll, pitch, and yaw lower estimation error, as depicted in Figure 5.17. These reflect also in the computation of the centroiding and then the azimuth and elevation of the body direction. As has been described before, in correspondence with poor illumination conditions, there are some centroiding biases, which are almost independent of the noise, and in fact, in this low noise example, they are comparable with the high noise case. On the other hand, the  $\sigma$  is significantly lower, and this is important as with the exception of a very poor observation scenario, the low noise case produces extremely accurate measurements to feed the navigation filter. Centroiding, and Azimuth and Elevation standard deviation results are shown respectively in Figures 6.7a and 6.7b.

### 5.5.2. JUPITER OBSERVATION

The same approach has been used to exploit Jupiter observation. The attitude estimation error for the high noise case is shown in Figure 5.19. Similar values to Venus observation are obviously obtained. It is worth noticing that the first half of the simulation has a higher number of stars in the FoV, which reflects in better accuracy.

Jupiter's centroiding has better performances because with an observer placed at 1 AU from the Sun, the observation does not experience particularly poor illumination conditions. The results are presented in Figures 5.20a and 5.20b.

Finally, the computation of azimuth and elevation is again accurate, and results are presented in Figures 5.21a and 5.21b.

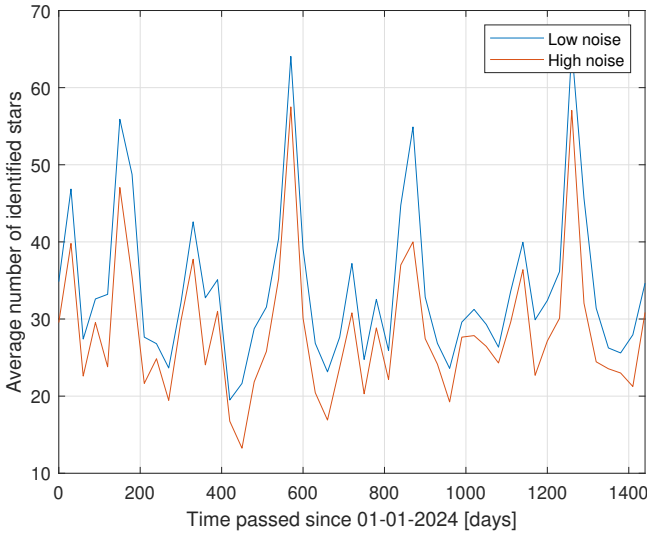


Figure 5.16: Average number of identified stars as a function of the observation time for Venus observation test case.

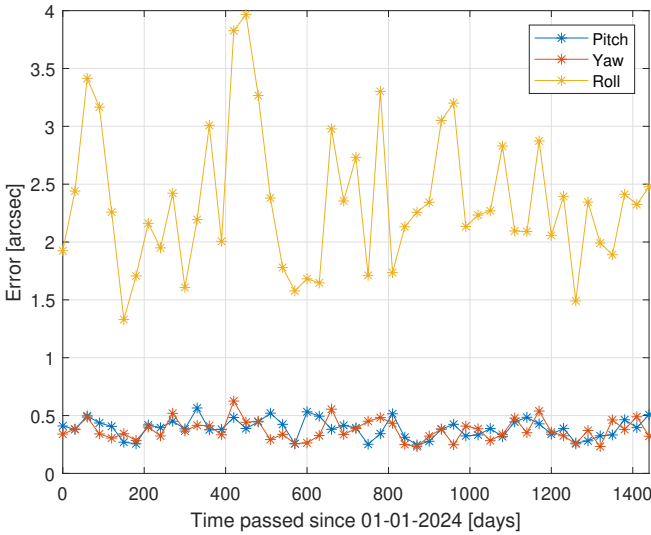


Figure 5.17: Attitude estimation standard deviation as a function of the observation time (Venus low noise case).

Again similarly to Venus, for the lower noise case, performance are improved. Respectively attitude estimation error, centroiding standard deviation and measurements

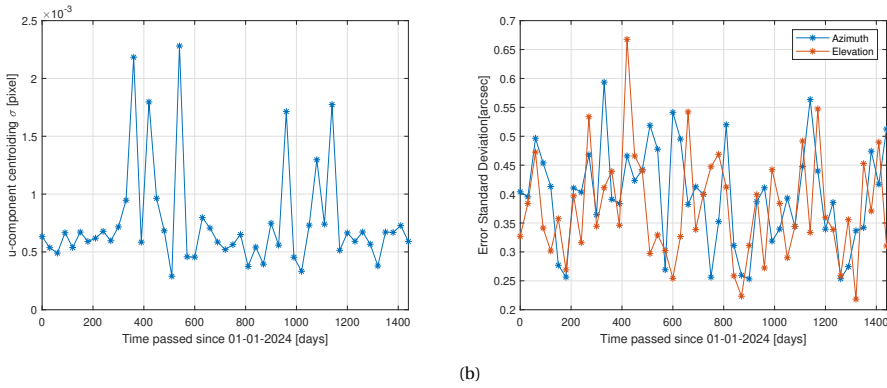


Figure 5.18: Venus centroiding error standard deviation (low noise) (a). Azimuth and Elevation error standard deviation (b) (Venus low noise case).

5

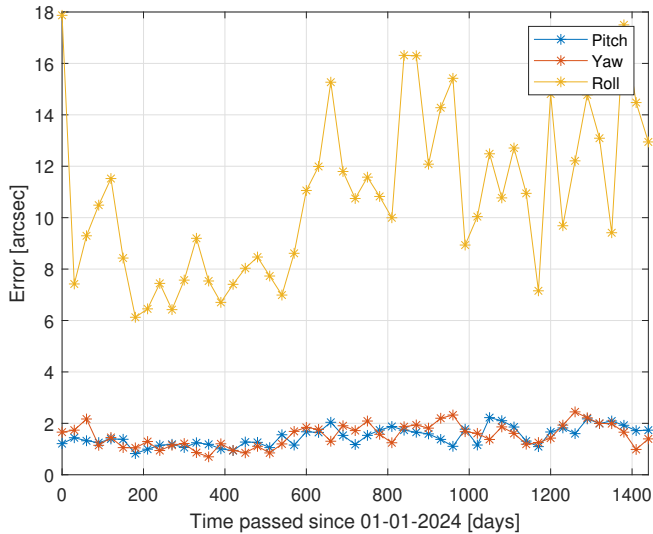


Figure 5.19: Attitude estimation standard deviation as a function of the observation time (Jupiter high noise case).

standard deviation results are shown in Figures 5.22, 5.23a and 5.23b.

Comparing the results of Azimuth and Elevation of both Jupiter and Venus, it is possible to observe that performance, despite the two having different sizes, distances, and brightness. This highlights again that the centroiding algorithm with IC provides high-accuracy measurements also in very different scenarios.

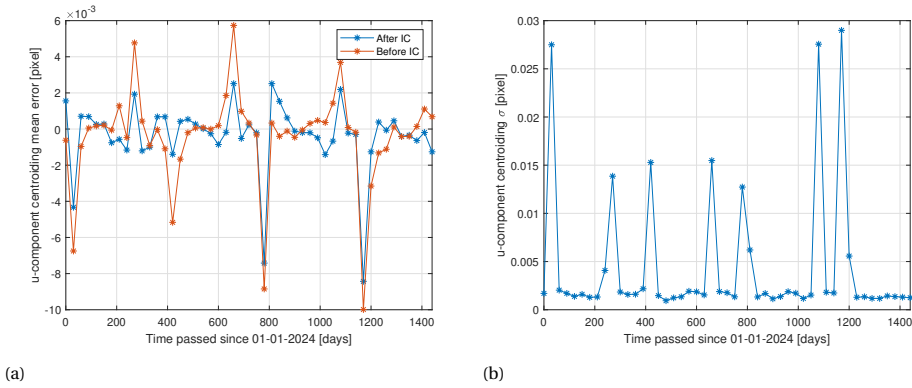


Figure 5.20: Jupiter centroiding error mean value (a). Centroiding error standard deviation (b) (Jupiter high noise case).

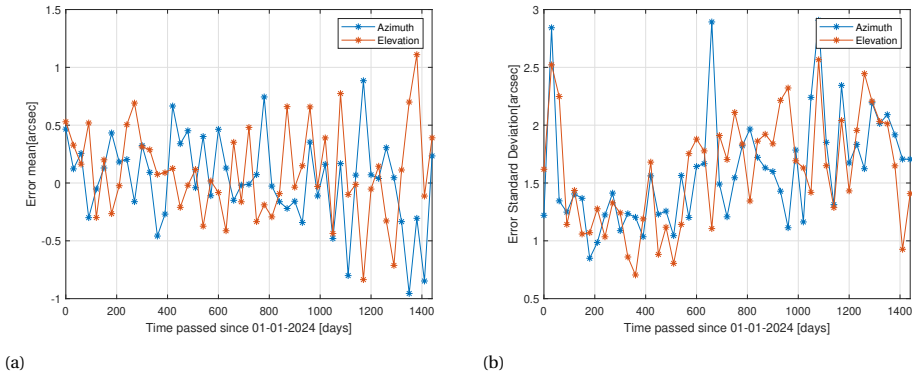


Figure 5.21: Jupiter Azimuth and Elevation error mean values (a). Azimuth and Elevation error standard deviation (b) (Jupiter high noise case).

## 5.6. SYNTHETIC-IMAGES-IN-THE-LOOP NAVIGATION ANALYSIS

The incorporation of image processing within the navigation loop represents a paradigm shift in deep-space autonomous navigation analysis. The methodology offers the possibility of analysing with deeper accuracy the required navigation filter, with a finer tuning of its parameters, in particular regarding the definition of the noise covariance matrix.

### 5.6.1. AEKF

The implementation of a ‘standard’ EKF has some caveats in this navigation technique, because it requires knowing with sufficient accuracy the noise distribution in the measurements, in order to properly tune the  $R_k$  matrix. This is particularly challenging as it would require an extremely accurate characterization of the hardware behaviour in orbit, which is not often possible. Moreover, even if this was possible, as we have been showing in previous sections, the measurement error distribution is far from being ho-

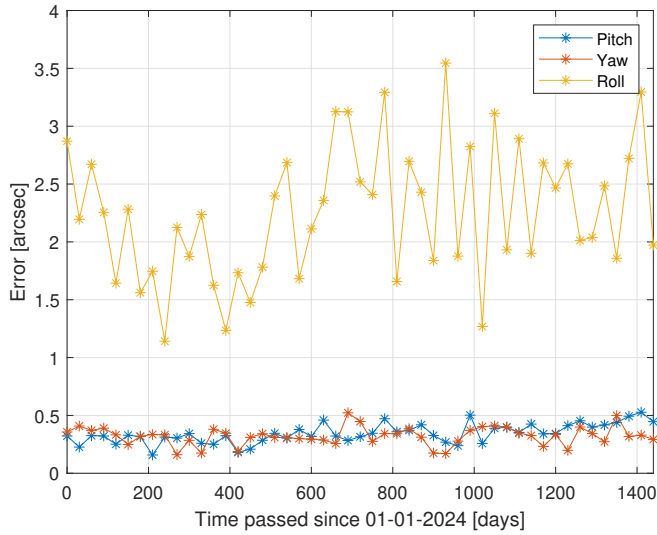


Figure 5.22: Attitude estimation standard deviation as a function of the observation time (Jupiter low noise case).

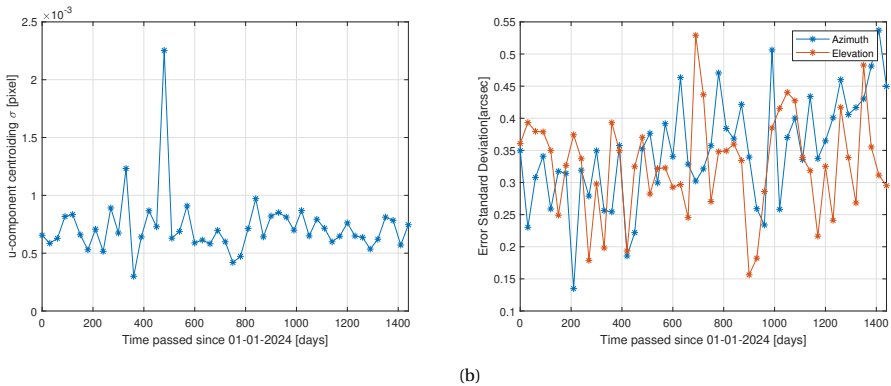


Figure 5.23: Jupiter centroiding error standard deviation (low noise) (a). Azimuth and Elevation error standard deviation (Jupiter low noise case).

mogeneous, as it depends extensively on attitude estimation and planet-centroiding accuracy. The former varies significantly as a function of the number, distribution, and magnitude of stars in the FoV, affecting especially the Roll component without intuitive relationships. The latter is influenced by the observation condition, in particular illumination. These two, combined with an unpredictable dark noise distribution (as a function of the temperature), imply the need for a navigation algorithm capable of dealing with a non-fully predictable varying measurement noise. This can be solved by implementing an Adaptive EKF (AEKF), following the approach suggested in Akhlaghi et al.,

2017. The original approach includes and adaptive estimation of both process noise covariance  $Q$  and measurement noise covariance  $R_k$ . In this analysis we did not include the adaptive estimation of  $Q$  as we implement a 2-Body Problem dynamics both in the generation of trajectory and within the filter. After the  $x_k$  has been computed, it is possible to recompute the measurement vector with the updated state, that here will be called  $y_k$ . Then it is possible to define the residual vector:

$$\vec{e}_k = \vec{y}_k - \hat{y}_k \quad (5.31)$$

and finally the  $R_k$  matrix can be updated as a function of it as:

$$R_k = \alpha R_{k-1} + (1 - \alpha)(\vec{e}\vec{e}^T + H_k \hat{P}_k H_k^T) \quad (5.32)$$

### 5.6.2. ANALYSIS

The simulation is initialized with a position error  $\sigma_{pos} = 10^4$  km and a velocity error  $\sigma_{vel} = 0.01$  km/s. A new observation is collected and fed to the filter every day. As we have been showing in previous sections the actual center location of the planet plays a role in the accuracy, but it is an uncontrollable parameter as it depends on the attitude control error. To streamline the analysis of the results, it has been assumed a planet is perfectly aligned with the boresight direction of the camera, but for further analysis, it is suggested to incorporate also this aspect into simulations.

To avoid complications and long discussions over the results, the only Venus-Jupiter observation is considered, but it is important to remark that many different options are possible. Usually, the best option in terms of estimation errors is the pair Venus-Mars, however, their observation is very similar due to similar disk sizes and distances. On the other hand, Jupiter observation usually provides lower performance, but being a further outer planet, its availability window is larger. Moreover, in this analysis, it allows us to test the observation of two planets with different observation characteristics, due to the larger Jupiter's disk size and distance from the observer.

The two selected test cases are an Earth-Mars transfer and a circular 1 AU heliocentric orbit. Besides the focus of the research being on NEA missions, the first one has been chosen because it allows the evaluation of the performance of the navigation technique in a scenario where distances between observed planets and observer spacecraft change more compared to a NEA mission. The second test case, similar to the approach of Chapter 3, has been chosen indeed to simulate a NEA mission region.

#### EARTH-MARS TRANSFER ORBIT

The first test case is Earth-Mars ballistic transfer, reported in Figure 5.24. Departure date is set as 22th June 2033, while arrival 25th December 2033, for a total ToF of 186 days.

Before diving into the results and tuning of the AEKF, it is interesting to explore the distribution of Azimuth and Elevation, analysing their mean and standard deviation evolution through the simulation epochs. Figures 5.25 and 5.26 show respectively the value of the mean error and standard deviation for both azimuth and elevation. As can be noticed, the evolution of the mean Azimuth values is not randomly scattered around 0, but it varies continuously with the simulation epoch, especially for the case of Venus observation. This is due to the constant change of the background stars scenario due to the

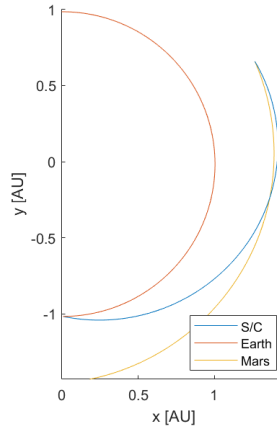
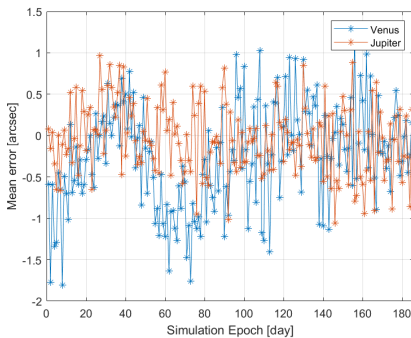
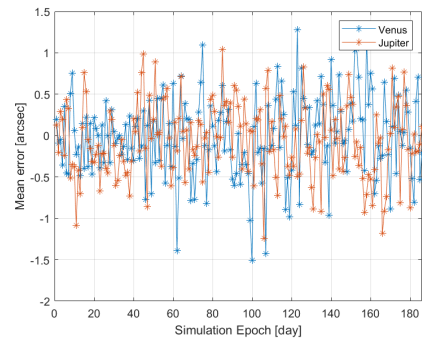


Figure 5.24: Earth-Mars transfer visualization

large rotational speed of the planet, while it happens in a smaller measure for Jupiter, which appears to be more static from the observation point of view. Similar oscillations are present in the standard deviation plots. These plots testify again to the need to have an adaptive formulation of the EKF, as both mean error and standard deviation change as a function of the observation scenario (number of location of stars in the FoV, illumination condition of the planet, distance from the planet).



(a)



(b)

Figure 5.25: Azimuth (a) and Elevation (b) mean value behaviours for Earth-Mars transfer.

By feeding the EKF with this set of measurements, it is possible to estimate the performance of the navigation routine as a function of the measurement noise covariance  $R_k$ . Figures 5.27 and 5.28 report the estimation of the x component of the state (just for simplicity, but similar conclusions can be drawn for all the other components), respectively setting the diagonal values of the  $R_k$  matrix to 1 arcsec and 2 arcsecs. As can be noticed, in the former case, the estimation error for some of the simulations exceeds the

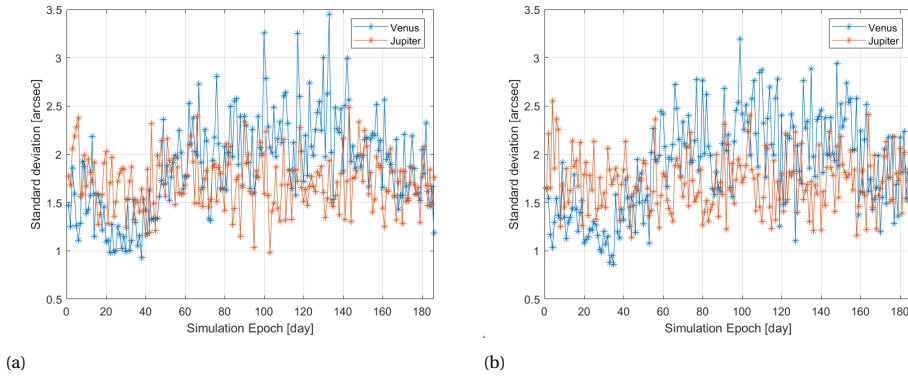


Figure 5.26: Azimuth (a) and Elevation (b) standard deviation behaviours for Earth-Mars transfer.

limit imposed by the  $3\sigma$  boundaries in some epochs, while in the latter it does not. For a correct filter tuning the error should never (99.7 %) exceed the  $3 - \sigma$  boundaries. These plots show again how sensitive the navigation filter based on a standard EKF is, as with a difference of only 1 arcsec, the  $3\sigma$  boundaries contain or not the error. This implies that tuning the EKF would be a very challenging and risky task, as underestimating the correct  $R_k$  value would result in a wrong estimation while overestimating it would lead to lower performance, as the goal is to keep the error below the  $3\sigma$  boundaries, but as close as possible to it, remind it the reader that in-orbit the true state will not be available to compute the actual error, and only covariance values are.

5

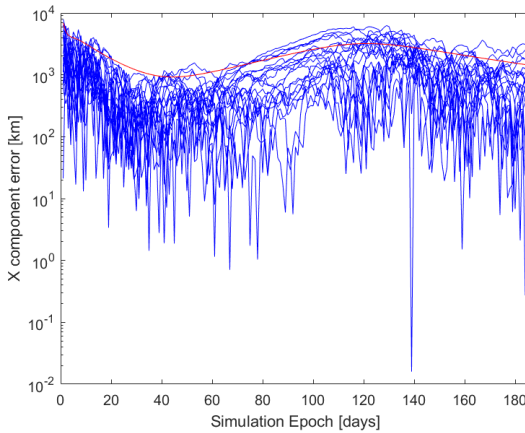


Figure 5.27: x component error for  $R_k$  value of 1 arcsec (EKF). Blue lines are the estimation error for each simulation, while red line is the  $3\sigma$  boundary.

For the above-mentioned reasons, it is important to design a filter which deal with an unpredictable and non-constant behaviour of the measurements. Figure 5.29 shows



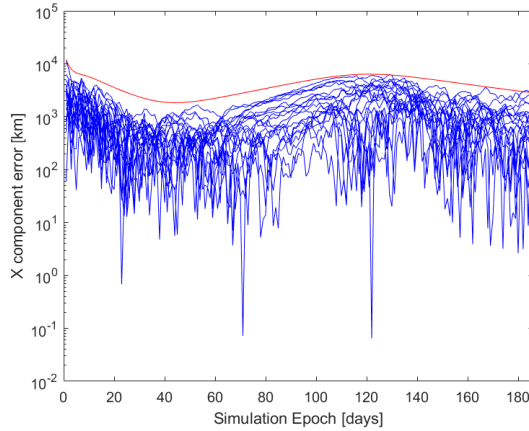


Figure 5.28: x component error for  $R_k$  value of 2 arcsec (EKF). Blue lines are the estimation error for each simulation, while red line is the  $3\sigma$  boundary.

5

the result of the x component employing a AEKF, with initial  $R_k$  value set to 1 arcsec, and  $\alpha = 0.7$ . As it can be noticed, there are some small cases in which the error slightly exceeds the boundaries, but with fine tuning it would be possible to reduce it to the bare minimum (also considering that by definition the  $3\sigma$  contains slightly less than the 100% of the error). It is also interesting to notice how the  $3\sigma$  boundaries are not always the same, and change as a function of the quality of the actual measurement. Finally, it

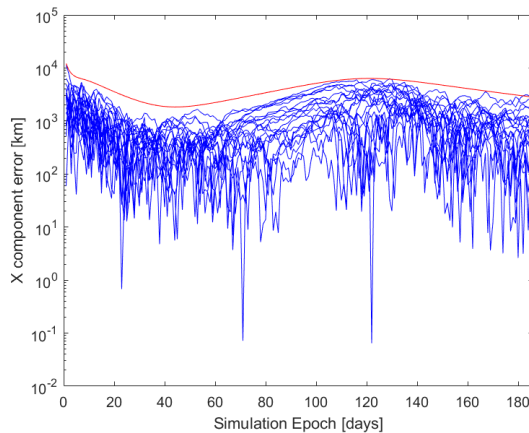


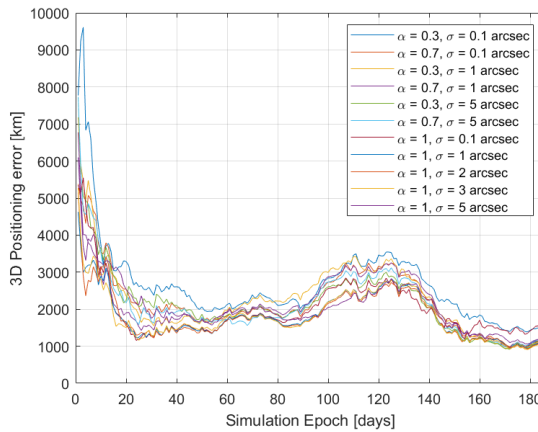
Figure 5.29: x component error for  $R_k$  initial value of 1 arcsec, and  $\alpha = 0.7$  (AEKF). Blue lines are the estimation error for each simulation, while red lines are the  $3\sigma$  boundaries.

is possible to compare the 3D position error as a function of the simulation epoch, and the tuning of the parameters (initial  $R_k$  and  $\alpha$ ). Figure 5.30 shows a comparison of many cases. An AEKF with  $\alpha = 1$  corresponds to a standard EKF. As can be noticed, the different

Semi-major axis	1 AU
Eccentricity	0.0
Inclination	1°
Argument of the Perihelion	30°
RAAN	30°
Initial True anomaly	90°

Table 5.3: Heliocentric orbit initial state.

tuning influences the error evolution in the first stages of the simulation, but at the end, the errors tend to overlap, with the exception of the standard EKF with a low 0.1 arcsec value, and the AEKF with initial value 0.1 arcsec, and low memory factor corresponding to 0.3.

Figure 5.30: 3D position error as a function of the simulation epoch for different AEKF's memory factors and initial  $R_k$  entries.

### CIRCULAR 1AU HELIOCENTRIC ORBIT

Another interesting test case is a circular heliocentric orbit with a radius similar to the one of the Earth because this region of the solar system is relevant for NEA exploration. The departure date is set for 1st January 2027, and ToF is 365 days, while initial orbital parameters are selected without any particular rationale, as it would not impact significantly the discussion relevant in this report, and are reported in Table 5.3.

The impact on the singular component estimation of the AEKF is very similar to the previous case, so to streamline the report's discussion, the attention is focused on the 3D position error behaviour only. Figure 5.31 reports the behaviour of the 3D position error as a function of the simulation epoch, and of the AEKF  $\alpha$  and  $R_k$  initial values, similarly to the previous case. It can be noticed that in this scenario, there is a common behaviour of each EKF 3D error, despite the different parameters, before simulation day 200. The same can be said for the AEKF distributions. After date 200, all the distributions tend to

overlap, showing similar performances, with the exception of the EKF with the lower  $R_k$  value, which tends to have a larger error. This again shows the importance of fine-tuning of the noise covariance matrix, not only to keep the error below the  $3\sigma$  boundaries but also to not underestimate it, as it would lead even to larger errors. As can be noticed, the EKF tend to reduce the error quickly, but in the long run (especially between date 70 and 230) the AEKF provides lower errors, despite the actual parameters tuning. So, the  $3\sigma$  boundaries behaviour is not the only advantage.

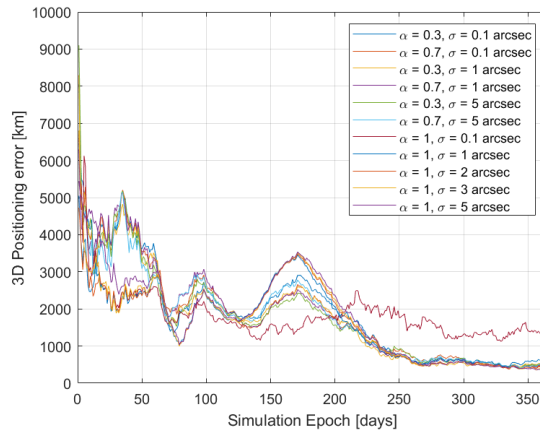


Figure 5.31: 3D position error as a function of the simulation epoch for different AEKF's memory factors and initial  $R_k$  entries.

## 5.7. CONCLUSIONS

This chapter presents a complete overview of the simulation, design, and performance evaluation of star-trackers algorithms for autonomous LoS navigation. This work can be considered a necessary piece of the road map towards the implementation of this navigation technique in real missions, especially in miniaturized spacecraft where autonomy during all mission phases is fundamental. The analysis hereby presented is complementary to the ones presented in Chapter 4, where the focus was on the navigation performance from mission and filter perspectives, and the measurement error was assumed Gaussian. In this chapter, the focus is shifted to the actual performance of the star tracker that collects measurements for the navigation filter (presented in Chapter 4).

First, the space image simulator theory available in literature has been improved in order to target the simulation of small disk planetary objects, which is relevant for LoS navigation in deep-space. Then, the current state-of-the-art attitude determination algorithms have been investigated and selected in order to design an appropriate attitude estimation chain, which maximizes the performance in deep-space cruising scenarios. Then, two approaches for planet centroiding and illumination compensation have been proposed. Finally, the complete image processing chain has been evaluated in different

relevant scenarios for deep-space, in particular for the observation of Venus and Jupiter. The observer has been placed at 1AU distance from the Sun to represent NEAs missions, however, different distances in other scenarios may slightly affect the error estimation. Results have shown that promising performance can be expected by the LoS extraction in terms of azimuth and elevation, as in the majority of the illumination observation scenarios, the measurements computation is in the range of 1-2 arcsecs for the high noise case, and reduce below 1 arcsec in a low noise case. Recalling the results presented in Chapter 4, these measurement error ranges allow to achieve positioning error below 1000 km.

It is important to remark that the actual planetary location within the single pixel, in combination with hardware characteristics such as saturation limit and quantization, do play a role, and they can slightly lower the performance. Moreover, this study has assumed a perfectly calibrated camera and further analysis needs to be performed to derive the influence of lens distortion when they are not properly taken into account.

Furthermore, once these behaviours have been observed, the need for a fine-tuning of certain Kalman filter parameters arose, leading to the definition of an AEKF, which is used in this analysis to test the performance of the navigation technique in a couple of interesting scenarios for deep-space exploration. The analysis of both Earth-Mars transfer trajectory and 1AU circular heliocentric orbit have shown comparable performance of an EKF and an AEKF filters, with the advantage of the latter of not needing to characterize perfectly on-ground the unknown measurement noise behaviour. The position 3D errors achieved in the two scenarios, with the considered hardware and image processing algorithms, are around 1000 km in the first case, and around 500 km in the second case, as the two have different observation conditions. In the second case in fact Venus is closer to the observer, and this is incredibly beneficial for the navigation performance, as it is shown in Chapter 4. These positioning errors satisfy the requirements drafted in Chapter 1.



# 6

## COMBINED LINE-OF-SIGHT RADIOMETRIC NAVIGATION FOR DISTRIBUTED DEEP-SPACE SYSTEMS

*Talent wins games, but teamwork and intelligence win championships.*

Michael Jordan

*This chapter aims to present and evaluate the applicability of combining optical LoS navigation, presented in Chapter 4, with crosslink radiometric navigation for deep-space cruising distributed space systems. To do so, a set of four distributed space systems architectures is presented, and for each of those, the applicability of the combination is evaluated, comparing it to the baseline solutions, which are based on only optical navigation. The comparison is done by studying the performance in a circular heliocentric orbit in seven different time intervals (ranging from 2024 to 2032) and exploiting the observation of all the pairs of planets from Mercury to Saturn. The distance between spacecraft is kept around 200 km. Later, a NEA mission test case is generated in order to explore the applicability to a more realistic case. This analysis shows that the technique can also cope with a variable inter-satellite distance, and the best performance is obtained when the spacecraft get closer to each other.*

---

Parts of this chapter have been published in Casini, Turan, et al., [2023](#)

## 6.1. INTRODUCTION

In recent years, there has been a growing interest in developing Distributed Space Systems (DSS) that can operate in unison to achieve common goals. However, a major challenge in developing such systems is the need for accurate and reliable navigation capabilities, particularly in deep-space cruising scenarios where traditional navigation methods may be limited or ineffective (Turan et al., 2022b), while in close proximity operations around targets it has been widely investigated. In particular, autonomous navigation for DSS has been analyzed around asteroids, with some techniques capable of estimating unknown asteroid's parameters together with the satellites' state ("Autonomous navigation of a spacecraft formation in the proximity of an asteroid", 2016). This challenge is further complicated when it comes to optimizing the mass and volume distributions, as well as operations planning, for miniaturized satellites, whose resources and capabilities are significantly reduced compared to those of larger spacecraft as seen in Chapter 2.

In this context, the integration of multiple navigation techniques has emerged as a promising solution. This chapter explores the combination of two distinct navigation methods, namely crosslink radiometric navigation and optical line-of-sight navigation, for a number of DSS consisting of either two or three satellites with varying sensor complements. The former is intrinsically related to the concept of distributed space systems, and it is based on measuring range and/or range-rate information between the satellites. It has been proven to be capable of estimating the satellite state in various range of scenarios, but it lacks of performance when it comes to estimating the state of two or more satellites whose orbits or trajectories are too similar under a dynamics point of view (Turan et al., 2023). On the other hand, the latter is a very promising technique capable of estimating the state of a deep-space cruising spacecraft, but, as it has been shown in Chapter 4, the simultaneous observation of two planets provides a lower estimation error.

The combination of the two for DSS has the advantage of enabling lighter and less complicated architectures, by exploiting the possibilities of exchanging range information among the spacecraft of the network.

The chapter presents a detailed description of the proposed navigation strategy, including the design and implementation of the crosslink radiometric and optical line-of-sight navigation methods. The performance of the system is evaluated through simulations and experiments, demonstrating its effectiveness in deep-space cruising scenarios.

Overall, the results presented in this chapter suggest that the integration of crosslink radiometric and optical line-of-sight navigation methods can offer significant advantages for distributed space systems, particularly in terms of reducing the onboard equipment required for navigation. This has important implications for the design and operation of future space missions, opening up new possibilities for exploration and scientific research.

The chapter is organized as follows: first, the concept of DSS is explained, and the network architectures considered in this study are detailed. Then both navigation techniques are presented, with them the EKF formulation for their combination. Later, a wide range of mission scenarios is considered in order to define the advantages and disadvantages of the combined navigation techniques, by considering circular heliocentric

orbits. After, a test mission to a Near-Earth Asteroid is generated and the combined navigation technique is tested. Finally, conclusions are reported, focusing on the next steps of the roadmap to enable these missions.

## 6.2. DISTRIBUTED SPACE SYSTEMS ARCHITECTURES

The term DSS encompasses a range of mission concepts that involves the utilization of multiple spacecraft to achieve mission objectives. Constellations, formation flying, and satellite swarms serve as instances of Distributed Space Systems (Guo et al., 2009). These systems, such as formations and swarms, present numerous cost benefits and open doors to fresh functional possibilities and improved performance. They also bring forth diverse scientific and engineering challenges. This, in turn, has the potential to result in innovative architectures, disruptive engineering methodologies, and novel technologies. Consequently, these advancements can enable new capabilities, enhance characteristics, and bring about cost reductions. In this chapter, the focus is on small satellites, in particular CubeSats. Nevertheless, the concept of DSS, and therefore the combined navigation, can be also applied to larger spacecraft architectures.

For these reasons, in this analysis, four different architectures have been considered. The first two architectures are based on a two-satellites network, as shown in Figure 6.1. The first architecture involves one camera per satellite and is applicable to mission scenarios that involve two identical CubeSats, such as Marco-A and -B (Klesh et al., 2018), as well as recent mission proposals like NEOCORE (R. Walker et al., 2017). It is referred to in this chapter as architecture A. The second architecture involves two cameras on one spacecraft and none on the other, resembling the mothercraft-daughtercraft concept or a DSS that is entirely split, with the navigation functionality restricted to one segment of the network. This is referred to as architecture B.

In the second macro category of architectures, a three satellites network has been considered, as depicted in Figure 6.2. The first, namely architecture C, involves a central spacecraft with no cameras onboard, ranging with two other satellites, each of those equipped with a camera. The second, namely architecture D, is characterized by the central spacecraft equipped with two cameras, and two other ranging satellites with no cameras onboard. Both architectures can be associated with DSS where the functions are split among elements, while the second can again refer to the case of a larger spacecraft accompanied by two small satellites. An additional range link can be established between the two side satellites, for both architectures C and D. Its utility is discussed later in the results section, however, it would slightly complicate the operations, since the additional range measurement shall be observed beforehand and then communicated by one of the two side spacecraft to the central one.

## 6.3. COMBINED LOS AND CROSSLINK RADIOMETRIC NAVIGATION

The goal of this chapter is to present the applicability of the combination of two powerful autonomous navigation techniques that can be exploited in deep-space for state estimation. LoS navigation involves the observation of visible celestial objects (mostly planets),



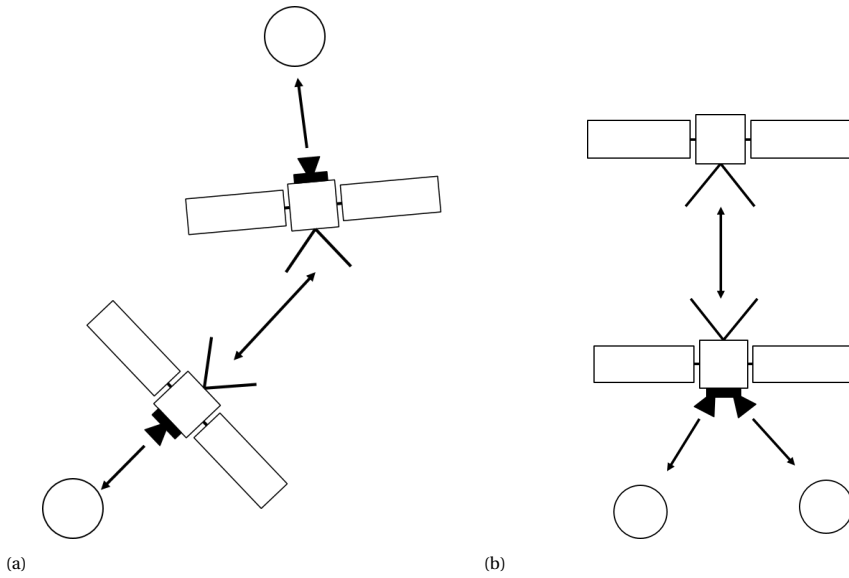


Figure 6.1: Architecture A with two satellites, each of them equipped with a camera (a). Architecture B with two satellites, one equipped with two cameras and one without (b). The double side arrows represent the range information.

6

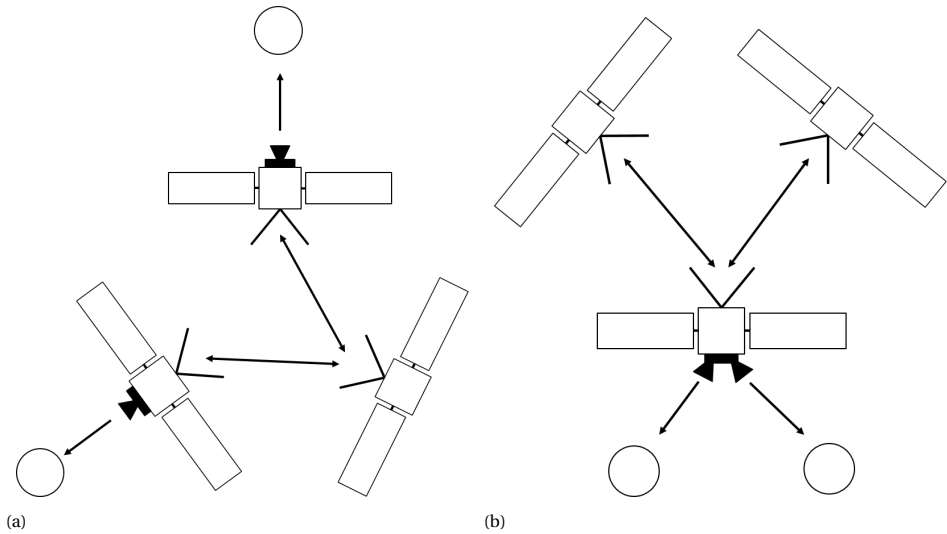


Figure 6.2: Architecture C with three satellites, two of them equipped with one camera each, and one of them without (a). Architecture D with three satellites, one of them equipped with two cameras, and the other two without (b). The double side arrows represent the range information.

whose direction is measured and used to estimate the state of the spacecraft with respect to an inertial frame, where the position of these objects can be easily retrieved. As has

been shown in Chapter 4, this technique offers notable better performances (e.g. lower estimation error) if two or multiple planets are observed, while they deteriorate in the case of single planet tracking. This implies that either the satellite should be equipped with two cameras or star-trackers in order to track simultaneously two planets, or that the satellite shall have the capabilities to re-orientate frequently in order to capture in the FoV multiple objects asynchronously. Both these options impact significantly the design of small satellites, as they require either additional hardware, which impacts mass, volume, and power budgets, or the capabilities of the AOCS, which again impact mass and volume budget (as more fuel would be required onboard), as well as complicate the operations.

On the other hand, crosslink radiometric navigation is a technique based on exchanging range (and eventually range-rate) information between the spacecraft, which are used as measurements for the state estimation within navigation. This technique offers extremely low estimation errors when applied to scenarios where the spacecraft are orbiting around a Lagrangian point or a small Solar System body (Turan et al., 2023), especially if the satellites are placed in sufficiently different orbits, characterized by different dynamics, while performance deteriorates when the satellites are orbiting in similar dynamics conditions. This is perhaps the case of cruising towards a deep-space target, as the DSS satellites would travel on sufficiently similar trajectories. This has been demonstrated in Qin et al., 2019, which shows that the crosslink ranging does not provide full-state estimation in 2-Body Problem dynamics. However, in this application, the range measurement is complementary to the planet observations, and it serves conceptually as a link between two or more spacecraft to share their individual planet observation.

For these reasons, this chapter proposes to combine the two in order to define a navigation strategy which helps the constrained mission design of miniaturized deep-space DSS, by reducing the mass, volume, power, and operations demand, while still offering low state estimation error.

For this application and analysis, the decision has been made to use a sequential estimation technique instead of a batch approach. The preference for a sequential algorithm stems from its applicability to autonomous deep-space CubeSats. By employing a sequential algorithm, there is a reduced need for onboard computational load, and the state estimation can be continuously updated, allowing for eventual manoeuvres and operations. A formulation based on the EKF (Tapley et al., 2004) has been developed for addressing the problem of the two-satellites network, but the same rationale can be applied to the three-satellites case. The state to be estimated is the twelve-dimensional Cartesian state expressed in a heliocentric frame (ECLIPJ2000):

$$\vec{X} = [x_1 \quad y_1 \quad z_1 \quad v_{x,1} \quad v_{y,1} \quad v_{z,1} \quad x_2 \quad y_2 \quad z_2 \quad v_{x,2} \quad v_{y,2} \quad v_{z,2}]^T \quad (6.1)$$

The equation of the dynamics can be expressed as:

$$\dot{\vec{X}} = f(\vec{X}(t)) \quad (6.2)$$

where vector  $\dot{\vec{X}}$  contains the time-derivatives of the state vector, and it is expressed as a function  $f$  of the state vector. In this analysis, a 2-Body Problem has been considered, in

order to simplify the analysis and to focus on the general characteristics:

$$\vec{f} = -\mu_s \cdot \frac{\vec{r}}{r^3} \quad (6.3)$$

where  $r$  is the 3D position vector, while  $\mu_s$  is the solar gravitational constant. The measurements fed to the EKF are the directions to one or more planets, expressed in terms of azimuth  $\theta$  and elevation  $\psi$  with respect to the observer (e.g. the spacecraft), and the range  $\rho$  between the satellites:

$$\vec{Y} = h(\vec{X}(t)) = [\theta_1 \quad \psi_1 \quad \theta_2 \quad \psi_2 \quad \rho]^T \quad (6.4)$$

The size of the vector  $\vec{Y}$  depends on the available measurements, but in this analysis, it has five entries in the two spacecraft case, and six entries in the three spacecraft case, as it is assumed that always two planets are tracked simultaneously. Directions to planets are expressed in the same heliocentric frame as the state, and they can be computed as:

$$\hat{r}_{pk} = \frac{\vec{r}_k - \vec{r}}{|\vec{r}_k - \vec{r}|} = \begin{bmatrix} x_{los,k} \\ y_{los,k} \\ z_{los,k} \end{bmatrix} \quad (6.5)$$

where  $\vec{r}_k$  is the heliocentric  $k^{th}$ -planet position vector. The spacecraft attitude is considered known and it is taken into account to define the LoS measurement error range. Respectively, Azimuth, Elevation, and Range can be computed from the state as follows:

$$\begin{bmatrix} \theta_k \\ \psi_k \end{bmatrix} = \begin{bmatrix} \arctan\left(\frac{y_{los,k}}{x_{los,k}}\right) \\ \arcsin(z_{los,k}) \end{bmatrix} \quad (6.6)$$

$$\rho = \sqrt{(x_1 - x_2)^2 + (y_1 - y_2)^2 + (z_1 - z_2)^2} + \Delta\rho \quad (6.7)$$

where  $\Delta\rho$  is range bias, which quantifies instrumental delays, and for this analysis, it has been assumed zero, while for further studies it can be estimated. In practical scenarios, it is necessary to account for light-time delay and velocity aberration corrections. However, in this study including both effects would not add any particular insight, so it has been neglected. Bold characters in the next equations indicate matrices. The state is propagated within the filter by solving the differential Equation 6.3, while the covariance matrix is propagated as:

$$\bar{\mathbf{P}}_k = \phi^T(t_k, t_{k-1}) \hat{\mathbf{P}}_{k-1} \phi(t_k, t_{k-1}) + \mathbf{Q} \quad (6.8)$$

where  $\phi(t_k, t_{k-1})$  is the state transition matrix and  $\mathbf{Q}$  is the process noise matrix, which is assumed to be diagonal with the position and velocity components values set respectively to  $10^{-12} \text{ km}^2$  and  $10^{-11} \text{ km}^2/\text{s}^2$ . These values have been preliminary tuned and kept small since the dynamics is assumed perfectly modelled within the filter. However, in realistic filter tuning scenarios, attention shall be devoted to their selection in order to account for unmodelled perturbances.

The state transition matrix is computed at each time interval by integrating:

$$\dot{\phi}(t) = \mathbf{F}\phi(t) \quad (6.9)$$

where  $\mathbf{F}$  is the Jacobian of the state, and in the 2-body problem formulation can be expressed as:

$$\mathbf{J}_{\mathbf{k}} = \begin{bmatrix} 0 & 0 & 0 & 1 & 0 & 0 \\ 0 & 0 & 0 & 0 & 1 & 0 \\ 0 & 0 & 0 & 0 & 0 & 1 \\ -\frac{\mu_s(1-\frac{3x_k^2}{r_k^2})}{r_k^3} & 3\mu_s\frac{x_k}{r_k^5} & 3\mu_s\frac{x_k z_k}{r_k^5} & 0 & 0 & 0 \\ 3\mu_s\frac{x_k y_k}{r_k^5} & -\frac{\mu_s(1-\frac{3y_k^2}{r_k^2})}{r_k^3} & 3\mu_s\frac{y_k z_k}{r_k^5} & 0 & 0 & 0 \\ 3\mu_s\frac{x_k z_k}{r_k^5} & 3\mu_s\frac{y_k z_k}{r_k^5} & -\frac{\mu_s(1-\frac{3z_k^2}{r_k^2})}{r_k^3} & 0 & 0 & 0 \end{bmatrix} \quad (6.10)$$

$$\mathbf{F} = \begin{bmatrix} \mathbf{J}_1 & \mathbf{0}_{6,6} \\ \mathbf{0}_{6,6} & \mathbf{J}_2 \end{bmatrix} \quad (6.11)$$

The state vector and covariance matrix update can be then expressed as:

$$\vec{\hat{X}}_k = \vec{\hat{X}}_k + \mathbf{K}_{\mathbf{k}}(\vec{Y}_k - \vec{\bar{Y}}_k) \quad (6.12)$$

$$\hat{\mathbf{P}}_{\mathbf{k}} = (\mathbf{I} - \mathbf{K}_{\mathbf{k}}\mathbf{H}_{\mathbf{k}})\bar{\mathbf{P}}_{\mathbf{k}} \quad (6.13)$$

where  $\vec{\hat{X}}_k$  is the propagated state vector,  $\vec{\bar{X}}_k$  is the updated state vector,  $\vec{Y}_k$  is the measurements vector,  $\vec{\bar{Y}}_k$  is the computed measurements vector,  $\bar{\mathbf{P}}_{\mathbf{k}}$  is the propagated covariance matrix,  $\hat{\mathbf{P}}_{\mathbf{k}}$  is the updated covariance matrix. Respectively, the observation matrix  $\mathbf{H}_{\mathbf{k}}$  and the Kalman gain matrix  $\mathbf{K}_{\mathbf{k}}$  can be expressed as:

$$\mathbf{C}_{\mathbf{k},i} = \begin{bmatrix} \frac{y_{los,i}}{r_{los,i}^2} & -\frac{x_{los,i}}{r_{los,i}^2} & 0 & 0 & 0 & 0 \\ \frac{x_{los,i}z_{los,i}}{r_{los,i}^3\sqrt{1-\frac{z_{los,i}^2}{r_{los,i}^2}}} & \frac{y_{los,i}z_{los,i}}{r_{los,i}^3\sqrt{1-\frac{z_{los,i}^2}{r_{los,i}^2}}} & \frac{z_{los,i}^2-r_{los,i}^2}{r_{los,i}^3\sqrt{1-\frac{z_{los,i}^2}{r_{los,i}^2}}} & 0 & 0 & 0 \end{bmatrix} \quad (6.14)$$

$$\Gamma = \begin{bmatrix} \frac{x_1-x_2}{\rho} & \frac{y_1-y_2}{\rho} & \frac{z_1-z_2}{\rho} & 0 & 0 & 0 \end{bmatrix} \quad (6.15)$$

$$\mathbf{H}_{\mathbf{k}} = \begin{bmatrix} \mathbf{C}_{\mathbf{k},1} & \mathbf{0}_{2,6} \\ \gamma \cdot \mathbf{C}_{\mathbf{k},1} & \delta \cdot \mathbf{C}_{\mathbf{k},1} \\ \Gamma & -\Gamma \end{bmatrix} \quad (6.16)$$

$$\mathbf{K}_{\mathbf{k}} = \bar{\mathbf{P}}_{\mathbf{k}}\mathbf{H}_{\mathbf{k}}^T(\mathbf{H}_{\mathbf{k}}\bar{\mathbf{P}}_{\mathbf{k}}\mathbf{H}_{\mathbf{k}}^T + \mathbf{R}_{\mathbf{k}})^{-1} \quad (6.17)$$

where  $\gamma$  is set to 0 when architecture A is analyzed and to 1 for B, while  $\delta$  is set conversely, and  $\mathbf{R}_k$  is the observation covariance matrix, assumed constant in this analysis:

$$\mathbf{R}_k = \begin{bmatrix} \sigma_{los1}^2 & 0 & 0 & 0 & 0 \\ 0 & \sigma_{los1}^2 & 0 & 0 & 0 \\ 0 & 0 & \sigma_{los2}^2 & 0 & 0 \\ 0 & 0 & 0 & \sigma_{los2}^2 & 0 \\ 0 & 0 & 0 & 0 & \sigma_\rho^2 \end{bmatrix} \quad (6.18)$$

where the diagonal values correspond to the standard deviations of the measurements.

These equations apply to a two-spacecraft architecture, however, the equations for the three spacecraft cases follow the same rationale and can be easily derived, but they are not shown in this dissertation.

LoS azimuth and elevation standard deviations mainly depend upon two main players: the attitude estimation accuracy that is used to convert the LoS direction from body-fixed to an inertial frame, and the planet centroiding accuracy, which is influenced by the observation scenario (e.g. distance and illumination condition from the planet), hardware characteristics, and centroiding algorithm. In this analysis,  $\sigma_{los} = 5 \text{ arcsec}$  is assumed as attitude estimation accuracy using CubeSat star-trackers ranges between a few to tens of arcsecs depending on both hardware characteristics and algorithms developed in Chapter 5.

Several methods exist for inter-satellite radiometric ranging, including conventional PN/Tone, telemetry, and frame ranging. In this study, telemetry-ranging has been adopted as the inter-satellite ranging method due to its high telemetry data transmission rate between satellites. Telemetry ranging does not rely on a separate downlink ranging signal and is dependent on the timestamping and identification of synchronized information frames. According to CCSDS 401.0-B-32 (CCSDS, 2021), telemetry ranging can achieve range accuracy of 1m ( $1\sigma$ ) when the coded symbol rate is 200ksymbol/s or greater under the specific ground station and spacecraft conditions. A high telemetry data rate can be advantageous for this ranging method due to the shorter symbol duration,  $T_{sd}$ . With inter-satellite distances around 200 km considered in this study, hundreds of kbps of data rates can be easily achieved. Moreover, using a telemetry window for navigation purposes enables constant tracking between satellites without requiring a separate time window for tracking. Its performance could be defined as follows (Andrews et al., 2010):

$$\sigma_{\rho_{SST}} = \sigma_{\rho_{TM}} = \left(1 - \frac{2\nu}{c}\right) \left( \frac{4c T_{sd}^2}{\pi T_l E_S / N_0} + \frac{c}{8f_{rc}} \sqrt{\frac{B_L}{(P_{RC} / N_0)}} \right) \quad (6.19)$$

where the telemetry symbol duration is denoted as  $T_{sd}$ ,  $c$  represents the speed of light,  $\nu$  is the relative velocity between satellites,  $T_l$  is the correlator integration time,  $E_S / N_0$  denotes the symbol-to-noise ratio,  $f_{rc}$  represents the frequency of the ranging clock component,  $P_{RC} / N_0$  is the signal power to noise spectral density ratio, and  $B_L$  denotes the one-sided loop noise bandwidth. It is assumed that the onboard time-tagging, related to the master clock frequency, is sufficiently precise and will not affect the overall system performance.

For this analysis, the radiometric parameters are reported in Table 6.1 according to CubeSat characteristics. It is assumed that the link established between the DSS does

not rely on X-Band, which is usually devoted to Earth communication. The given configuration provides around  $\sim 7\text{-}8\text{m}$  ( $1\sigma$ ) inter-satellite ranging error so that the EKF is set with  $\sigma_\rho = 10\text{m}$ , in order to take into account eventual unmodelled disturbances and to be more conservative with the results. Figure 6.3 shows the expected range error as a function of the inter-satellite data-rate.

	<b>Downlink</b>	<b>Uplink</b>
Frequency	2200 MHz	2100 MHz
TX Power	3 dBW	3 dBW
TX Path Losses	1 dB	1 dB
TX Antenna Gain	6.5 dBi	6.5 dBi
Data Rate (max dist.)	10 kbps	10 kbps
Required Eb/N0	2.5 dB	2.5 dB
Link Margin	3 dB	3 dB
Range Clock Frequency $f_{rc}$	N/A	1 MHz
Integration Time $T_I$	1 s	1 s
$P_{RC}/N_0$	N/A	20 dBHz

Table 6.1: Crosslink characteristics

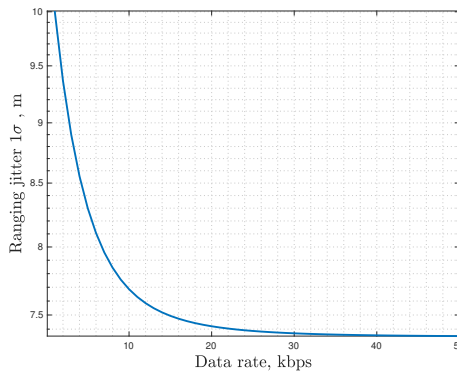


Figure 6.3: Expected Inter-satellite range measurement error as a function of the inter-satellite data-rate.

### 6.3.1. PERFORMANCE OF THE TWO SPACECRAFT DSS ARCHITECTURE

As previously discussed, the two satellite architectures are mainly associated with two mission scenarios: a pair of deep-space cruising CubeSats (or more generally SmallSats), and the mothercraft-daughtercraft configuration. Since the objective of this chapter is to compare the performance of combined navigation with respect to standalone optical navigation, the results are presented as a comparison between singular planet observation, double planet observation, and combined navigation. Singular and double planets observation cases are referred to in the chapter as baseline solutions. However,

due to the constantly changing observation geometry, it is not easy to define the steady-state behaviour for LoS navigation, and this generates oscillation in the estimation error. Therefore, presenting the results on a wide-scale comparison is not possible. Thus, this chapter chooses to present the results as the difference between the mean 3D position error between the techniques. Keeping this in mind, the mean error is calculated after an 'assessment period' of 200 days. This number is a good trade-off for displaying results and is chosen based on the convergence time analysis reported in Chapter 4.

For the purpose of this analysis, a circular heliocentric reference orbit with a radius of 1 AU has been considered. This choice is based on the definition of NEAs, which are characterized by having a perihelion distance of up to 1.3 AU and an aphelion distance of at least 0.983 AU (Morbidelli et al., 2002), so missions towards these bodies are expected to happen in this portion of the Solar System. The inter-satellite range is fixed at 200 km throughout all simulations. Results are averaged RMSE of a Monte Carlo Simulation with 50 trials and then presented as percentage change with respect to a baseline solution. Initial position and velocity dispersions are set respectively to  $10^3$  km and 0.001 km/s.

The results for architecture A are presented in tables in Figure 6.4, and in most cases, the combined navigation approach shows higher accuracy. The table shows the percentage improvement or worsening between the singular planet baseline solution and the combined navigation, so the larger the value, the larger the performance improvement with the combined navigation technique. However, whether the improved accuracy is worthwhile or not depends on the specific mission navigation requirements and on the difficulty of exchanging range information between satellites in the specific scenario. It is noteworthy to remark on how the improvement in the estimation error is more dominant when outer planets are observed, and this is of course connected to the results presented in Chapter 4, where it is shown how the observation of farther planets usually leads to worse performance. So, when only outer planets are available to observe, the combined navigation strategy increases notably the performance. On the other hand, when observing closer bodies, on average the combined navigation still offers improved performance, which for asteroid missions can be fundamental. It has to be remarked that there are few cases characterized by a low worsening of performance. This happens with outer planets Jupiter and Saturn, which are sometimes associated with performance lowering even in the baseline solutions when their position is not convenient for optical navigation.

The results for architecture B are shown in tables in Figure 6.5. The spacecraft for which the results are displayed is the one not observing any object. Again, the results are particularly improved in most of the scenarios, or at least similar. Nevertheless, the crucial outcome is the ability to estimate the second spacecraft's state even without direct observation of any planet. The results of the comparison with the observation of two planets are shown in Figure 6.6. On the left, the comparison is for architecture A, which is characterized by a very similar performance as it was aimed in this analysis. Then each scenario is characterized by a different behaviour, but the difference between the two is usually contained within 100 km. On the right, the comparison is for architecture B, whose performance is usually slightly worst, even if in some cases they are better. However, in this case, it is impressive to see how the spacecraft not observing any object, simply by ranging with the other companion, is able to estimate almost with the same

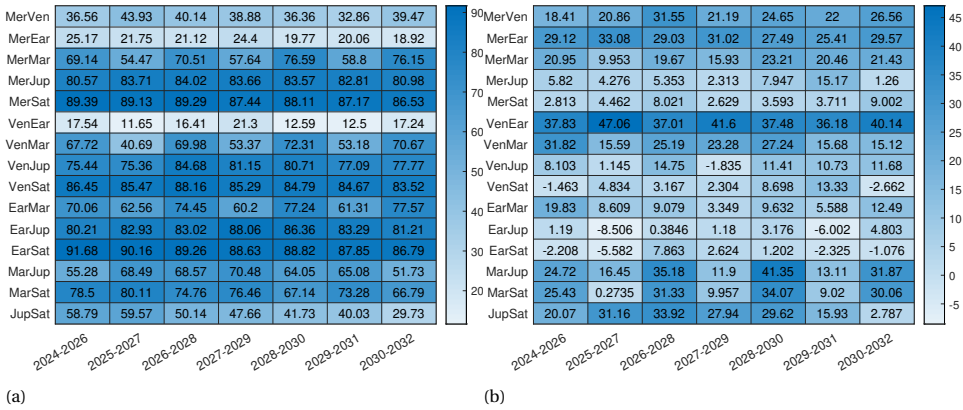


Figure 6.4: Percentage change in 3D position estimation error between combined navigation architecture A and optical navigation with only one planet. In (a) the one planet is the second, while in (b) is the first.

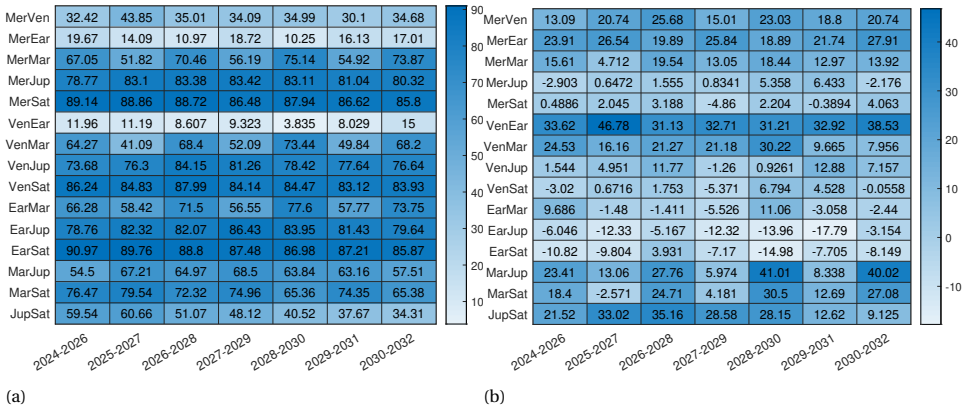


Figure 6.5: Percentage change in 3D position estimation error between combined navigation architecture B and optical navigation with only one planet. In (a) the one planet is the second, while in (b) is the first.

accuracy its position in deep-space. This aligns with the objective of this chapter, which isn't to demonstrate that the combined navigation technique outperforms sole optical navigation. Instead, it highlights that diminishing the necessary count of onboard sensors still permits achieving similar performance.

### 6.3.2. PERFORMANCE OF THE THREE SPACECRAFT DSS ARCHITECTURE

As has been previously mentioned, a DSS composed of three spacecraft can be associated mainly with two applications: a larger spacecraft with two small satellites as companions, and a fleet of small satellites. The results of architecture D are very similar to those of architecture B, both if the navigation filter is based on integrating all three members in the estimation, and if the estimation technique is based on separating the analysis into two simulations similar again to architecture B. For this reason, this subsection



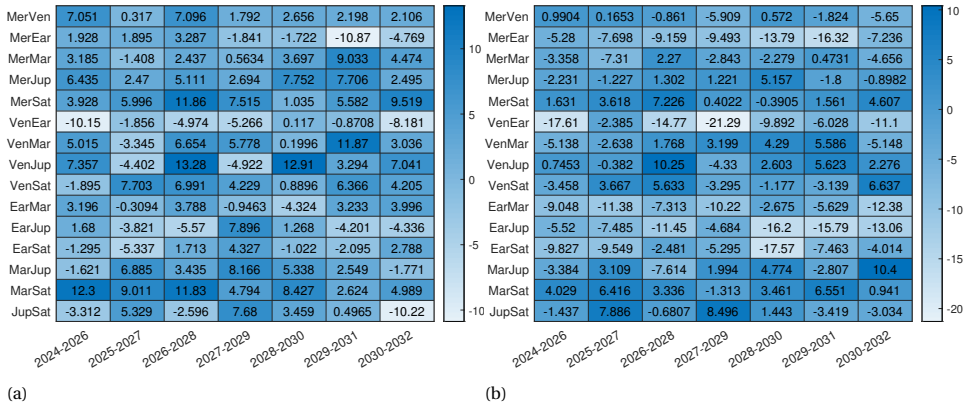


Figure 6.6: Percentage change in 3D position estimation error between combined navigation and optical navigation with only two planets. Architecture A in (a), architecture B in (b)

is aimed to show the performance of architecture C. In this case, it is interesting to explore the performance of the central spacecraft, which is the one not directly observing any visible planet but is only sharing range information with its two companions, both of them capable of observing two different visible bodies. Architecture C+ is defined as architecture C with the addition of a third range link between the two lateral satellites, whose distance is fixed at 400 km.

Results are reported in Figure 6.7, where it is shown that architecture C (with and without the additional third range link) is capable of offering comparable performance to the baseline navigation strategy observing two planets. In the majority of the cases, the error is slightly higher than the baseline, however in this case the spacecraft under analysis does not observe directly any planet, simplifying notably the budgets. There is no evident and systematic improvement or deterioration of the performance with the addition of the third link, and this really depends on the scenarios. It is important to report that this architecture is on the limit concerning observability, with the estimation of an 18-components state with only six or seven measurements. This has an impact when the initial error in position and velocity is larger than the one assumed in this analysis, and it leads to some scenarios in which convergence is not always guaranteed. This problem is however mitigated if the third range is added in the loop, but in general, is less stable than the two-satellites network.

### 6.3.3. MISSION TO NEA EXAMPLE

This section is aimed to show the results of a test case based on the exploration of NEA. The target asteroid is 2008 UA202, and to design the trajectory, Lambert's problem has been solved, considering a release delay of 45 minutes which generates the range behaviour reported in Figure 6.8a. The time-of-flight for this mission is 455 days, identified with a semi-grid search in order to retrieve the propulsion cheaper option. Figure 6.8b shows the three position components estimation in the case of a standalone satellite capable of tracking two planets. This is the result of one simulation, while later in the sec-

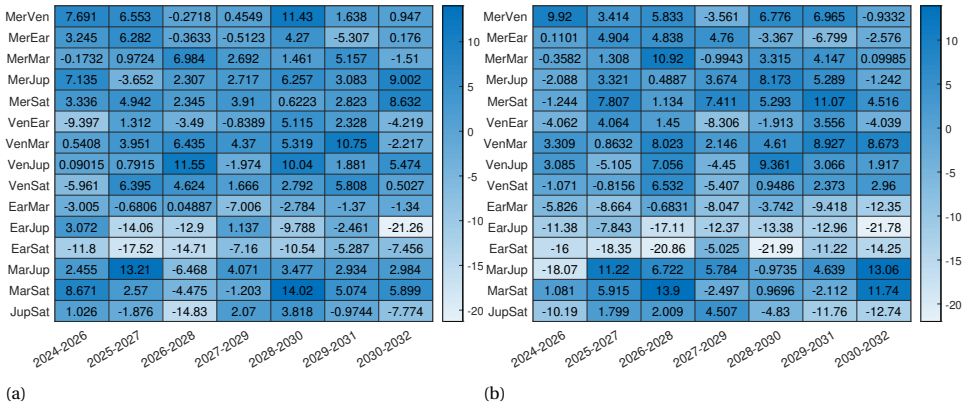


Figure 6.7: Percentage change in 3D position estimation error between combined navigation and optical navigation with only two planets. Architecture C in (a), architecture C with additional range in (b)

tion the results are presented as averaged Monte Carlo output. To have a properly tuned filter, it is needed that the error is always contained within the  $3\sigma$  boundaries indicated by the red lines.

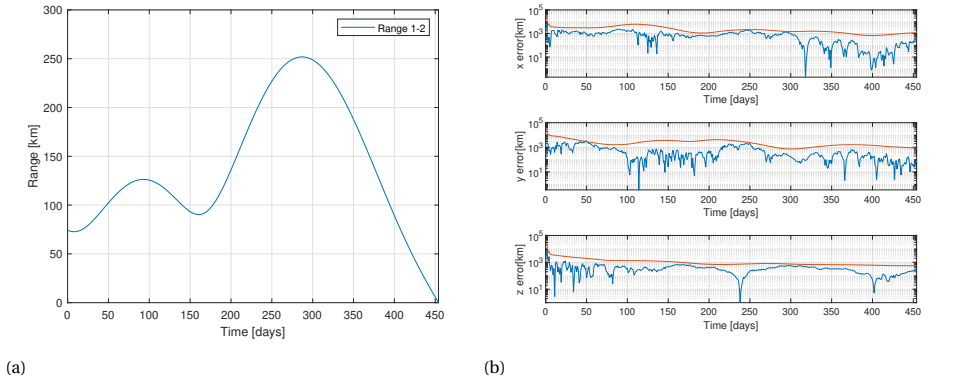


Figure 6.8: Range profile in (a). 3-components position estimation for the single satellite equipped with two cameras, observing Mars and Venus (b).

The observation of Mars and Venus is selected for this example, as it usually represents the optimal observation strategy for a NEA mission. Results of the comparison are presented in the form of average 3D position and 3D velocity error respectively in Figures 6.9 and 6.10, where the errors are compared between the baseline two bodies observation (in blue), the architecture A (in red), and the architecture B (in yellow). The errors are computed as the averaged RMSE of a Monte Carlo simulation with 100 trials. Position and velocity errors present similar trends. As can be noticed in the left plots, after the convergence, the three strategies present almost overlapping behaviours as predicted in the sections before. The results are slightly different for the plots on the right,

for which the error in the architecture B is slightly higher, while at the end (when the range between the satellites becomes minimum) it overlaps again. This is expectable as spacecraft 2 in the architecture B is not able to directly observe any objects, and its state estimation relies exclusively on the range information with the other spacecraft. So, even without an inertial information on the second satellite, the inertial position and velocity components can be estimated pretty accurately. These results are just an example of the power of this technique, which shows that even in variable range scenarios, the technique is capable of reconstructing the state of the cruising spacecraft comparably to what it would have been able to estimate alone, if equipped with multiple cameras to observe a pair of planets.

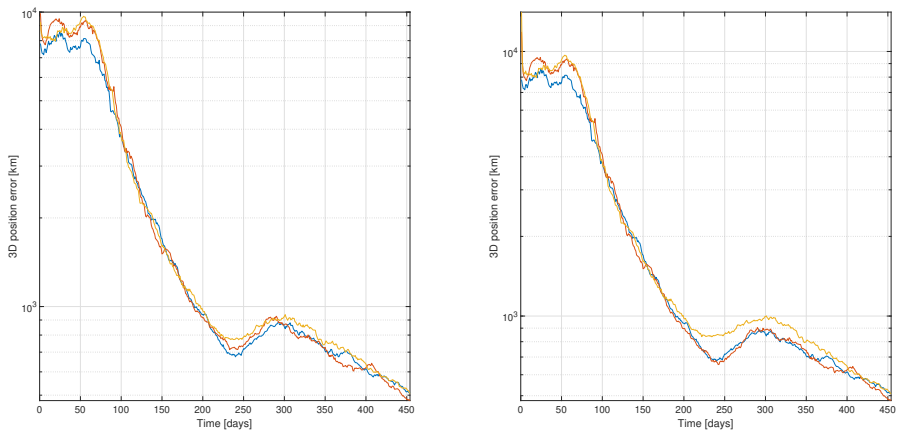


Figure 6.9: 3D Position estimation error for spacecraft 1 (a) and spacecraft 2 (b). In blue baseline solution, in red architecture A, in yellow architecture B.

## 6.4. CONCLUSIONS

The chapter presented an assessment of combining Line-of-Sight optical navigation and crosslink radiometric navigation in deep-space cruising scenarios for DSS. The evaluation of this combined technique is deemed necessary as it enables a wide range of mission architectures, and allows the elements of the DSS to be lighter and more compact. In fact, inter-satellite link is assumed to be always established in these applications, and it is used to exchange range information, which compensates for the need to observe multiple objects with the same satellite. In this way, the architecture of the single satellite can be streamlined, allowing more compact architectures in terms of volume, mass, and power consumption. Moreover, it helps also reduce the required AOCS capabilities, as each satellite does not need to constantly re-orientate in order to align in its FoV with a different object.

First in a general framework, considering a circular heliocentric orbit, and by fixing the range at 200 km, the performance is assessed, showing how this combined technique offers significantly better performance than the ones obtained by observing one object

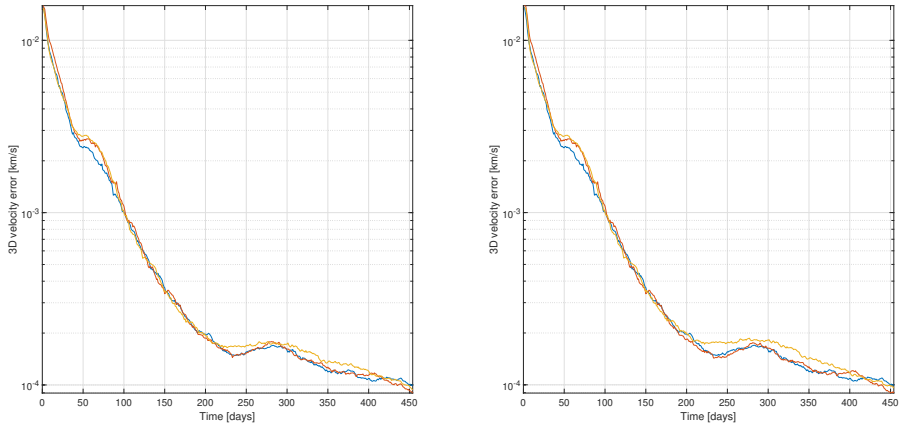


Figure 6.10: 3D Velocity estimation error for spacecraft 1 (a) and spacecraft 2 (b). In blue baseline solution, in red architecture A, in yellow architecture B.

per each satellite, and comparable depending on the scenario with the ones achieved with the observation of the same pair of planets with the same satellite. After this, a test mission to a NEA is generated in order to simulate a variable range, and also in this case the results show that the combined navigation offers very promising performance.

The results show that simply by exchanging the range information between the satellites of the network, even a blind satellite can estimate with comparable accuracy its position and velocity in deep-space, and the same applies to the case of satellites observing only one planet each. In all the architectures, the combined navigation technique shows promising performance, that allows to reduce the mass, volume, power, and operations demand. However, while for the two-satellites network, the technique presents very stable performance, in the three-satellite network, the larger number of states to be estimated with few measurements, generate some instability when the initial position and velocity errors are too large (e.g. larger than  $10^3 km$ ). This effect is slightly mitigated if architecture C+ is considered.

Moreover, the results presented in this chapter are obtained in a wide range of scenarios, where general trends have been highlighted. However, navigation geometry is always an important factor leading the performance. In fact, there is a restricted number of scenarios where the combined technique offers slightly lower performance than the singular planet observation baseline. This testifies again that each mission profile has its optimal navigation strategy, which in the large majority of the cases corresponds to the combined technique, but the baseline strategy shall always be investigated.

It is crucial to emphasize that the analyses presented in this chapter rely on simplified dynamics and methods, aiming to demonstrate the feasibility of the concept. Subsequently, it becomes necessary to examine how perturbations and deviations from ideal conditions affect the models. Specifically, there is a need to outline the strategy for acquiring measurements, both range and the planet's LoS direction, as well as for facil-

itating information exchange among the spacecraft within the system. Additionally, it is imperative to evaluate the consequences of potential delays, as performing entirely simultaneous operations is unfeasible.

To conclude, the analysis presented in this chapter presents a first proof of concept in combining navigation techniques for DSS deep-space mission, and in the near future, it would be wise to expand the set of analyses to conclusively prove the applicability and capabilities of this approach that can broaden significantly the opportunities for deep-space exploration.

# 7

## CONCLUSION

*If I have seen further, it is by standing on the shoulders of giants.*

Isaac Newton

*The conclusion chapter aims to summarize the analysis and results presented in the previous chapters. After a summary, the main findings with conclusions are highlighted by answering the Research Questions formulated in Chapter 1. Then, it is analyzed how the innovations presented in this dissertation contribute to the current literature. Finally, future recommendations are provided, proposing further analysis that can enhance the results presented in this dissertation.*

## 7.1. SUMMARY

This dissertation investigated the feasibility of miniaturized deep-space missions, especially focusing on NEA targets. This is done with a multidisciplinary approach that starts from the definition of mission requirements and the design of a 3U CubeSat platform, exploiting COTS components, and identifying limitations in each subsystem that should be overcome to allow such missions. In Chapter 3, attention is paid to the AOCS, a challenging subsystem for such missions. First, the performance of the available COTS chemical and electric propulsion systems is investigated, highlighting how for chemical propulsion systems there is a wide range of targets that can be reached, while for electric propulsion systems, this may be more challenging. Moreover, the case of Earth Escape is investigated, showing that the electric propulsion system state-of-the-art does not allow fully standalone missions. In the second half of the chapter, the attitude control system is studied, deriving an optimal reaction thruster configuration for reaction wheels de-saturation, and testing the performance of the reaction wheels and RCT for de-tumbling, and optimal frame tracking (keeping the asteroid in the FoV during fly-by, and maintaining the optimal firing direction).

Then, the focus is shifted to autonomous navigation, the core of the dissertation, which represents one of the most important challenges in the near future to enable miniaturized deep-space missions. Autonomous navigation is deemed necessary for these applications, as it would cut down the cost associated with the ground segment. Moreover, this research investigates optical LoS navigation, which does not require extensive additional onboard hardware, as star trackers for attitude estimation can also function as a measurement collector for the navigation filter. LoS navigation is investigated in its total complexity. First, general considerations are reported in Chapter 4, where the specific geometry impact is analyzed, together with the effect of different measurement noise. Then, in Chapter 5, the complete measurement extraction chain is designed, and tested with a synthetic space image simulator. Finally, in Chapter 6, this technique is combined with crosslink radiometric navigation for distributed space systems, where it is shown how the requirement of at least two cameras onboard can be overcome if two or more satellites share range information.

## 7.2. MAIN FINDINGS AND CONCLUSIONS

The main findings of this dissertation are discussed by answering the research questions with their related subquestions.

### RQ1: IS IT POSSIBLE TO DESIGN A 3U CUBE-SAT PLATFORM FOR NEAS FLY-BY MISSIONS?

Chapter 2 investigates the current state-of-the-art COTS technologies for CubeSat and their applicability to deep-space scenarios. Sequentially, all subsystems are explored (RQ1.1). The best option identified for the ADCS is the Hyperion iADCS-2000, removing its magnetometers to save mass, as they cannot be used in deep-space. The ADCS is later explored also in Chapter 3, where attitude control functionalities are tested for the defined platform. The power system depending on the actual scenario can be quite challenging, and the most promising option has been identified as the combination of MMA Design HaWK 17AS42 and GomSpace P31u. The former is a pair of fully deployable solar panels, with a gimbaling option, which allows up to 50W of input power at 0.9

AU, and up to 35 W at 1.1 AU. The latter is a set of batteries with 19.5 Wh of capacity. Regarding the OBC, the Hyperion CP400.85 stands out as the top choice for this application, thanks to its 64 GB optional memory that provides up to 48 minutes of scientific phase. Its compact size, lightweight design, and ample memory storage make it the ideal option. For data transmission, using X-band transmitter and receiver appears to be the most performant, especially if the AAC Clyde Space Pulsar Data is combined with the Endurosat 4x4 Patch antenna. Also, the propulsion system is investigated, but a more detailed description will be given by answering RQ4.

A custom payload within 1 U and 400 g can fit this platform, however, an optical payload combined with an IR spectrometer can allow the measurement of important asteroid characteristics that can enlarge the available dataset for scientific purposes. The limited timeframe of a NEA fly-by can allow the characterization of the asteroid shape and terrain mapping, with some basic surface composition analysis. Together with this, a close fly-by combined with good navigation performance enable also the refinement of the ephemerides for potentially hazardous asteroids, and preliminary asteroid mass computation. For such reasons, this platform can be seen as a low-cost explorer of a large number of asteroids for different purposes. The description of the shape and surface of the asteroid can help future larger missions to limit the navigation failures about the body. Moreover, this platform can identify if a target is potentially interesting for larger spacecraft exploration (RQ1.3).

In this framework, the defined platform, with a custom payload option, and with different propulsion system, can be seen as a standard 3U option for NEA fly-by missions, as all the relevant subsystems meet the requirements in a various range of scenarios (RQ1.2).

#### RQ2: IS LOS NAVIGATION EXPLOITABLE BY DEEP-SPACE CUBESATS DURING A CRUISE TOWARDS A NEA?

Chapter 4 explores LoS navigation from a higher perspective. First, the influence of the geometry on the navigation performance is investigated. This is done by defining a benchmark with four planets that rotate around the Sun at the same rate as the satellite (placed on a 1 AU heliocentric orbit). In this way, the geometry characteristics between the observer satellite and observed planets are kept constant through the simulation time, and the final results give an indication of the impact of the geometry. Results show that better scenarios for planet observation occur when the observed object is as close as possible to the observer, and when the separation angle between to observed planets is as close as possible to  $90^\circ$  (RQ2.1).

Then, within the same simulation framework, the influence of the measurement error and the tracking frequency is analyzed. The results show that the main impact in combination with geometry is given by the measurement error which is a driving parameter, while the tracking frequency does influence notably only the convergence to a solution, rather than the asymptotic error values. A measurement error in the range 1-10 arcsec allows to meet the positioning  $3\sigma$  requirement below 1000 km, but it is also shown how decreasing the error below 1 arcsec would lead to incredibly low estimation errors (RQ2.2).

After this, a FoM previously described in the literature (Franzese and Topputo, 2020) is applied to define interesting NEA mission scenarios, where the exploitation of LoS



navigation is particularly favourable. The results show the existence of a ring, with a 2 AU distance from the Sun, where the LoS navigation accuracy decreases because of the Solar System geometry, while in the proximity of closer NEA targets to the Earth, LoS navigation offers very good performance (RQ2.3).

Observing two planets rather than one is proved to provide a lower estimation error. This implies that in a real mission, having two cameras capable of observing simultaneously two planets is an advantage. Moreover, in Chapter 6, the optical LoS technique is combined with radiometric navigation for distributed deep-space systems, showing how two and three satellite networks can have only one camera onboard, and by only sharing the range information between them, it is possible to achieve performance comparable to a case where all satellites would carry onboard two cameras. This is extremely advantageous, as it allows to reduce the required onboard instrumentation and to simplify the observation campaigns (RQ2.4).

### RQ3: WHAT COMPLETE ALGORITHM CHAIN GUARANTEES THE EXTRACTION OF ACCURATE MEASUREMENTS FOR THE NAVIGATION FILTER?

Chapter 5 explores the design of the measurements extraction chain, the set of algorithms which starts from the image scanning and that gives as output the direction of the observed planet.

It is shown how the number of stars in the FoV is one of the main parameters to influence the attitude estimation error. This of course depends on the actual star density and average magnitude in a certain direction, but it is also influenced by the FoV of the camera, and the sensor noise, as the number of detected stars increases for large FoV and low noise (RQ3.1 and RQ3.2).

The final attitude estimation chain is based on a Least Squares Gaussian Fitting algorithm for the centroiding, which is proven to decrease the error, on a three-star pattern matching algorithm, and on a Wahba's Problem solver based on Singular Value Decomposition. In the high noise scenario, the attitude estimation has a pitch-yaw  $1\sigma$  error of around 2-3 arcseconds, and a roll  $1\sigma$  error of around 10-15 arcseconds depending on the number and location of stars in the FoV. In the low noise scenario, the pitch-yaw  $1\sigma$  error decreases to about 0.5 arcseconds and the roll  $1\sigma$  error to 2-4 arcseconds (RQ3.3).

The chapter also focuses on the simulation of synthetic images that are later used to test the full measurements extraction chain. To simulate the stars, more conventional approaches are exploited, while for the planet a new approach is followed. The latter uses the magnitude from the formulas used to compute the values for the planetary almanack, and it projects geometrically the planet's surface points on the sensor plane, which is discretized in subpixels to calculate the exact fraction of light impacting each pixel (RQ3.5).

With the synthetic images, the full chain is tested, showing as test cases the observation of Venus and Jupiter. The algorithm also includes an analytical illumination compensation routine, which guarantees a further decrease in the error. For both Venus and Jupiter, in the high-noise case, Azimuth and Elevation  $1\sigma$  error is in the range 1-3 arcseconds, while in the low-noise case, it is in the range 0.2-0.6 arcseconds (RQ3.4).

Finally, the results of the testing are used to design an Adaptive Extended Kalman Filter, which is capable of coping with the variable error behaviour of the measurements (RQ3.6).

#### RQ4: WHAT AOCS DESIGN GUARANTEES THE ACCOMPLISHMENT OF ALL THE TASKS FOR NEAs MISSIONS?

Chapter 3, starting from the preliminary designed platform of Chapter 2, explores the design of the AOCS system. First, the propulsion system is investigated. It is proven that the Aerojet Rocketdyne MPS-130 is able to deliver up to  $\Delta V = 380\text{-}390$  m/s (in Chapter 2), which is sufficient to escape Earth's gravitational attraction, starting from a SSGTO, and injecting the satellite in a heliocentric transfer capable of intercepting a large number of NEAs. Then, three electric micropropulsion systems are analyzed, namely ThrustMe NPT, Enpulsion IFN, and AASC MPT. It is shown how their characteristics allow them to barely escape the Earth, but they still comply with a mission starting from outside the Earth sphere-of-influence, and that they can propel the CubeSat to close NEA targets (RQ4.1 and RQ4.2).

In the second half of the chapter, the attitude control system is studied. First, using the characteristics of the RCT Aurora Technologies ARM-A, an optimization to find the placement and orientation of the reaction thrusters is carried out. Then this system is used to de-saturate the reaction wheels, with a very small amount of propellant (about 1-2 g per de-saturation). Then the same system in combination with the reaction wheels, is shown to be able to detumble the satellite for an initial tumbling rate of up to 30 deg/s. Both algorithms are based on a LQR. Finally, the set of reaction wheels, with characteristics similar to the one of the Hyperion iADCS 2000, are proven to be capable of manoeuvring correctly the satellite to follow the optimal firing direction during Earth Escape, and to be able to keep the NEA in the camera FoV during the fly-by for multiple mission scenarios (RQ4.3 and RQ4.4).

### 7.3. KEY INNOVATIONS AND CONTRIBUTIONS OF THE DISSERTATION

The main objective of this dissertation was to further prove the feasibility of miniaturized deep-space missions, in particular to NEA, with a particular focus on the development of the autonomous optical LoS navigation technique. This resulted in the following main eight contributions:

- the review of miniaturized COTS components and the **design of a 3U CubeSat platform** capable of performing NEA fly-by, since so far only larger platforms have been employed and/or considered for such missions. The analysis of the applicability of currently commercially available components has shown the possibility of designing a fully capable 3U platform, which can be seen as an optimal compromise between reducing the associated cost and the performance. Such platform can provide all vital functionalities to the mission.
- the **characterization of the geometrical properties of LoS navigation**, through semi-analytical approach in a simplified benchmark. This analysis expanded and confirmed the analysis presented in Franzese and Topputo, 2020, and it helps understand the behaviour of optical LoS navigation as a function of the geometric properties. Such analysis can be useful for future missions' design in order to define optimal observation strategy, and at the same time to design trajectories as a

function of the navigation performance.

- the **characterization of optical LoS navigation for NEA missions**, which led to the identification of a Solar System area where the technique offers the worst performance. This analysis filled a gap in the literature, as an association between design parameters and state estimation performance was not available, in particular the link between measurement error and state estimation error. This can serve for systems engineering purposes, in order to preliminary select the hardware as a function of the mission requirements.
- the **design of a complete LoS measurement extraction chain for star-trackers**, capable of providing  $1\sigma$  errors in the order of few arcseconds in the high-noise case, and lower than 1 arcsecond in a low-noise case. A complete chain of star-tracker algorithms with associated performance was not available in the literature, and this analysis filled the gap. The proposed algorithms take into account the requirements for such applications, and can be further evaluated with different hardware characteristics, as a function of the mission requirements.
- the **development of an illumination compensation algorithm**, capable of reducing the planet centroiding error in poor illumination conditions, which was required to fill the missing gap in the literature, where the focus was on resolved planets, and the case of smaller planets in the FoV was ignored. This is vital in order to further enable optical LoS navigation technique in a wide set of mission scenarios.
- the **design of a synthetic image simulator for unresolved planets**, based on calculating the precise incident light fraction on each pixel, following the magnitude distribution of the planetary almanac, a geometrical projection of the planet shape, and discretization in subpixels of the sensor plane. This is an extension of the model presented in Marin and Bang, 2020, with the addition of planets simulation which was missing and required to extend the analysis for LoS navigation. This synthetic image simulator can be very important when integrating the navigation analysis with the complete AOCS simulation chain.
- the **integration of synthetic images in the loop** for navigation simulation, which led to the **development of an AEKF navigation filter**, capable of taking into account the dynamical behaviour of the measurements. The previous works lacked the integration of a set of measurements not following a Gaussian distribution, and this limited the design and tuning of an appropriate navigation filter for realistic applications. Then, this study advanced the knowledge of designing and tuning algorithms for real-life applications. This is required especially as a first step, before validating the navigation technique with in-orbit technology demonstration.
- the **design of a combined LoS and crosslink radiometric navigation strategy for distributed space systems**, analyzing its exploitability in networks of two or three satellites. This analysis proposes an innovative navigation technique which can be exploited by DSS in deep-space, whose navigation strategy is not fully treated in the literature. This analysis fills this gap, showing the potential of the fusion

of two navigation techniques. Furthermore, it can be used to define innovative mission scenarios, that may be crucial in the next decades to expand significantly deep-space exploration at lower cost.

## 7.4. RECOMMENDATIONS

The topics of miniaturized deep-space missions and autonomous navigation in deep-space scenarios are under the spotlight nowadays, because they can open the door to a new space exploration era. In this framework, this dissertation attempts to progress our understanding of such topics and tries to give some hints for future research.

Some limitations can be highlighted, which broaden topics of discussion for future work:

- The analysis presented in Chapter 2 involves preliminary design and sizing for each subsystem, aiming at defining which COTS component better suits the design of the platform. In this framework, the analysis to establish the data rate, the onboard computational load, and the power budget can be refined during later design stages, involving more detailed models and further descriptions of the mission scenarios;
- The performance of the control algorithms presented in Chapter 3 shows promising behaviours suggesting their applicability to real mission scenarios. However, it is required to verify such algorithms with a higher-fidelity attitude dynamics model, to further assess their applicability. Furthermore, as remarked in the chapter, the RCT thrusters layout optimization can be further refined by analyzing the Pareto front, in order to improve even more the performance of the solution;
- The benchmark test case presented in Chapter 4 is physically not possible, as planets have different rotational speeds depending on their distance to the Sun, but it is a ploy to simplify the geometry for the analysis;
- Limitations in Chapter 5 lie in the modelling of the lens and camera, which are assumed to be perfectly calibrated. In real mission scenarios, disturbances will impact the accuracy, so proper in-orbit calibration is required;

Such limitations, in combination with other considerations, can be tackled in future work. So the following recommendations are provided:

- performing hardware-in-the-loop testing to the attitude control algorithms, to completely assess the applicability of both algorithms and hardware;
- completing the measurement extraction analysis by incorporating the simulation of the other four interesting planets (Mercury, Earth, Mars, and Saturn), and eventually their moons, and investigating in further detail the fine-tuning of the AEKF parameters as a function of the scenario;
- performing hardware-in-the-loop testing in a controlled environment to further validate the image processing (measurement extraction chain). This requires very

precise laboratory setup, with a large resolution in the screen where synthetic images are projected; as a rule of thumb, at least four pixels of the screen shall be associated with one pixel of the camera sensor, in order to simulate the star's center location within the sensor's pixel, emulating the subpixel accuracy;

- testing the measurement extraction chain with real space images and correlating the results with the ones from the synthetic images analysis. This can be done either with ground images, captured in clean sky conditions (and accounting for the atmosphere distortion), or with in-orbit images with similar hardware;
- exploring the possibility of designing deep-space cruising trajectories incorporating navigation considerations in the performance index, in order to define trajectories whose observability conditions provide low navigation estimation errors. This would allow to further link different aspects of the GNC design, allowing, depending on the mission scenario, to prioritize the optimization goals, as better observability or better propellant consumption performance;
- using in the simulation framework a full dynamic modelling and associated uncertainties, such as planets ephemerides;
- including in the navigation simulations the modelling of AOCS performance to take into account also their associated uncertainties. This would require integrated modelling of the orbital and attitude dynamics, together with the fine modelling of all onboard hardware. The use of Simulink can help towards reaching this goal;
- expanding the set of analyses for the combined navigation technique to conclusively prove the applicability and capabilities of this approach that can broaden significantly the opportunities for deep-space exploration.

In addition to outlining recommendations for future research directions, it is pertinent to briefly highlight some insights gleaned from my experience in hardware-in-the-loop testing for star-tracker algorithms. These insights were not included in the dissertation due to insufficient result quality, attributed to the specific characteristics of the hardware and camera.

Hardware-in-the-loop testing aims to recreate synthetic space images in a controlled environment, capturing them with a camera, and subjecting the algorithms to various tests. In practice, the challenge arises from the fact that stars, acting as point sources of light, are virtually infinitely distant from the camera. Consequently, the light from a given star would ideally hit a specific point in a single pixel of the camera, barring distortions. This lack of sub-pixel accuracy in attitude estimation is addressed by intentionally defocusing the lenses, and spreading the light information across multiple pixels.

To replicate this scenario in a controlled setting, the screen onto which synthetic images are projected must possess a resolution significantly higher than that of the camera's sensor. This allows for the association of multiple pixels on the screen with a single pixel on the sensor, facilitating the recreation of the precise positioning of light information within that single pixel. An optimal compromise in terms of both screen prices and

performance would involve associating 9 pixels on the screen with 1 pixel on the sensor, thereby ensuring that the screen has a resolution three times higher than that of the camera sensor.

Shifting focus, drawing from the first year of experience in the PhD program, particularly in the context of navigation analysis, it is recommended to avoid the integration of diverse scripting languages. Instead, it is proposed to opt for a single scripting language through a careful trade-off assessment and constructing the entire simulation framework within that chosen language.



# BIBLIOGRAPHY

- Akhlaghi, S., Zhou, N., & Huang, Z. (2017). Adaptive adjustment of noise covariance in kalman filter for dynamic state estimation. *2017 IEEE power & energy society general meeting*, 1–5.
- Andreis, E., Franzese, V., Topputo, F., et al. (2021). An overview of autonomous optical navigation for deep-space cubesats. *INTERNATIONAL ASTRONAUTICAL CONGRESS: IAC PROCEEDINGS*, 1–11.
- Andrews, K., Hamkins, J., Shambayati, S., & Vilnrotter, V. (2010). Telemetry-based ranging. *2010 IEEE Aerospace Conference*, 1–16. <https://doi.org/10.1109/AERO.2010.5446926>
- Autonomous navigation of a spacecraft formation in the proximity of an asteroid [Advances in Asteroid and Space Debris Science and Technology - Part 2]. (2016). *Advances in Space Research*, 57, 1783–1804. <https://doi.org/10.1016/j.asr.2015.07.024>
- Balaram, J., Aung, M., & Golombek, M. P. (2021). The ingenuity helicopter on the perseverance rover. *Space Science Reviews*, 217(4), 56.
- Barr, A. H. (1981). Superquadrics and angle-preserving transformations. *IEEE Computer Graphics and Applications*, 1(1), 11–23.
- Bennett, K. A., Fox, V. K., Bryk, A., Dietrich, W., Fedo, C., Edgar, L., Thorpe, M. T., Williams, A. J., Wong, G. M., Dehouck, E., et al. (2023). The curiosity rover's exploration of glen torridon, gale crater, mars: An overview of the campaign and scientific results. *Journal of Geophysical Research. Planets*, 128(1).
- Beshore, E., Lauretta, D., Boynton, W., Shinohara, C., Sutter, B., Everett, D., Gal-Edd, J., Mink, R., Moreau, M., & Dworkin, J. (2015). The osiris-rex asteroid sample return mission. *2015 ieee aerospace conference*, 1–14.
- Bhaskaran, S. (2012). Autonomous navigation for deep space missions. In *Spaceops 2012* (p. 1267135).
- Bouwmeester, J., Gill, E., Speretta, S., & Uludad, S. (2017). A new approach on the physical architecture of cubesats pocketqubes. *Proceedings of the 15th Reinventing Space Conference*,
- Burkhard, C., & Weston, S. (2021). The evolution of cubesat spacecraft platforms. *AVT-336 Specialist Meeting*.
- Burton, M., Buratti, B., Matson, D., & Lebreton, J.-P. (2001). The cassini/huygens venus and earth flybys: An overview of operations and results. *Journal of Geophysical Research: Space Physics*, 106(A12), 30099–30107.
- CalPoly. (2022). *CubeSat Design Specification Rev. 14.1* (tech. rep.). <https://www.cubesat.org/>
- Cappelletti, C., & Robson, D. (2021). Cubesat missions and applications. In *Cubesat handbook* (pp. 53–65). Elsevier.



- Carpenter, J., & D'Souza, C. (2018). Navigation filter best practices. *Technical report NASA/TP 2018 219822*.
- Casini, S., Fodde, I., Monna, B., Cervone, A., & Gill, E. (2021). Novel 3U stand-alone cubesat architecture for autonomous near Earth asteroid fly-by. *Aerospace*, 8(9).
- Casini, S., Monna, B., Cervone, A., & Visser, P. (2022). Line-of-sight navigation observability analysis for near-earth asteroids exploration with cubesat. *INTERNATIONAL ASTRONAUTICAL CONGRESS: IAC PROCEEDINGS*.
- Casini, S., Monna, B., Cervone, A., & Visser, P. (2023). Simulation of deep-space autonomous line-of-sight navigation using synthetic images in the loop. *INTERNATIONAL ASTRONAUTICAL CONGRESS: IAC PROCEEDINGS*.
- Casini, S., Cervone, A., Monna, B., & Gill, E. (2022). On line-of-sight navigation for deep-space applications: A performance analysis. *Advances in Space Research*. <https://doi.org/https://doi.org/10.1016/j.asr.2022.12.017>
- Casini, S., Cervone, A., Monna, B., & Visser, P. (2023). Design and testing of star tracker algorithms for autonomous optical line-of-sight deep-space navigation. *Applied Optics*, 62(22), 5896–5909.
- Casini, S., Fodde, I., Engelen, S., Monna, B., Cervone, A., & Gill, E. (2020). Towards the use of commercial-off-the-shelf small-satellite components for deep-space cubesats: A feasibility and performance analysis. *SmallSat 2020-34th Small Satellite Conference*.
- Casini, S., Turan, E., Cervone, A., Monna, B., & Visser, P. (2023). Combined optical line-of-sight and crosslink radiometric navigation for distributed deep-space systems. *Scientific Reports*, 13(1), 16253.
- CCSDS. (2021, October). *Radio Frequency and Modulation Systems Part 1 Earth Stations and Spacecraft CCSDS 401.0-B-32* (tech. rep.). <https://public.ccsds.org/Pubs/414x0g2.pdf>
- Chai, R., Savvaris, A., Tsourdos, A., Chai, S., & Xia, Y. (2019). A review of optimization techniques in spacecraft flight trajectory design. *Progress in aerospace sciences*, 109, 100543.
- Cheetham, B., Gardner, T., Forsman, A., Kayser, E., & Clarkson, M. (2022). Capstone: A unique cubesat platform for a navigation demonstration in cislunar space. In *Ascend 2022* (p. 4382).
- Cheng, A. F., Agrusa, H. F., Barbee, B. W., Meyer, A. J., Farnham, T. L., Raducan, S. D., Richardson, D. C., Dotto, E., Zinzi, A., Della Corte, V., et al. (2023). Momentum transfer from the dart mission kinetic impact on asteroid dimorphos. *Nature*, 616(7957), 457–460.
- Chesley, S., Farnocchia, D., Vokrouhlicky, D., Chodas, P., Milani, A., Spoto, F., Rozitis, B., Benner, L., Bottke, W., Busch, M., Emery, J., Howell, E., & Lauretta, D. (2014). Orbit and bulk density of the osiris-rex target asteroid (101955) bennu. *Icarus*, 235.
- Christian, J. A. (2010). *Optical navigation for a spacecraft in a planetary system* [Doctoral dissertation, The University of Texas at Austin].
- Cohen, B. A., Hayne, P. O., Greenhagen, B., Paige, D. A., Seybold, C., & Baker, J. (2020). Lunar flashlight: Illuminating the lunar south pole. *IEEE Aerospace and Electronic Systems Magazine*, 35(3), 46–52.

- Desai, M. I., Allegrini, F., Ebert, R. W., Ogasawara, K., Epperly, M. E., George, D. E., Christian, E. R., Kanekal, S. G., Murphy, N., & Randol, B. (2019). The cubesat mission to study solar particles. *IEEE Aerospace and Electronic Systems Magazine*, 34(4), 16–28.
- Dida, A. H. (2019). Design and modeling of useful tool for satellite solar array preliminary sizing and power system analysis. *2019 European Space Power Conference (ESPC)*, 1–4. <https://doi.org/10.1109/ESPC.2019.8932060>
- Dotto, E., Della Corte, V., Amoroso, M., Bertini, I., Brucato, J., Capannolo, A., Cotugno, B., Cremonese, G., Di Tana, V., Gai, I., et al. (2021). Liciacube-the light italian cubesat for imaging of asteroids in support of the nasa dart mission towards asteroid (65803) didymos. *Planetary and Space Science*, 199, 105185.
- Dymock, R. (2007). The h and g magnitude system for asteroids. *Journal of the British Astronomical Association*, vol. 117, no. 6, p. 342-343, 117, 342–343.
- Farley, K. A., Williford, K. H., Stack, K. M., Bhartia, R., Chen, A., de la Torre, M., Hand, K., Goreva, Y., Herd, C. D., Hueso, R., et al. (2020). Mars 2020 mission overview. *Space Science Reviews*, 216, 1–41.
- Ferrari, F., Franzese, V., Pugliatti, M., Giordano, C., & Topputo, F. (2021). Preliminary mission profile of hera's milani cubesat. *Advances in Space Research*, 67(6), 2010–2029.
- Franzese, V., Topputo, F., Ankersen, F., & Walker, R. (2021). Deep-space optical navigation for M-ARGO mission. *The Journal of the Astronautical Sciences*, 68, 1034–1055.
- Franzese, V., Di Lizia, P., & Topputo, F. (2018). Autonomous optical navigation for lumio mission. *2018 Space Flight Mechanics Meeting*, 1977.
- Franzese, V., & Topputo, F. (2020). Optimal beacons selection for deep-space optical navigation. *The Journal of the Astronautical Sciences*, 67, 1775–1792. <https://doi.org/10.1007/s40295-020-00242-z>
- Freeman, R. H. (2022). Cubesat-based infrared lunar astronomy: In search of water-ice signatures. *Journal of Space Operations & Communicator (ISSN 2410-0005)*, 18(2).
- Funase, R., Ikari, S., Miyoshi, K., Kawabata, Y., Nakajima, S., Nomura, S., Funabiki, N., Ishikawa, A., Kakihara, K., Matsushita, S., et al. (2020). Mission to earth-moon lagrange point by a 6u cubesat: Equuleus. *IEEE Aerospace and Electronic Systems Magazine*, 35(3), 30–44.
- Getchius, J., Long, A., Farahmand, M., Winternitz, L. M., Hassouneh, M. A., & Mitchell, J. W. (2019). Predicted performance of an x-ray navigation system for future deep space and lunar missions. *Annual AAS Guidance, Navigation and Control Conference*, (AAS 19-097).
- Glassmeier, K.-H., Boehnhardt, H., Koschny, D., Kührt, E., & Richter, I. (2007). The rosetta mission: Flying towards the origin of the solar system. *Space Science Reviews*, 128, 1–21.
- Goldberg, H., Karatekin, O., & Ritter, B. (2019). The juvenas cubesat in support of esa's hera mission to the asteroid didymos. *33rd Annual AIAA/USU Conference on Small Satellites*.
- Graf, J. E., Zurek, R. W., Eisen, H. J., Jai, B., Johnston, M., & DePaula, R. (2005). The mars reconnaissance orbiter mission. *Acta Astronautica*, 57(2-8), 566–578.

- Greco, C., Di Carlo, M., Walker, L., & Vasile, M. (2018). Analysis of neos reachability with nano-satellites and low-thrust propulsion. *Small Satellites, Systems and Services Symposium*.
- Guo, J., Maessen, D., & Gill, E. (2009). Fractionated spacecraft: The new sprout in distributed space systems. *Proc. 60th International Astronautical Congress, Daejeon (KR)*.
- Hanson, J. E. (1996). *Principles of x-ray navigation*. Stanford University.
- Hardgrove, C., Starr, R., Lazbin, I., Babuscia, A., Roebuck, B., DuBois, J., Struebel, N., Colaprete, A., Drake, D., Johnson, E., et al. (2020). The lunar polar hydrogen mapper cubesat mission. *IEEE Aerospace and Electronic Systems Magazine*, 35(3), 54–69.
- Hashimoto, T., Yamada, T., Otsuki, M., Yoshimitsu, T., Tomiki, A., Torii, W., Toyota, H., Kikuchi, J., Morishita, N., Kobayashi, Y., et al. (2019). Nano semihard moon lander: Omotenashi. *IEEE Aerospace and Electronic Systems Magazine*, 34(9), 20–30.
- Henry, C. A. (2002). An introduction to the design of the cassini spacecraft. *Space science reviews*, 104(1-4), 129–153.
- Hestroffer, D., Segret, B., Chen, H., Agnan, M., Vannitsen, J., Rosenblatt, P., Quinsac, G., Miau, J., & Li, Y. (2018). Birdy-planetary geodesy of small bodies \_through cubesats in autonomous navigation. *42nd COSPAR Scientific Assembly*, 42, B0–2.
- Hill, K., & Born, G. H. (2007). Autonomous interplanetary orbit determination using satellite-to-satellite tracking. *Journal of guidance, control, and dynamics*, 30(3), 679–686.
- Izzo, D. (2014). Revisiting Lambert's problem. *Celestial Mechanics and Dynamical Astronomy*, 121, 1–15.
- Jean, I., Ng, A., & Misra, A. (2019). Impact of solar radiation pressure modeling on orbital dynamics in the vicinity of binary asteroids. *Acta Astronautica*, 165, 167–183.
- Jerde, E. A. (2021). Chapter 2 - the apollo program. In A. Longobardo (Ed.), *Sample return missions* (pp. 9–36). Elsevier. <https://doi.org/https://doi.org/10.1016/B978-0-12-818330-4.00002-1>
- Jiang, F., Baoyin, H., & Li, J. (2012). Practical techniques for low-thrust trajectory optimization with homotopic approach. *Journal of guidance, control, and dynamics*, 35(1), 245–258.
- Johnson, T. V., Yeates, C. M., Young, R., & Dunne, J. (1991). The galileo venus encounter. *Science*, 253(5027), 1516–1518.
- Karimi, R., & Mortari, D. (2015). Interplanetary autonomous navigation using visible planets. *Journal of Guidance, Navigation, and Control*, 38(6).
- Klesh, A., & Baker, J., J. Krajewski. (2019). Marco: Flight review and lessons learned. *Proceedings of 33rd Annual AIAA/USU Conference on Small Satellites*.
- Klesh, A., Baker, J., Bellardo, J., Castillo-Rogez, J., Cutler, J., Halatek, L., Lightsey, G., Murphy, N., & Raymond, C. (2013). Inspire: Interplanetary nanospacecraft pathfinder in relevant environment. *AIAA SPACE 2013 Conference and Exposition*.
- Klesh, A., Clement, B., Colley, C., Essmiller, J., Forgette, D., Krajewski, J., Marinar, A., Martin-Mur, T., Steinkraus, J., Sternberg, D., Werne, T., & Young, B. (2018). Marco: Early operations of the first cubesats to mars. *Proceedings of 32nd Annual AIAA/USU Conference on Small Satellites*.

- Kluever, C. A. (1993). *Optimal low-thrust, earth-moon trajectories*. Iowa State University.
- Kohlhase, C., & Penzo, P. A. (1977). Voyager mission description. *Space science reviews*, 21(2), 77–101.
- Leighton, R. B., Murray, B. C., Sharp, R. P., Allen, J. D., & Sloan, R. K. (1965). Mariner iv photography of mars: Initial results. *Science*, 149(3684), 627–630.
- Liebe, C. (2002). Accuracy performance of star trackers - a tutorial. *IEEE Transactions on Aerospace and Electronic Systems*, 38(2), 587–599. <https://doi.org/10.1109/TAES.2002.1008988>
- Ma, X., Chen, X., Fang, J., Liu, G., & Ning, X. (2016). Observability analysis of autonomous navigation for deep space exploration with LOS/TOA/velocity measurements. *Proc. of the IEEE Aerospace Conference, Big Sky (MT)*, 1–9. <https://doi.org/10.1109/AERO.2016.7500663>
- Machuca, P., Sanchez, J.-P., Masdemont, J., & Gomez, G. (2020). High-fidelity trajectory design to flyby near-earth asteroids using cubesats. *Acta Astronautica*, 146–163.
- Mallama, A., & Hilton, J. (2018). Computing apparent planetary magnitudes for the astronomical almanac. *Astronomy and Computing*, 25, 10–24. <https://doi.org/https://doi.org/10.1016/j.ascom.2018.08.002>
- Malphrus, B. K., Brown, K. Z., Garcia, J., Conner, C., Kruth, J., Combs, M. S., Fite, N., McNeil, S., Wilczewski, S., Haught, K., et al. (2019). The lunar icecube em-1 mission: Prospecting the moon for water ice. *IEEE Aerospace and Electronic Systems Magazine*, 34(4), 6–14.
- Marin, M., & Bang, H. (2020). Design and simulation of a high-speed star tracker for direct optical feedback control in adcs. *Sensors*, 20(8). <https://doi.org/10.3390/s20082388>
- McNutt, L., Johnson, L., Clardy, D., Castillo-Rogez, J., Frick, A., & Jones, L. (2014). Near-earth asteroid scout. *Proceedings AIAA Space Conference*.
- McNutt Jr, R. L., Solomon, S. C., Grant, D. G., Finnegan, E. J., Bedini, P. D., Team, M., et al. (2008). The messenger mission to mercury: Status after the venus flybys. *Acta Astronautica*, 63(1-4), 68–73.
- Michel, P., Küppers, M., Bagatin, A. C., Carry, B., Charnoz, S., de Leon, J., Fitzsimmons, A., Gordo, P., Green, S. F., Hérique, A., Juzi, M., Karatekin, Ö., Kohout, T., Lazzarin, M., Murdoch, N., Okada, T., Palomba, E., Pravec, P., Snodgrass, C., . . . Carnelli, I. (2022). The esa hera mission: Detailed characterization of the dart impact outcome and of the binary asteroid (65803) didymos. *The Planetary Science Journal*, 3(7), 160. <https://doi.org/10.3847/PSJ/ac6f52>
- Morante, D., Sanjurjo Rivo, M., & Soler, M. (2021). A survey on low-thrust trajectory optimization approaches. *Aerospace*, 8(3), 88.
- Morbidelli, A., Jr, W., & Michel, P. (2002). Origin and evolution of near-earth objects. *Asteroids III*, 3.
- NASA. (2022). *NASA State of the Art Small Spacecraft Technology report* (tech. rep.). <https://www.nasa.gov/wp-content/uploads/2023/05/2022-soa-full.pdf>
- NASA JPL. (2023). Small Body database browser [Accessed: 2023-05-12].
- Novak, D., & Vasile, M. (2011). Improved shaping approach to the preliminary design of low-thrust trajectories. *Journal of Guidance, Navigation, and Control*, 34.

- Oneil, W., & Mitchell, R. (1983). Galileo mission overview. *21st Aerospace Sciences Meeting*, 96.
- Pätzold, M., Häusler, B., Tyler, G. L., Andert, T., Asmar, S. W., Bird, M. K., Dehant, V., Hinson, D., Rosenblatt, P., Simpson, R., et al. (2016). Mars express 10 years at mars: Observations by the mars express radio science experiment (mars). *Planetary and Space Science*, 127, 44–90.
- Pei, Z., Wang, Q., & Tian, Y. (2015). Technology roadmap for chang'e program. *Journal of Deep Space Exploration*, 150. <https://doi.org/http://jdse.bit.edu.cn/sktxcb/en/article/doi/10.15982/j.issn.2095-7777.2015.02.00>
- Pirrotta, S., Cotugno, B., di Tana, V., Patruno, S., Ingiosi, F., & Simonetti, S. (2021). Argomoon: The italian cubesat for artemis1 mission. *European Planetary Science Congress*, EPSC2021–879.
- Pizzetti, A., Rizza, A., & Topputo, F. (2023). Autonomous wheel off-loading strategies for deep-space cubesats. *Aerotecnica Missili & Spazio*, 102(1), 3–15.
- Prockter, L., Murchie, S., Cheng, A., Krimigis, S., Farquhar, R., Santo, A., & Trombka, J. (2002). The near shoemaker mission to asteroid 433 eros. *Acta Astronautica*, 51(1-9), 491–500.
- Publications, U. N. (2017). *Handbook on space research communication*. UNITED NATIONS PUBLN. <https://books.google.nl/books?id=kBkLjwEACAAJ>
- Puig-Suari, J., Turner, C., & Ahlgren, W. (2001). Development of the standard cubesat deployer and a cubesat class picosatellite. *2001 IEEE aerospace conference proceedings (Cat. No. 01TH8542)*, 1, 1–347.
- Qin, T., Qiao, D., & Macdonald, M. (2019). Relative Orbit Determination Using Only Intersatellite Range Measurements. *Journal of Guidance, Control, and Dynamics*, 42(3), 703–710. <https://doi.org/10.2514/1.g003819>
- Renzetti, A. (1975, May). *DSN Functions and Facilities* (tech. rep.). [https://ipnpr.jpl.nasa.gov/progress\\_report2/42-28/28A.PDF](https://ipnpr.jpl.nasa.gov/progress_report2/42-28/28A.PDF)
- Ricco, A. J., Santa Maria, S. R., Hanel, R. P., & Bhattacharya, S. (2020). Biosentinel: A 6u nanosatellite for deep-space biological science. *IEEE Aerospace and Electronic Systems Magazine*, 35(3), 6–18.
- Rijlaarsdam, D., Yous, H., Byrne, J., Oddenino, D., Furano, G., & Moloney, D. (2020). A survey of lost-in-space star identification algorithms since 2009. *Sensors*, 20(9). <https://www.mdpi.com/1424-8220/20/9/2579>
- Romaine, S., Kraft, R., Gendreau, K., Crawford, I., Nittler, L. R., Kring, D., Hong, J., Petro, N., Mitchell, J., Winternitz, L., et al. (2018). Cubesat x-ray telescope (cubex) for lunar elemental abundance mapping and millisecond x-ray pulsar navigation. *42nd COSPAR Scientific Assembly*, 42, B0–2.
- Romero Calvo, A., Biggs, J., Topputo, E., et al. (2019). Attitude control for the lumio cubesat in deep space. *INTERNATIONAL ASTRONAUTICAL CONGRESS: IAC PROCEEDINGS*, 1–13.
- Schaub, H., & Junkins, J. L. (2003). *Analytical mechanics of space systems*. Aiaa.
- Schiattarella, V., Spiller, D., & Curti, F. (2017). A novel star identification technique robust to high presence of false objects: The multi-poles algorithm. *Advances in Space Research*, 59(8), 2133–2147. <https://doi.org/https://doi.org/10.1016/j.asr.2017.01.034>

- Schwarz, T. (2015). *Prototyping of a star tracker for pico-satellites* [Doctoral dissertation, Luleå University of Technology].
- Sheikh, S. I., Pines, D. J., Ray, P. S., Wood, K. S., Lovellette, M. N., & Wolff, M. T. (2006). Spacecraft navigation using x-ray pulsars. *Journal of Guidance, Control, and Dynamics*, 29(1), 49–63.
- Silani, E., & Lovera, M. (2006). Star identification algorithms: Novel approach and comparison study. *IEEE Transactions on Aerospace and Electronic Systems*, 42(4), 1275–1288. <https://doi.org/10.1109/TAES.2006.314572>
- Slyuta, E. (2021). Chapter 3 - the luna program. In A. Longobardo (Ed.), *Sample return missions* (pp. 37–78). Elsevier. <https://doi.org/https://doi.org/10.1016/B978-0-12-818330-4.00003-3>
- Soffen, G. A. (1976). Scientific results of the viking missions. *Science*, 194(4271), 1274–1276.
- Solomon, S. C., McNutt, R. L., Gold, R. E., & Domingue, D. L. (2007). Messenger mission overview. *Space Science Reviews*, 131, 3–39.
- Sonett, C. P. (1963). A summary review of the scientific findings of the mariner venus mission. *Space Science Reviews*, 2(6), 751–777.
- Speretta, S., Cervone, A., Sundaramoorthy, P., Noomen, R., Mestry, S., Cipriano, A., Topputo, F., Biggs, J., Di Lizia, P., Massari, M., et al. (2019). Lumio: An autonomous cubesat for lunar exploration. *Space operations: inspiring Humankind's future*, 103–134.
- Spratling, B. B., & Mortari, D. (2009). A survey on star identification algorithms. *Algorithms*, 2(1), 93–107. <https://www.mdpi.com/1999-4893/2/1/93>
- Squyres, S. (2005). *Roving mars: Spirit, opportunity, and the exploration of the red planet*. Hachette UK.
- Tapley, B., Schutz, B., & Born, G. (2004). Chapter 4 - fundamentals of orbit determination. In Elsevier (Ed.), *Statistical orbit determination* (pp. 159–284). Academic Press. <https://doi.org/https://doi.org/10.1016/B978-012683630-1/50023-0>
- Team, A., Riedel, J., Bhaskaran, S., Desai, S., Han, D., Kennedy, B., Null, G., Synnott, S., Wang, T., Werner, R., et al. (2000). Autonomous optical navigation (autonav) ds1 technology validation report. *Jet Propulsion Laboratory, California Institute of Technology*.
- Tsiotras, P. (1995). A passivity approach to attitude stabilization using nonredundant kinematic parameterizations. *Proceedings of 1995 34th IEEE Conference on Decision and Control*, 1, 515–520.
- Turan, E., Speretta, S., & Gill, E. (2022a). Autonomous crosslink radionavigation for a lunar cubesat mission. *Frontiers in Space Technologies*, 3, 919311.
- Turan, E., Speretta, S., & Gill, E. (2022b). Autonomous navigation for deep space small satellites: Scientific and technological advances. *Acta Astronautica*, 193, 56–74. <https://doi.org/https://doi.org/10.1016/j.actaastro.2021.12.030>
- Turan, E., Speretta, S., & Gill, E. (2023). Performance analysis of crosslink radiometric measurement based autonomous orbit determination for cislunar small satellite formations. *Advances in Space Research*, 72(7), 2710–2732.

- Vago, J., Witasse, O., Svedhem, H., Baglioni, P., Haldemann, A., Gianfiglio, G., Blancquaert, T., McCoy, D., & De Groot, R. (2015). Esa exomars program: The next step in exploring mars. *Solar System Research*, 49, 518–528.
- Visser, G. H. (2017). *Development and verification of a star tracker algorithm chain* [Doctoral dissertation, Delft University of Technology].
- Vondrak, R., Keller, J., Chin, G., & Garvin, J. (2010). Lunar reconnaissance orbiter (lro): Observations for lunar exploration and science. *Space science reviews*, 150, 7–22.
- Wahba, G. (1965). A least squares estimate of spacecraft attitude,”. *SIAM Review*, 7(3), 409.
- Walker, L., Di Carlo, M., Greco, C., Vasile, M., & Warden, M. (2021). A mission concept for the low-cost large-scale exploration and characterisation of near earth objects. *Advances in Space Research*, 67(11), 3880–3908.
- Walker, R., Koschny, D., Bramanti, C., & Team, E. C. S. (2017). Miniaturised asteroid remote geophysical observer (m-argo): A stand-alone deep space cubesat system for lowcost science and exploration missions. *6th Interplanetary CubeSat Workshop*.
- Watanabe, S.-i., Tsuda, Y., Yoshikawa, M., Tanaka, S., Saiki, T., & Nakazawa, S. (2017). Hayabusa2 mission overview. *Space Science Reviews*, 208, 3–16.
- Wertz, J., Everett, D., & Puschell, J. (2011). *Space mission engineering: The new smad*. Microcosm Press. <https://books.google.nl/books?id=VmQmtwAACAAJ>
- Wilcox, B., & Nguyen, T. (1998). *Sojourner on mars and lessons learned for future planetary rovers* (tech. rep.). SAE Technical Paper.
- Yoshikawa, M., Kawaguchi, J., Fujiwara, A., & Tsuchiyama, A. (2015). Hayabusa sample return mission. *Asteroids IV*, 1(397-418), 1.

# ACKNOWLEDGEMENTS

In the last four years, or maybe even before starting to pursue a PhD at TU Delft, I have been asked multiple times the questions: 'What is a PhD?', 'What does it mean?', 'Ok, but I didn't understand, do you work or do you study?'. Clearly, these questions were mostly asked by people who do not hold or are not pursuing a PhD, such as my grandparents or peers having a completely different career path. To be fair, I bet that even most of the people holding a PhD would not be able to give a specific definition, valid universally. I have to be honest, I found it very difficult to answer these questions, especially when I started. Initially, I had the feeling that only those who are actually enrolled in a PhD program would be able to give a definition. But I guess I was wrong. First, because I debated multiple times with fellow PhD candidate colleagues about it, and each's definition never matched the other's. Secondly, because my definition has evolved through the years. My latest answer to these questions has been: 'The PhD is a growing process to learn the art of discovering novelties, not only at the technical level'. Be aware that this is my personal definition, and it can collide with yours. Surely, many people would not grasp the essence of this definition, but it is the best I can do. Furthermore, I learnt that a PhD is more than a simple job because a PhD candidate has two bosses. Obviously, the first is your supervisory team, which demands results as any other boss in a different job. The second is yourself, because, at the end of the day, you need to produce results to graduate at some point. So, here is the first contradiction with my definition: how can a growing process be so deeply connected with producing (publishable) results? The answer to this question is something that I indeed learned during the process, as part of it is to understand how to aid for results, and more importantly when to stop a certain analysis without ending up in a bottomless spiral.

Being my personal definition and my personal growing process, I decided to metaphorically describe my PhD experience through the opening quote of each chapter. First, you start by realizing that actually you do not know anything (Chapter 1). Then, you find motivation in understanding that even if your contribution will be small, you will still be contributing (Chapter 2), and so you start with your work (Chapter 3). After an initial disorientation, you find your path (Chapter 4), and at a certain point, you start seeing everything more clearly (Chapter 5). However, it is only when you realize that no matter how good you are (or you think you are), you cannot do everything by yourself, and you can learn a lot from people working with you (Chapter 6). Finally, when you look back at what you achieved, you realized that your results were only possible thanks to the amount of other people's work before you (Chapter 7).

I have to say that the essence of this growing process is indeed deeply related to the people around you (as I suggest with the Chapter 6 quote), from all perspectives, not necessarily technical. This is why I wish to spend some words to thank all the people who played a role, even minimal, in achieving this result.

I want to thank all the supervisors who guided me through these four years. Dr. An-



gelo Cervone, my daily supervisor, had the ability to leave me freedom in the research and be present whenever I needed guidance. Listening to stories of other PhD friends (luckily not in our department) who struggled to receive any kind of feedback from their supervisors, I felt very lucky to have a daily supervisor whose responses consistently reached me within an hour of my inquiries. Dr. Bert Monna, my industrial supervisor, always provided me with keen opinions, different perspectives, and out-of-the-box advice that helped throughout my entire research. Prof. Eberahrd Gill, my promotor during the first two years, shared with me his experience that guided me through the definition of the research project. Prof. Pieter Visser, my promotor in the last two years, dived very quickly into the research topic and guided me through my last years with his experience and technical knowledge, adding an important perspective on my research.

Remaining on the technical side, a special thanks goes to Prof. Francesco Topputo, who hosted me for three months at his DART Lab, and Dr. Paolo Panicucci, for guiding me through the set-up of the hardware-in-the-loop testing for star trackers.

At TU Delft I met many special individuals, my DEAR COLLEAGUES. I wish to thank (in alphabetic order, so don't get offended) Erdem, for sharing every single important step of these four years, Fiona, for being the most welcoming person ever during my beginning, Joshua, for being the kindest and most helping person in the Solar System, Lorenzo, for being the coolest colleague I could ask for, Mario, for forcing me in coming to the gym and helping me to practice my Spanish, Rens, for standing my daily dose of bad jokes without reporting to HR, Sevket, for being the wisest advisor on many troubles I had, Victor, for teaching me how to guide the new PhDs at their start (also Mario, Rens, and Josh thank you I guess), and all the others, Ruipeng, Jingyi, Rashik, Pallab, Gitte for sharing lunches and coffees through these years.

During these four years in Delft, I shared many moments with incredible people. I could write a book on each of you, so forgive me if I have to summarize my thanks in a few words. Again here in alphabetical order, I thank Arianna, for being a special friend always ready to listen to my complaints, help me and have fun, Ari and Ste, for bringing a healthy dose of swag on our nights out, Brent, for introducing me to the guru Zedpapi, Caffettino for sharing literally everything, from football discussions to padel, from apple pies to beers, Ceci1, for being a sagoma, Ceci2, for being a happy presence in our life, Edo, for sharing many funny moments and introducing me to Poing, Gigi, for his incredibly high culinarian abilities, Lisa and Matte, for being the kindest friends I could meet, O' Fraaa, for sharing the funniest memories, from Bar Sil to entrepreneurship, and Uncio, for never actually leaving Delft. We shared many happy moments, but we also needed to go through together a disgraceful tragedy. This harsh moment we went through together contributed to redefining the important values that we have in life. I am grateful I crossed my path with Debe, and I am sure his memory will always be at my (and our) side.

I wish to remember that one of the reasons why I came to Delft for a PhD is Livia, as I was complaining about my previous job and she had the brilliant idea of telling me 'Why don't you come to Delft for a PhD?'. So, I found the position and I applied. But besides that, Livia has been a large part of my stay in Delft, ranging from the multiple times she hosted me for dinner, to the thousands of questions she received regarding PhD related things. So, thank you. Ah yes, thanks also to Alessandro.

In four years I changed three houses and 4/5 flatmates, but special thanks go to Ombretta and il signor Jonathan Ben Kamp for sharing with me the first months of the pandemic. I think Ombretta somehow helped us in keeping our mental health, while I really thank il signor Jonathan Ben Kamp for sharing hours and hours on the football pitch in front of our house. Lately, I met and started living with Alessandro, who I will never thank enough for standing my mental and physical chaos.

During my three months in Milan, I met wonderful people, in particular Alessandro, Andrea, Carmine, Claudio, Felice, Gianfranco, Gianmario, Mattia, Paolo (here as a friend and not as a supervisor), who made my stay very special.

Special thanks to all my friends from Roma, who made me feel welcome every time I came back, Alessandro, Alice, Augusto, Davide, Francesco, Gianluca, Giorgio, Lorenzo, Tommaso, and Vincenzo.

Covid has been a harsh period for everybody, but I have to say that thanks to Alessandro, Andrea, Gabriele, Leonardo, Massimo, Mattia, Nicolo', Pier, and our online gaming sessions I somehow managed to keep my mental health in order.

I wish to thank all my family, my grandparents, Bruna and Franco, for their guidance and wisdom, my aunt Silvia and my uncle Andrea, and my cousins, Francesco and Davide, for the unconditional love they showed me despite the distance.

I wish to thank my brother, Matteo, because, even if he doesn't know it, his strength and commitment during harsh times have been inspirational to me, and have provided me with new perspectives on many things.

The PhD is just the tip of the iceberg of a process that started 29 years ago. Even though my parents, Laura and Diego, did not play an active role in the PhD perse', they have always helped and supported me through every decision I made. I wish to thank them for the values they transmitted to me since when I was a kid, and for all the time I received help without asking (and often without saying thank you). The combination of all these small pieces made me the person I am today, and if today I am a person who's defending a PhD, it is for sure their merit.

All of these people played major and minor roles in my PhD, but nobody has helped me as much as Dionysia, even if she doesn't know anything about space engineering. I wish to thank her for being at my side through this process, for her patience in standing me during my bad mood periods, and more importantly for her underlying resilience, which served as a profound source of motivation over the years. Besides the love she always gave me, aspiring to embody her qualities and values has served as a beacon, guiding me toward maintaining balance and order in my life. I am grateful to have shared with her successes and failures over the last five years.





# NAVIGATION REQUIREMENTS

The definition of requirements is necessary to assess the applicability of a specific navigation technique to the mission scenario. In this dissertation, the attention is focused on asteroid (in particular NEA) missions, as in this framework the exploitation of miniaturized satellites can have a significant impact. Navigation requirements for the close proximity phase are related to the scientific return that can be achieved with such missions. Requirements for cruising are connected to the required estimation error when it comes to correcting the trajectory towards the target when it is identified by the spacecraft imager. Then, requirements can be defined considering three main contributions:

- the asteroid detectability prior to fly-by, which defines the time frame when correction manoeuvres can be actuated;
- the asteroid ephemeris uncertainties, which quantifies the region where the target is expected to be during the fly-by;
- the available  $\Delta V$  budget, which defines how much the nominal trajectory can be deviated to compensate for the actual position of the asteroid.

This section shows the requirements specification for absolute navigation at the end of the cruising phase. In other words, the required position and velocity accuracy needed at the end of the absolute navigation around the Sun, to enter successfully the relative navigation phase in the close proximity of the fly-by.

First, asteroid position (and velocity) uncertainties are quantified, then the correction manoeuvres are considered, followed by consideration of the star tracker performances for optical navigation. Finally, all the considerations are summed up to define requirements.

## A.1. ASTEROID EPHEMERIS UNCERTAINTIES

Asteroids orbital parameters are constantly updated by many institutions by means of ground observation. Pisa University, sponsored by ESA, provides the orbital characteris-

tics of 33583 objects, available at NeoDys<sup>1</sup>. However, if orbit determination is not performed to update the asteroid ephemeris, the position and velocity uncertainties grow with time. This is the case of autonomous CubeSats, which cannot receive target asteroid updated ephemeris and they have to rely on the propagated ephemeris available prior to the launch date. In the best-case scenario, the last ephemeris update will be on the launch date, but this implies problems with the integration of the satellite in the launcher, so the last update is more likely to happen some days before the integration. A semi-autonomous CubeSat would limit this drawback by receiving from the ground the updated ephemeris. However, a completely autonomous CubeSat is intended as a system which only downlinks data.

So the ephemeris of the target asteroid should be stored onboard and propagated to define the uncertainties in position and velocity at the fly-by time.

To estimate the uncertainties of the asteroid ephemeris at the fly-by time, first, the initial uncertainties at the launch time are converted to cartesian coordinates (from orbital parameters available on the database) via a Monte Carlo simulation, then the covariance matrix is propagated as:

$$P_{end} = \Phi(t_0, t_{end})P_0\Phi^T(t_0, t_{end}) \quad (\text{A.1})$$

where  $\Phi(t_0, t_{end})$  is the state (deviation) transition matrix obtained with a 2-Body Problem approach.

Finally, the propagation time strongly depends on the mission scenario. Asteroid targeting trajectory may take from 100 up to 900 days.

A sample calculation is carried out for two representative cases, considering 300 days as an average Time-of-Flight (ToF). The initial date is set as 31st May 2020. It is important to remark that every mission has specific requirements, depending on the actual target and on the cruising phase length. However, this section is aimed to show the suggested procedure and to understand the range of required estimation accuracy. For these reasons, two well-known NEAs are considered, namely (433) Eros and (2100) Ra-Shalom.

### A.1.1. (433) EROS UNCERTAINTIES PROPAGATION

Initial orbital parameters and uncertainties are reported in Table A.1 (from the NeoDys2 database).

Parameter	Numerical Value	1- $\sigma$ accuracy	Units
a	1.45805	$2.42 \cdot 10^{-10}$	AU
e	0.222951	$1.004 \cdot 10^{-8}$	-
i	10.831	$2.436 \cdot 10^{-6}$	deg
$\Omega$	304.299	$9.865 \cdot 10^{-6}$	deg
$\omega$	178.882	$1.092 \cdot 10^{-5}$	deg
$\nu$	271.072	$2.903 \cdot 10^{-6}$	deg

Table A.1: (433) Eros initial conditions and uncertainties

<sup>1</sup> <https://newton.spacedys.com/neodys/index.php?pc=0>

The Monte Carlo conversion in cartesian coordinates leads to the initial uncertainty ellipsoid presented in Figure A.1. Here the initial covariance is assumed to be diagonal and the largest uncertainty axis is in the z-direction, and it is contained within 250 km. When this uncertainty ellipsoid is propagated for 300 days, it grows in size, leading to Figure A.2. The final ellipsoid is characterized by significantly larger uncertainties, up to 2000 km, and it loses its initial symmetry. Similar considerations can be derived for the velocity uncertainty ellipsoid, however, for simplicity, only position is considered for the generation of requirements, considering that the ratio between velocity and position errors scales down approximately as the mean motion of the satellite's orbit.

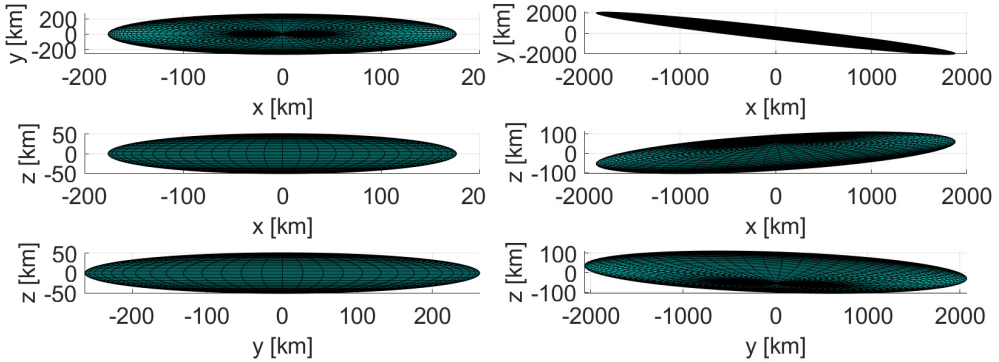


Figure A.1: Initial positions uncertainty ellipsoid for (433) Eros. Figure A.2: Final positions uncertainty ellipsoid for (433) Eros.

### A.1.2. (2100) RA-SHALOM UNCERTAINTIES PROPAGATION

Initial orbital parameters and uncertainties are reported in Table A.2.

Parameter	Numerical Value	1- $\sigma$ accuracy	Unites
a	0.832048	$1.794 \cdot 10^{-10}$	AU
e	0.436543	$1.436543 \cdot 10^{-8}$	-
i	15.753	$7.172 \cdot 10^{-7}$	deg
$\Omega$	170.804	$4.438 \cdot 10^{-6}$	deg
$\omega$	356.051	$2.425 \cdot 10^{-6}$	deg
$\nu$	171.762	$8.999 \cdot 10^{-6}$	deg

Table A.2: (2100) Ra-Shalom initial conditions and uncertainties

Following the same approach adopted before, these values are converted in Cartesian coordinates, whose uncertainty ellipsoid can be observed in Figure A.3. Figure A.4 shows the evolution of the ellipsoid after 300 days of propagation. The initial maximum uncertainty below 150 km is propagated in a larger maximum uncertainty below 1500 km.

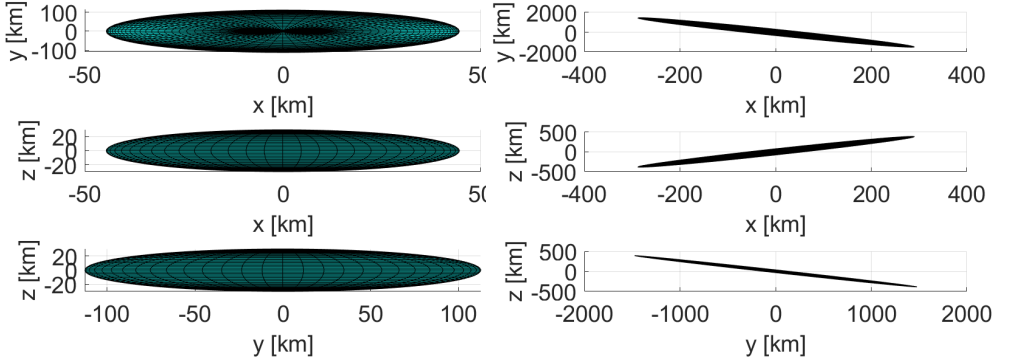


Figure A.3: Initial positions uncertainty ellipsoid for (2100) Ra-Shalom. Figure A.4: Final positions uncertainty ellipsoid for (2100) Ra-Shalom.

It is important to remark again that these values are representative of these two asteroids, and can differ from other targets by small quantities. Moreover, a larger ToF would imply even larger uncertainty in the final position of the asteroid. However, these two examples allow us to identify the range of expected uncertainty at the fly-by time. This value is later coupled with two other considerations:  $\Delta V$  capabilities and asteroid observability.

## A.2. DETECTABLE MAGNITUDE

Celestial bodies, including stars, planets, and asteroids, are characterized by a certain apparent magnitude, which quantifies their brightness. The scale uses Vega as a reference, whose magnitude is chosen as 0. The scale is reverse logarithmic ( $-2.5 \log_{10}$ ), meaning that the larger the number, the lower the brightness. This means that a star with magnitude 0 is 2.512 times as bright as a star with magnitude 1.

Micro star trackers available for CubeSats usually are not able to detect very faint objects. The most performant star trackers are able to detect objects up to an apparent magnitude of 7. On the other hand, asteroids are by nature really faint objects because of their small dimension and their surface composition which reflect the solar light. In other words, the asteroid can be detected onboard by the star trackers just some days before the fly-by, so the actual time slot available to correct the spacecraft trajectory is small.

It is possible to describe the phase curves of the asteroid, which represent the apparent magnitude of the body as (Dymock, 2007):

$$V = H + 5 \log_{10}(r\Delta) - 2.5 \log_{10}((1 - G)e^{-3.33atan^{0.63}(\alpha/2)} + Ge^{-1.87atan^{1.22}(\alpha/2)}) \quad (\text{A.2})$$

where  $H$  is the absolute magnitude,  $r$  is the relative distance spacecraft-asteroid,  $\Delta$  is the distance Sun-asteroid, and  $\alpha$  is the phase angle (the angle between the two directions).  $G$  is defined as the slope parameter, mainly depending on the albedo of the asteroid, and it quantifies how fast the apparent magnitude increases when the distance from

the observer decreases. Figures A.5 and A.6 show the apparent magnitude of (433) Eros ( $H=10.9$ ,  $G=0.46$ ) respectively at its perihelion and aphelion, as a function of the relative distance from the observer and the phase angle.

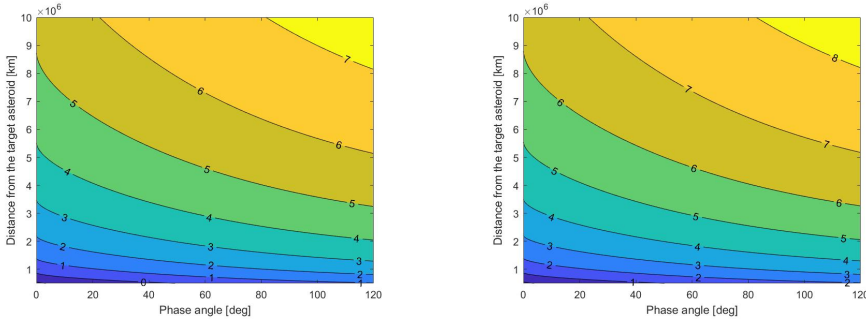


Figure A.5: Eros apparent magnitude at orbit's perihelion. Figure A.6: Eros apparent magnitude at orbit's aphelion.

By reversing the process used to generate the apparent magnitude plots, it is possible to fix a certain magnitude (7 in this case, corresponding to the star tracker limit) to determine the relative distance at which the asteroid has that apparent magnitude as a function of the phase angle and the distance asteroid-Sun. This relative distance represents the maximum distance at which the asteroid will appear in the Field-of-View (FoV). After that, it is possible to approximate as linear the spacecraft motion to compute how many days before the actual fly-by the asteroid will be visible for relative navigation and correction manoeuvres. For numerical computation, a heliocentric velocity of 27 km/s is assumed, since many interesting NEA targets have a semi-major axis slightly larger than Earth's, so the transfer orbit's velocity would be slightly less than the Earth's velocity. This leads to the plot reported in Figure A.7, showing how many days before the fly-by the asteroid will be actually visible from the onboard instrumentation, still as a function of the phase angle and distance asteroid-Sun. The plot shows indeed that in the best case, the asteroid will be detectable 7-8 days before the fly-by, so the actual correction capabilities (to compensate for position accuracy) are reduced.

### A.3. $\Delta V$ CAPABILITIES

The  $\Delta V$  budget is strongly connected with navigation requirements because it represents the control capability of the CubeSat to correct its trajectory towards the asteroid when both states (asteroid and CubeSat) are uncertain.

This means that the propulsion system needs to be able to compensate for the possible position uncertainties, and the time of the actuation will depend on the detectability of the asteroid as explained in the previous section.

It is possible to calculate the displacement from the nominal trajectory end position as a function of the impulsive  $\Delta V$ , the time interval between the actuation and the fly-by, and the direction of thrusting. For numerical computation, a 1.1 AU circular heliocentric orbit has been considered since it is characterized by constant velocity and can be



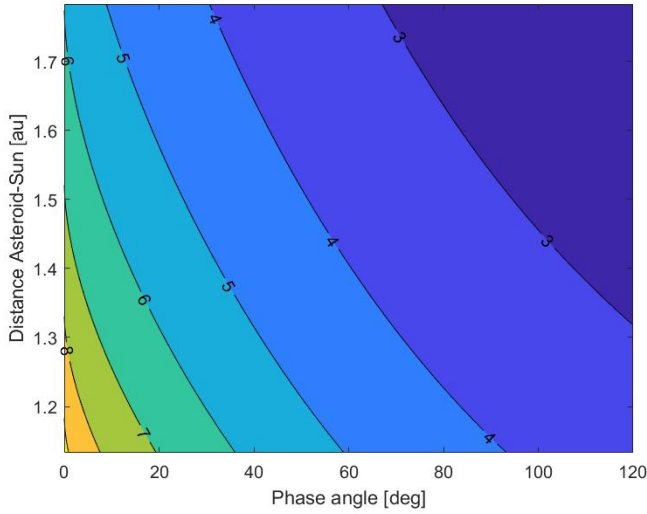


Figure A.7: (433) Eros visibility in terms of days before fly-by

used to simulate NEA region missions. Then, a certain  $\Delta V$  is applied in multiple directions, and the final displacement from the nominal orbit is computed as a function of the thrust direction and the time interval after the actuation. Figures A.8 and A.9 show the allowable displacement from the nominal position as a function of the time interval between the manoeuvre and fly-by dates, and of the correction  $\Delta V$  direction, respectively for  $\Delta V = 5\text{ m/s}$  and  $\Delta V = 10\text{ m/s}$ . The allowable displacement is visualized from all perspectives and has a symmetric behaviour. The plots show a simplified approach (2-body problem propagation and impulsive manoeuvre) which is enough to quantify how much the  $\Delta V$  and the manoeuvre date influence the final displacement from the nominal end position, which may be corrected to take into account the uncertainties in the state of the asteroid and in the state of the CubeSat, which needs to be set as a requirement after all these considerations. The set of reachable positions increases as the days prior to fly-by and/or the available  $\Delta V$  increase. With  $\Delta V$  in the range of 5-10 m/s, a few days before the fly-by, it is possible to correct the trajectory by some thousands of km.

It has to be remarked that more complicated trajectory correction strategies can be actuated, but these plots give much information on the sensibility of correction manoeuvres and they can be incorporated in the navigation requirements definition.

#### A.4. REQUIREMENTS DEFINITION

Coupling the considerations presented in the previous sections, the navigation requirements definition should follow the following approach:

- Define a nominal trajectory;

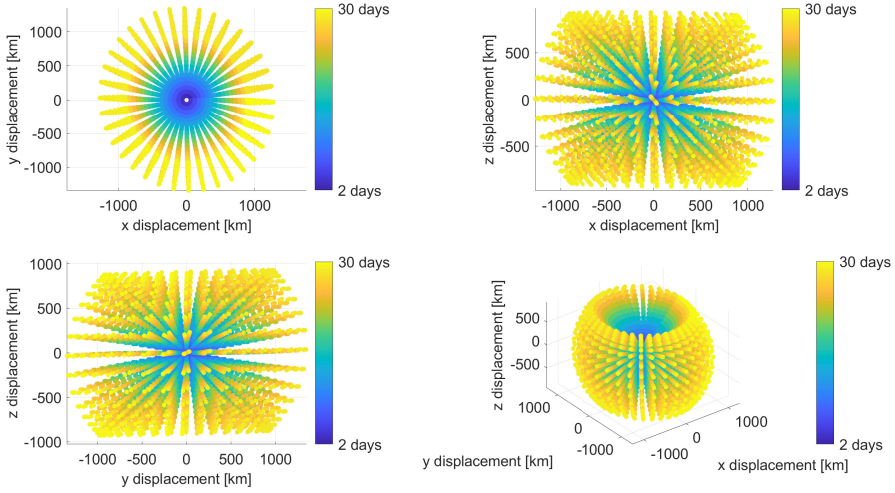


Figure A.8: Allowable displacement for  $\Delta V = 5/\text{ms}$  as a function of the thrust direction and the time interval between fly-by and manoeuvre dates.

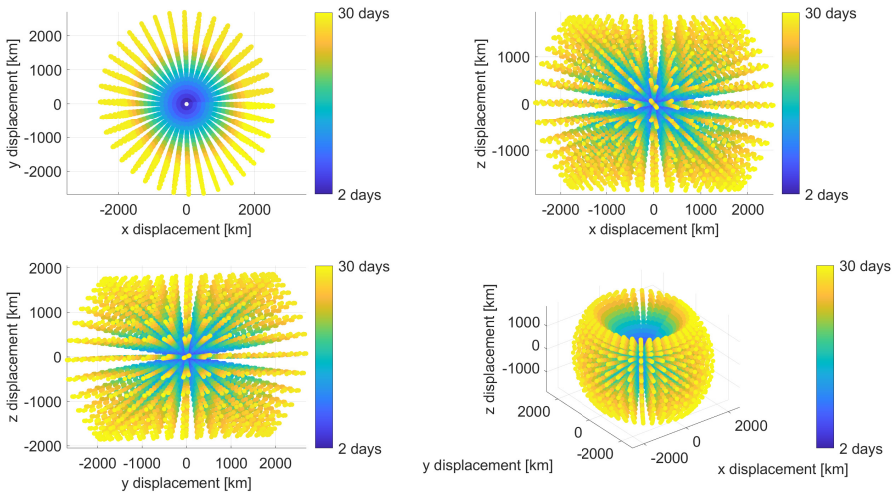


Figure A.9: Allowable displacement for  $\Delta V = 10/\text{ms}$  as a function of the thrust direction and the time interval between fly-by and manoeuvre dates.

- Evaluate the apparent magnitude of the asteroid as a function of the relative distance observer-asteroid, Sun-asteroid, and the phase angle;
- By linearizing the problem and by setting the detectable magnitude limit of the star tracker, estimate how many days before the fly-by, the asteroid will be visible

in the FoV to start the relative navigation and correction manoeuvres;

- Evaluate the correction capabilities of the spacecraft on the day the relative navigation begins (see previous bullet) as a function of the available  $\Delta V$ ;
- Retrieve the asteroid position uncertainties ellipsoid;
- Link the correction capabilities to the asteroid ellipsoid to define the maximum allowable position uncertainties of the CubeSat.

In the case of asteroid (433) Eros will be visible 8 days before fly-by (best case). Figure A.10 shows the correction capabilities 8 days before the fly-by. Assuming  $\Delta V = 5 \text{ m/s}$ , the plots show that the CubeSat can be deviated by approximately 3000 km in 8 days. This means that, considering the worst-case scenario, the CubeSat position should be known within 1500 km accuracy, in order to redirect it to the asteroid. This can be further lowered to 1000 km as a margin, to take into account possible delayed manoeuvres or asteroid detection, larger asteroid uncertainties, and non-idealities.

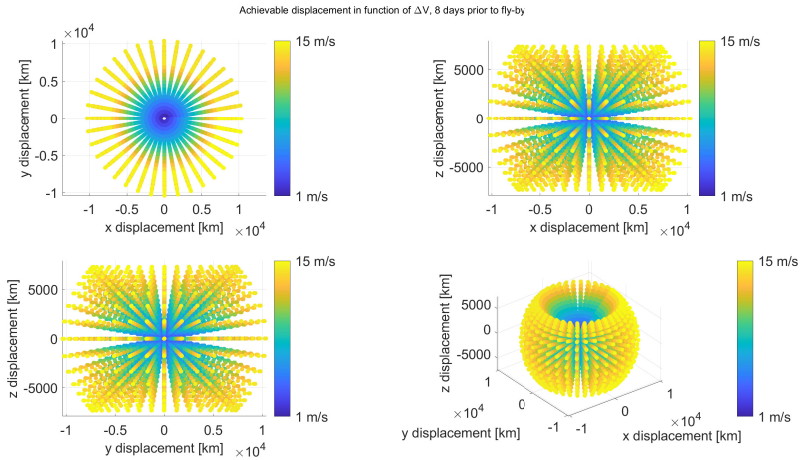


Figure A.10: (433) Eros correction capabilities 8 days before fly-by

This simplified approach can be improved to obtain a more accurate estimation. As it has been remarked, many assumptions have been made. The strongest are:

- 2-body problem propagation both for asteroid uncertainties and control capabilities;
- linear approach to defining the asteroid visibility vs days before the fly-by.

However, this approach is useful to define a rough number for navigation accuracy requirements in terms of position.

It is possible to compute the velocity navigation requirements exploiting the mean motion of the satellite because it is in the same order as the ratio of velocity accuracy

and position accuracy. For a CubeSat in a heliocentric transfer with a semi-major axis equal to 1.1 AU, the mean motion is  $1.72575 \cdot 10^{-7} s^{-1}$ .

Finally, each asteroid has different characteristics (ephemerides uncertainties, brightness, etc.), so this approach should be followed to define requirements for each mission and target, but in general, the position requirements can be assumed around  $3\sigma = 1000 km$ , and therefore, exploiting the mean motion, the velocity requirement can be assumed around  $3\sigma = 1e^{-4} km/s$ .



# CURRICULUM VITÆ

## Stefano CASINI

05-08-1994      Born in Rome, Italy.

### EDUCATION

2013–2016      BSc in Aerospace Engineering  
Sapienza University of Rome

2016–2019      MSc in Space and Astronautical Engineering  
Sapienza University of Rome

2019–2024      PhD in Aerospace Engineering  
Delft University of Technology

### WORK EXPERIENCE

2018–2019      Thermal Engineer  
Italian National Institute for Nuclear Physics (INFN)

2024–Now      AOCS and GNC Engineer  
OHB System AG

### EXCHANGE EXPERIENCE

2015              Erasmus+ Mobility  
Universidad Carlos III (Madrid)

2018              Erasmus+ Mobility  
Instituto Superior Tecnico (Lisbon)

2021              Visiting Research Period  
  
Polytechnic University of Milan



# LIST OF PUBLICATIONS

## JOURNAL

4. **S. Casini, E. Turan, A. Cervone, B. Monna, P. Visser**, *Combined optical line-of-sight and crosslink radiometric navigation for distributed deep-space systems*, [Scientific Reports](#) **13**, 1 (2023).
3. **S. Casini, A. Cervone, B. Monna, P. Visser**, *Design and testing of star tracker algorithms for autonomous optical line-of-sight deep-space navigation*, [Applied Optics](#) **62**, 22 (2023).
2. **S. Casini, A. Cervone, B. Monna, E. Gill**, *On line-of-sight navigation for deep-space applications: A performance analysis*, [Advances in Space Research](#) **72**, 7 (2023).
1. **S. Casini, I. Fodde, B. Monna, A. Cervone, E. Gill**, *Novel 3U stand-alone cubesat architecture for autonomous near earth asteroid fly-by*, [Aerospace](#) **8**, 1 (2020).

## CONFERENCE

3. **S. Casini, A. Cervone, B. Monna, P. Visser**, *Simulation of deep-space autonomous Line-of-Sight navigation using synthetic images in the loop*, International Astronautical Congress, Baku, Azerbaijan, 2-6 October 2023.
2. **S. Casini, A. Cervone, B. Monna, P. Visser**, *Line-of-Sight Navigation Observability Analysis for Near-Earth Asteroids Exploration with CubeSat*, International Astronautical Congress, Paris, France, 18-22 September 2022.
1. **S. Casini, I. Fodde, A. Cervone, B. Monna, E. Gill**, *Towards the Use of Commercial-off-the-Shelf Small-Satellite Components for Deep-Space CubeSats: a Feasibility and Performance Analysis*, SmallSat Conference, Logan, Utah, August 2020.

## BEFORE PHD

2. **S. Casini**, *Thermal Influence of the Screw Axial Load on a 1-mm Accuracy Laser Ranged Satellite*, [Aerotecnica Missili & Spazio](#) **98**, 3 (2019).
1. **L. Pollice, G. Cascioli, L. Federici, P. Iannelli, I. Di Stefano, M. Ciallella, S. Casini, S. De Gasperis, F. Corallo, CA. Rasoni, V. Filice, M. Eugeni, G. Palermo, P. Gaudenzi**, *A Preliminary Design of a Mission to Triton: A Concurrent Engineering Approach*, [Advances in Astro-nautics Science and Technology](#) **1**, 1 (2018).